

IMAGING AND INVERSION OF REFLECTED SURFACE WAVES

A Dissertation Presented to
the Faculty of the Department of Earth and Atmospheric Sciences
University of Houston

In Partial Fulfillment
of the Requirements for the Degree
Doctor of Philosophy

By

Craig W. Hyslop

May 2015

IMAGING AND INVERSION OF REFLECTED SURFACE WAVES

Craig W. Hyslop

APPROVED:

Dr. Robert R. Stewart, Chairman

Dr. Aibing Li

Dr. Stig Hestholm

Dr. Robert W. Wiley

**Dean, College of Natural Sciences and
Mathematics**

ACKNOWLEDGEMENTS

My sincerest thanks go to Dr. Robert R. Stewart for his enthusiastic encouragement and guidance throughout all stages of this research. I offer my thanks to Dr. Stig Hestholm whose corrections and suggestions have greatly improved the manuscript. My appreciation goes to Dr. Aibing Li and Dr. Robert W. Wiley for their valuable comments and useful critiques. I extend my grateful thanks to Allied Geophysical Labs, in particular, Nikolay Dyaur and Anoop William; both generously donated their time and expertise, providing me with a treasure trove of data from the lab and the field.

I have had the fortune throughout my studies to have been in contact with many brilliant experts in the field of geophysics. I am deeply indebted to insight and assistance given by Gert-Jan van Groenestijn, Mamadou Diallo, Chris Krohn, Warren Ross, and Valeriy Brytik.

My deepest gratitude goes to my wife, who has supported me throughout my struggles toward this goal and has patiently offered her encouragement and love.

IMAGING AND INVERSION OF REFLECTED SURFACE WAVES

An Abstract of a Dissertation

Presented to

the Faculty of the Department of Earth and Atmospheric Sciences

University of Houston

In Partial Fulfillment

of the Requirements for the Degree

Doctor of Philosophy

By

Craig W. Hyslop

May 2015

ABSTRACT

Surface waves that reflect, or backscatter, from lateral changes in the near surface provide information about the location and depth of anomalies as well as their properties such as reflectivity and velocity. We develop 2D and 3D algorithms that forward model surface waves and image surface-wave reflectors. Our forward model is based on surface-wave propagation in a vertically layered model. We extend solutions to account for lateral heterogeneity in 2D and 3D.

By using high-resolution dispersion-curve estimation and array-windowing schemes, we improve upon existing methods of determining shear-wave velocity from direct surface waves. Surface-wave reflection imaging along the survey line provides a 2D estimate of lateral surface-wave reflectivity as a function of spatial location and frequency (or depth). The 2D reflectivity image has sharper lateral resolution than shear-wave velocity models estimated from direct surface-waves. We verify our method of modeling and extracting reflectivity using numerical and physical modeling. The normalized root-mean-square deviation between our forward modeling and extracted reflectivity from data generated by SPECFEM2D is 14%. Extracted reflectivity from a physical model with a vertical fault also matches reflectivity predictions. Reflectivity maps from Hockley Fault near Houston, Texas are consistent with evidence for faults in traditional body-wave reflection images.

By modifying the dispersion relations for wavefield extrapolation methods, we model and migrate surface-waves across the 2D free surface to create a 3D reflectivity image. Given a single survey line we show that the wavefield within the direct surface-wave cone, often identified as noise, contains valuable reflections that should be used for imaging. Migrated surface-wave images from the Bradford 3D seismic survey in Pennsylvania and seismic data from the Arctic Slope of Alaska correspond to topographical features in the

area. Using synthetic models, we show that having sources and receivers within the image greatly improves migration results.

We use reflectivity to update surface-wave phase-velocities (determined by picking dispersion curves) across the survey line. By inverting the updated phase-velocities, we estimate a shear-wave velocity model that is sharply defined in the lateral direction. The updated velocity model for the Hockley Fault system near Houston, Texas helps identify normal faulting and a small graben feature near the main fault. Imaging and inversion of reflected surface waves promises to deliver an augmented picture of the near surface.

Contents

Introduction	1
1 Modeling surface waves: Fundamentals	5
1.1 Overview	5
1.2 Body waves and surface waves	6
1.3 Inhomogeneous waves	7
1.4 Equation of motion	11
1.5 Love waves	16
1.5.1 Love wave modes	20
1.6 Rayleigh waves: free case	23
1.7 Vertically stratified layers	27
1.8 Phase and group velocity	35
1.9 Summary	37
2 Modeling surface waves: 2D	38
2.1 Overview	38
2.2 Numerical modeling	39
2.2.1 Finite difference	41
2.2.2 Spectral elements	46
2.2.3 Elements and meshing	53
2.3 Semi-analytic modeling	59
2.3.1 Modeling surface-wave reflections with elastic properties	61
2.3.2 Modeling surface-wave reflections using phase velocities	65
2.3.3 Elastic properties versus phase-velocities for reflection coefficients	66
2.3.4 Source wavelet effect	68
2.3.5 Modeling shot record with semi-analytic method	70
2.4 Comparison of 2D methods	73
2.5 Summary	75
3 Imaging using surface waves: 2D	77
3.1 Overview	77
3.2 Multi-channel phase-velocity estimation and inversion	79
3.2.1 Synthetic example	80
3.2.2 Determining lateral phase-velocity variation.	81
3.2.3 High-resolution dispersion imaging	83
3.2.4 Dispersion image resolution	87
3.2.5 Multi-channel windowing schemes	89

3.2.6	Inversion for shear-wave velocity	94
3.3	Estimating surface-wave reflectivity	98
3.3.1	Step 1: Separating the wavefield	99
3.3.2	Step 2: Isolating incident reflections	104
3.3.3	Step 3: Create reflectivity map	107
3.3.4	Example: Physical Model, 2D line perpendicular to fault	115
3.3.5	Example: Field, Hockley 2D line	122
3.3.6	Example: Multi-line processing	129
3.3.7	Example: Sub-vertical faults	131
3.4	Summary	137
4	Modeling surface waves: 3D	138
4.1	Overview	138
4.2	One-way surface-wavefield extrapolation	139
4.2.1	Theory	139
4.2.2	Example	145
4.3	Two-way surface-wavefield extrapolation	148
4.3.1	Theory	148
4.3.2	Examples	149
4.4	Summary	154
5	Imaging using surface waves: 3D	155
5.1	Overview	155
5.2	Imaging condition	156
5.2.1	Option 1: Ray-traced time curve	157
5.2.2	Option 2: Cross-correlation	157
5.2.3	Option 3: Deconvolution	158
5.3	Example: Imaging conditions	159
5.3.1	Comparison: time curve, correlation, and deconvolution	159
5.3.2	Extrapolating wavefields	163
5.4	Example: Physical Model, 2D line 20 degrees to fault	165
5.5	Example: Complex Synthetic	171
5.6	Example: Field, Bradford	174
5.7	Example: Field, Arctic Slope, Alaska	179
5.8	Dual-receiver lines and wavefield separation	182
5.8.1	Theory	184
5.8.2	Example: Synthetic	185
5.9	Multi-receiver line migration	191
5.9.1	Theory	191
5.9.2	Example: Synthetic	192
5.9.3	Example: Multi-shot finite-difference	193
5.9.4	Migration	197
5.10	Summary	201
6	Estimating shear-wave velocity from reflectivity	203
6.1	Overview	203
6.2	Theory	205
6.3	Reflected surface-wave processing vs. Direct surface-wave processing	209

6.4	Example: Field, Hockley 2D line	211
6.5	Summary	214
Conclusions		215

Introduction

Depending on the model and particle motions of an incident wave, boundary conditions at the free surface set up two unique types of surface waves, the Love wave and the Rayleigh wave. Love waves arise when the SH-wave becomes trapped by becoming post-critical in the layer between the free surface and a lower boundary. Rayleigh waves arise solely from special boundary conditions at the free surface where P and SV waves couple. Surface-waves have a unique quality in that particle displacement decays exponentially from the free surface.

When a Rayleigh or Love wave propagates across the free-surface of a model in which differing vertical layers of shear-wave velocities exist below, the surface wave will extend into, or see, different layers depending on its frequency spectrum. Small wavelengths are sensitive only to shallow layers and larger wavelengths are sensitive to deeper layers. It follows that the actual velocity of the surface-wave in terms of its phase (i.e. phase-velocity), differs as a function of frequency. This type of propagation is called dispersion and surface-wave phase-velocity is often referred to as a dispersion-curve. The summation of different wavelengths of phase-velocities across the continuum of frequencies form an envelope traveling at the group-velocity. In layered models, in addition to the fundamental-mode dispersion-curve, higher-mode dispersion-curves exist due to the harmonic nature of surface waves.

The relationship between surface-wave phase-velocity and shear-wave velocity of the model is a useful tool in near-surface exploration. Investigation based on surface-wave phase-velocity generally follow the steps of (1) extracting dispersion curves to determine phase-velocities per frequency (Nazarian, 1984, Park et al., 1998, Stokoe et al., 1989) and (2) inverting phase-velocity as a function of frequency to shear-wave velocity as a function of depth (Xia et al., 1999). Phase-velocity inversion is a 1D operation. To extend the method to 2D and capture lateral change in the model, it is common to determine many 1D shear-wave velocity profiles from corresponding 1D dispersion-curve inversions in an area and combine the results spatially in 2D or 3D by interpolation. As a result, lateral change is smooth and not as well defined as vertical change.

An alternative to surface wave phase-velocity inversion are group-velocity techniques such as ray-based surface-wave tomography (Kafka and Reiter, 1987, Long and Kocaoglu, 1999, Tarr, 1969), and wave-based surface-wave tomography, (Abbott et al., 2006) and (Haney and Douma, 2010). An inversion is posed to determine the shear-wave velocity model by setting up an objective function which matches the travel-times between simulated seismic data and recorded data. Surface wave tomography is inherently a 2D or 3D operation, providing an effective determination of smooth lateral change in the model.

One may also devise an inversion to match the entire waveform, not just time-arrivals, resulting in a higher resolution model than travel-time tomography (Operto et al., 2004). Given advances in modeling the seismic surface-waves (Komatitsch and Tromp, 2002) and the application of the adjoint method (Tarantola, 1984), full-waveform inversions are an attractive technique. However, there are substantial challenges inherent to the method. It is non-unique and under-determined, and it requires powerful computers to run complex seismic propagation simulations and invert large matrices. Also, all tomography methods

use the direct surface-wave and are limited by the bin size, thereby only providing smooth lateral change in the model.

Another approach to resolve lateral change in the model is to use surface-wave scattering and reflections. Given a known shear-wave velocity model, an approximate integral can be used to represent the wave field of laterally scattered surface waves (Blonk and Herman, 1994), and by re-framing the problem, upcoming body waves that scatter to surface waves can also be used for imaging scatterer distribution (Campman et al., 2005).

Surface-waves that scatter and reflect contain unique information about sharp model properties at depth as shown by methods that estimate reflection and transmission coefficients from vertical boundaries (Keilis-Borok, 1986, Malischewsky, 1976, McGarr, 1967). Although the general case for surface-wave reflection is complex, equations have been developed to account for oblique reflections and conversions (Meier et al., 1997). Methods which estimate reflection and transmission coefficients all assume a quarter-space type model (two half spaces welded together), where each quarter-space has vertically heterogeneous shear-wave velocities.

We bring the concept of processing surface-waves one step further by imaging with surface-wave reflections. Surface-waves reflect from vertically oriented features, thereby identifying features that are otherwise difficult to determine using direct surface waves or traditional seismic processing. By processing and migrating surface-wave reflections we create a reflection image of sub-vertical features near the surface. Because surface-wave dispersion is dependent on shear-wave velocity properties below the surface, the spatial frequency of the reflection image can be mapped to depth. As a result, our developed methods yield both 2D and 3D reflectivity images.

We approximate surface-wave propagation by modifying the dispersion relation in phase-shift and one-way wave equation formulations. By using deconvolution as an imaging condition we estimate reflectivity in the image. Considerable detail about surface-wave propagation is presented as foundation for our methods of 2D and 3D modeling, imaging, and inversion. Using migration to create a 3D image has intriguing implications in regards to the geometry of the survey. If several lines of receivers are active for each source, wavefields from each line will be additively stacked in the migration process, increasing the signal-to-noise ratio. Our primary goal is to identify vertical features, in particular features that have no surface expression. We test our method with various synthetic models, physical models, and field data.

Chapter 1

Modeling surface waves:

Fundamentals

1.1 Overview

Surface waves observed in the field are typically very complicated. This is due to inherent characteristics of surface waves and 3D heterogeneity of the earth. Although our overarching objective is to model and process surface waves in a 3D heterogeneous earth, in this chapter, we investigate the simplest models required to produce surface waves. We use fundamental properties and algorithms from simple models as a foundation for developing methods presented in subsequent chapters. We first investigate an SH boundary wave and model particle motion near the boundary. We then examine the free surface boundary. We use the elastic equation of motion to derive necessary algorithms for modeling Love and Rayleigh waves in a vertically layered model.

1.2 Body waves and surface waves

Seismologists often broadly group seismic waves into two general categories: body waves and surface waves. Body waves are those which travel through the earth's inner layers only, and surface waves are those which travel across the surface of the earth. Mathematicians, who first formulated the theoretical ground work for wave propagation, group seismic waves slightly differently. Waves are grouped into those which propagate in unbounded media, and those which propagate at a boundary. A body wave may travel through unbounded media or be transmitted, reflected, and refracted at an inner boundary. The surface wave, however, may only travel at the boundary of the free surface.

Boundary conditions at the free surface set up two unique types of surface waves: the Love wave and the Rayleigh wave. Whether a Love wave or Rayleigh wave is generated is dependent on the model and the particle motions of the incident wave. The simplest model needed to generate Love waves is an elastic layer welded to an elastic half-space as shown in Figure 1.1a. All that is needed to generate the Rayleigh-wave is an elastic homogeneous half-space depicted in Figure 1.1b.

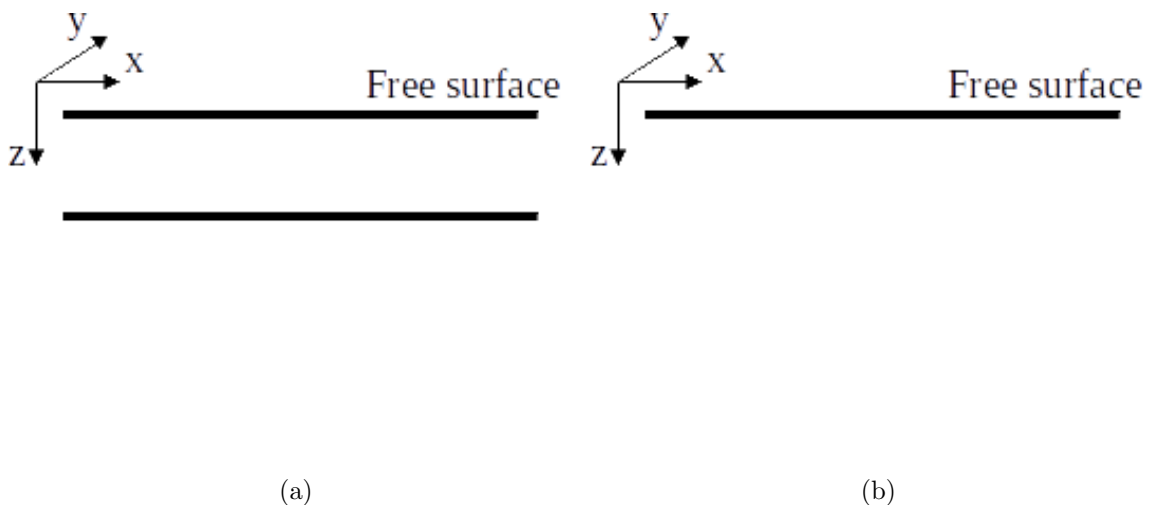


Figure 1.1: Simple models used to formulate surface-wave propagation. (a) Simple model for generating Love waves and (b) simple model for generating Rayleigh waves.

A horizontally polarized shear-wave (SH-wave) produces the Love wave and a combination of the pressure wave (P-wave) and vertically polarized shear-wave (SV-wave) produces the Rayleigh wave. Particle motions for the Love wave and Rayleigh wave are shown in Figure 1.2

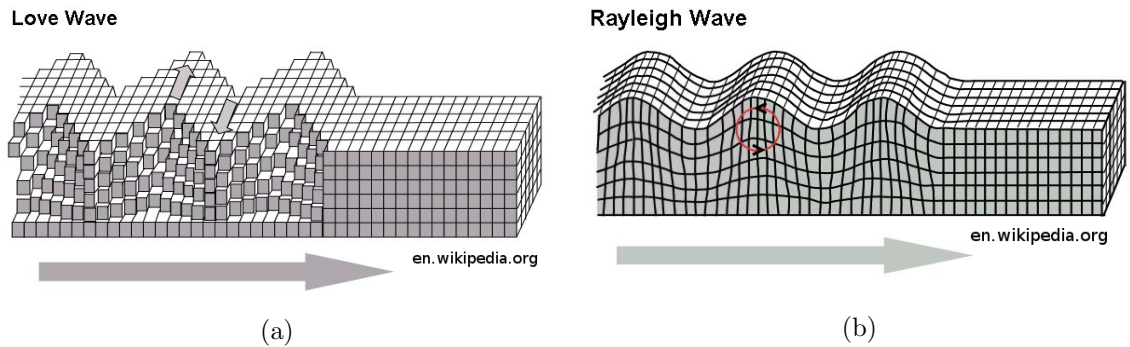


Figure 1.2: (a) Love-wave propagation, (b) Rayleigh-wave propagation.

Propagation of both the Love wave and Rayleigh wave is governed by the boundary. In this case, the boundary is the free surface. Surface waves share many similar properties with other waves that travel along a boundary, such as post-critical waves, or head waves. Extensive formulations exist for both boundary-wave and surface-wave propagation in a 1D model and have been compiled by Aki and Richards (1980) and Heaton (2014). It is worth revisiting the fundamentals of boundary-wave and surface-wave propagation in a 1D model as a preparatory step for approaching the 2D and 3D problems.

1.3 Inhomogeneous waves

It is useful to consider inhomogeneous wave propagation before investigating the surface waves because both exhibit similar properties and it is easier to formulate inhomogeneous wave propagation. Using basic ray theory and trigonometry we can formulate propagation

for the inhomogeneous wave. We start by describing a SH-wave incident on a boundary,

$$u(x, y, z, t) = A_y e^{i(kx - \omega t)}, \quad (1.1)$$

where u is particle displacement as a function of space, (x, y, z) , and time t . The modulus of the amplitude of the wave is defined as A_y , traveling in vector direction \mathbf{x} , with vector wavenumber, k , and frequency, f . In the case of a SH-wave (a transversely polarized wave) there is no particle motion in the x or z directions.

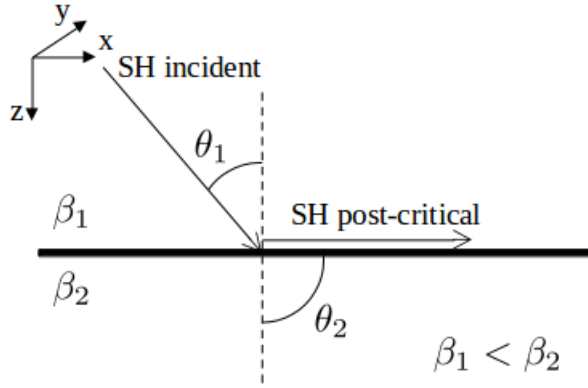


Figure 1.3: Post-critical SH wave.

Given a particular angle of incidence, θ_1 , at a boundary between two layers with shear velocities, β_1 , and, β_2 , we can write displacement in the transverse direction for the transmitted wave as,

$$u_y = A_y e^{ik(x \sin \theta_2 + z \cos \theta_2 - \beta_2 t)}. \quad (1.2)$$

If the angle of incidence is greater than the critical angle, as shown in Figure 1.3, then effectively $\sin \theta_2$ would be > 1 and $\cos \theta_2$ becomes imaginary because $\cos \theta_2 = \sqrt{1 - \sin^2 \theta_2}$.

Using Snell's law,

$$\sin \theta_2 = \left(\frac{\beta_2}{\beta_1} \right) \sin \theta_1, \quad (1.3)$$

in a post-critical case, we can rewrite equation 1.2, with an exponential term added to the amplitude part of the wave,

$$u_{y_{postcritical}} = e^{-\gamma z} A_y e^{ik(x \sin \theta_2 - \beta_2 t)}, \quad (1.4)$$

where,

$$\gamma = k \sqrt{\left(\frac{\beta_2^2}{\beta_1^2}\right) \sin^2 \theta_1 - 1}. \quad (1.5)$$

This means that displacement in the lower layer decays exponentially from the boundary. A wave that decays in this manner is referred to as an inhomogeneous wave or an evanescent wave. We now have all the necessary equations for modeling a boundary SH-wave. Consider a model where the shear-wave velocity in medium 1, β_1 , and medium 2, β_2 , is 250 m/s and 500 m/s respectively. Snell's law dictates that the transmitted wave becomes post-critical at 30 degrees. Waves transmitted from incident angles beyond 30 degrees obey propagation given by equation 1.4. Figure 1.4 compares the result of particle displacement below a boundary from an incident wave at 30 degrees and 50 degrees respectively.

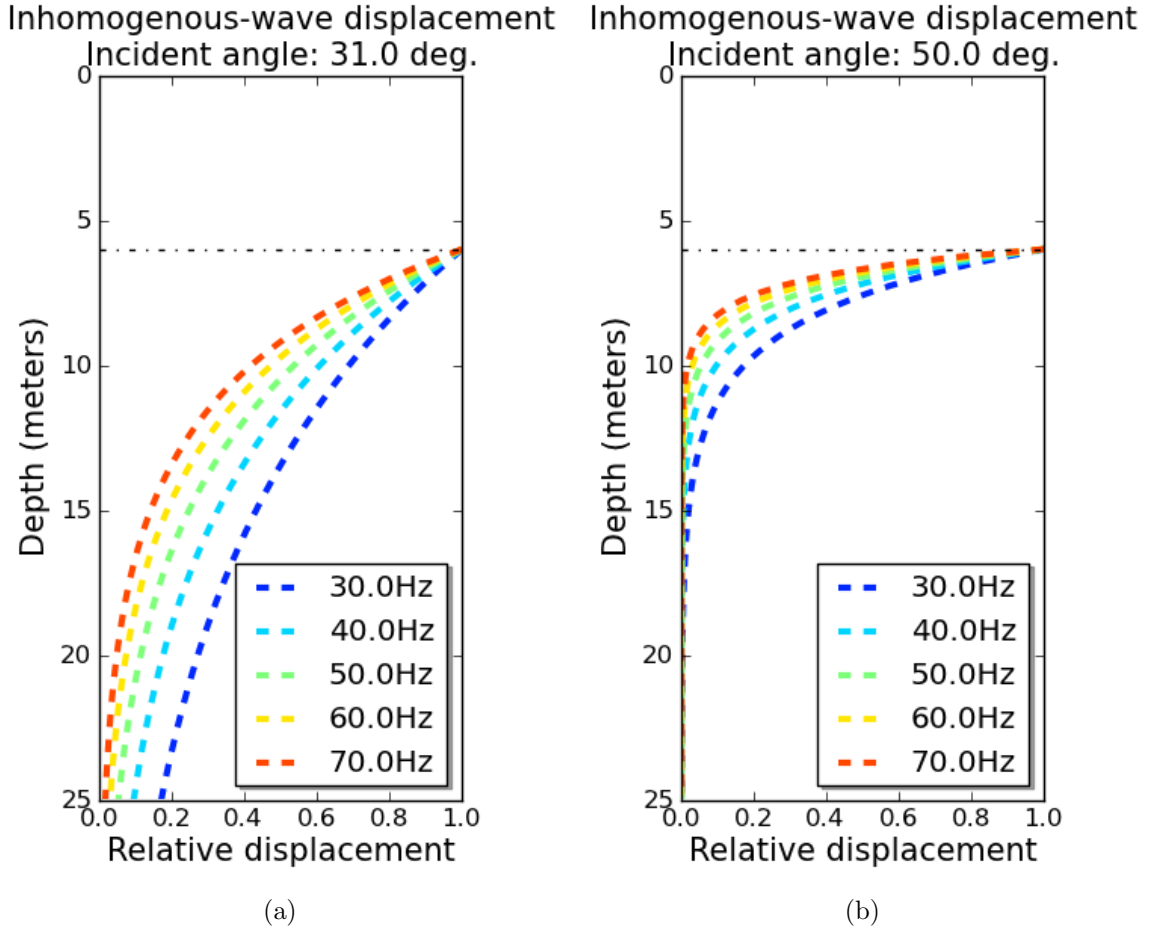


Figure 1.4: A comparison particle of displacement due to inhomogeneous wave propagation for two different incident angles. The dashed horizontal line indicates the location of the boundary between medium 1 and 2. Particle displacement for several frequencies are plotted. The two incident angles shown are: (a) incident angle just beyond post-critical reflection, 31 degrees (b) incident angle at 50 degrees.

Particle displacements for a range of frequencies are calculated below the boundary. As a result of the wavenumber term in equation 1.5, particle displacement at longer wavelengths extend further at depth than short wavelengths. Interestingly, as the incident angle increases, less energy is transmitted to the inhomogeneous wave below the boundary. The decrease in evanescent energy as the angle of incidence increases is consistent with the decrease in transmitted energy into the lower layer. Figure 1.5 shows the Zoeppritz solution for the SH-wave transmission coefficient as a function of angle.

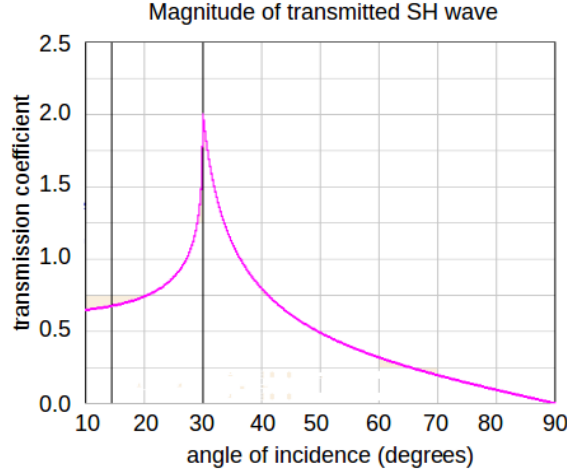


Figure 1.5: Exact solution of Zoeppritz equations for transmitted SH waves using the same two-layer model used to generate inhomogeneous waves on the boundary.

As the angle of incidence increases in the pre-critical case, transmitted energy also increases. At 30 degrees, the angle of incidence causes the wave to be post-critical. At the post-critical angle the transmitted energy sharply changes and decreases as the angle of incidence continues to increase. Transmitted energy beyond the post-critical angle is in the form of the inhomogeneous wave shown in Figures 1.4a and 1.4b.

1.4 Equation of motion

Before formulating the Love and Rayleigh wave, we must pause to define the wave equation in a linear elastic solid. We begin by reviewing motion. Recall that motion is a function of both time and space. Newton's second law states that acceleration, \mathbf{a} , is produced when a force, \mathbf{f} , acts on a mass, m ,

$$\mathbf{f} = m\mathbf{a}. \tag{1.6}$$

Our goal will be to recast Newton's familiar equation of motion in terms of displacements such that we can formulate expressions for the Love and Rayleigh wave motion. Focusing

on the right-hand side of the equation, acceleration is the rate of change of velocity, which in turn is the rate of change of displacement, $\mathbf{a} = \frac{\partial^2 \mathbf{u}}{\partial t^2}$. Considering a point object with density, ρ , and infinitesimal dimensions, dx_1, dx_2, dx_3 , equation 1.6 can be rewritten as,

$$\mathbf{f} = \rho dx_1 dx_2 dx_3 \frac{\partial^2 \mathbf{u}}{\partial t^2}. \quad (1.7)$$

The left-hand side of the equation is trickier to cast in terms of displacement. First, we will relate force to traction, then traction to stress, and finally stress to strain and displacement. Starting with the first step, consider that the same point object will experience traction, T , or force per unit area, acting on it in three dimensions. In this case we think of our point object as a cube, with a three-dimensional traction acting on a three-dimensional object. Force on the point object can be expressed as a summation of all i^{th} traction components on the faces of the cube,

$$\sum_{i=1}^3 f_i = \sum_{i=1}^3 \left(dT_i^1 dx_2 dx_3 + dT_i^2 dx_1 dx_3 + dT_i^3 dx_1 dx_2 \right). \quad (1.8)$$

Each traction component can also be written in terms of stress, τ , where the i^{th} component acts on the j^{th} face. Now, switching to Einstein's summation convention is helpful in compressing the expressions. With Einstein's notation any repeated index signifies summation over three spatial coordinates,

$$dT_i^j = \frac{\partial \tau_{ij}}{\partial x_j} dx_j. \quad (1.9)$$

We can now replace the left side in Newton's second law equation,

$$\frac{\partial \tau_{ij}}{\partial x_j} dx_1 dx_2 dx_3 = \rho dx_1 dx_2 dx_3 \frac{\partial^2 u_i}{\partial t^2}, \quad (1.10)$$

or, in compressed form,

$$\tau_{ij,j} = \rho \ddot{u}_i. \quad (1.11)$$

If the point object is in the presence of an external force we write equation 1.11 as,

$$\tau_{ij,j} + \rho f_i = \rho \ddot{u}_i. \quad (1.12)$$

We now invoke Hooke's Law to describe the elastic relationship between stress and strain, ε , of the point object,

$$\tau_{ij} = C_{ijkl} \varepsilon_{kl}, \quad (1.13)$$

where C_{ijkl} is the stiffness tensor of the object which linearly maps 9 components of stress to 9 components of strain. The stiffness tensor is an intrinsic property of the material and is represented by 81 indices of a 3 X 3 X 3 X 3 matrix. Because the stress-strain tensor is symmetric, there are 21 independent elastic constants. If we assume anisotropy, i.e., a transversely isotropic medium, the number of independent elastic constants drops to 5. If we assume the material is isotropic the number of elastic coefficients drops to 2 and Hooke's Law, as expressed in equation 1.13, can be rewritten as,

$$\tau_{ij} = \lambda \varepsilon_{kk} \delta_{ij} + 2\mu \varepsilon, \quad (1.14)$$

where δ_{ij} is the Kronecker delta function and the two elastic constants are denoted as Lamé's modulus, λ , and shear modulus, μ . The two elastic constants are part of a larger set of Lamé's parameters for an isotropic solid. Table 1.1 shows the relationships between other parameters such as Young's modulus, E , the bulk modulus, K , and Poisson's ratio, σ . All are useful in describing the stress-strain relationship.

	Lame's (λ)	Shear (μ)	Young's (E)	Poisson's (σ)	Bulk (K)
λ, μ			$\frac{\mu(3\lambda+2\mu)}{\lambda+\mu}$	$\frac{\lambda}{2(\lambda+\mu)}$	$\frac{3\lambda+2\mu}{3}$
λ, E		irrational		irrational	irrational
λ, σ		$\frac{\lambda(1-2\sigma)}{2}$	$\frac{\lambda(1+\sigma)(1-2\sigma)}{\sigma}$		$\frac{\lambda(1+\sigma)}{3\sigma}$
λ, K		$\frac{3(K-\lambda)}{2}$	$\frac{9K(K-\lambda)}{3K-\lambda}$	$\frac{\lambda}{3K-\lambda}$	
μ, E	$\frac{(2\mu-E)\mu}{E-3\mu}$			$\frac{E-2\mu}{2\mu}$	$\frac{\mu E}{3(3\mu-E)}$
μ, σ	$\frac{2\mu\sigma}{1-2\sigma}$		$2\mu(1+\sigma)$		$\frac{2\mu(1+\sigma)}{3(1-2\sigma)}$
μ, K	$\frac{3K-2\mu}{3}$		$\frac{9K\mu}{3K+\mu}$	$\frac{3K-2\mu}{2(3K+\mu)}$	
E, σ	$\frac{\sigma E}{(1+\sigma)(1-2\sigma)}$	$\frac{E}{2(1+\sigma)}$			$\frac{E}{3(1-2\sigma)}$
E, K	$\frac{3K(3K-E)}{9K-E}$	$\frac{3EK}{9K-E}$		$\frac{3K-E}{6K}$	
σ, K	$\frac{3K\sigma}{1+\sigma}$	$\frac{3K(1-2\sigma)}{2(1+\sigma)}$	$3K(1-2\sigma)$		

Table 1.1: Lamé's parameters.

By using the relationship of strain to displacement in the following expression,

$$\varepsilon_{ij} = \frac{1}{2} (u_{i,j} + u_{j,i}), \quad (1.15)$$

we obtain all the physical relationships needed to define an equation of motion in terms of displacements. By substituting equation 1.14 into 1.12 with equation 1.15 we arrive at,

$$\mu u_{i,jj} + (\lambda + \mu) u_{j,ji} + f_i = \rho \ddot{u}_i, \quad (1.16)$$

which is Navier's equation for an isotropic elastic medium. It is worth noting that on the left-hand side of the equation the 2^{nd} derivatives of displacements are with respect to space. While on the right hand side, the acceleration term is a 2^{nd} derivative with respect to time. Both sides of the equation are linearly related.

Although Navier's equation provides the solution to any 3D problem, there is not an analytical solution for every 3D problem (notably the problem of 3D heterogeneity). However, we can restrict the problem to be uniform in one or all direction/s resulting in a solution

for a 2D or 1D problem. A useful problem to solve is a stack of horizontal plane layers because of its analog to geologic formations. The solution to a stack of horizontal plane layers is presented a little later in this chapter. The other way to solve Navier's equation in 3D is to do so numerically using techniques like finite difference or spectral elements. Both numerical techniques are shown in later chapters.

Regardless of the number of dimensions in the problem it is useful to decompose the wavefield into the compressional wave (P wave) and shear wave (S wave). To show how a simplification of Navier's equation (equation 1.16) decomposes a wavefield into the P wave and S wave we start by writing Navier's expression in vector notation as,

$$\mu \nabla^2 \mathbf{u} + (\lambda + \mu) \nabla \nabla \cdot \mathbf{u} + \mathbf{f} = \rho \ddot{\mathbf{u}}. \quad (1.17)$$

Now we can decompose the vector field into the gradient of a scalar and the curl of the zero divergence vector. Using the Helmholtz decomposition we express the total displacement field as the sum of potentials,

$$\mathbf{u} = \nabla \phi + \nabla \times \psi, \quad (1.18)$$

where the scalar and vector potentials are ϕ and ψ respectively. By taking the divergence of equation 1.17 and applying the condition $\nabla \cdot (\nabla \times \psi) = 0$ we obtain,

$$\nabla^2 (\nabla \cdot \mathbf{u}) = \frac{1}{\alpha^2} \frac{\partial^2 (\nabla \cdot \mathbf{u})}{\partial t^2}, \quad (1.19)$$

where α is the P-wave velocity defined by,

$$\alpha = \sqrt{\frac{\lambda + 2\mu}{\rho}}. \quad (1.20)$$

By taking the curl of equation 1.17 and applying the condition $\nabla \times (\nabla \cdot \phi) = 0$ we obtain,

$$\nabla^2(\nabla \times \mathbf{u}) = \frac{1}{\beta^2} \frac{\partial^2(\nabla \times \mathbf{u})}{\partial t^2}, \quad (1.21)$$

where β is the S-wave velocity defined by,

$$\beta = \sqrt{\frac{\mu}{\rho}}. \quad (1.22)$$

We now have the building blocks to formulate equations for the Love and Rayleigh waves as well as find solutions for them.

1.5 Love waves

Generation of the Love wave is very similar to the inhomogeneous wave described in section 1.3. It is an SH wave that generates the Love wave, the difference being that there is a free surface above the boundary (Figure 1.6).

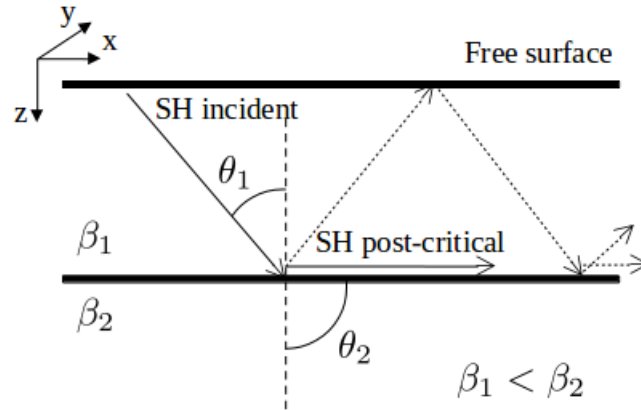


Figure 1.6: Generation of the Love wave.

Love waves arise when the SH wave becomes trapped in the layer between the free surface and the boundary. Love-wave velocity is dictated by the shear-wave velocity of the

two layers: $\beta_1 < c_{Love} < \beta_2$. Lower frequency Love waves will tend to have velocities closer to the lower layer and higher frequency Love waves will tend to have velocities closer to the upper layer. Given that it takes at least two layers to set up the necessary conditions for the Love wave, it follows that the Love wave is intrinsically dispersive.

Solving Love-wave particle displacement for the simple model of two layers requires application of boundary conditions to the general equation of motion. To solve Love-wave particle displacement as a function of depth and time we begin with the wave equation for a shear wave, equation 1.21, and simplify it by only considering the displacement in the transverse direction, u_2 ,

$$\rho \frac{\partial^2 u_2}{\partial t^2} = \mu \left(\frac{\partial^2 u_2}{\partial x_1^2} + \frac{\partial^2 u_2}{\partial x_3^2} \right). \quad (1.23)$$

We assume displacement is related to the plane wave solution where the propagation is in the x_1 direction,

$$\mathbf{u}(x_1, x_2, x_3, t) = \left(0, D(x_3)e^{i(kx_1 - \omega t)}, 0 \right), \quad (1.24)$$

with an amplitude, $D(x_3)$, in the x_2 direction, that decays a function of depth x_3 . Substituting equation 1.24 into equation 1.23 results in,

$$\frac{\partial^2 D(x_3)}{\partial x_3^2} = \left(k^2 - \frac{\omega^2}{\beta_i^2} \right) D(x_3), \quad (1.25)$$

where $i = 1$ denotes the upper layer and $i = 2$ denotes the lower half-space. We solve for $D(x_3)$ in both the upper and lower layer and substitute the result back into equation 1.24 to arrive at,

$$u_2(x_1, x_2, x_3, t) = \left(A_i e^{-\sqrt{k^2 - \frac{\omega^2}{\beta_i^2}} x_3} + B_i e^{+\sqrt{k^2 - \frac{\omega^2}{\beta_i^2}} x_3} \right) e^{i(kx_1 - \omega t)}. \quad (1.26)$$

The constants A_i and B_i will help with applying boundary conditions. The boundary conditions will also help constrain the problem. These boundary conditions are:

1. displacements tend to zero when x_3 goes to infinity
2. no stress at the free surface, and
3. stresses and displacements are continuous at the boundary.

Applying boundary condition (1.), the constant $B_2 = 0$, and the expression:

$$\text{Real} \left(\sqrt{k^2 - \frac{\omega^2}{\beta_i^2}} \right) < 0, \quad (1.27)$$

changes only the equation for the lower layer ($i = 2$). By applying boundary condition (2.), $\frac{\partial u_2(x_3=0)}{\partial x_3} = 0$, the equation for the upper layer is changed. After applying the first two boundary conditions the solution for Love-wave particle displacement in the two layer case can be written as:

$$u_{y_{upper}} = 2A_1 \cos \left(i \sqrt{k^2 - \omega^2 / \beta_1^2} z \right) e^{i(kx - \omega t)}, \quad (1.28)$$

for the upper layer and,

$$u_{y_{lower}} = A_2 e^{-\sqrt{k^2 - \omega^2 / \beta_2^2} z} e^{i(kx - \omega t)}, \quad (1.29)$$

for the lower layer. Note that it is the lower layer that has the term which dictates a decaying amplitude with depth. Although it is not a true representation of the true particle displacement we can model the upper layer and lower layer separately and investigate its effects to understand fundamentally how the equation works. If we assume a model where

shear-wave velocity in the upper layer, $\beta_1 = 250$ m/s, is lower than the lower layer, $\beta_2 = 300$ m/s, and the depth to the boundary between layer 1 and layer 2 is 6 m we will set up the proper conditions necessary to produce a Love wave. Figure 1.7 shows the result of the modeling at a snapshot of time for several different frequencies.

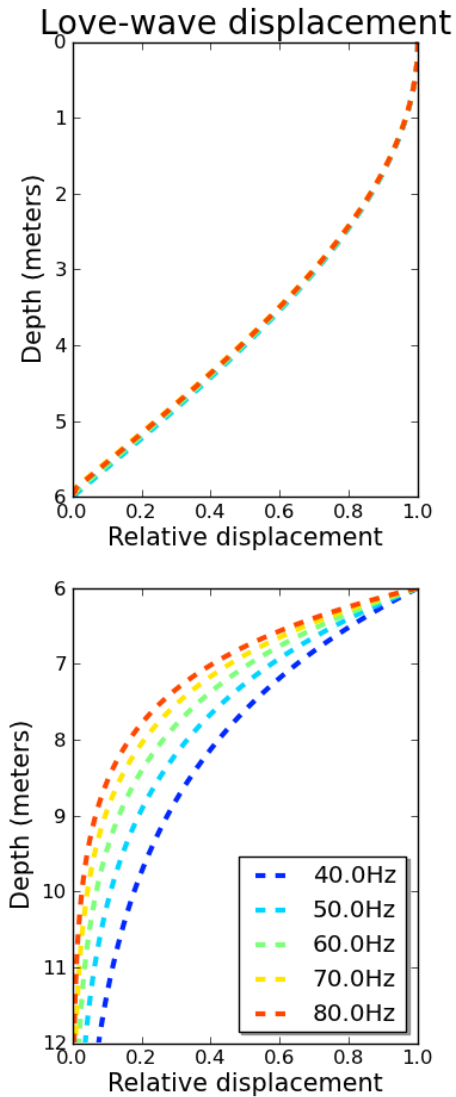


Figure 1.7: Particle displacement for the Love wave as a function of depth for the shear-wave velocity model: ($\beta_1 = 250$ m/s, $\beta_2 = 300$ m/s). Depth to the boundary is 6 m. Displacement for the upper layer is shown above and displacement for the lower layer is shown below. Lines are colored according to solutions for various frequencies.

Again, we have not applied boundary condition (3.) therefore the result shows the hypothetical case for the interface being unwelded. We will show a more complete result below when formulating the Love wave and modeling with a vertically heterogeneous models. Nevertheless, there are some interesting results to see at this point. Displacement is constant for all frequencies in the upper layer. It is only the lower layer which contains an evanescent wave much like the inhomogeneous propagation shown before. As expected the lower frequencies decay less in terms of particle motion than the higher frequencies indicating dispersion.

1.5.1 Love wave modes

To investigate the higher modes of the Love waves and model their behavior we can use equations 1.28 and 1.29 and introduce boundary condition (3.). To describe that there is a continuity of displacements at the boundary we explicitly set $x_3 = H$ and then set the two equations equal to each other. After dividing both sides by the time-dependent exponential we obtain two equations,

$$\begin{aligned}
 2A_1 \cos \left(i\sqrt{k^2 - \omega^2/\beta_1^2} H \right) &= A_2 e^{-\sqrt{k^2 - \omega^2/\beta_2^2} H}, \\
 2\mu_1 A_1 i\sqrt{k^2 - \omega^2/\beta_1^2} \sin \left(i\sqrt{k^2 - \omega^2/\beta_1^2} H \right) &= \mu_2 \sqrt{k^2 - \omega^2/\beta_2^2} A_2 e^{-\sqrt{k^2 - \omega^2/\beta_2^2} H}.
 \end{aligned}
 \tag{1.30}$$

There are four arbitrary parameters: A_1 , A_2 , ω , and k seen in two equations 1.30. Because there are more parameters than equations there is not one single solution but a spectrum of solutions that can be solved as an eigenvalue problem. Physically, this means that Love wave energy can travel at several different velocities given a certain frequency.

The solution for the eigenvalue problem will be shown in the section for vertically heterogeneous media. For now, we can investigate the behavior of the Love wave by setting

the equations up such that phase-velocity characteristics can be determined numerically. If we find the ratio of A_2/A_1 in equations 1.30 and substitute $k = \omega/c$ we arrive at,

$$\tan\left(\omega H \sqrt{\frac{1}{\beta_1^2} - \frac{1}{c^2}}\right) = \frac{\mu^2 \sqrt{\frac{1}{c^2} - \frac{1}{\beta_2^2}}}{\mu_1 \sqrt{\frac{1}{\beta_1^2} - \frac{1}{c^2}}}. \quad (1.31)$$

To solve the above equation numerically and find valid values for phase-velocity, c , a range of frequencies are calculated for both the left side and right side of the equation. The correct phase-velocity is picked by determining the frequency at which the two sides equal each other. Because there are a spectrum of solutions there will be more than one frequency for each phase-velocity where Love-wave modes exist. Using the same shear-wave velocity model as before, ($\beta_1 = 250$ m/s, $\beta_2 = 300$ m/s, $H = 6$ m), corresponding phase-velocities of the Love wave can be determined. Figure 1.8 shows dispersion characteristics of the fundamental mode and higher modes.

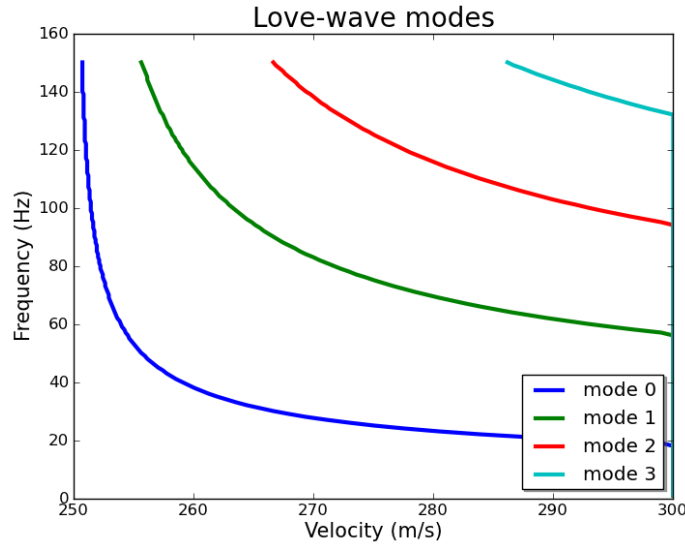


Figure 1.8: Phase-velocities for the Love wave given the shear-wave velocity model: ($\beta_1 = 250$ m/s, $\beta_2 = 300$ m/s). The fundamental mode and three higher modes are indicated with colored lines.

As can be seen in the figure above, all modes of the Love wave exhibit dispersive behavior. Also note that the higher modes only exist at higher frequencies. Using the phase-velocity solutions for Love-wave modes we can now calculate Love-wave displacements at the higher modes (Figure 1.9).

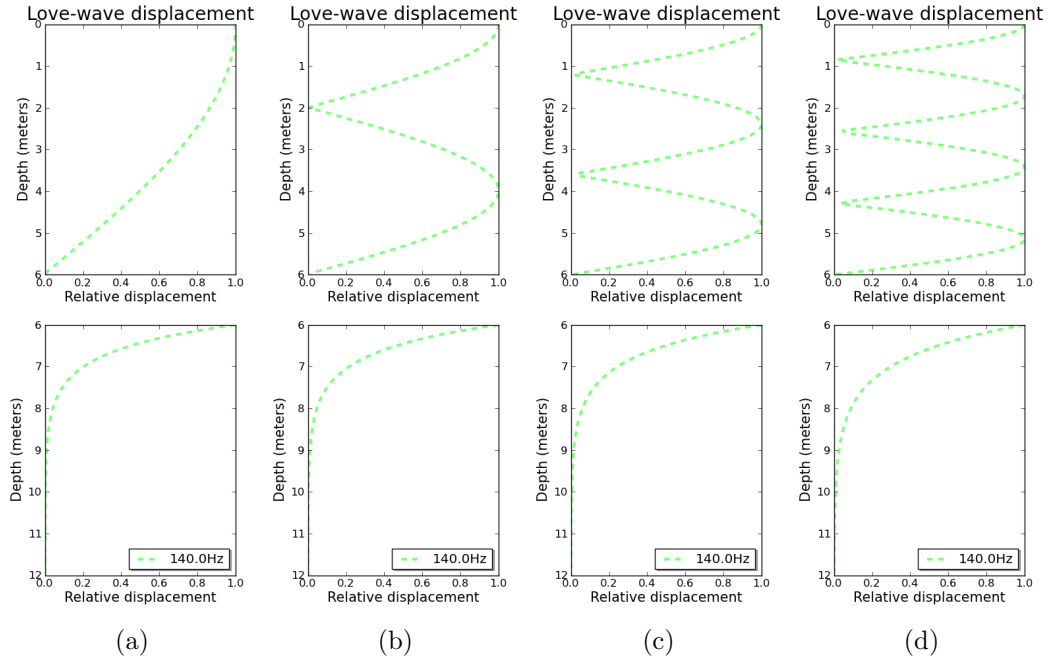


Figure 1.9: Particle motion of the Love-wave for a single frequency of 140Hz. Upper plots show displacement in upper layer and lower plots show displacement in lower layer. Order of modes increases from left to right: (a) fundamental mode (b) first higher mode (c) second higher mode (d) third higher mode.

Again, because the two layers have been modeled as if they are uncoupled, this is not a true result, but it still helps understand the fundamental physics. As can be seen, the order of the mode has a distinct effect on love-wave particle displacement in the upper layer and much less effect on the lower layer.

1.6 Rayleigh waves: free case

Rayleigh waves are the result of special boundary conditions at the free surface. These boundary conditions are the same conditions described above for the Love wave; however, the Rayleigh wave is the result of the P and SV wave coupling along the free surface. Given an incident P wave from within the medium, there will be conversions from P to SV, at the free surface (Figure 1.10).

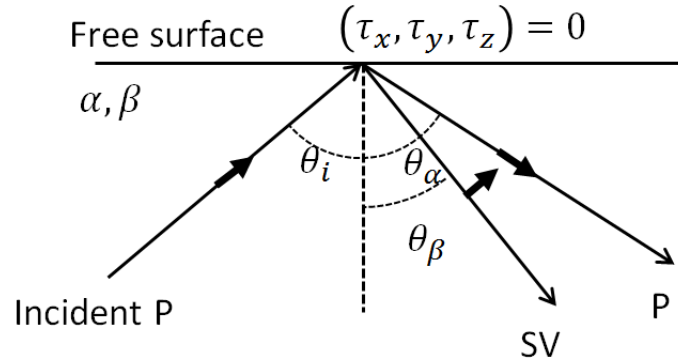


Figure 1.10: Diagram showing the model used to formulate the free Rayleigh wave. An incident P reflection at the free surface. Bold arrows indicate the direction of particle motion.

Considering the conversions, the down-going reflected waves from an incident P wave will exhibit the following slowness, s_P , s_{SV} , and ray-parameters, p_P , p_{SV} .

$$s_P = p_P = \left(\frac{\sin \theta_\alpha}{\alpha}, 0, \frac{\cos \theta_\alpha}{\alpha} \right), \quad (1.32)$$

$$s_{SV} = p_{SV} = \left(\frac{\sin \theta_\beta}{\beta}, 0, \frac{\cos \theta_\beta}{\beta} \right). \quad (1.33)$$

Note that in the y direction, there is zero slowness, as there is no motion that can be reflected in this direction given an incident P wave. The P-wave velocity of the model is defined as α , and the S-wave velocity defined by β .

If the ray parameter is less than, $\frac{1}{\alpha}$, as represented by an incidence angle less than 90 degrees and originating from within the media which it is incident, the result is a reflected P and SV body wave. However, if the ray parameter becomes greater than $\frac{1}{\alpha}$, both P and SV waves will be channeled across the boundary. Similar to the post-critical SH wave, the P and SV waves are inhomogeneous. Given equations 1.32 and 1.33 it can be seen that, $\sin \theta_\alpha = \alpha p$, and, $\cos \theta_\alpha = \sqrt{1 - \alpha^2 p^2}$, so that inhomogeneous P-wave displacement can be defined as,

$$u_P = A_P \left(\alpha p, 0, i \sqrt{\alpha^2 p^2 - 1} \right) e^{-\omega \sqrt{p^2 - \frac{1}{\alpha^2}} z} e^{i\omega(px-t)}, \quad (1.34)$$

and the inhomogeneous SV wave defined as,

$$u_{SV} = A_{SV} \left(i \sqrt{\beta^2 p^2 - 1}, 0, -\beta p \right) e^{-\omega \sqrt{p^2 - \frac{1}{\beta^2}} z} e^{i\omega(px-t)}. \quad (1.35)$$

The first term is the amplitude as a function of direction, the second term represents the decaying component in depth, and the third term is phase velocity of the plane wave.

It is important to note that it is not a superposition of the inhomogeneous P and SV waves which cause the Rayleigh wave to arise, rather a coupling of the two. One can show how the P and SV waves couple at the free surface using the wave equation and the displacement formulation (Aki and Richards, 1980). For brevity, we show the particle motion of the Rayleigh wave after Lamé's parameters are assumed to be $\mu = \lambda$, (ie., Poisson's ratio equal to .25),

$$u_{Rx} = A \left(e^{-.8475 \frac{\omega}{c_R} z} - .5773 e^{-.3933 \frac{\omega}{c_R} z} \right) \sin \left(\omega t - \frac{\omega}{c_R} x \right), \quad (1.36)$$

in the x direction, and,

$$u_{Rz} = A \left(-0.8475 e^{-0.8475 \frac{\omega}{c_R} z} - 1.4679 e^{-0.3933 \frac{\omega}{c_R} z} \right) \sin \left(\omega t - \frac{\omega}{c_R} x \right), \quad (1.37)$$

in the z direction. For the above case, Rayleigh-wave phase-velocity, c_R , is nearly equal to the shear-wave velocity, $c_R = .9194\beta$. Comparing particle motions from two different elastic half-space models is helpful for understanding the Rayleigh wave. Figure 1.11 shows particle motions from two different models. Shear-wave velocity is 200 m/s in model 1 and 300 m/s in model 2. An elastic relationship of $\mu = \lambda$ is assumed to be true for both models.

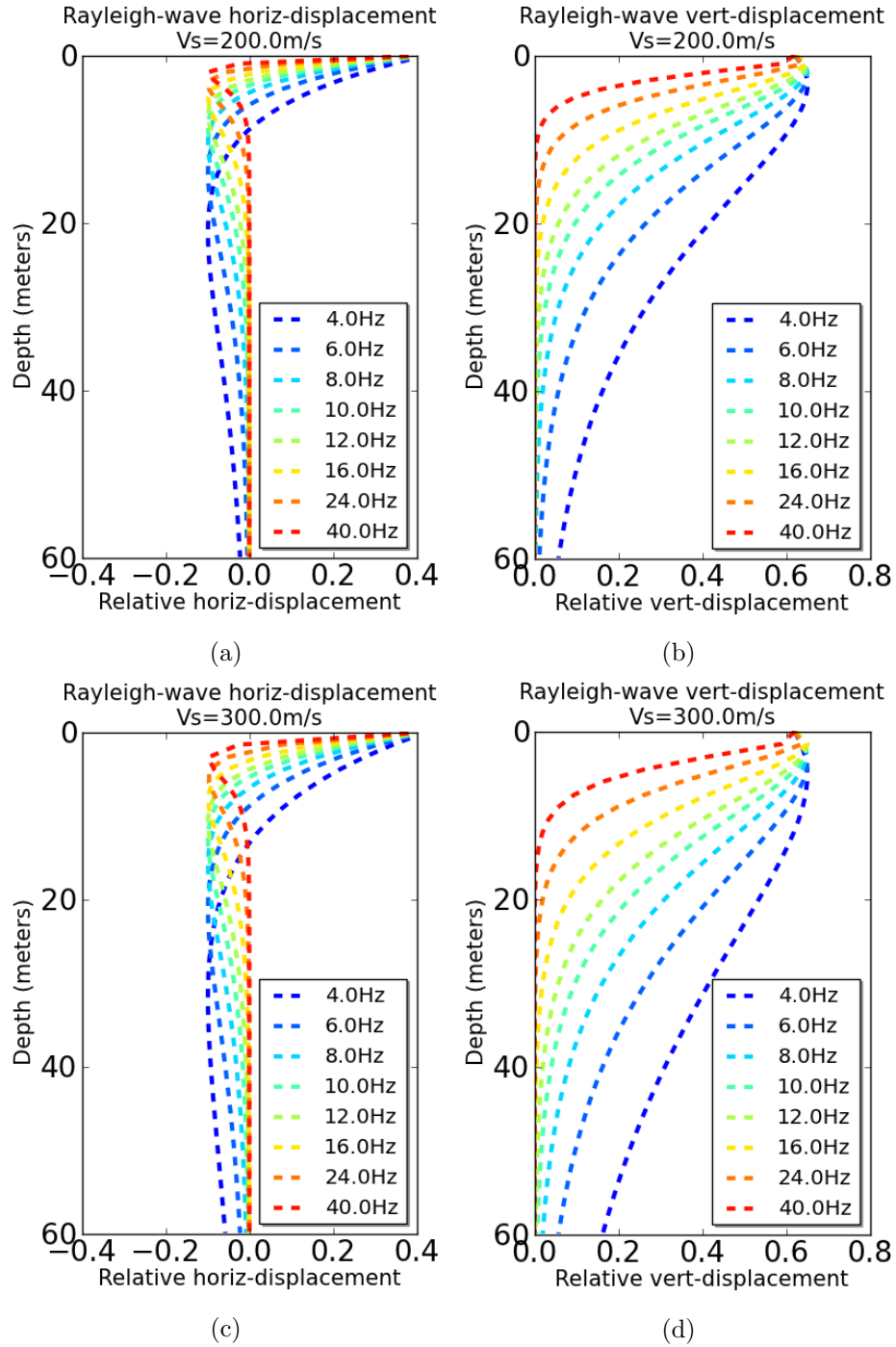


Figure 1.11: Particle motion of the Rayleigh wave. (a) 200 m/s shear-wave velocity, (b) 200 m/s shear-wave velocity, (c) 300 m/s shear-wave velocity, (d) 300 m/s shear-wave velocity.

Note that although vertical displacement is shown on the horizontal scale it is still vertical displacement is in the vertical direction. Just as for the Love wave, particle motions

decay less at depth for lower frequencies. However, it is important to note that because there is only one velocity in the model, the free case of the Rayleigh wave is not dispersive.

Although lower frequencies sample deeper, they still exhibit particle motion at shallow depths. The horizontal component exhibits displacement in both the positive and negative direction, whereas the vertical displacement shows only displacement in the positive direction. Horizontal displacement is constrained slightly more to the shallow depths compared to vertical displacement. Finally, one can see that the faster velocities result in deeper particle displacement than the slower velocities. Also, because the free Rayleigh wave is not dispersive there are also no multiple modes of the free Rayleigh wave.

1.7 Vertically stratified layers

A common model to consider is the case where the medium is only vertically heterogeneous, in particular, a stack of horizontal layers. To set up the solution for the surface-wave we first set a Cartesian space where basis vectors, \mathbf{e}_z , denote the Cartesian coordinates. Navier's equation of motion defines surface wave propagation in a vertically inhomogeneous model. In vector form this equation is,

$$\rho \frac{\partial^2 \mathbf{u}}{\partial t^2} = \mu \nabla^2 \mathbf{u} + (\lambda + \mu) \nabla \nabla \cdot \mathbf{u} + \mathbf{e}_z \frac{d\lambda}{dz} \nabla \cdot \mathbf{u} + \frac{d\mu}{dz} \left(\mathbf{e}_z \times \nabla \times \mathbf{u} + 2 \frac{\partial \mathbf{u}}{\partial y} \right). \quad (1.38)$$

The second derivatives of displacement with respect to time on the left side of the equation are linearly related to second derivatives of displacement with respect to space on the right side. By defining displacement and stress in a specific way, a convenient matrix can be constructed that leads towards a solution of Navier's equation for surface-wave propagation. For the Love wave, the variables $l_1(z, k, \omega)$ and $l_2(z, k, \omega)$ will be set aside

for the displacement and stress eigenfunctions respectively. For the Rayleigh wave, two pairs of variables $\{r_1(z, k, \omega), r_2(z, k, \omega)\}$ and $\{r_3(z, k, \omega), r_4(z, k, \omega)\}$ will be set aside for the displacement and stress eigenfunctions respectively. We now continue with deriving the equation of motion for both the Love wave and Rayleigh wave. Recall that Love waves are caused by SH waves and therefore only exhibit displacement in the y direction,

$$(u_x = 0, u_y = l_1(z, k, \omega)e^{i(\omega t - kx)}, u_z = 0), \quad (1.39)$$

Rayleigh waves, being a combination of P and SV waves, couple to create an overall elliptical motion. Rayleigh waves exhibit displacement in the x and z direction, but not the y direction,

$$(u_x = r_1(z, k, \omega)e^{i(\omega t - kx)}, u_y = 0, u_z = ir_2(z, k, \omega)e^{i(\omega t - kx)}). \quad (1.40)$$

Returning to the boundary conditions for the half-space we now add an additional condition that stress and displacement must be continuous at all layer interfaces, while λ , μ , and ρ are allowed to be discontinuous. Remember that Hooke's law is,

$$\sigma_{ij} = \lambda \varepsilon_{kk} \delta_{ij} + 2\mu \varepsilon_{ij}, \quad (1.41)$$

where σ_{ij} and ε_{ij} are the components of the stress and strain tensors, λ and μ are Lamé's parameters, and δ_{ij} is the Kronecker delta. Using Hooke's law and the displacements defined by equation 1.39, stresses can be determined for the Love wave in terms of displacement

(l_1),

$$\begin{aligned}
\tau_{xx} &= \tau_{zz} = \tau_{yy} = \tau_{zx} = 0, \\
\tau_{yz} &= \mu \frac{dl_1}{dz} e^{i(\omega t - kx)}, \\
\tau_{xy} &= ik\mu l_1 e^{i(\omega t - kx)}.
\end{aligned} \tag{1.42}$$

Because stresses are continuous across the layer interfaces the stress acting on the y-plane from the z direction, τ_{yz} is defined in terms of stress (l_2) as,

$$\tau_{yz} = l_2(z, k, \omega) e^{i(\omega t - kx)}. \tag{1.43}$$

Likewise, stresses can be determined using Hooke's Law and displacements defined by equation 1.40 for the Rayleigh wave in terms of displacement (r_1, r_2),

$$\begin{aligned}
\tau_{yz} &= \tau_{xy} = 0, \\
\tau_{xx} &= i \left[\lambda \frac{dr_2}{dz} + k(\lambda + 2\mu)r_1 \right] e^{i(\omega t - kx)}, \\
\tau_{yy} &= i \left(\lambda \frac{dr_2}{dz} + k\lambda r_1 \right) e^{i(\omega t - kx)}, \\
\tau_{zz} &= i \left[(\lambda + 2\mu) \frac{dr_2}{dz} + k\lambda r_1 \right] e^{i(\omega t - kx)}, \\
\tau_{zx} &= \mu \left(\frac{dr_1}{dz} - kr_2 \right) e^{i(\omega t - kx)}.
\end{aligned} \tag{1.44}$$

Again, because stresses are continuous across the layer interfaces in the z direction, τ_{zx} and τ_{zz} are defined in terms of stress (r_3, r_4) as,

$$\begin{aligned}
\tau_{zx} &= r_3(z, k, \omega) e^{i(\omega t - kx)}, \\
\tau_{zz} &= r_4(z, k, \omega) e^{i(\omega t - kx)}.
\end{aligned} \tag{1.45}$$

Displacements for the the Love wave and Rayleigh wave, equations 1.40 and 1.39, can be substituted into Navier's equation and stresses for the Love wave and Rayleigh wave. Equations 1.42, 1.43, 1.44, and 1.45 are rearranged into matrix form of a set of first order differentials for both the Love wave and Rayleigh wave. For the Love wave:

$$\frac{d}{dz} \begin{bmatrix} l_1 \\ l_2 \end{bmatrix} = \begin{bmatrix} 0 & \mu(z)^{-1} \\ k^2\mu(z) - \omega^2\rho(z) & 0 \end{bmatrix} \begin{bmatrix} l_1 \\ l_2 \end{bmatrix}, \quad (1.46)$$

and for the Rayleigh wave:

$$\frac{d}{dz} \begin{bmatrix} r_1 \\ r_2 \\ r_3 \\ r_4 \end{bmatrix} = \begin{bmatrix} 0 & k & \mu^{-1}(z) & 0 \\ -k\lambda(z) [\lambda(z) + 2\mu(z)]^{-1} & 0 & 0 & [\lambda(z) + 2\mu(z)]^{-1} \\ k^2\zeta(z) - \omega^2\rho(z) & 0 & 0 & k\lambda(z) [\lambda(z) + 2\mu(z)]^{-1} \\ 0 & -\omega^2\rho(z) & -k & 0 \end{bmatrix} \begin{bmatrix} r_1 \\ r_2 \\ r_3 \\ r_4 \end{bmatrix}, \quad (1.47)$$

where,

$$\zeta(z) = \frac{4\mu(z) [\lambda(z) + \mu(z)]}{[\lambda(z) + 2\mu(z)]}. \quad (1.48)$$

As stated before, the eigenfunctions for Love waves are displacement, l_1 , and stress, l_2 . And the eigenfunction pairs for Rayleigh waves are displacement, (r_1, r_2) , and stress, (r_3, r_4) . Both the Love wave equation, 1.46, and Rayleigh wave equation, 1.47, can be written in a generalized compact form,

$$\frac{d\mathbf{f}(z)}{dz} = \mathbf{A}(z) \cdot \mathbf{f}(z), \quad (1.49)$$

where $\mathbf{f}(z)$ is the $n \times 1$ vector corresponding to eigenfunctions and \mathbf{A} is the corresponding $n \times n$ matrix. The value of n depends on whether the problem being solved is the Love wave ($n = 2$), or Rayleigh wave ($n = 4$).

By solving equation 1.49 for Love or Rayleigh waves we can determine displacement as a function of depth, stress as a function of depth, as well as the modes for phase-velocities. However, the solution to both eigen-problems are non-trivial because the velocity and density are a function of depth.

There are many methods to solve the eigenvalue-eigenvector problem we have formed in equation 1.49. One can chose a numerical method like Runge-Kutta or one can chose to use semi-analytic methods like the propagator matrix method (Haskell, 1953, Kennett, 1983, Thomson, 1950). The propagator matrix method is used for this study due to it's speed of execution.

A sequence of matrix multiplications for each layer is formed while imposing continuity of stress and displacement at the interfaces between layers. Eigenfunctions, as noted by $\mathbf{f}(z)$, in equation 1.49, are found for each layer, between depths, z , at k indices,

$$\mathbf{f}(z) = \mathbf{P}(z, z_{k-1})\mathbf{P}(z_{k-1}, z_{k-2})\dots\mathbf{P}(z_1, z_0)\mathbf{f}(z_0) = \mathbf{P}(z, z_0). \quad (1.50)$$

The propagator matrix, $\mathbf{P}(z, z_0)$, is substituted into equation 1.49 as,

$$\frac{d}{dz}\mathbf{P}(z, z_0) = \mathbf{A}(z)\mathbf{P}(z, z_0), \quad (1.51)$$

where elements of $\mathbf{P}(z, z_0)$ for both the Rayleigh wave and Love wave contain dispersion relations.

We again return to the model, ($\beta_1 = 250$ m/s, $\beta_2 = 300$ m/s, $H = 6$ m), shown in Figure 1.12a. This model, which only has two layers, is the simplest version of the vertically heterogeneous model described above. Using the propagator matrix method we

solve for stress, displacement, and phase-velocities for the Rayleigh wave. Phase-velocities for the fundamental mode and two higher modes are shown in Figure 1.12b.

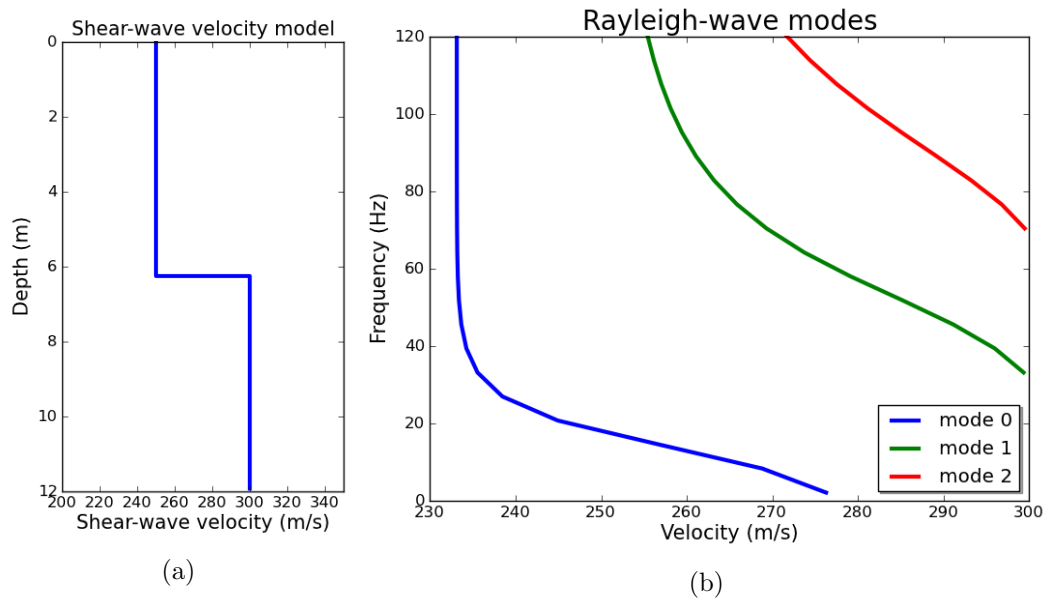


Figure 1.12: Rayleigh wave, general case (vertically inhomogeneous layers), (a) Shear-wave velocity model, and (b) resultant fundamental mode and two higher modes.

Rayleigh phase velocities are dispersive in the presence of a layered velocity model. The limits of phase-velocities for the fundamental mode are bounded roughly by the velocity of the shear-wave velocity model. Higher modes have both higher frequency and larger velocities than the fundamental mode. Physically, the higher modes of the Rayleigh wave are different than the fundamental mode. Higher modes are a channel wave formed between boundaries in the velocity model. Figure 1.13 shows the solution for displacements of the fundamental mode.

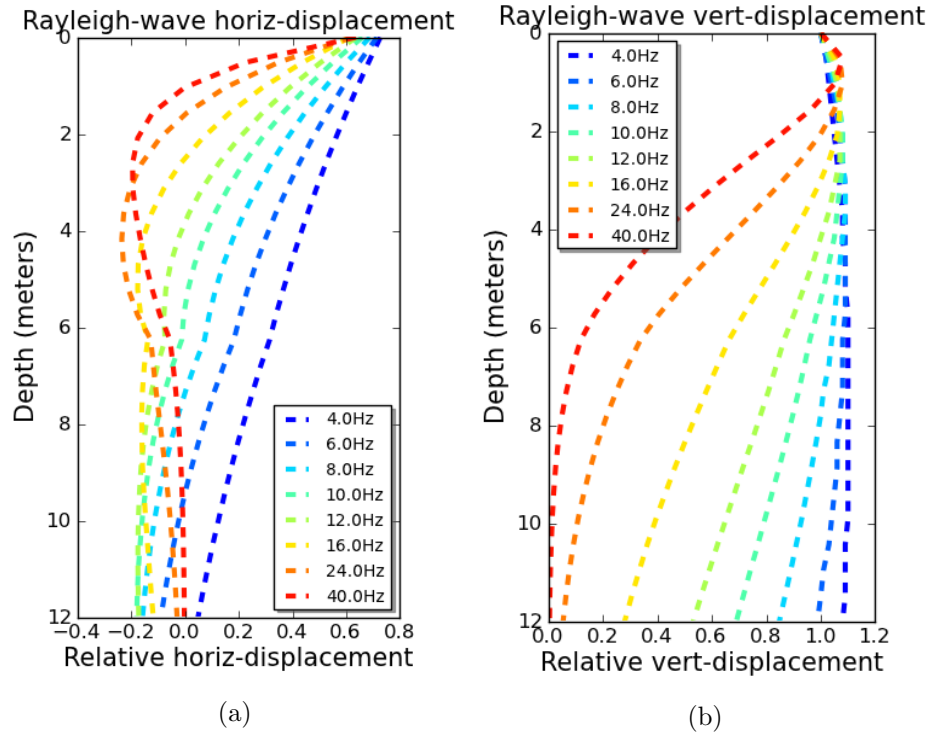


Figure 1.13: Fundamental mode of Rayleigh wave, general case (vertically inhomogeneous layers). Displacements for (a) horizontal axis, and (b) vertical axis.

Rayleigh wave displacements in a vertically heterogeneous model are similar to displacements found in the free Rayleigh wave case, Figure 1.11. Particle displacement due to lower frequencies sample deeper than higher frequencies. Particle displacement in the horizontal direction (Figure 1.13a) indicates a slight change in the trend at 6 m, the same depth as the boundary. In this respect, horizontally moving particles seem to be more sensitive to changes in the velocity profile than vertically moving particles, Figure 1.13b.

Rayleigh wave propagation can be modeled given any number of layers and any variation of elastic properties. Even a complicated model where elastic properties are multi-valued as a function of depth may be used with the modeling template. Figure 1.14a shows a multi-valued shear-wave velocity profile.

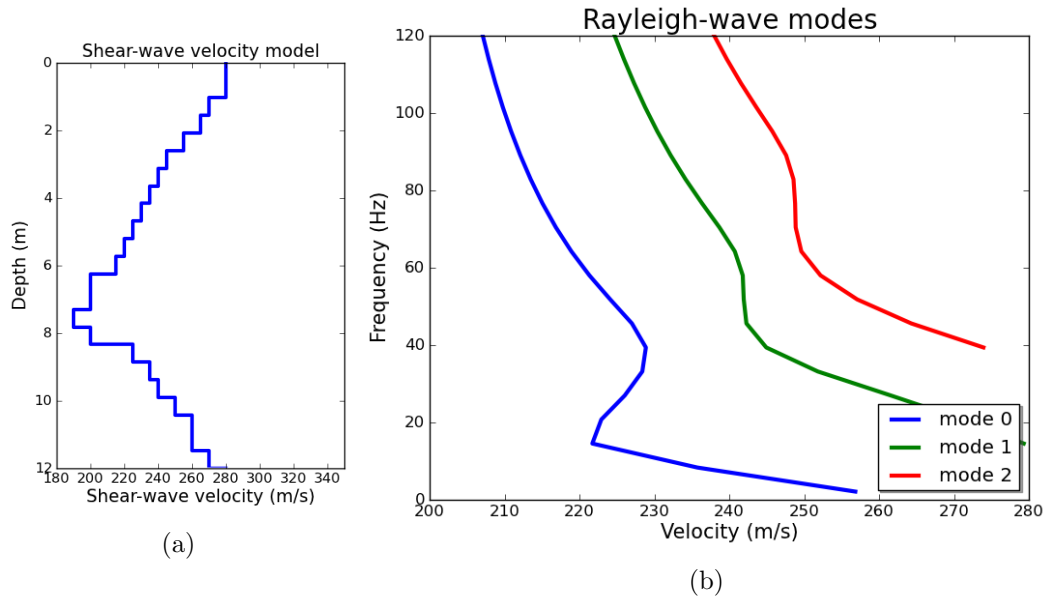


Figure 1.14: Rayleigh wave, general case, Vertically inhomogeneous layers (a) Shear-wave velocity model, (b) resultant fundamental mode and two higher modes.

Phase velocities are drastically affected by a multi-valued profile. Reverse dispersion is observed in the fundamental mode from 20 to 40 Hz, Figure 1.14b. Particle displacement for this type of model is also unusual, as seen in Figure 1.15.

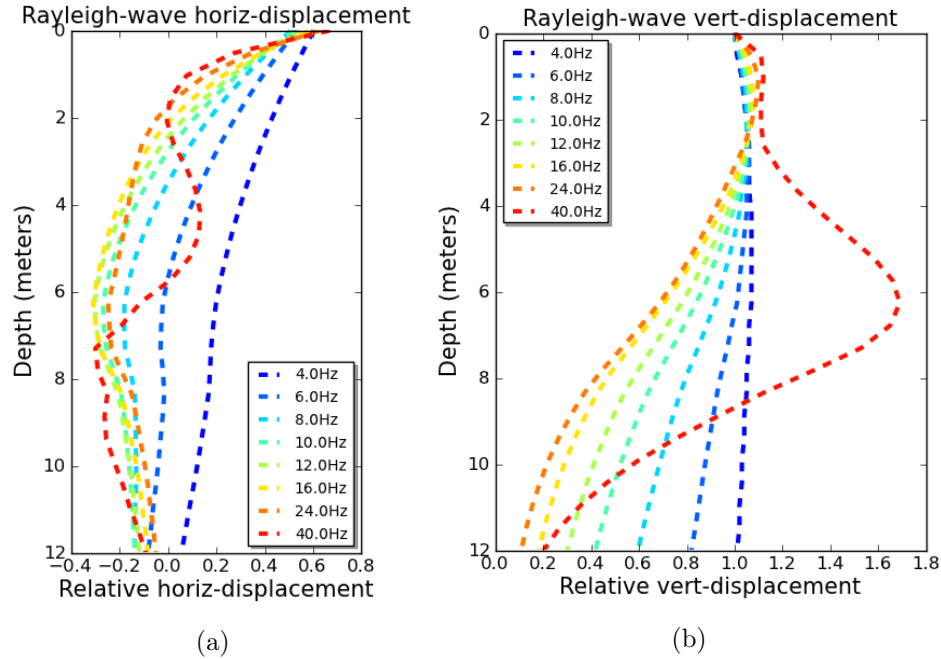


Figure 1.15: Rayleigh wave, general case, complex model (vertically inhomogeneous layers). Particle displacement for (a) horizontal axis, and (b) vertical axis.

Unlike the free Rayleigh case (Figure 1.11) and the simple two layer case (Figure 1.13) where particle displacements uniformly decrease with depth for all frequencies, this complex case causes particle displacements to appear somewhat erratic as a function of depth and frequency. Higher frequencies (approximately 40Hz) tune to the depth of the gradient change in the velocity profile causing largest displacements. Note that 40 Hz is also the inflection point of the phase-velocity curve where reverse dispersion turns back into normal dispersion.

1.8 Phase and group velocity

Consider again a simple two layer model which supports either Love or Rayleigh wave propagation. The surface wave is dependent on the shear-wave velocities, β , of the model, but the actual velocity of the surface wave in terms of its phase (i.e., phase-velocity, c),

differs as a function of frequency. Surface-wave phase velocity is also known as a dispersion curve. Phase velocity of the surface wave will be modulated by an envelope traveling at the group-velocity, g . Essentially, the envelope forms because there is a summation across the continuum of frequencies represented in the surface wave. Different wavelengths, cause constructive and destructive interference, shaping the envelope. Given that phase velocity is expressed as,

$$c = \frac{\omega}{k}, \quad (1.52)$$

group velocity is determined by taking the derivative,

$$g = \frac{d\omega}{dk}. \quad (1.53)$$

For the standard subsurface model, where lower layers are higher velocity than upper layers, phase velocity is greater than group velocity, as seen in Figure 1.16.

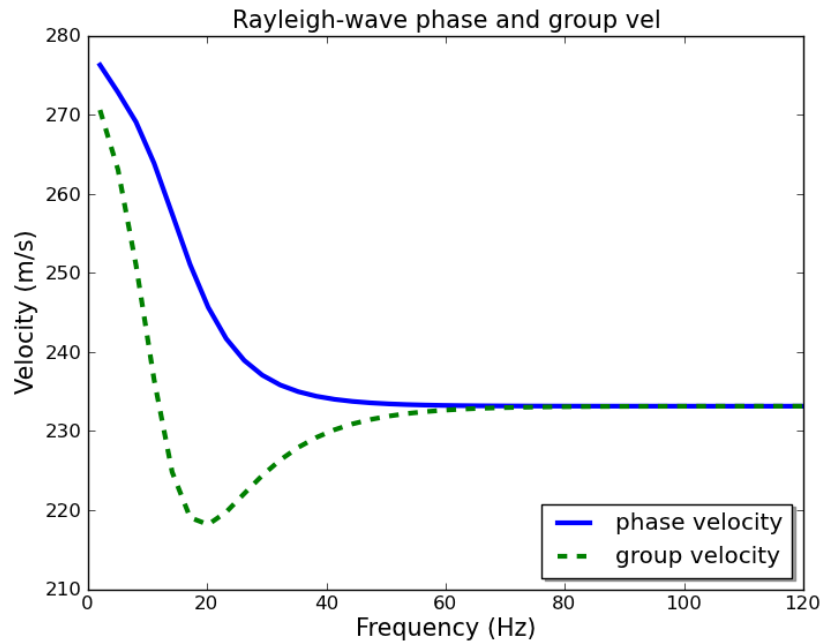


Figure 1.16: Dispersion curves for fundamental mode. Both phase and group velocity are indicated.

The dip in the group velocity is often referred to as the Airy phase. The Airy phase is located at the inflection point of the dispersion curve (defined by phase velocities). If a signal is bandlimited, the Airy phase often coincides with the central, or dominant, frequency of the surface wave.

1.9 Summary

Although surface waves are complicated, simplified modeling provides insight about fundamental surface wave characteristics. We expect specific propagation characteristics because surface waves are a type of boundary wave. Boundary waves exhibit a zone of particle displacement on the transmitted side the boundary. Displacement decays as distance from the boundary increases (known as inhomogeneous or evanescent behavior). Because the Love wave requires, at a minimum, two layers in the model, it follows that the Love wave is intrinsically dispersive. A Rayleigh wave can exist in a half-space with constant elastic properties and therefore is not intrinsically dispersive. In a vertically heterogeneous model, where evanescent characteristics cause the Rayleigh wave to sample the model differently depending on wavelength, the Rayleigh wave becomes dispersive.

The direct surface wave can be modeled in 2D and 3D, for a vertically layered model, by only slightly modifying equations shown here. We extend these equations in subsequent chapters to account for lateral heterogeneity and model reflected surface waves.

Chapter 2

Modeling surface waves: 2D

2.1 Overview

In the previous chapter we modeled surface waves given a 1D depth profile of elastic properties. In this chapter we model surface waves in two dimensions. Given constant or smooth elastic properties throughout the model, only direct surface waves are expected. If sharp lateral change exists in the model, surface wave reflections will occur. There are several ways to simulate surface waves in a model that is heterogeneous in two dimensions. Analytic and semi-analytic equations, based on equations in chapter 1, can be easily extended to simulate direct surface waves. However, as we will show, additional theory is needed to simulate reflected surface waves using semi-analytic methods.

Alternatively, numeric approximation can be used for complex 2D models that have sharp lateral change. Oftentimes, a known, exact analytic solution is used to verify a numerical method (using a simple model for comparison). We will instead use numerical approximation to verify our semi-analytic solution (using a complex model for comparison). In this chapter, two variations of numerical modeling are investigated: finite difference and

spectral element. In addition, we investigate a semi-analytic method based on elastic properties and develop a semi-analytic method based on surface-wave phase-velocities. Finally, all methods, both semi-analytic methods, finite difference, and spectral element are compared. The model used for the comparisons is a 2D with heterogeneity in both dimensions and sharp lateral heterogeneity. The semi-analytic method developed here is preferred for the following reasons:

1. relative speed of computation, and
2. ability to isolate parts of the solution.

Numerical methods can be seen as superior to analytic methods because, due to discretization inherent to the numerical formulation, they naturally handle heterogeneity in two or three dimensions. However, the discretization of models needed for numerical methods create large matrices. In order to determine a solution for these large matrices a high performance computer with multiple cores is often needed to split up the task and parallelize the problem. Although analytic methods cut corners with assumptions made to simplify models, the solutions are usually much less computationally demanding. Another advantage of analytic methods is that parts of the solution can be isolated and determined separately. For example, in the determination of phase-velocities of the surface wave, any number of modes for the wave can be included and excluded from the solution. This can be helpful when isolating properties of the surface wave.

2.2 Numerical modeling

Numerical methods for ordinary differential equations (ODEs), such as the wave equation, are a class of methods used to find numerical approximations to the solutions of ordinary

differential equations. Finite-difference and finite-element methods approximate physical properties with many discrete grid values or elements to solve the wave equation. Solutions are found for a series of discrete time steps. In other words, a snapshot of the wavefield for the entire model is found for each time step in the series. Finite-difference methods specify the model at a series of grid points and approximate the spatial and temporal derivatives by using the model values at nearby grid points. Finite-element methods divide the model into a series of volume elements with specified properties and match the appropriate boundary conditions among adjacent elements. Spectral elements uses numerical integration to elegantly handle boundary conditions.

Finite-difference methods are simple to implement. Their gridding scheme naturally matches the layout of matrices used for models. More work is needed to map finite elements and spectral elements to the usual matrices used for models and inversion. However, element methods are more suited to correctly handling boundary conditions at sharp interfaces due to adaptation to boundaries and the natural form of boundary condition specification by integrals. Topography at the free-surface is also naturally suited for element-based methods.

Numerical methods can accurately solve complicated 2D models if the gridding or meshing scheme has enough resolution. In general, there must be a sufficient amount of grid points or model elements per seismic wavelength to accurately represent the wavefield. If the resolution of grid points or elements are increased the number of time steps needed also increases. As smaller wavelengths are modeled the computational task required increases rapidly. The most challenging modeling for numerical methods is in low velocity models where grid or element densities must be high and at high frequencies. The order of approximation for numerical methods effect accuracy and grid/element density. First-order schemes for spatial derivatives in finite differencing are fast, but they need more grid

points per wavelength to match the accuracy of high-order schemes. Element methods are often high-order because of adaptation of each element to the boundary, and the method's resolution.

2.2.1 Finite difference

Although the topic of this chapter is surface-wave modeling in 2D models, terms are kept simple by showing the formulation for an SH wave. As long as boundary conditions for the free-surface are enforced, the given equations will produce surface waves. We can represent a SH wave traveling in the x direction, as the wave equation,

$$\frac{\partial}{\partial x} \left[\mu(x) \frac{\partial u_2}{\partial x} \right] = \rho(x) \frac{\partial^2 u_2}{\partial t^2}, \quad (2.1)$$

where μ is the shear wave modulus and u_2 indicates particle motion in the transverse direction. We can simplify our terms by using particle velocity and by recognizing the relationship between stress, τ , shear modulus, and displacement $\tau = \mu \frac{\partial u_2}{\partial x}$. Because this is an elastic equation we have a set of equations with particle velocity, c , and stress, τ , that are solved,

$$\begin{aligned} \frac{\partial \tau}{\partial x} &= \rho(x) \frac{\partial c}{\partial t}, \\ \frac{\partial c}{\partial x} &= \frac{1}{\mu(x)} \frac{\partial \tau}{\partial t}. \end{aligned} \quad (2.2)$$

We seek to solve the above equation by a time step process where time, t , on the right side of the equation is discretized and known, Δt , and the left hand is calculated for a discrete uniform grid of x points indicated by Δx . A Taylor series expansion is used to approximate the first-order derivatives. For example, if we want to predict stress at some point we must

consider the surrounding points $(x + \Delta x, x - \Delta x)$. We can expand the stress part in equation 2.2 as,

$$\begin{aligned}\tau(x + \Delta x) &= \tau(x) + \frac{\partial \tau}{\partial x} \Delta x + \frac{1}{2} \frac{\partial^2 \tau}{\partial x^2} (\Delta x)^2 + \frac{1}{6} \frac{\partial^3 \tau}{\partial x^3} (\Delta x)^3 + \dots, \\ \tau(x - \Delta x) &= \tau(x) - \frac{\partial \tau}{\partial x} \Delta x + \frac{1}{2} \frac{\partial^2 \tau}{\partial x^2} (\Delta x)^2 - \frac{1}{6} \frac{\partial^3 \tau}{\partial x^3} (\Delta x)^3 + \dots\end{aligned}\tag{2.3}$$

By solving for the difference, $\frac{\partial \tau}{\partial x}$, we obtain the equations,

$$\begin{aligned}\frac{\partial \tau}{\partial x} &= \frac{1}{\Delta x} [\tau(x + \Delta x) - \tau(x)] - \frac{1}{2} \frac{\partial^2 \tau}{\partial x^2} (\Delta x) - \frac{1}{6} \frac{\partial^3 \tau}{\partial x^3} (\Delta x)^2 - \dots, \\ \frac{\partial \tau}{\partial x} &= \frac{1}{\Delta x} [\tau(x) - \tau(x - \Delta x)] + \frac{1}{2} \frac{\partial^2 \tau}{\partial x^2} (\Delta x) - \frac{1}{6} \frac{\partial^3 \tau}{\partial x^3} (\Delta x)^2 - \dots,\end{aligned}\tag{2.4}$$

which can be averaged together to arrive at (dropping the higher terms),

$$\frac{\partial \tau}{\partial x} = \frac{1}{2\Delta x} [\tau(x + \Delta x) - \tau(x - \Delta x)].\tag{2.5}$$

This is also known as a stencil of the first order. The same stencil is applied to spatial derivatives of phase velocity as well as the temporal part of the set of equations 2.2, resulting in the finite difference version of the expression,

$$\begin{aligned}\frac{\tau_{j+1}^i - \tau_{j-1}^i}{2\Delta x} &= \rho_j \frac{c_j^{i+1} - c_j^{i-1}}{2\Delta t} \\ \frac{c_{j+1}^i - c_{j-1}^i}{2\Delta x} &= \frac{1}{\mu_j} \frac{\tau_j^{i+1} - \tau_j^{i-1}}{2\Delta t}\end{aligned}\tag{2.6}$$

The simplest grid to use with the stencil is the grid with phase-velocities and stresses stored at the same location as in Figure 2.1. By using a staggering grid (Virieux, 1986) results can be improved. Nonetheless, certain limitations still exist. The time interval, Δt , must be smaller than $\Delta x/c_j$ otherwise the next place to calculate stress and velocity is too far given the spacing. In addition, numerical-dispersion can also be problematic.

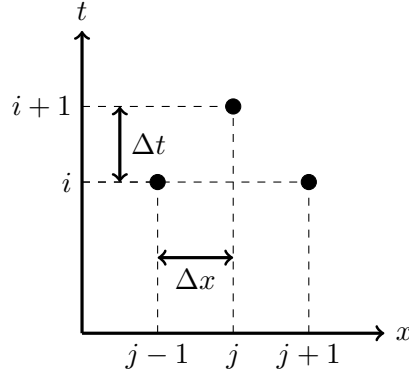


Figure 2.1: Simple grid for 1D finite difference where both the stresses and velocities are stored at the same point.

Thus far, the derivation for the SH wave has been shown in 1D. The system of equations can be extended to 2D for either the SH or P-SV case. In order to solve for both the Love wave (SH motion) and Rayleigh wave (P and SV motion) the system of equations should be described in 3D. Although we continue by presenting equations in 3D, note that we will proceed in the chapter considering a 2D model. By considering a 3D system of equations we will be able to model particle displacement in and out of the plane (SH and Love motion) of a 2D model. Boundary conditions must be applied to the free surface ($z = 0$) to generate Love and Rayleigh waves. The free surface boundary conditions are,

$$\frac{\partial u_y}{\partial z} + \frac{\partial u_z}{\partial x} = \tau = 0, \quad (2.7)$$

for tangential stress, and

$$(\lambda + 2\mu) \frac{\partial u_y}{\partial x} + \frac{\partial u_z}{\partial z} = \tau = 0, \quad (2.8)$$

for normal stress. There are two main classes of numerical approximations for the free surface. The first class of methods add a fictitious layer above the free surface to deal with the boundary. Derivatives with respect to x are replaced by central differences and

derivatives with respect to z are either replaced by central-difference, replaced by one-sided differences, or implicitly centered. The second class of methods does not add a fictitious layer above the free surface. Derivatives can either be composed differently by replacing z derivatives with x and t derivatives or the governing equations at the boundary can be modified. Here, we show the method which implicitly centers both x and z derivatives between the fictitious layer and the layer below the free surface layer. Equations 2.7 and 2.8 can be discretized and rewritten as second order differences,

$$\mathbf{u}_{x0} - \frac{1}{4}\mathbf{A}\mathbf{u}_{z0} = \mathbf{u}_{x1} + \frac{1}{4}\mathbf{A}\mathbf{u}_{z1}, \quad (2.9)$$

for tangential stress, and

$$\mathbf{u}_{z0} - \frac{1}{4}\mathbf{D}\mathbf{A}\mathbf{u}_{x0} = \mathbf{u}_{z1} + \frac{1}{4}\mathbf{D}\mathbf{A}\mathbf{u}_{x1}, \quad (2.10)$$

for normal stress. The subscripts 0 and 1 indicate the fictitious layer and the layer below the free surface. The matrix \mathbf{D} contains the elastic parameters, λ and μ , across the free surface and the matrix \mathbf{A} is bidiagonal with superdiagonals equal to 1 and subdiagonals equal to -1. Apart from a modified condition at the left and right edges of the layer (Vidale and Clayton, 1986), equations 2.9 and 2.10 can be solved for the displacements, \mathbf{u}_{x0} and \mathbf{u}_{z0} , to describe particle motion at the free surface.

We consider a model with a single vertical blind fault, Figure 2.2. Synthetic data is generated using a time domain elastic finite-difference method using a staggered grid (Yan and Sava, 2008). A point source with a 25 Hz Ricker wavelet is placed just below the surface to excite surface waves. One shot is simulated on the left side of the model. Vertical component receivers are simulated at a 1 m spacing along the entire extent of the model.

A constant density of 2800 kg/m^3 and a constant V_P/V_S value of 2 is used throughout the entire model. Attenuation is excluded from the simulation. The full extent of the model used for the numerical simulation is not shown. For visual clarity only the shallow portion at the location of the survey line is shown. The greater extent of the actual model used for the simulation reduces artifacts reflecting from the boundaries.

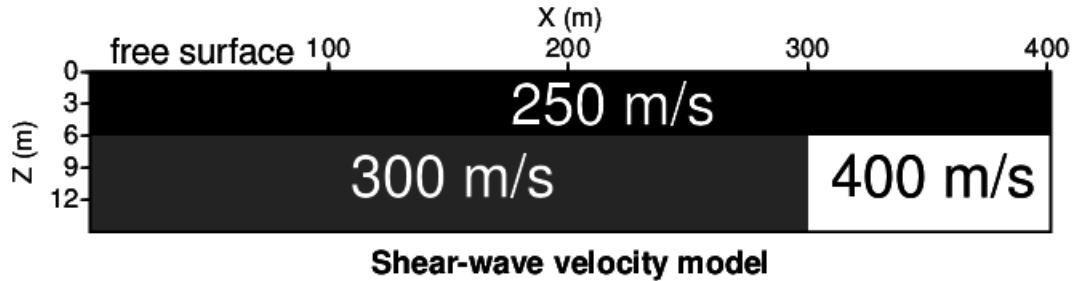


Figure 2.2: Shear-wave velocity model used for numerical modeling of the surface wave.

Data generated from the model includes all arrivals expected from a 2D elastic solution, Figure 2.3. The first arrival is the P-wave and the dispersive surface wave is evident traveling at slower velocity. Although it is not detectable visually, the S wave exists at the outermost (fastest) part of the surface wave. Reflected surface-wave energy from the vertical boundary can be seen originating from the direct surface-wave and traveling back in the other direction.

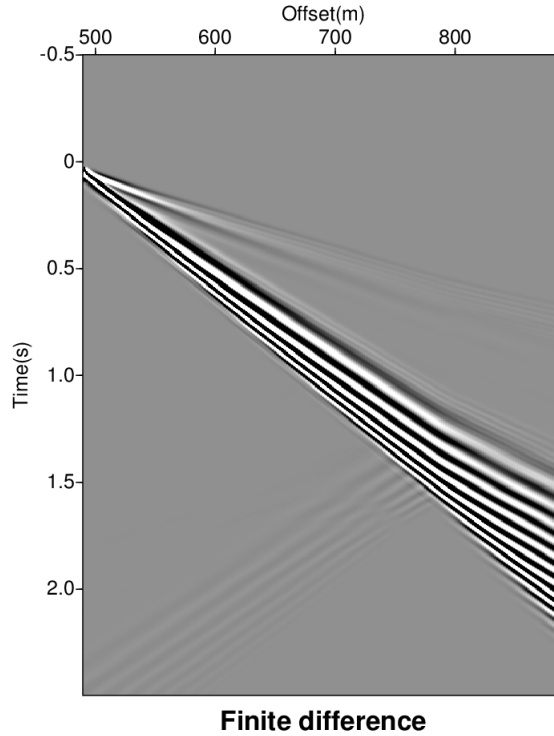


Figure 2.3: Synthetic record collected from off end shot on left hand side. Wavefield generated using finite difference.

As can be seen, the source wavelet is traveling at different velocities depending on the frequency and is constructively and destructively interfering to create a wavetrain. More will be said in the next chapter on how to extract dispersion information from the record. Surface-waves in this simulation are due only to the Rayleigh wave. The Love wave is not present in this simulation as no displacement is modeled in and out of the 2D plane.

2.2.2 Spectral elements

The spectral element method (SEM) expands the solution for the wave equation with a trigonometric series. Expanding the solution in this way results in a high order approximation (therefore requiring less grid points to satisfy numerical dispersion constraints). In addition, error in the approximation decreases exponentially as the order increases making

the exact solution easier to approximate. In finite-difference methods, a small anomaly in the model requires a fine grid whereas with SEM larger elements may be able to resolve the effect of the anomaly.

The trigonometric polynomials used in SEM have an orthonormal basis. The functions used in SEM are piecewise polynomial basis functions like orthogonal Chebyshev polynomials or very high order Legendre polynomials over non-uniformly spaced elements. Non-uniformity of elements helps to make the mass matrix diagonal. Below is an outline (Schubert, 2003) of major steps in the implementation of SEM:

1. weak formulation for linear system,
2. mapping function for irregular grids to element domain,
3. interpolation and integration over elements,
4. forming a mass matrix and stiffness matrix, and
5. assembly for global matrix equation.

The term “weak form” means that instead of solving a differential equation, an integral function is solved. The integral function is easier to solve yet it implicitly contains the differential equations. Finite-difference methods introduce conditions that must be satisfied by the solution, therefore they are considered the “strong form”. Methods based on an integral equation, the “weak form”, state that conditions need to be satisfied in an average sense.

Consider the boundary condition for stresses on the free surface. In the finite-difference method we solve for no traction on the surface (strong form) forcing stress to be zero. In SEM, there will be residual stress on the surface. As the mesh is refined, the stress value at

the traction-free-surface approaches zero. We illustrate SEM by writing the wave equation as equal to a source term, $f(x)$,

$$f(x) = \rho \frac{\partial^2 u}{\partial t^2} - \frac{\partial}{\partial x} \left(\mu \frac{\partial u}{\partial x} \right), \quad (2.11)$$

where u denotes displacement and μ is shear wave modulus. We represent equation 2.11 in weak form as,

$$\int_{\Omega} c f \, dx = \int_{\Omega} \rho c \ddot{u} \, dx - \int_{\Gamma} c \mu \nabla u \, dx + \int_{\Omega} \nabla c \mu \nabla u \, dx, \quad (2.12)$$

where we integrate by parts over the entire model volume Ω and show the integrating term for the absorbing boundary, Γ , as well. If we consider the free surface boundary condition, $\mu \frac{\partial u}{\partial x} = \tau = 0$, where stress, τ goes to zero, then equation 2.12 simplifies to,

$$\int_{\Omega} c f \, dx = \int_{\Omega} \rho c \ddot{u} \, dx + \int_{\Omega} \nabla c \mu \nabla u \, dx, \quad (2.13)$$

which can also be represented as a linear system of equations,

$$M\ddot{U} + KU = F, \quad (2.14)$$

where F is the source term, M is the global mass matrix, K is the global stiffness matrix, and U is displacement.

The next step is to map the physical coordinates of the elements, x , to the local element coordinates, ξ , (natural coordinates) for the entire domain, Ω . The purpose is to describe the elements shape and location with a computationally efficient matrix. Each element, $\Omega_b, b = 1, \dots, n_b$, is defined in terms of location by a set of control points, $n_a, a = 1, \dots, n_a$.

In addition, the shape of the element is described by a set of shape functions, $N_a(\xi)$. The shape function itself is defined by Lagrange polynomials, $\ell_n^{n_\ell}(\xi)$, of polynomial orders of degree, n_ℓ . Accordingly, the mapping for the entire mesh model is then,

$$x(\xi) = \sum_{a=1}^{n_\ell} N_a(\xi)x_a. \quad (2.15)$$

At this point the mapping is not quite complete. The Jacobian, J , is needed to correct the coordinate transformation after calculating derivatives and integrals. For example, an element of length dx for a given element, Ω_e , is related to an element of length $d\xi$ in the reference cube by,

$$dx = J_e d\xi, \quad (2.16)$$

where,

$$J_e = \left| \frac{\partial x}{\partial \xi} \right|. \quad (2.17)$$

By taking the derivative of the original mapping, equation 2.15, we calculate the Jacobian and arrive at the needed correction,

$$\frac{\partial x(\xi)}{\partial \xi} = \sum_{a=1}^{n_\ell} \frac{\partial N_a(\xi)}{\partial \xi} x_a. \quad (2.18)$$

Space between the control points in an element is first interpolated and then integrated. Interpolation is done using Lagrange polynomials defined by Gauss-Lobatto-Legendre (GLL) points where the polynomial degree, n_ℓ , for interpolation is higher than that for the mapping (on the order of 5-10). For example, displacement and gradient for an element, u_e and

∇u_e , are calculated by,

$$\begin{aligned} u_e(\xi) &= \sum_{i=1}^{n_\ell} u_e(\xi) \ell_i(\xi) \quad \text{where} \quad \ell_i = \prod_{j=0}^{n_\ell} \frac{\xi - \xi_j}{\xi_i - \xi_j}, \\ \nabla u_e(\xi) &= \sum_{i=1}^{n_\ell} u_e(\xi) \ell'_i(\xi) \quad \text{where} \quad \ell_i(\xi_j) = \delta_{ij}. \end{aligned} \quad (2.19)$$

Weights from the integration of an element are determined by using the GLL integration rule. Returning to the example for displacement we obtain,

$$\int_e u(\xi) dx = \sum_{i=0}^{n_\ell} w_i f(\xi_i), \quad (2.20)$$

where the weights, w_i are,

$$\begin{aligned} w_i &= \frac{2}{n_\ell(n_\ell + 1)[P_{n_\ell}(\xi_i)]^2} \quad \text{for} \quad (\xi_i \neq \pm 1), \\ w_i &= \frac{2}{n_\ell(n_\ell + 1)} \quad \text{for} \quad (\xi_i = \pm 1). \end{aligned} \quad (2.21)$$

Here, the Lagrange polynomials of degree n_ℓ are noted as P_{n_ℓ} . The next step is to form the mass matrix (the first term in equation 2.14, $M\ddot{U}$) and stiffness matrix (the second term in equation 2.14, KU). The mass matrix is a diagonal matrix and the stiffness is not. To form the mass matrix we start with the weak form, equation 2.13, and substitute in the Jacobian mapping, interpolation, and weights from the integration,

$$\int_{\Omega} \rho c \ddot{u} dx = \sum_{k=0}^{n_\ell} \left\{ \rho(\xi_k) w_k \left[\sum_{i=0}^{n_\ell} c_i \ell_i(\xi_k) \right] \left[\sum_{j=0}^{n_\ell} \ddot{u}_j \ell_j(\xi_k) \right] J(\xi_k) \right\}, \quad (2.22)$$

we can simplify the expression using the Kronecker delta, δ , to arrive at the newly formed mass matrix for any element, e ,

$$me_{ij} = \rho_i w_i J_i \delta_{ij}. \quad (2.23)$$

In a similar manner, excluding the simplification with the Kronecker delta, we can factor the stiffness term into a matrix,

$$ke_{ij} = \sum_{k=0}^{n_\ell} \mu_k w_k \ell'_i(\xi_k) \ell'_j(\xi_k) J_k. \quad (2.24)$$

A connectivity matrix, C , is required to assemble all the elements together. Each mesh will have a unique connectivity matrix. The matrix shows how the elements are connected, which elements share nodes, and which elements contribute to a node. If we now redefine i to represent element number and j , and k to indicate N nodes, we can write equations to describe the connection of elements in the mass matrix and the stiffness matrix,

$$\begin{aligned} M(C_{j,i}) &= M(C_{j,i}) + me_j^i, \\ K(C_{k,i}, C_{j,i}) &= K(C_{k,i}, C_{j,i}) + ke_{k,j}^i. \end{aligned} \quad (2.25)$$

In order to solve the equations we can calculate the global stiffness matrix. For example, to solve strain at node, i , we would use,

$$\frac{\partial u_i}{\partial x} = \sum_j u_j \ell'_j(\xi_i) \cdot \mathbf{J}_i^{-1}, \quad (2.26)$$

where \mathbf{J} is the Jacobian. As stated before, the free surface boundary conditions are naturally handled by the spectral element method. The weak formulation implicitly includes the

condition, therefore calculating displacement as,

$$U_{t_{i+1}} = \Delta t^2 \cdot M^{-1} F + 2U_{t_i} - U_{t_{i-1}}, \quad (2.27)$$

at each time step correctly accounts for the free surface. Other conditions such as absorbing or rigid boundaries can be applied to elements on the edge.

Consider again the model with a single vertical blind fault, Figure 2.2. Synthetic data is generated using a continuous Galerkin spectral-element method, SPECFEM2D (Komatitsch and Tromp, 2002). Survey parameters used for SPECFEM2D are identical to the previous parameters for finite difference. A 25 Hz Ricker wavelet is used as point source just below the surface. A single shot at the left side of the model is simulated and vertical component receivers at a 1 m spacing record the wavfield. Density and V_P/V_S are a constant value of 2800 kg/m^3 and 2, respectively, throughout the model. No attenuation is included in the simulation.

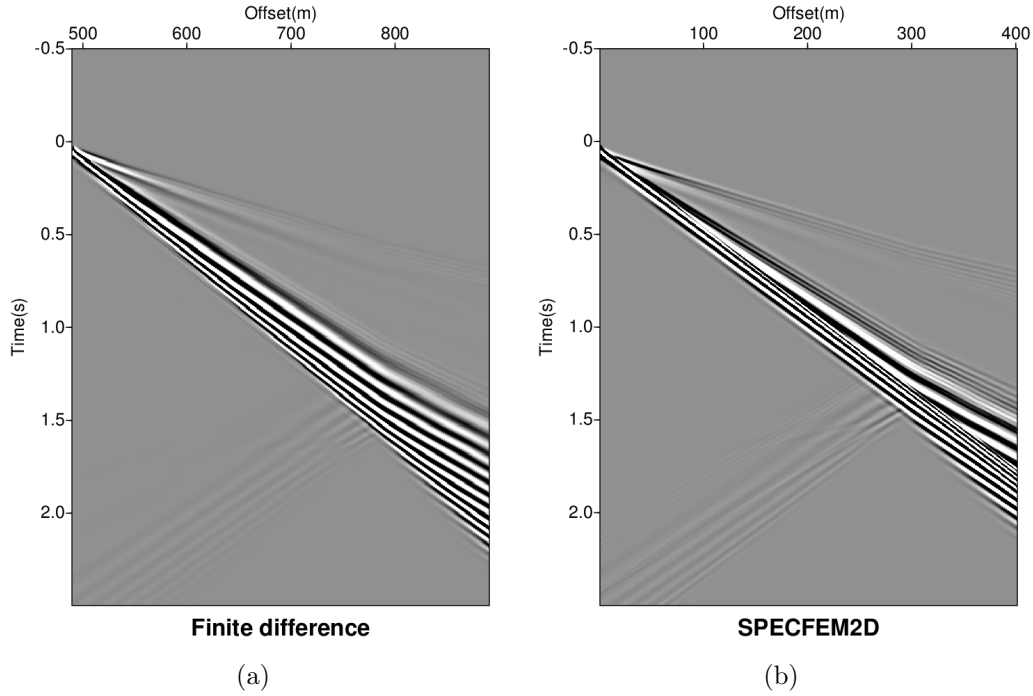


Figure 2.4: Comparison of synthetic records. (a) wavefield generated by (a) finite difference and (b) spectral element (SPECFEM2D).

The data modeled from the spectral element method, 2.4b, is very close in appearance to data modeled from finite difference, Figure 2.4a. The overall structure of the wavefield is similar as are the velocities. The interior of the surface wavetrain shows some dissimilarity. This is due to differences between the way the spectral element method and finite difference method handle boundary conditions at the free surface. It is difficult to tell at this point which is more correct. However, the analytic results, presented later in this chapter, will help validate one or the other.

2.2.3 Elements and meshing

The spectral element method is represented in a discrete way using meshes. Meshes are classified by cell type and grid type. Common cell types in 2D are triangular and quadrilateral. Common cell types in 3D are tetrahedral and hexahedral. The grid type is either

structured (connected regularly), unstructured, (connected irregularly), or a hybrid of the two.

Sections below outline some unique uses of meshes for modeling surface waves. These uses include: stretching the mesh to save computational time, mapping to meshes from regular grids (arrays), and modeling topography.

Stretching mesh

Spectral-element methods are slower than finite-difference methods due to the extra steps of mapping and interpolation. However, there are two ways to speed up calculation. Nodes defining elements can be spaced further apart than grids in the finite-difference method. The high order inherent to the spectral-element approximation allows for greater spacing. Secondly, the flexibility of the element allows the mesh to be adaptable to the velocity model. A fine mesh can be used where velocities are slow (usually near the surface) and the mesh can be expanded where velocities are faster (usually at depth). The spectral-element method, therefore, avoids being constrained by the slowest velocities. Figure 2.5 shows a simple model with two different grid spacing assuming that velocity increases with depth.

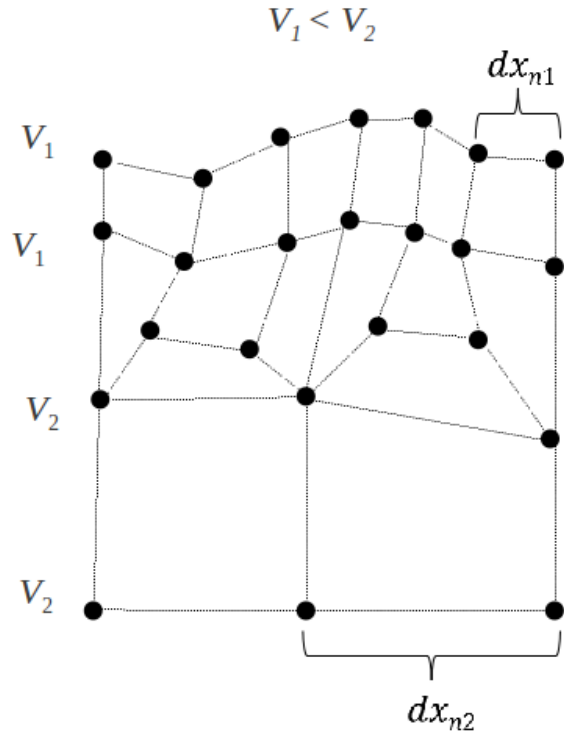


Figure 2.5: Spacing between nodes can be stretched based on velocity values.

Mapping grids to mesh

In order to compare data generated by finite difference (and semi-analytic) methods with spectral elements, the same model must be used. The structure of a regular array model and a mesh model are, however, different. One solution is to map the regular array model to a mesh model. There are a number of different ways to perform the mapping. Figure 2.6 shows two different variations of mapping a regular array to a mesh. Keep in mind, it is assumed that the regular array is sampled on a finer grid than what is needed in a mesh for the higher order spectral-element method.

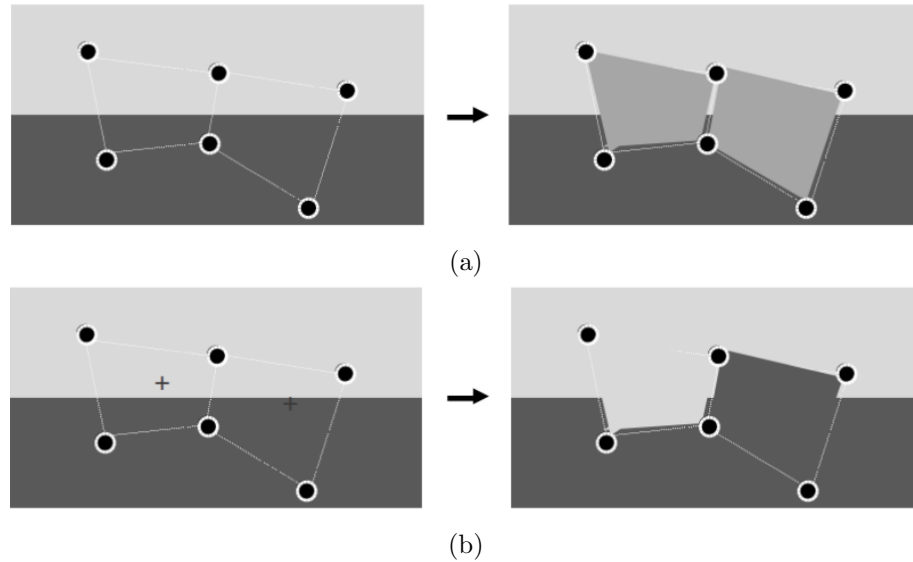
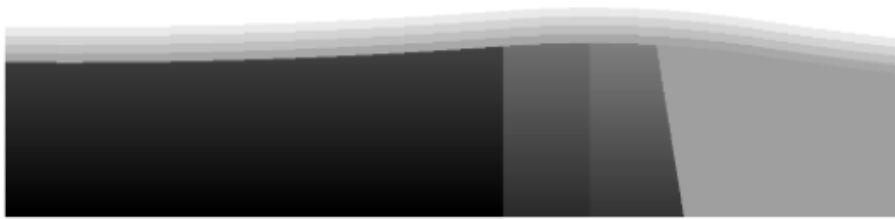


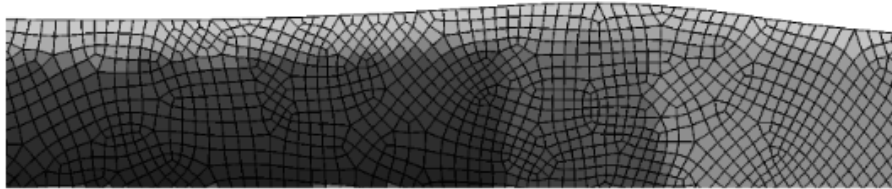
Figure 2.6: Options for mapping regular grid to meshed surface: (a) average velocities from points assigned to grid, (b) average positions from points assigned to grid.

For example, an element can be assigned an averaged velocity from several nodes, or velocities can be assigned based on the central position of the node. Either way, because the mesh is less dense than the grid, there is a risk that sharp interfaces and horizons, may not be preserved in a model.

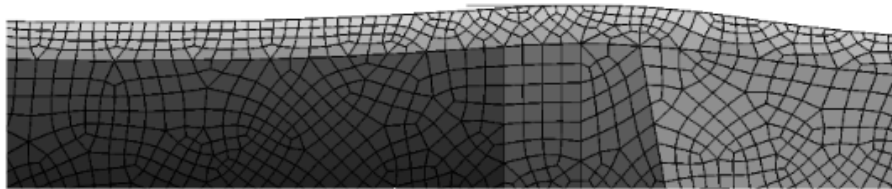
In order to preserve interfaces and horizons they need to be either predefined or detected as edges in the regular grid prior to meshing. Figure 2.7a shows an example of a regular grid built for the purpose of meshing. It exhibits gentle topography with layers below the free surface and several blind faults.



(a)



(b)



(c)

Figure 2.7: Options for mapping regular grid to meshed surface (a) regular grid. (b) points averaged (c) edge detection used for meshes

If the constructed model is built using averaged velocities or averaged positions, Figure 2.7b, it can be seen that resolution is lost. By predefining the location of horizons, interfaces, and edges the location and resolution of major faults can be kept in the final mesh, Figure 2.7c. The mesh with edges preserved is an example of a hybrid mesh.

Topography

Spectral elements have an advantage over finite difference and semi-analytic methods because topography is naturally accounted for in the mesh. Initial tests with topography show that surface wave reflection is dependent on the spatial periodicity of topography. Consider

two models, one model with a broad hill, Figure 2.8a and another with a smaller hill, Figure 2.8b.

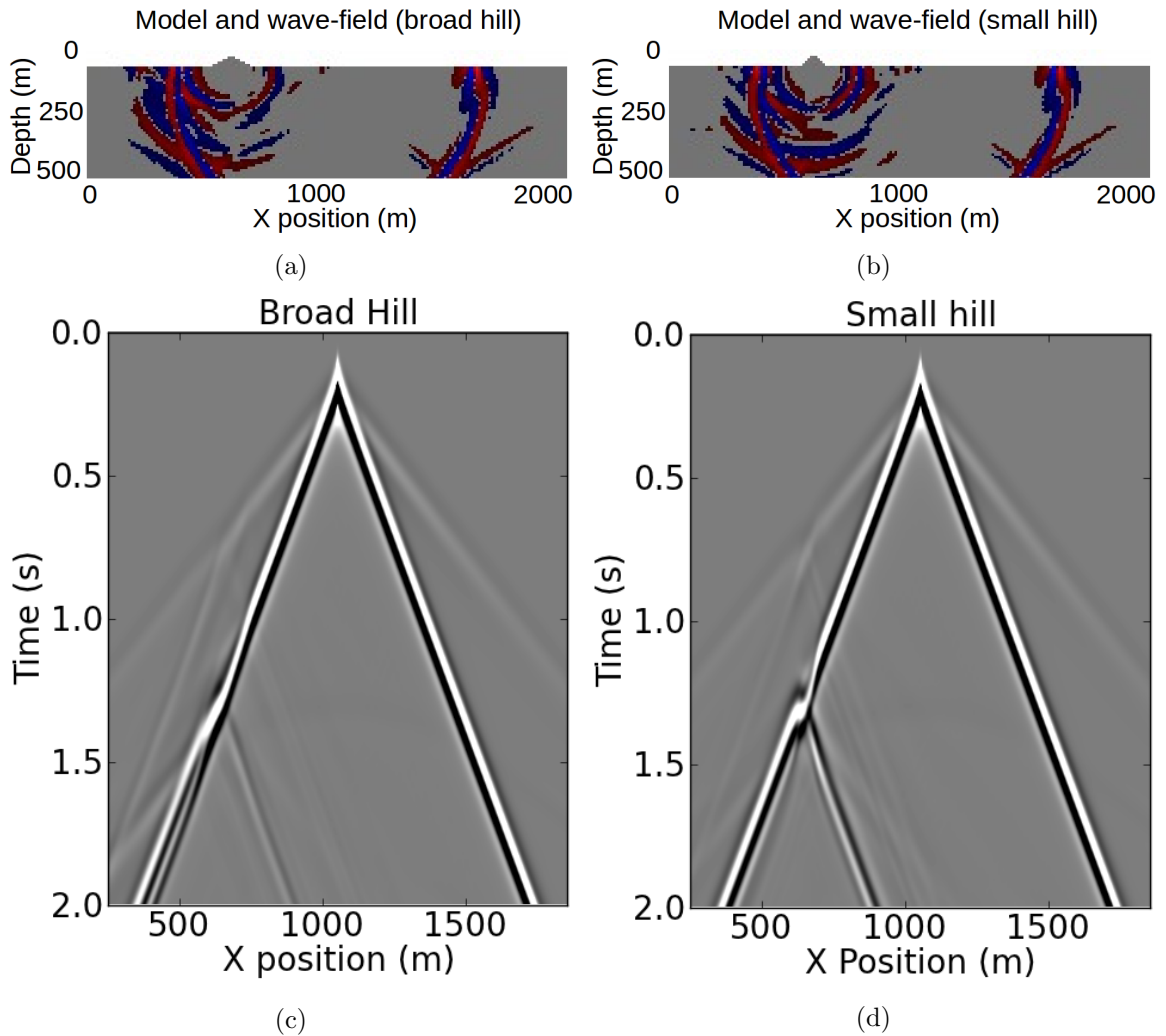


Figure 2.8: A comparison of surface wave reflections from a small hill and a broad hill: (a) model of broad hill, (b) model of small hill, (c) data from broad hill reflection, and (d) data from a small hill reflection.

A snapshot of the wavefield after reflecting from the hill is overlaid on the model. Figures 2.8c and 2.8d show the resultant shot record from a shot in the middle of the model. Note the strength of the reflected surface wave. The reflection of the surface wave from the hill which has a smaller periodicity than the surface-wave’s wavelength reflects more energy.

2.3 Semi-analytic modeling

Modeling surface-wave propagation using a 1D depth profile is valid for 2D if the depth profile remains laterally constant. In chapter 1 we, more or less, ignored the direction the wave was propagating, x . The model can be simplified so that semi-analytic expressions are valid in describing the nature of surface-wave propagation, including surface-wave reflections.

We assume that a shot record, D , is comprised of traces which have recorded the outgoing surface wave (the direct wave moving away from the source), O , incoming surface wave (the reflected wave moving toward the source), I , and noise, N , which includes all other energy,

$$D = O + I + N. \quad (2.28)$$

In the frequency domain, an outgoing surface wave propagating to a point, x_l , at lateral reflector, l , is described by:

$$O(\omega, x_l) = L(x_l)A(\omega)e^{-i[k(\omega)x_l - \omega t]}e^{-\alpha\omega x_l}e^{i\phi(\omega, x_l)}, \quad (2.29)$$

where $A(\omega)$ is the source wavelet that undergoes amplitude loss due to geometric spreading, $L(x_l)$, and attenuation, $\alpha(\omega)$. Dispersion due to layering in the near surface is expressed by a frequency-dependent phase-shift, where wavenumber, k , is a function of frequency, ω . The exponential terms containing ϕ describes the dispersion due to attenuation. As shown by Lee and Ross (2008) and Krohn (2010), the phase shift at a particular location along the ray-path is dependent on phase-velocities which are averaged across the length of the path. Assuming phase-velocities are known for N positions at constant spacing, dx , along

the ray-path from the source to x_l , the phase-shift of a surface wave is defined by,

$$k(\omega)x_l = N \cdot dx \left[\frac{1}{N} \left(\frac{1}{c(\omega)_1} + \frac{1}{c(\omega)_2} + \dots + \frac{1}{c(\omega)_N} \right) \right] \cdot \omega, \quad (2.30)$$

The wave returning back towards the source, incoming along x , from an incident at x_l is then the result of the convolution of reflectivity, $R(\omega, x_l)$, with the outgoing wave at the incident location:

$$I(\omega, x, x_l) = O(\omega, x_l)R(\omega, x_l)P_I, \quad (2.31)$$

where P_I is the propagation term necessary to generate dispersive waves at each trace along the incoming ray-path for the surface wave:

$$P_I = L(x - x_l)e^{-i[k(\omega)(x-x_l)-\omega t]}e^{-\alpha\omega(x-x_l)}e^{i\phi(\omega, x-x_l)}. \quad (2.32)$$

When the outgoing surface wave encounters the fault, the fault location acts as a scatterer or secondary source; this results in a reflected surface wave (the incoming wave) propagating back toward the true seismic source and a transmitted wave (the outgoing wave) continuing away from the source. The process is much like the concept of secondary sources in traditional imaging principles where each location in the subsurface is considered to be a potential source.

The key assumption is that semi-analytic modeling only requires coarse discretization in comparison with numerical modeling. At minimum, only properties at trace locations and lateral boundaries are needed to model the surface wave using a semi-analytic approach. Therefore, semi-analytic modeling has the potential to be much more computationally efficient than numerical modeling

Equation 2.29 is discretized in frequency, ω_i , and space, x_j , where i is the frequency index of m frequencies, $i = 1, \dots, m$, and j is the positional index of n positions, $j = 1, \dots, n$. Reflectors, l , are located along the j th position. We write the outgoing wave, $O(\omega_i, x_j)$, in simplified form as $O(\omega)_j$. We represent a 2D shear-wave model of size $m \times n$ where lateral positions of the model coincide with trace locations. Using the propagator matrix method (Haskell, 1953, Kennett, 1983, Thomson, 1950), we forward model the fundamental mode of n 1D dispersion curves, $c(\omega)_j$, for every lateral position and then model the outgoing wave, $O(w)_j$.

In order to calculate surface-wave reflections and the incoming surface-wave, the reflection coefficient, $R(\omega, x_l)$, in equation 2.31 must be estimated. Many semi-analytic methods exist for the calculation of reflection and transmission coefficients at sharp lateral boundaries in the shear-wave velocity model (Keilis-Borok, 1986, McGarr, 1967, Meier et al., 1997) where it is assumed that propagation is through vertically welded, stratified media. We propose a simplified semi-analytic solution for reflectivity based on the phase-velocity model rather than elastic properties. Both methods of calculating reflection coefficients are presented in the sections below. We also compare the results of the methods at one lateral boundary.

2.3.1 Modeling surface-wave reflections with elastic properties

Only solutions for the Rayleigh wave are presented; however, the equations can be modified to also account for the Love wave. Consider one boundary in an elastic model, Figure 2.9, where two vertically stratified quarter-spaces are welded together.

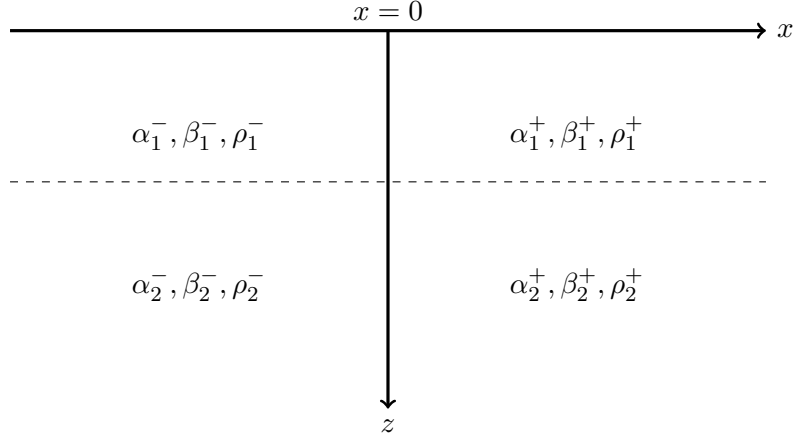


Figure 2.9: Semi-analytic representation of single lateral boundary in model.

The plane surface wave is assumed to travel from left ($-$) to right ($+$) across the vertical plane. If the Rayleigh wave has normal incidence at the interface, $x = 0$, there will be no conversions to the Love wave or other SH waves. It is also assumed that the incident Rayleigh wave at the vertical interface only results in transmitted and reflected Rayleigh waves. No other converted modes are considered.

To set up equations to calculate reflection coefficients the vertical plane between the quarter-spaces is set at $x = 0$. Equations are kept clear by adopting the same notation used by Keilis-Borok (1986) for the following variables:

ξ = wavenumber with continuous spectrum (previously identified as $k(\omega)$)

A_i = reflection coefficient for the i^{th} mode of the surface wave,

B_j = transmission coefficient for the j^{th} mode of the surface wave

$V^{(1)} = V_z$ = z component of displacement

$V^{(2)} = iV_x$ = x component of displacement

$V_i^{(1)} = i^{th}$ mode of z component of displacement

$V_i^{(1)-}$ = reflected i^{th} mode of z component of displacement, on the left (-)

$V_i^{(2)-}$ = reflected i^{th} mode of x component of displacement

$V_j^{(1)+}$ = transmitted j^{th} mode of z component of displacement, on the right (+)

$V_j^{(2)+}$ = transmitted j^{th} mode of x component displacement

Surface-wave reflection and transmission coefficients are derived by comparing displacements across lateral discontinuities. The solution to the 1D problem in chapter 1 gave us displacement as a function of depth, termed V , in this chapter's notation. Displacement as a function of both x and z is termed $u(x, z)$ here. The equation relating the two is,

$$u(x, z) = V_i(z)e^{-i\xi x}. \quad (2.33)$$

If we know the phase properties, or wavenumber, of the surface wave, ξ , we know how the wave will travel as a function of x by applying $e^{-i\xi x}$.

We consider the model with a single lateral discontinuity as shown in Figure 2.10. Solving for surface-wave propagation across the vertical boundary is initiated by constraining the displacements and the stresses to satisfy the following boundary conditions (in both media):

1. there must be no stress at the free surface ($z = 0$)
2. displacement must vanish as $z \rightarrow \infty$
3. at the lateral discontinuity, $x = 0$, there is continuity of displacements and stresses (i.e., welded)

Then, starting with a single, s^{th} mode of the surface wave,

$$u_s(x, z, \omega)e^{i\omega t}, \quad (2.34)$$

incident on the interface then for a fixed frequency, ω , the reflected wave is,

$$\sum_{i=1}^m A_i u_i^{-*}(x, z, \omega)e^{i\omega t}, \quad (2.35)$$

and the transmitted wave is,

$$\sum_{j=1}^n B_j u_j^+(x, z, \omega)e^{i\omega t}, \quad (2.36)$$

where i and j are equal to the reflected and transmitted mode respectively, ($i = 1, 2, \dots, n$), and, ($j = 1, 2, \dots, m$). The expression $e^{i\omega t}$ is omitted in the following equations. Following the Green function presented by Its and Yanovskaya (1977) we arrive at equations for the transmission coefficient,

$$A_i = - \sum_{j=1}^n B_j P_{ij}, \quad (2.37)$$

and reflection coefficient,

$$B_j = S_{ij}^* - \sum_{i=1}^m A_i P_{ij}^*. \quad (2.38)$$

The coupling coefficients for the Rayleigh wave are,

$$\begin{aligned} P_{ij} &= Q_{ij}^- - Q_{ij}^+ - M_{ij}^- + M_{ij}^+ - L_{ij}^- + L_{ij}^+ - R_{ij}^- + R_{ij}^+, \\ S_{ij} &= Q_{ij}^- + Q_{ij}^+ + M_{ij}^- + M_{ij}^+ + L_{ij}^- + L_{ij}^+ - R_{ij}^- + R_{ij}^+, \end{aligned} \quad (2.39)$$

where the coefficients are,

$$\begin{aligned}
Q_{ij}^- &= \xi_i^- \int_0^\infty (\lambda^- + 2\mu^-) V_i^{(2)-} V_j^{(2)+} dz, \\
Q_{ij}^+ &= \xi_i^+ \int_0^\infty (\lambda^+ + 2\mu^+) V_i^{(2)-} V_j^{(2)+} dz, \\
M_{ij}^- &= \int_0^\infty \mu^- \frac{\partial V_i^{(2)-}}{\partial z} V_j^{(1)+} dz, \\
M_{ij}^+ &= \int_0^\infty \mu^+ \frac{\partial V_j^{(2)+}}{\partial z} V_i^{(1)-} dz, \\
L_{ij}^- &= \xi_i^- \int_0^\infty \mu^- V_i^{(1)-} V_j^{(1)+} dz, \\
L_{ij}^+ &= \xi_i^+ \int_0^\infty \mu^+ V_i^{(1)-} V_j^{(1)+} dz, \\
R_{ij}^- &= \int_0^\infty \lambda^- \frac{\partial V_j^{(1)+}}{\partial z} V_i^{(2)-} dz, \\
R_{ij}^+ &= \int_0^\infty \lambda^+ \frac{\partial V_i^{(1)-}}{\partial z} V_j^{(2)+} dz.
\end{aligned} \tag{2.40}$$

The unknowns in the equations for the calculation of reflection and transmission coefficients are the displacements on the left side ($-$) of the vertical boundary, $(V_i^{(1)-}, V_i^{(2)-})$, and the displacements on the right side ($+$) of the vertical boundary, $(V_j^{(1)+}, V_j^{(2)+})$. These displacements are also a function of depth, z . We determine displacement for each side using the 1D formulation of surface waves and the propagator matrix method outlined in chapter 1. We then use equations 2.37 and 2.38 to calculate reflection coefficients.

2.3.2 Modeling surface-wave reflections using phase velocities

We present an alternative method of using Rayleigh-wave phase-velocity, instead of elastic properties, to calculate reflection coefficients. This approach is convenient because it is easy to estimate the Rayleigh phase-velocity model directly from data by extracting dispersion curves (this will be described in chapter 3).

The calculation of reflectivity, $R(\omega)_j$, at each trace location is simplified to terms of frequency-dependent, phase velocities,

$$R(\omega)_j = \frac{c(\omega)_j - c(\omega)_{j+1}}{c(\omega)_j + c(\omega)_{j+1}}. \quad (2.41)$$

Reflectivity due to density is indirectly accounted for in the forward modeling of dispersion curves. To model the incident reflection in the frequency domain, the following product is calculated, $O(\omega)_j R(\omega)_j$, corresponding to a convolution in the time domain. The resultant incident reflection at each location is then considered a source for the incoming surface-wave, $I(\omega)_j$. The complete forward modeled surface wave is then $O(\omega)_j + I(\omega)_j$.

2.3.3 Elastic properties versus phase-velocities for reflection coefficients

We consider one lateral boundary and estimate surface-wave reflectivity using both elastic properties and phase-velocities. Recall our model with two vertically stratified quarter-spaces welded together, Figure 2.10.

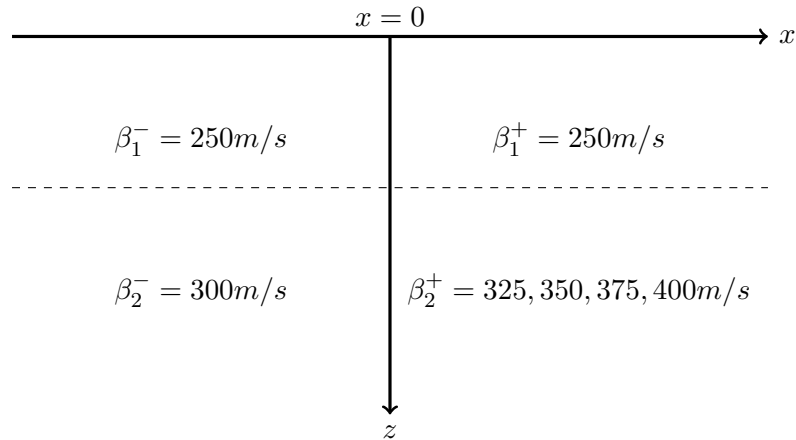


Figure 2.10: Semi-analytic representation of model. Four different shear-wave velocities are tested.

We use a fairly simple model with only two layers on either side. We model reflection coefficients at the boundary given four different shear-wave velocities for the lower layer on the right side, (325 m/s, 350 m/s, 375 m/s, and 400 m/s). We use a constant density of 2800 kg/m³ throughout the model and a constant value of 2 for V_P/V_S . Our objective is to compare the two methods of calculating reflectivity assuming that a surface wave is traveling across the boundary from left to right. The models are, in effect, blind-fault models with varying degrees of heterogeneity.

Figure 2.11, shows reflection coefficient results from calculations based on both elastic properties and phase-velocities for all four models. Reflection coefficients from elastic properties (shown as a solid line in the plots) are determined using algorithms from Corchete (2011), while our simple derivation is used to determine reflectivity from phase-velocities.

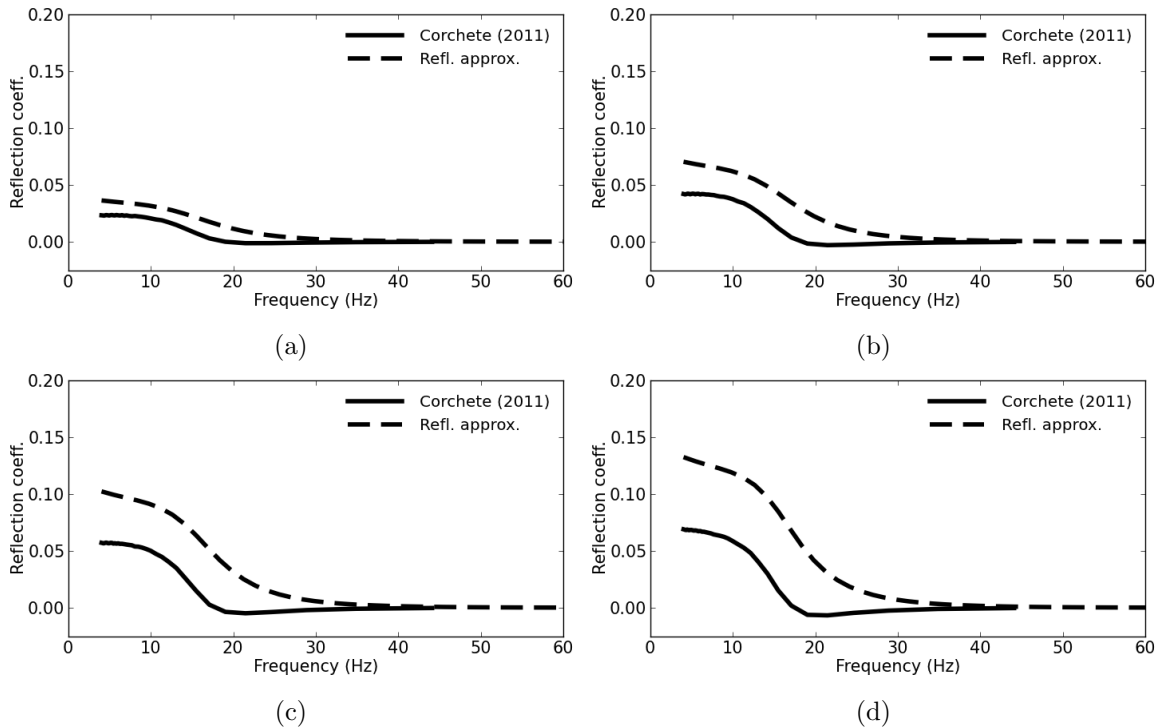


Figure 2.11: Reflection coefficients calculated at lateral boundary. Solid line calculated from elastic properties of the model. Dashed line calculated from phase-velocities. Shear-wave velocity in lower right layer set to different values: (a) 325 m/s, (b) 350 m/s, (c) 375 m/s, and (d) 400 m/s.

Surface-wave reflection coefficients are a function of frequency and are sensitive to the amount of lateral heterogeneity. We compare the two methods of calculating reflection coefficients using the Normalized-Root-Mean-Squared-Deviation (NRMSD) as defined by,

$$\text{NRMSD} = \frac{\|R - R_{approx}\|_{\bar{2}}}{\max(R) - \min(R_{approx})} \cdot 100, \quad (2.42)$$

where the deviation is expressed in terms of percent and R is reflectivity calculated from elastic properties and R_{approx} is reflectivity calculated from phase-velocities.

Reflectivity calculated from phase-velocity slightly over-predicts reflectivity calculated from elastic properties for all models. As the velocity difference between two mediums narrow, the disparity between the two results also narrow. The NRMSD for the four models in terms of the lower right layer, which is changed, is as follows: 400 m/s = 51.2%, 375 m/s = 43.4%, 350 m/s = 36.7%, and 325 m/s = 30.7%.

2.3.4 Source wavelet effect

Returning to the blind fault model, Figure 2.10, with a shear-wave velocity of 400 m/s in the lower right layer, we determine the reflection coefficient from a wave traveling left to right by solving for the eigenfunctions of displacement and using equation 2.38. Figure 2.12a shows surface-wave reflectivity at the boundary. For a dispersive surface wave the reflection coefficient is by nature a function of frequency. The result, however, does not take into account the source wavelet. As such, it is not bandlimited and does not represent how reflectivity would be recorded by a numerical simulation or in the field. We can estimate the effect of limited bandwidth by simulating the spectrum of a Ricker wavelet, Figure 2.12b, and applying it to reflectivity result, Figure 2.12c.

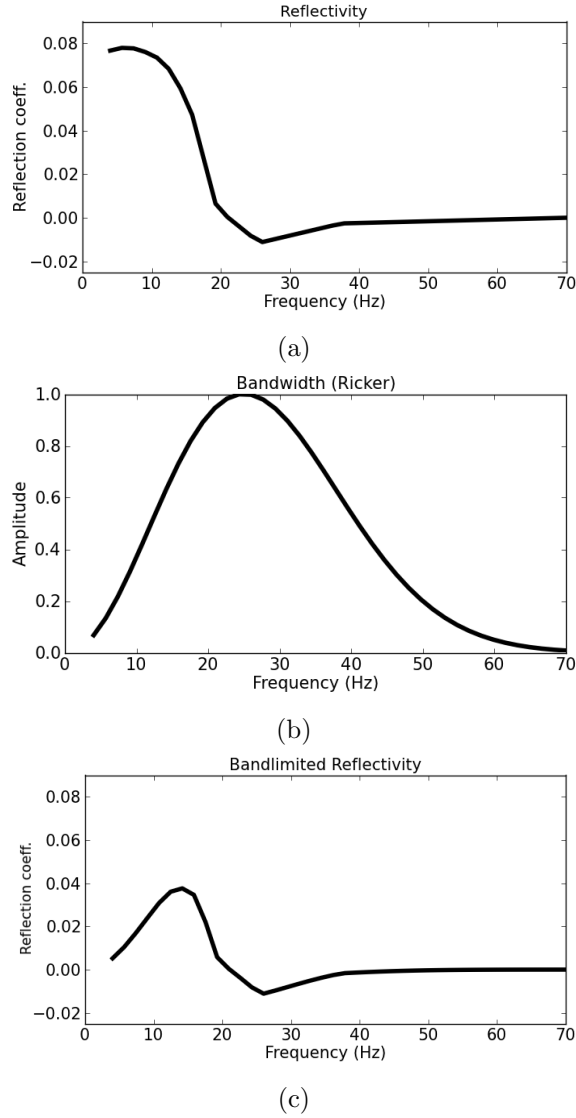


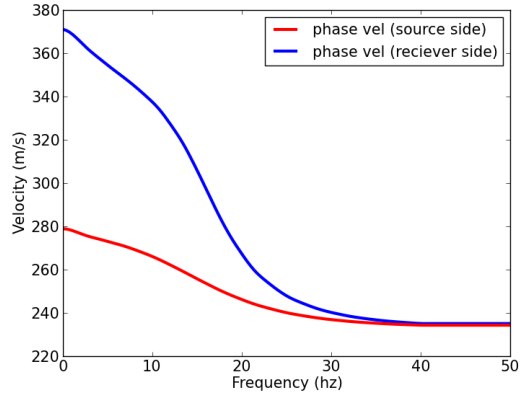
Figure 2.12: (a) Reflectivity as a function of frequency, (b) bandwidth of Ricker wavelet with dominant frequency at 25 Hz, and (c) bandlimited reflectivity.

The effect of the source wavelet will be applied in equation 2.31 during the semi-analytic modeling process. However, it is instructive to investigate the effects of the source wavelet. Theoretically, surface waves may be sensitive to structures at a great depth, however, if there is not sufficiently low frequency content in the source wavelet to begin with structures at depth will not be sensed.

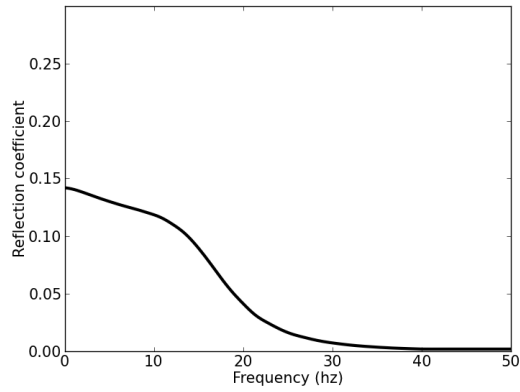
2.3.5 Modeling shot record with semi-analytic method

Recall that the shear-wave velocity model (Figure 2.2) is comprised of two layers. The first layer has a constant velocity of 250 m/s down to a 6 m depth, and the second layer is split by a vertical fault at $x=300$ m with a different velocity, 300 m/s and 400 m/s respectively, on either side. A constant density of 2200 kg/m^3 and a constant V_P/V_S value of 2 is used throughout the entire model. One shot is simulated on the left side of the model with a 25 Hz Ricker wavelet. A single vertical component receivers is investigated at the 300 m location.

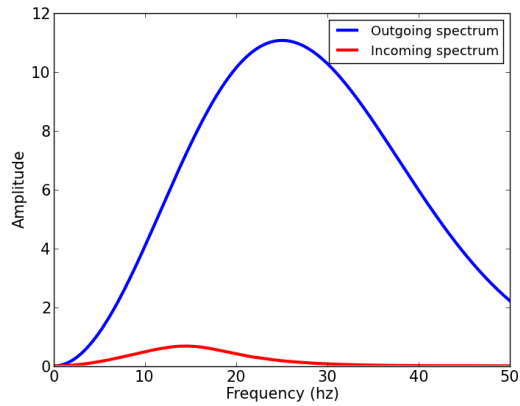
Figure 2.13, shows the entire process for creating an outgoing and incoming wave for a particular trace. On the left, Figure 2.13a, are the phase-velocities from either side of the fault. The phase-velocity model is used to calculate the reflection coefficient shown in Figure 2.13b. The amplitude spectrum of the outgoing wave at the boundary (which is similar to the source wavelet) is shown in blue, and the reflected (incoming) wave calculated from reflectivity is shown in red, Figure 2.13c.



(a)



(b)



(c)

Figure 2.13: Figures illustrate the entire process for calculated reflectivity. Properties are shown at the vertical fault (a) phase-velocities on either side of the fault, (b) reflectivity calculated from phase velocities, and (c) amplitude spectrum of the outgoing and incoming waves.

Note that the reflected surface wave is much lower in amplitude than the outgoing wave. Also, the spectrum for the incoming wave is shifted towards the lower frequencies.

We expect only low frequencies to reflect from structures at depth, which is the case for this blind fault model.

Figure 2.14a shows the trace at the source location. Figures 2.14b and 2.14c show the modeled outgoing trace and incoming trace at the boundary, respectively. Figure 2.14c shows the outgoing and incoming part of the wavefield separately, before they are combined.

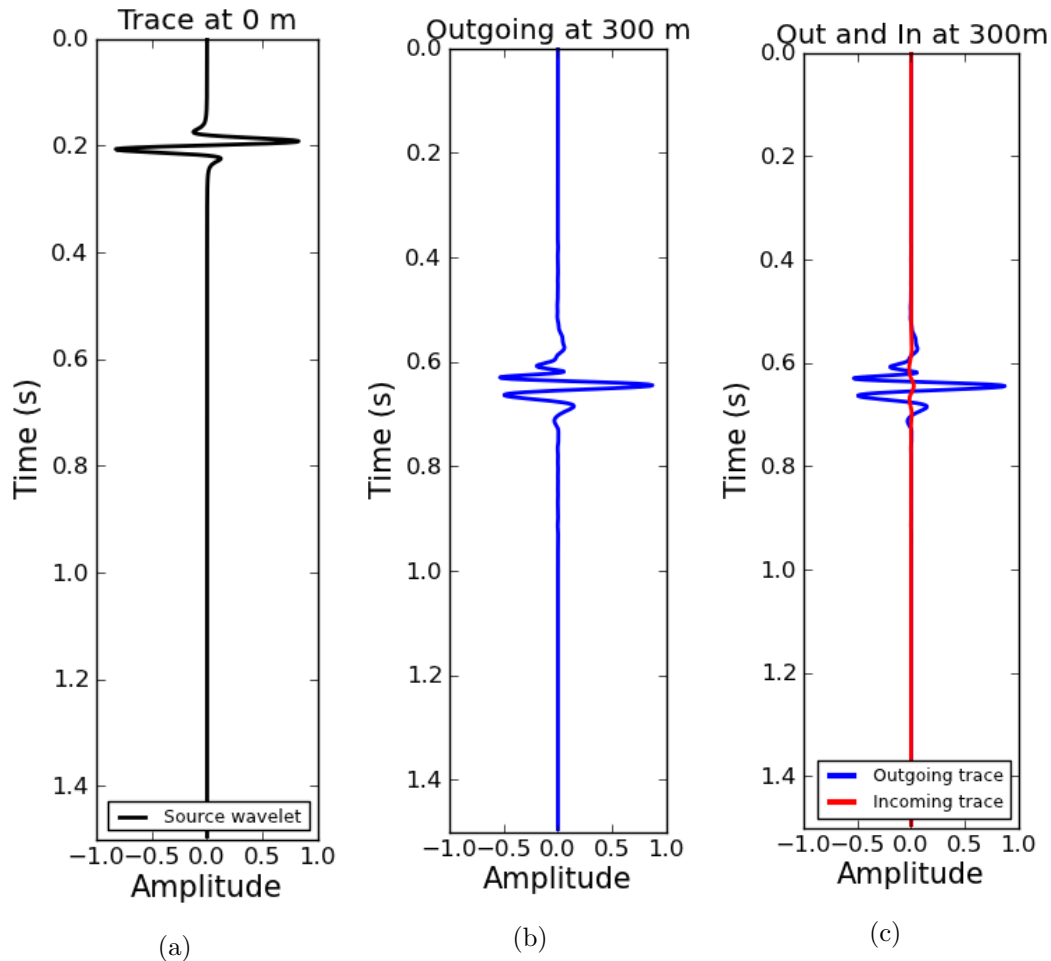


Figure 2.14: (a) Trace at 0 m is equivalent of source wavelet. (b) Modeled outgoing trace at the vertical fault. (c) Modeled outgoing trace with modeled incoming trace overlaid at the vertical fault.

Note that Figure 2.14 only shows two traces. The same process can be quickly calculated for all traces along the survey line. The next section will show the output shot record for receivers at a 1 m spacing across the extent of the blind fault model.

2.4 Comparison of 2D methods

Now all methods: finite-difference, spectral-elements, semi-analytic with shear-wave velocity model, and semi-analytic with phase-velocity model can be compared. Figure 2.15 shows data generated from each of the methods. Again, the most notable difference between data generated using numeric methods (finite difference and spectral elements) and data generated using semi-analytic methods (calculated from V_S and Rayleigh phase-velocity) is that the semi-analytic data does not include any arrivals or conversions associated with the P and S body waves.

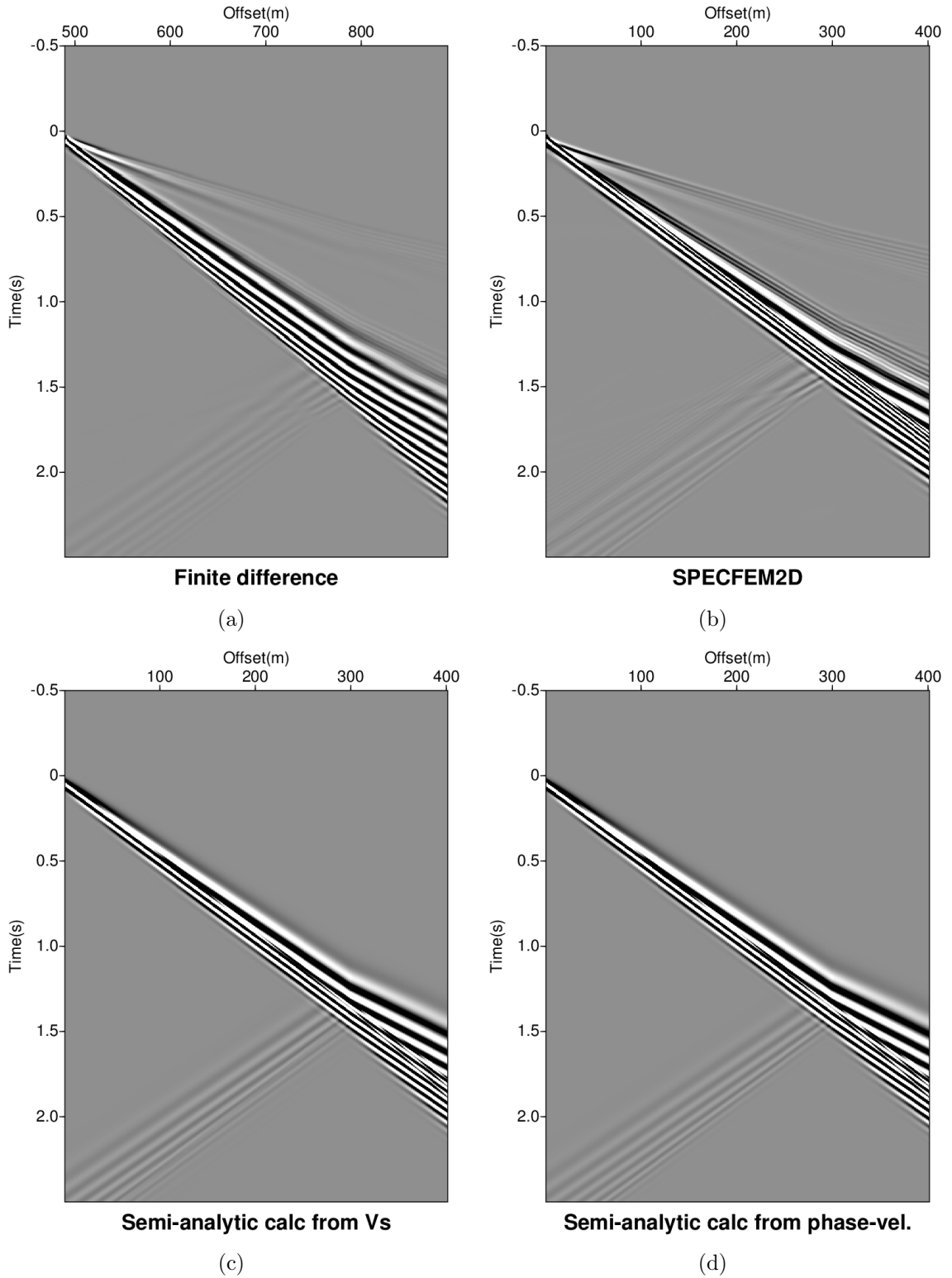


Figure 2.15: A comparison for an off-end shot of (a) finite difference, (b) numerical modeling via spectral elements, (c) semi-analytic modeled from shear-wave velocity model, and (d) semi-analytic from phase-velocity model.

It is interesting to note that the outgoing surface-wave in data generated by the semi-analytic methods (Figure 2.15a) are most similar to data generated by the spectral element data, Figure 2.15b. There is not a discernible visible difference between the two semi-analytic methods.

For simplicity, we assumed that the fundamental mode contributes more energy to the surface-wave than higher modes. However, higher mode dispersion curves can be modeled with the propagator matrix method and the same phase-shifting algorithm can be applied to higher modes for the outgoing wave.

The simple plane-wave estimation of reflectivity was used for the forward model because it is very simple to rearrange the equation and invert for phase-velocity from reflectivity (as we shall see in chapter 6). Other kernels can be used to calculate reflectivity in the forward model that could directly account for density and account for conversions to other modes. We chose the method used by Corchete (2011) to calculate reflectivity however many other methods exist.

Regardless, these comparisons show that our modeled data for the surface-wave is similar to data produced by more sophisticated, albeit more computationally demanding, numerical methods. Run time on our single processor using semi-analytic modeling was about 8 s. The finite difference's run time was almost 10 min and the spectral-element method's run time was over 80 min.

2.5 Summary

We have shown how to model surface waves in the presence of lateral heterogeneity. Numerical methods sufficiently model the wavefield in the presence of heterogeneity in 2D. Unfortunately, generating surface waves with numerical methods is computationally expen-

sive, It is also difficult to separate effects from body waves and converted waves from surface waves using numerical methods. Semi-analytic methods are potentially much faster given that less discretization is needed.

There are several ways to calculate the reflectivity coefficient at vertical boundaries, which is needed to generate reflected surface waves. We find that our approximation of reflectivity is reasonably accurate in comparison with other semi-analytic approaches. The similarity in results suggests our theory is sufficient for use in a processing flow to determine surface-wave reflectivity discussed in chapter 3.

Chapter 3

Imaging using surface waves: 2D

3.1 Overview

Processing surface waves directly can provide information about lateral change in the subsurface. Surface wave tomography (Abbott et al., 2006) and phase-velocity inversion (Park et al., 1998, Socco and Strobbia, 2004) are common surface-wave processing methods that give a shear-wave velocity model. For exploration-scale surveys, these shear-wave velocities have proven helpful for static corrections (Dulaijan and Stewart, 2010) and (Durá-Gómez and Zurek, 2011). Shear-wave velocity models from surface-wave tomography and surface-wave phase-velocity inversion have also been useful in determining smooth lateral discontinuities (Douma and Haney, 2011) and (Roy et al., 2013). The lateral resolution of discontinuities can be improved by varying the size of spatial windows of traces used to image dispersion curves (Bergamo et al., 2012). Alternatively, imaging with scattered surface-waves has been shown to be effective in locating point objects in the near-surface (Blonk et al., 1995, Herman et al., 2000). Reflected, horizontal propagating surface waves offer an opportunity to determine sharp lateral change in the near-surface. In addition

to providing information about the lateral location of a discontinuity, the frequency spectrum for surface-wave reflectivity provides information about the depth to the discontinuity (Shtivelman, 2000).

When dispersive surface-waves propagate through heterogeneity in the near-surface, the outgoing (away from the source) wave masks the onset of the incoming (toward the source) wavefield. This complicates the identification of the location of the discontinuity. Therefore, a primary challenge in locating a discontinuity, or change, is in separating and identifying the incoming wavefield. A straight-forward approach to isolate the incoming wavefield is to use linear move-out to align the outgoing wave and a dip filter to remove the aligned outgoing wave (Sloan et al., 2010). A frequency dependent move-out, such as Dynamical Linear Move-Out (DLMO), improves alignment of the outgoing wave for removal (Leparoux et al., 2000). By stacking over common-receiver gathers the incoming wavefield is enhanced and the image can be interpreted for the location of discontinuities in the time domain or frequency domain.

Observing the pattern of waves in a Vertical Seismic Profile (VSP), see Ross and Shah (1987), Stewart (1985), helps in formulating a method to image incident locations for back-reflected waves. The newly formulated method must take into account that data geometry is horizontal instead of vertical and the added complexity of accounting for significant dispersion. Similar to DLMO, a series of phase-velocity matching operations (Herrmann and Russell, 1990) are used to flatten the outgoing surface wave. Also presented, is a way to invert for the laterally-averaged, phase velocity necessary for flattening the outgoing wave. By retaining the outgoing wave, in addition to the incoming wavefield, a deterministic deconvolution can be used to recover reflectivity of lateral discontinuities.

The new method of extracting reflectivity agrees with previous analytic solutions based on the shear-wave velocity model and the approximation of calculating reflectivity proves to be satisfactory for the models tested in this paper. Band-limited lateral-reflectivity from velocity discontinuities at depth are shown to be uniquely dependent on the depth to those discontinuities. The main fault of the Hockley, Texas field data set (Khan et al., 2013) is identifiable in the lateral-reflectivity image and there is correlation between the lateral-reflectivity image and a traditional seismic image.

3.2 Multi-channel phase-velocity estimation and inversion

Multi-channel analysis of surface waves, often referred to as MASW, was developed in the 1990's by Park et al. (1999) and Xia et al. (1999). The method improved upon previous methods in which the spectral component of two receivers were used to determine dispersion characteristics of the surface wave (Nazarian, 1984). Only using two receivers to image dispersion suffered from low signal-to-noise and cumbersome acquisition. Multi-channel analysis surveys acquire data in much the same way as traditional (CMP-based) geometry. The combination of multiple channels also increases signal-to-noise. This is important when attempting to image the separate fundamental and higher modes.

The primary goal of MASW (and previous methods of surface wave analysis) is to determine a shear-wave velocity model across the survey line. There are essentially two steps in the process.

1. Extract dispersion-curves along the survey line, and
2. Invert for shear-wave velocity from extracted dispersion curves .

In practice, to capture 2D effects many dispersion curves must be extracted along the survey-line and then each profile is inverted independently. Commonly, in MASW, a dispersion curve is determined for each shot gather. The shot gather itself excludes near-offsets, where non-planar components exist, and far offsets, where higher modes, body waves, and guided waves dominate the record.

Below, a synthetic example is first presented to illustrate multichannel processing. After a review of extraction techniques, methods which aim to increase resolution of both the dispersion curve and lateral heterogeneity in the model are presented. Several different schemes of windowing data are investigated. Finally, the inversion used to determine shear-wave velocity is tested.

3.2.1 Synthetic example

To illustrate the process of forming dispersion images we return to the model with a single vertical blind fault as discussed in the previous chapter, Figure 3.9a.

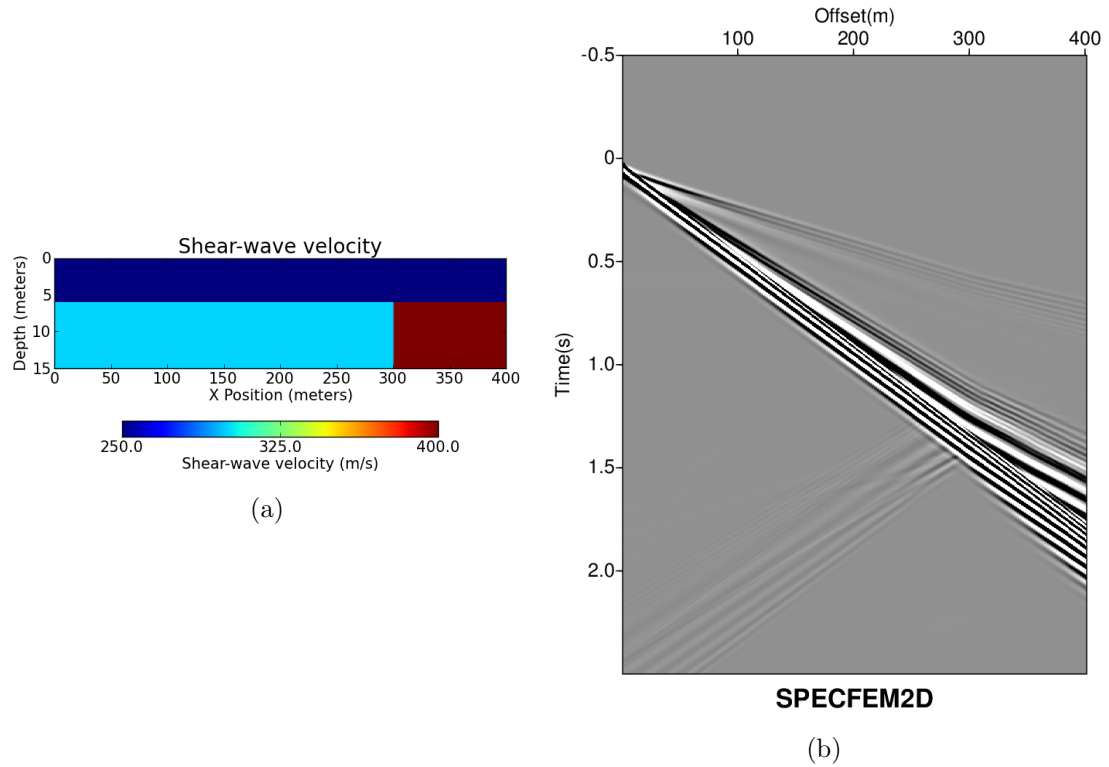


Figure 3.1: (a) Shear-wave velocity of simple blind fault model (b) Simulated shot record using the spectral element method.

Synthetic data is generated using a continuous Galerkin spectral-element method, SPECFEM2D. A point source with a 25 Hz Ricker wavelet is placed just below the surface to excite surface waves. A single shot is simulated at the left side of the model. Vertical component receivers are placed at a 1 m spacing along the entire extent of the model. A constant density of 2800 kg/m^3 and a constant V_P/V_S value of 2 is used throughout the entire model. Attenuation is excluded from the simulation. Again, the full extent of the model used for the numerical simulation is not shown. Figure 3.1b shows the shot record from the simulation.

3.2.2 Determining lateral phase-velocity variation.

A straight forward method to determine phase-velocity properties of a shot record is to transform data to the frequency-wavenumber (f-k) domain. Dispersive energy due to the

surface wave is distinguished by a curved signature as opposed to the linear signature of body-waves in the f-k domain.

In practice, noise (body-waves and scattered surface waves) can be excluded from the estimation of phase-velocity properties by muting around the surface wave-train. Figure 3.2a shows a mute around the simulated shot.

The imaged curve in the f-k plot of the the simulated shot (Figure 3.2b) represents the laterally-averaged phase-velocity characteristics from the source to the last receiver in the line.

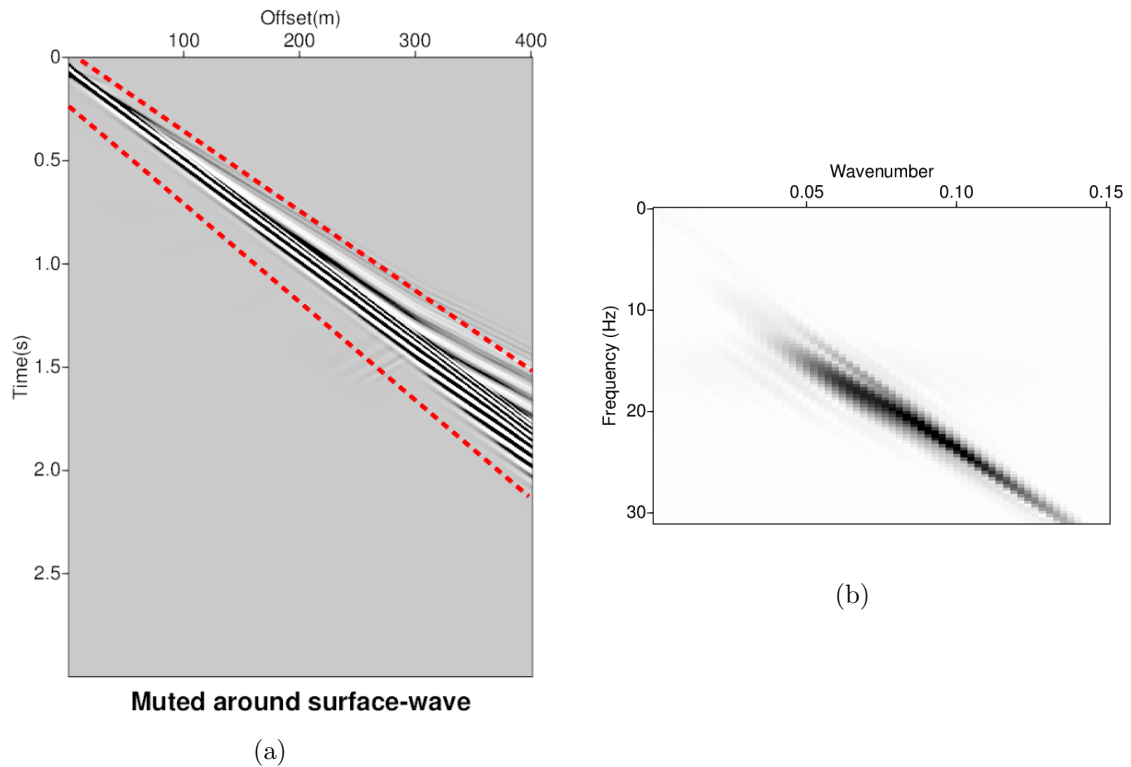


Figure 3.2: (a) Simulated shot record with mute applied around the surface wave. The mute is indicated with red dashed lines. (b) Image of dispersive energy in the f-k domain.

To determine phase-velocity, variation across the survey line dispersion should be "imaged" in some spatially windowed manner. Common practice is to form dispersion images (via an f-k or other transform) from an array which spans only a segment of the survey line.

The dispersion image is picked and the resultant dispersion curve is assigned to a location at the center of the array. The array is then moved laterally and the process is repeated and interpolated to obtain a lateral profile of phase-velocities. A smaller array potentially increases the degree of heterogeneity that can be resolved, but due to Fourier duality there are limits as to how small the spatial window can be made.

3.2.3 High-resolution dispersion imaging

Simply transforming surface-wave data to the f-k or slowness-frequency (p - ω) domain requires a very large number of traces to resolve an image of dispersive energy. The traces must also cover a large range of offsets. The resolution of dispersive energy is especially critical in the presence of higher modes where higher resolution provides separation between unique modes.

We follow the method outlined by Park et al. (1998) to image dispersion curves. Using Park's method, less traces are required and both a higher resolution of the dispersion image and a higher spatial resolution in the final model can be attained.

The transformation process described below is applied in a window of frequencies, ω , and offsets, x , for a shot gather. We begin by defining the Fourier transformation of an offset-time (x, t) shot gather as,

$$U(x, \omega) = \int u(x, t)e^{i\omega t} dt. \quad (3.1)$$

The term $U(x, \omega)$ can be split into two terms representing the phase, $P(x, \omega)$, and amplitude, $A(x, \omega)$, spectrum:

$$U(x, \omega) = P(x, \omega)A(x, \omega). \quad (3.2)$$

Note that $U(x, \omega)$ is a function of frequency. The phase spectrum term, $P(x, \omega)$, contains information about arrival time and about dispersion and the amplitude spectrum term, $A(x, \omega)$, contains information about attenuation and spherical spreading.

There is a specific frequency and phase-velocity at which the surface wave exists. The unique values of frequency and phase velocity can be represented as a wavenumber, $\Phi = \omega/c(\omega)$, and equation 3.2 can be rewritten as,

$$U(x, \omega) = e^{-i\Phi x} A(x, \omega), \quad (3.3)$$

Now, presume a phase shift, $e^{i\phi x}$, is applied to the shot gather as,

$$V(x, \omega) = \int e^{i\phi x} U(x, \omega) dx. \quad (3.4)$$

The phase-shift term above is dependent on offset and wavenumber, ϕ . If we consider each frequency component as completely separated from other frequencies the phase-shift term can be written as,

$$e^{i\phi x} = e^{i\phi(\omega)x} = e^{i\frac{\omega}{c(\omega)}x}. \quad (3.5)$$

By putting equations 3.3, 3.4, and 3.5 together we arrive at the following type of transformation,

$$\begin{aligned} V(\omega, \phi) &= \int e^{i\phi(\omega)x} \left(\frac{U(x, \omega)}{|U(x, \omega)|} \right) dx, \\ &= \int e^{-i(\Phi(\omega) - \phi(\omega))x} \left(\frac{A(x, \omega)}{|A(x, \omega)|} \right) dx. \end{aligned} \quad (3.6)$$

The expression above sums across offsets of wave-fields per frequency after applying a phase shift. The process is like a slant stack except it is applied in the frequency domain. The

transformation will exhibit a peak of energy for each frequency where,

$$\phi = \Phi = \frac{\omega}{c(\omega)}. \quad (3.7)$$

In practice, a selection of frequencies and phase-velocities associated with the phase-shift wavenumber, ϕ , are "scanned". A dispersion image occurs where peak energy exists. Usually peak frequency occurs at frequencies and phase-velocities associated with the fundamental mode. However, if substantial surface-wave energy exists in the higher modes, they too will be imaged.

Examples

Three separate dispersion images are formed from three separate spatial windows, each 100 m wide, located across the simulated shot gather. Each window is comprised of data from receivers that exist within the spatial extent of the window. Figure 3.3 shows dispersion images extracted from three different locations along a line.

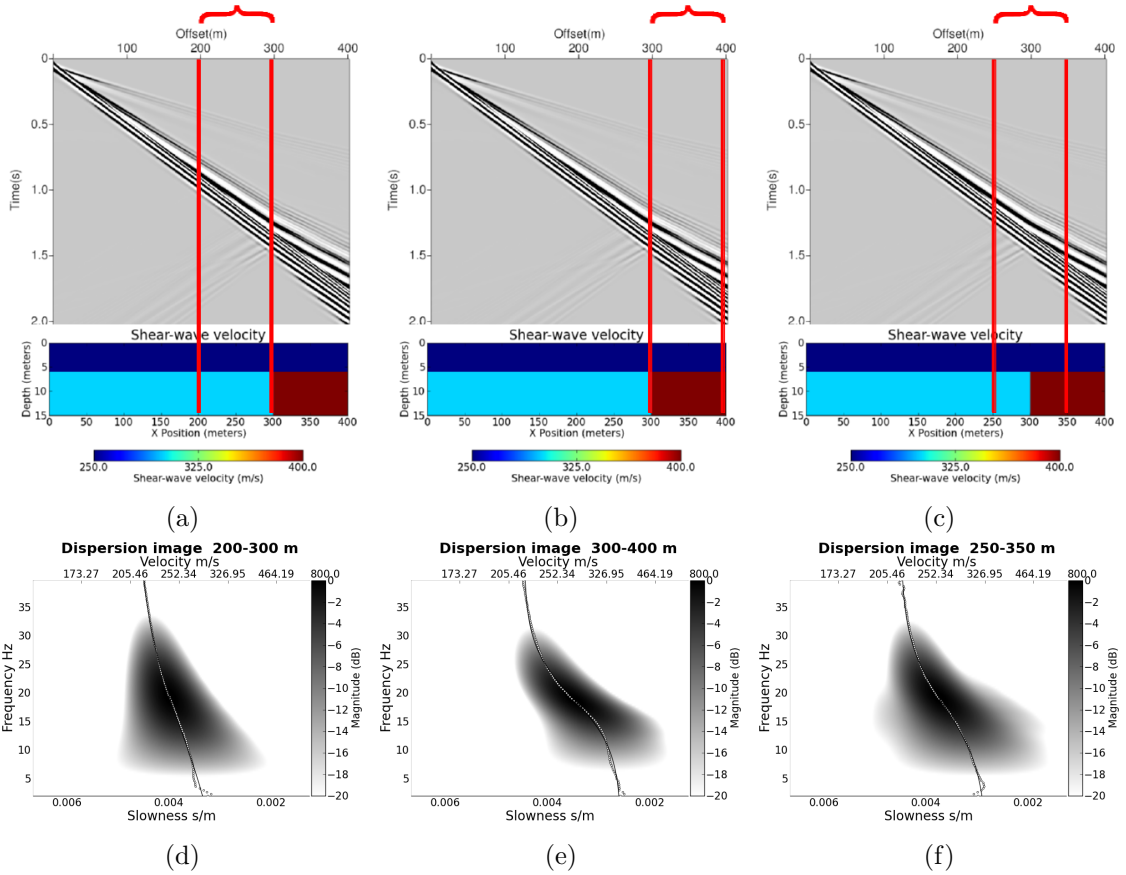


Figure 3.3: Three examples of imaged dispersive energy from simulated shot gather. The 100m spatial window is shown on shot gather and model with red bracket and red lines from location (a) to the left of fault, (b) to the right of fault, and (c) spanning the fault. Respective dispersion images from location (d) to the left of fault, (e) to the right of the fault, and (f) spanning the fault. The picked dispersion curve is shown with the white dots and black line.

As can be seen, given the relatively small section of receivers, the dispersion images using the high-resolution transform from all three windows are better resolved than the f-k transform previously shown in Figure 3.2b. The location windows are chosen to illustrate the sensitivity of the transform to the underlying shear-wave velocity model. Note that phase-velocity at higher frequencies is constant for the three dispersion images, Figures 3.3d, 3.3e, and 3.3f. This is consistent with the laterally constant shear-wave velocity in the shallow part of the model. Phase-velocities at lower frequencies in the dispersion images

on either side of the fault (Figures 3.3d and 3.3e) are markedly different due to the two different underlying shear-wave velocities in the lower layer.

Note that even the high resolution method of imaging dispersion curves averages phase-velocities laterally. The dispersion image estimated from the spatial window, which spans the fault (Figure 3.3f), is an averaged combination of properties on either side.

3.2.4 Dispersion image resolution

All multi-channel techniques suffer from constraints due to the Fourier Scaling property. This includes the higher resolution dispersion imaging presented above. The Fourier Scaling property states that a function, $g(t)$, scaled in time by a constant, c , is represented in the Fourier domain as,

$$g(ct) = \frac{1}{|c|} G\left(\frac{f}{c}\right). \quad (3.8)$$

The scaling in time is inversely proportional in the Fourier domain. In other words, the duration of a signal in time is inversely proportional to its bandwidth in frequency. This concept also holds true for spatially recorded samples. If the number of receivers selected for imaging a dispersion curves increases, the resolution of the dispersion image increases. As less receivers are selected for imaging a dispersion curve, the resolution of the dispersion image decreases.

Examples

Three separate dispersion images are formed from three differently sized spatial windows from the simulated shot gather. Each window is comprised of data from receivers that exist within the spatial extent of the window. Figure 3.4 shows dispersion images extracted from the three differently sized windows.

A high resolution dispersion image is produced from the large 300 meter window, Figure 3.4d. The trade-off, however, is lower lateral resolution. A small window, which could potentially provide high lateral resolution, does not result in dispersion image that can reliably be picked for a dispersion curve, Figure 3.4f. Therefore, when deciding on sizes of windows for capturing lateral heterogeneity, a compromise needs to be made. In this case, a 50 meter window (Figure 3.4e) (or possibly slightly larger) provides dispersion images from which reliable dispersion curves can be picked.

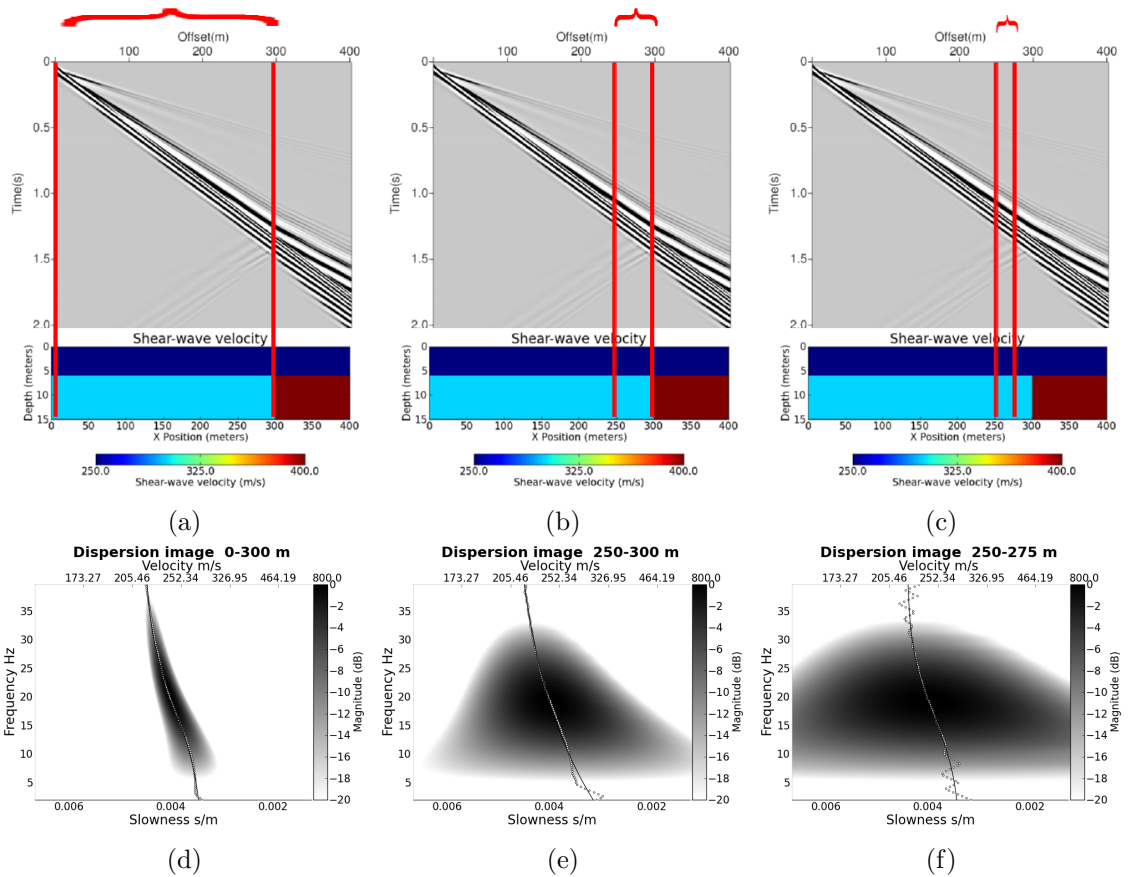


Figure 3.4: Three examples of imaged dispersive energy from simulated shot gather. Spatial windows are shown on shot gather and model with red bracket and red line for (a) 300 meter window, (b) 50 meter window, and (c) 25 meter window. Respective dispersion images are shown from (d) 300 meter window, (e) 50 meter window, and (f) 25 meter window. The picked dispersion curve is shown with the white dots and black line.

3.2.5 Multi-channel windowing schemes

As explained earlier, MASW-based methods make use of the same survey geometry which is used for traditional reflection processing. Oftentimes, surveys have a fixed receiver spread and shots progressing at intervals across the line.

In MASW processing, a dispersion curve is estimated for each shot gather (excluding nearest and farthest offsets) and assigned to the center of the gather. This is repeated for all shot gathers in a line and the dispersion curves are spatially interpolated at the end to create a phase-velocity model.

Other configurations of shots and receivers may be used with the same precautions for the nearest and farthest offsets. By forming super-shots, i.e. including more than one shot for dispersion curve estimation, higher resolution for both the dispersion image and lateral direction can be achieved.

If shot and receiver spacing are the same a simple windowing can be used. Figure 3.5 shows an example of overlapping windows.

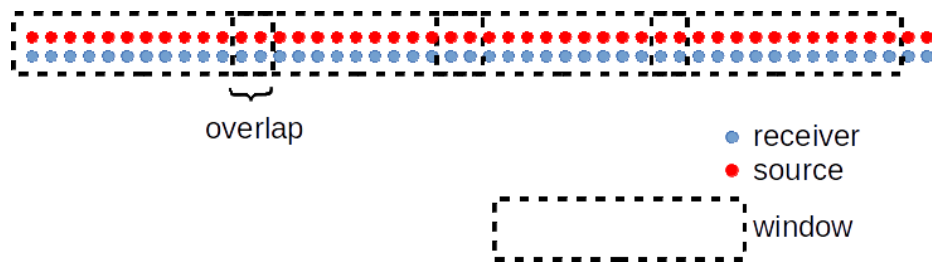


Figure 3.5: Diagram of survey with sources in red and receivers in blue. Window scheme indicated with dashed lines.

A slightly different windowing scheme is needed to optimize resolution when source spacing is at a larger interval than receiver spacing. For shot gathers, phase-velocities at a specific location are dictated primarily by the receivers at that location. Although the sur-

face wave may have traveled through an anomaly, altering the surface wave, along the way from a particular source to the window of receivers, the dispersion image from the transform is indicative of phase-velocities at that location. Apart from changes due to attenuation, extracted phase-velocities are independent of source location. Therefore, a second source aperture window should be designed around the receivers to optimize resolution. Figure 3.6 shows a diagram for the window scheme with sources at a larger interval than receivers.

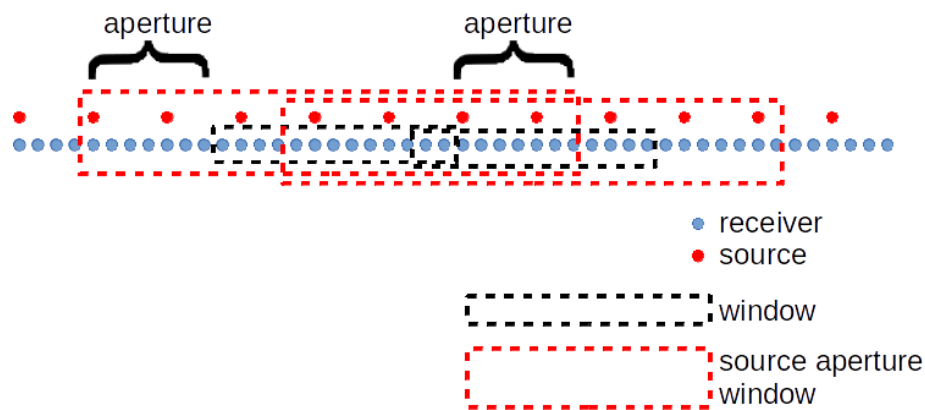


Figure 3.6: Diagram of survey with sources in red and receivers in blue. Window scheme indicated with black dashed lines for receiver window and red dashed lines for source aperture window.

Examples

For this example, 20 shots at a 20 m spacing across the model are simulated using the same blind fault model as before and same source settings (a point source with a 25 Hz Ricker wavelet placed just below the surface).

Several dispersion images from a single spatial window are shown in Figure 3.7. The shear-wave velocity model with sources and receivers indicated at the surface is shown on the left frames and corresponding dispersion images shown on the right. As can be seen in Figures 3.7a and 3.7b, simply choosing a small spatial window has an adverse effect on

the dispersion image when there is only one shot in the window. Including an additional shot (Figures 3.7c and 3.7b) improves the resolution of the dispersion image somewhat. For this example, by choosing a source aperture window that is 50 meters on either side of the receiver window (Figures 3.7e and 3.7f) a dispersion image is produced with satisfactory resolution.

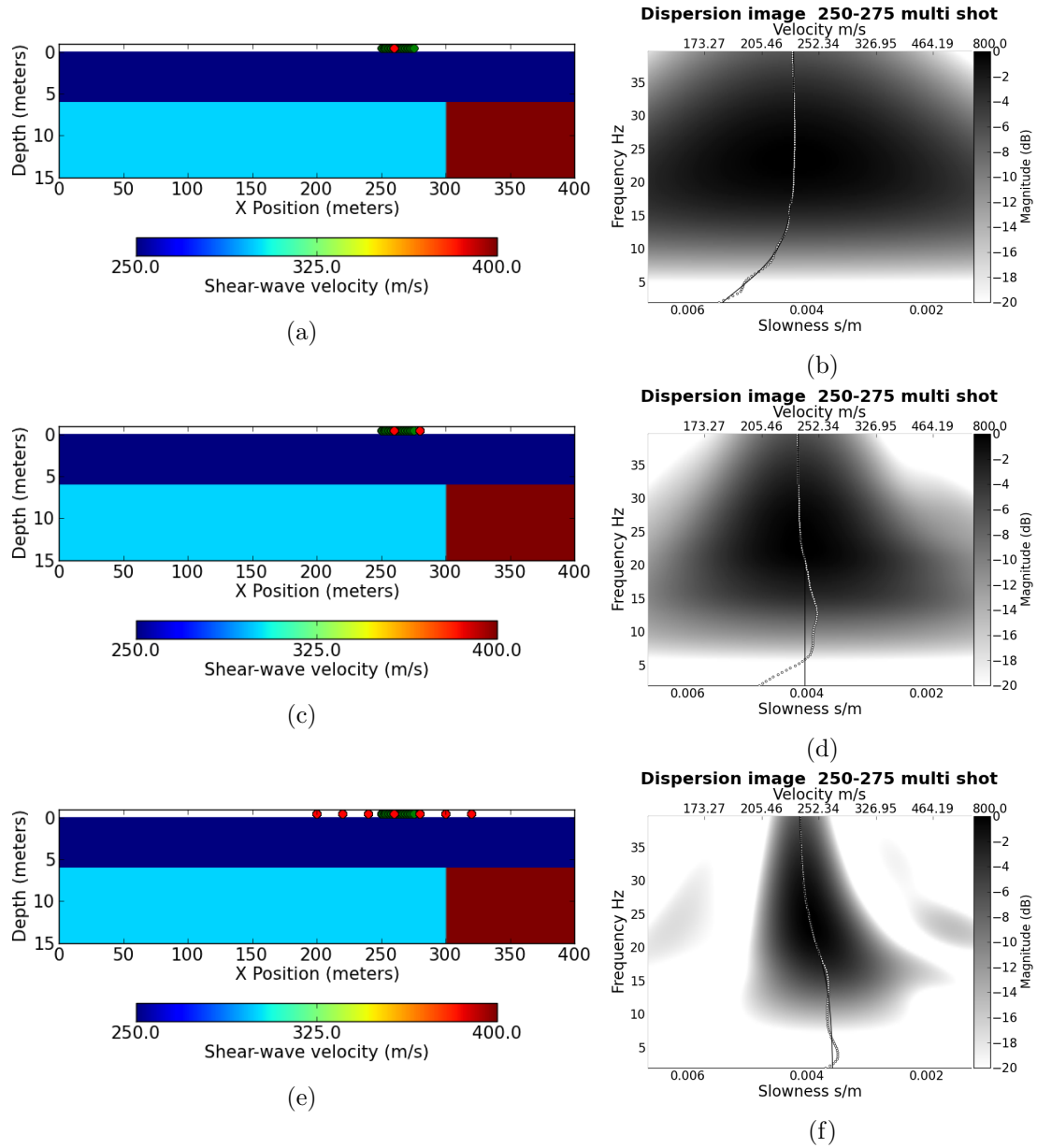


Figure 3.7: Three examples of imaged dispersive energy from spatial windows of simulated shot gather. Sources (red) and receivers (green) which fall inside the spatial window are plotted on the shear-wave velocity model for the case of: (a) one shot and (b) corresponding dispersion image, (c) two shots and (d) corresponding dispersion image, and (e) 7 shots selected with 50 meter aperture and (f) corresponding dispersion image. The picked dispersion curve is shown with the white dots and black line.

With an understanding of how windows are optimized to increase both lateral resolution and dispersion image resolution a windowing scheme for the entire survey can now be chosen. The windowing scheme consists of a receiver window of 25 meters and a source aperture

window of 50 meters on either side. An overlap of 5 meters is used for every receiver and the nearest and farthest offsets are excluded from each spatial window. Dispersion curves are picked for each window and assigned to the center of the window. Dispersion curves are then combined for the entire survey line by spatial interpolation. Figure 3.8 show the phase-velocity model produced from the synthetic data.

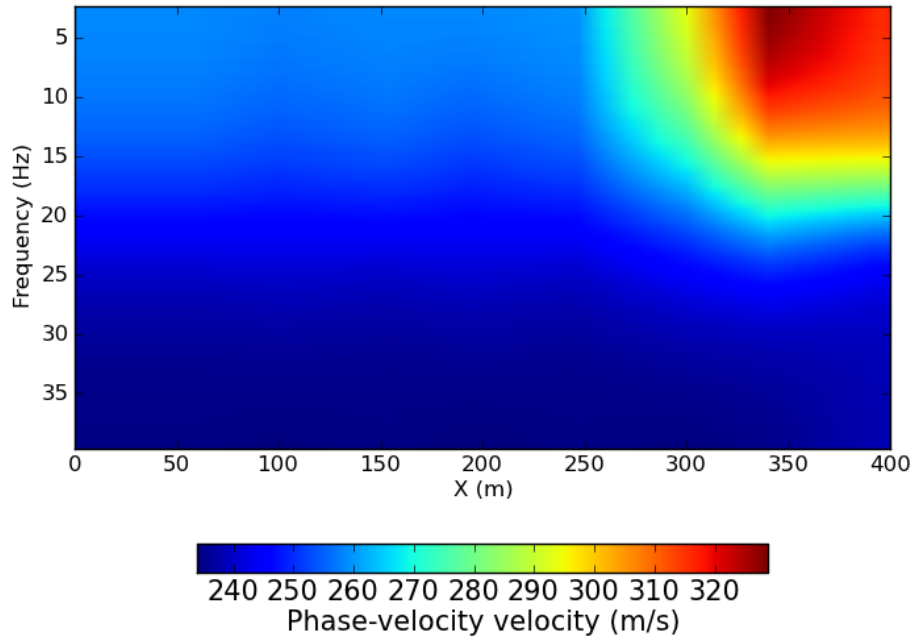


Figure 3.8: (a) Initial flattened data using extracted phase-velocities described in Step 1. (b) Improved flattened data using least squares fit.

The phase-velocity model corresponds to the shear-wave velocity model. Higher phase-velocities at lower frequencies (long wavelengths) exist at the same lateral location as the high-velocity section of the blind fault model. Note that the model produced shows smooth lateral change at the 300 meter mark. Sharp lateral change cannot be resolved due to interpolation between windows and the Fourier Scaling property.

3.2.6 Inversion for shear-wave velocity

Each dispersion curve determined along the line is independently inverted to determine shear-wave velocity. The inversion itself is a 1D process. In this sense, the resulting shear-wave velocity model is an approximation of a 2D solution built from many 1D solutions along the survey line.

The inverse problem for surface waves is ill-posed and the solution is non-unique and unstable. For this reason, a priori knowledge is needed. Phase-velocity is closely linked to shear-wave velocity, while density and compressional-wave velocity are much less linked to phase-velocity. Therefore, one can solve for shear-wave velocity by holding compressional-wave velocity and density fixed.

The problem can be set in terms of phase-velocity and shear-wave velocity perturbation. A linear inversion is formulated by finding the perturbations of shear-wave velocity that minimize the perturbation (or difference from) the phase-velocity model (Russell, 1987).

First, the Love wave and Rayleigh wave solutions for phase-velocity, $c(\omega)$, must be defined in terms of perturbations, δc and $\delta\beta$.

The Love wave is defined as,

$$\delta c(\omega) = \int_0^\infty A_L(\omega, z)\delta\beta(z)dz, \quad (3.9)$$

where amplitude, $A_L(\omega, z)$, is dependent on shear-wave modulus, μ , wavenumber k , and the eigenfunction, (l_1) , defined in the previous chapter,

$$A_L(\omega, z) = \frac{\mu c}{\beta k W} \left[k^2 l_1 + \left(\frac{dl_1}{dz} \right)^2 \right], \quad (3.10)$$

and the term W is,

$$W = k \int_0^\infty \mu l_1^2 dz. \quad (3.11)$$

The Rayleigh wave is defined as,

$$\delta c(\omega) = \int_0^\infty A_R(\omega, z) \delta \beta(z) dz, \quad (3.12)$$

where amplitude, $A_R(\omega, z)$, is dependent on shear-wave modulus, μ , Lamé's parameter, λ , wavenumber k , and the eigenfunctions, (r_1, r_2) , defined in the previous chapter,

$$A_R(\omega, z) = \frac{\mu c}{\beta k W} \left[\left(k^2 r_2 + \frac{dr_1}{dz} \right)^2 + 4k r_1 \frac{dr_2}{dz} \right], \quad (3.13)$$

and the term W is,

$$W = k \int_0^\infty [(\lambda + 2\mu)r_1^2 + \mu r_2^2] dz + \int_0^\infty \left(\mu r_2 \frac{dr_1}{dz} - \lambda r_1 \frac{dr_2}{dz} \right) dz. \quad (3.14)$$

The inversion is implemented the same whether we are using Love-wave or Rayleigh-wave phase velocities. Assuming that there are m number of frequencies in the dispersion-curve (phase velocities), equations 3.9 and 3.12 can be written as,

$$\delta c_i = \int_0^\infty A_i(z) \delta \beta dz, \quad i = 1, 2, \dots, m, \quad (3.15)$$

if velocity is a function of depth (where the structure is vertically stacked layers). Equation 3.15, can be written slightly differently as,

$$\delta c_i = \sum_{j=1}^n A_{ij} \delta \beta_j, \quad j = 1, 2, \dots, n, \quad (3.16)$$

where n is the number of stacked layers and the amplitude term, A_{ij} , is defined as,

$$A_{ij} = \int_{z_j}^{z_{j+1}} A_i(z) dz. \quad (3.17)$$

An iterative least squares problem can now be set up using the perturbations, δc and $\delta\beta$. The first iteration is started by providing an initial guess of the shear-wave velocity profile, B_j^0 , and determining phase-velocity, c_i^0 , using the 1D forward model previously presented in chapter 1. The perturbation in phase-velocity is then the difference between the actual measured phase velocity (extracted dispersion curve), c_i^m , and the initial guess,

$$\delta c_i = c_i^m - c_i^0. \quad (3.18)$$

The problem can now be set up to find the perturbations, $\delta\beta_j$, that minimizes the residuals, ϵ in,

$$\delta c_i = \sum_{j=1}^n A_{ij} \delta\beta_j + \epsilon_i, \quad (3.19)$$

or, in matrix form,

$$\delta \mathbf{c} = \mathbf{A} \delta \boldsymbol{\beta} + \boldsymbol{\epsilon}. \quad (3.20)$$

where $\delta \mathbf{c}$ is a vector of $(m \times 1)$ frequencies of phase-velocity perturbations, $\delta \boldsymbol{\beta}$ is the vector of unknown $(n \times 1)$ for shear-wave velocity model parameters for every depth-layer, \mathbf{A} is the $(m \times n)$ matrix of known amplitude coefficients, and $\boldsymbol{\epsilon}$ is a $(m \times 1)$ column vector of residuals to minimize.

After the first iteration, when $\delta \boldsymbol{\beta}$ is determined, the original estimate is updated by,

$$\boldsymbol{\beta}^u = \boldsymbol{\beta}^0 + \delta \boldsymbol{\beta}. \quad (3.21)$$

Updated shear-wave velocities, β^u , are used to determine amplitudes, \mathbf{A} , in an iterative manner. The least squares inversion is solved by,

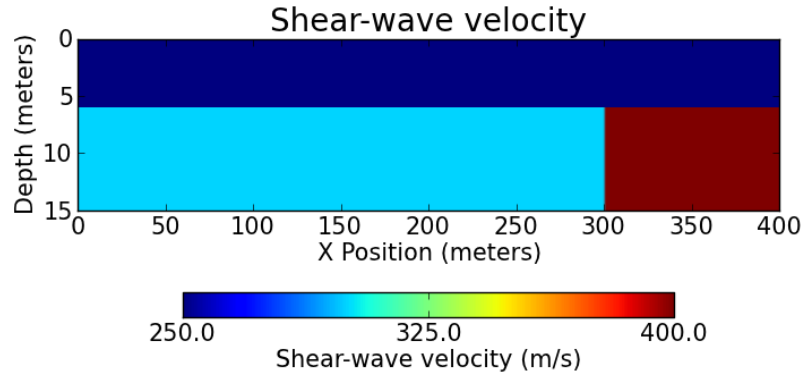
$$\delta\beta = (\mathbf{A}^T \mathbf{A})^{-1} \mathbf{A}^T \delta\mathbf{c}, \quad (3.22)$$

and the sum of the squares of the residuals is used to minimize the solution,

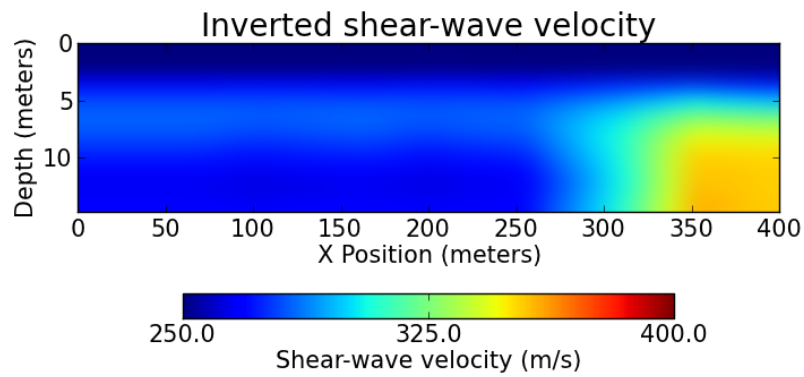
$$\epsilon^T \epsilon = (\delta\mathbf{c} - \mathbf{A} \delta\beta)^T (\delta\mathbf{c} - \mathbf{A} \delta\beta). \quad (3.23)$$

Example:

Let us return to the model with a single vertical blind fault and use the phase-velocity model processed previously from the simulated 20 shots at a 20 meter spacing. Each spatial sample point in the phase-velocity model is treated as a 1-D profile, which is inverted for shear-wave velocity using the method described above. Figure 3.9 shows the results of the inversion.



(a)



(b)

Figure 3.9: (a) True shear-wave velocity model. (b) Inverted shear-wave velocity model from multi-channel processing.

The overall character of the shear-wave velocity model is retained. A slow layer exists above a faster lower layer. On the right side, the faster section to the right of the fault has been estimated. The inverted model is a smoothed version of the true model.

3.3 Estimating surface-wave reflectivity

Processing steps are shown by the flowchart in Figure 3.10. These processing steps are grouped into three main steps for producing a reflectivity map:

1. Separating reflected surface waves from direct surface waves,

2. Isolating the incident location of reflected surface waves which results in an image representative of lateral locations of reflectors, and
3. Creating a reflectivity map by deconvolving reflected surface waves and converting to depth.

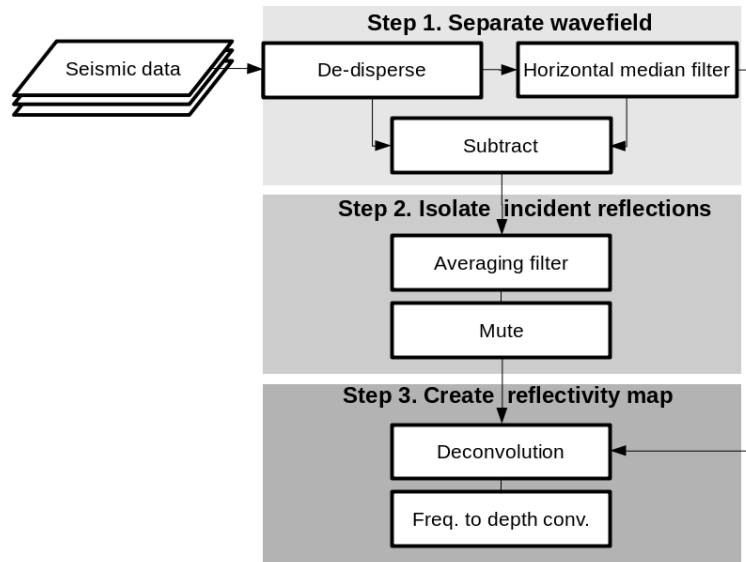


Figure 3.10: Flowchart of processing steps to: 1) separate the wavefield, 2) isolate incident reflections, and 3) create a reflectivity map. Operations are identified by straight rectangles, and data is identified by slanted rectangles.

We use the model and survey parameters described in section 3.2.1 for the first three steps of our processing flow. For the fourth step in the processing flow we use a slightly more complex model. The data used for the entire processing flow is generated by SPEC2D.

3.3.1 Step 1: Separating the wavefield

When dispersive surface-waves propagate through heterogeneity in the near-surface, the outgoing wave masks the onset of the incoming wavefield. This complicates the identification of the location of the discontinuity. Therefore, a primary challenge in locating a discontinuity, or change, is in separating and identifying the incoming wavefield. A straight-

forward approach to isolate the incoming wavefield is to use linear move-out to align the outgoing wave and a dip filter to remove the aligned outgoing wave (Sloan et al., 2010). A frequency dependent move-out, such as Dynamical Linear Move-Out (DLMO), improves alignment of the outgoing wave for removal (Leparoux et al., 2000). Similar to DLMO, we use a series of phase-velocity matching operations (Herrmann and Russell, 1990) defined by extracted dispersion properties of the wave to de-disperse, or flatten, the outgoing surface wave. In addition to determining the incoming wave we also preserve the outgoing wave for the step of creating the reflectivity map.

Determining the phase-velocity model and flattening the surface wave

A correctly defined phase shift will flatten the outgoing surface-wave allowing us to apply a filter to separate the incoming wavefield. However, the laterally-averaged phase-velocity needed to flatten the outgoing wave is unknown. We use a two-part process to determine the laterally-averaged phase-velocity which best flattens the outgoing wave. First, we determine dispersion curves within spatial windows and integrate across the ray-path to determine a laterally-averaged, phase velocity model for the phase-shift. Second, using the laterally-averaged phase-velocity model determined in step one as initial parameters, we improve the flatness of the outgoing wave with a least-squares fit.

The second part is a trace-by-trace operation starting at the source location and ending with the last trace along the ray-path. Each trace is fit to a flattened goal, $S(t)$. If the location of the trace is at index j , the flattened goal is a previously fit trace nearer to the source location, $j - 1$. The objective is to minimize the difference in energy, E , between the flattened goal and a function that flattens the trace given a transfer function, $H(\omega, p)_j$, based on the phase terms in equations (2.29) through (2.32) and a vector of parameters, p ,

which define the average phase-velocities for each trace,

$$E_j = \|S(t)_{j-1} - \mathcal{F}^{-1}\{O(\omega)_j H(\omega, p)_j\}\|^2. \quad (3.24)$$

An analytic function is used to define the average phase-velocities using only a few parameters for each trace (Tang et al., 2009). Here, we express the outgoing surface-wave, $O(t)_j$, recorded at positional index, j , as having both amplitude and phase,

$$O(t)_j = A(\omega)_j e^{-ik(\omega, x_j)x_j}. \quad (3.25)$$

Dispersion due to layering can be removed by applying a transfer function, H_j , to the outgoing wave, resulting with essentially the source wavelet, $S(\omega)$,

$$S(\omega) = H_j O(\omega)_j. \quad (3.26)$$

The transfer function is defined by the unique laterally averaged dispersive properties at the location of trace, x_j .

$$H_j = e^{ik(\omega, x_j)x_j}. \quad (3.27)$$

We adapt Tang's formula to represent the dispersion curve in slowness $s(\omega)$,

$$s(\omega) = m + r \arctan(n * (\omega - q)) \quad (3.28)$$

where the parameters are:

- m - inflection point on slowness axis
- r - slowness range, ie, extents of dispersion-curve

- n - inflection "steepness" on frequency axis
- q - inflection point on frequency axis

Equations 3.27 and 3.28 are combined to further describe the transfer function,

$$H(\omega, m, r, n, q)_j = e^{i(m+r \arctan(n*(\omega-q)))*\omega x_j}. \quad (3.29)$$

This function constrains the solution for a dispersion curve and allows us to remove residual dispersion subject to a flattened goal, $S(t)$, using a least-squares fit,

$$E = \|S(t) - \mathcal{F}_\omega^{-1}\{O(\omega)_j H(\omega, m, r, n, q)_j\}\|^2. \quad (3.30)$$

Figure 3.11a shows the outgoing surface-wave flattened using only the first part of the process described above, and Figure 3.11b shows the improved result using the least squares fit to remove the residual dispersion.

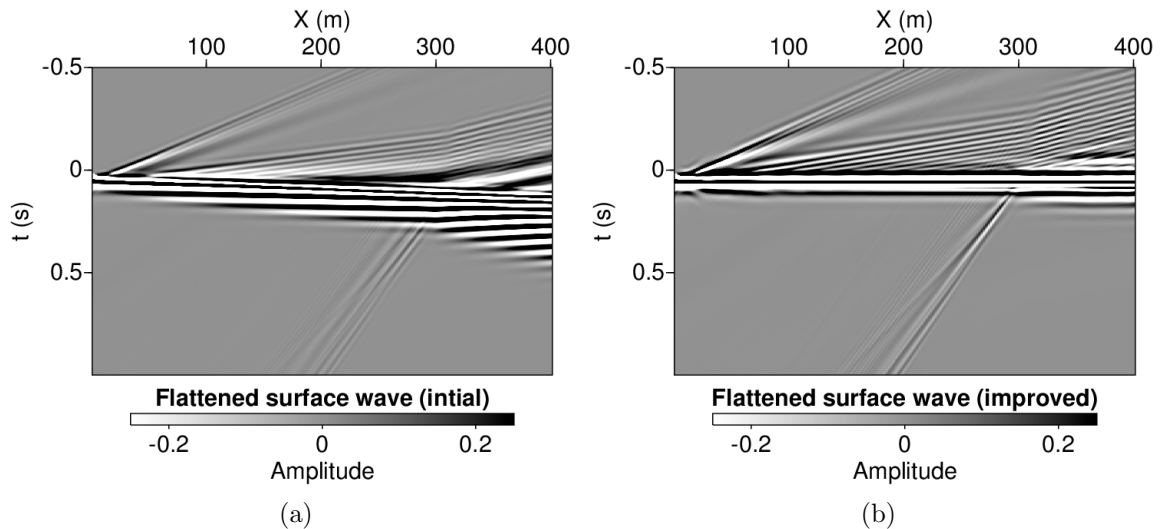


Figure 3.11: (a) Initial flattened data using extracted phase-velocities. (b) Improved flattened data using least squares fit.

Outgoing/Incoming separation

Once accurate velocities for the phase-shift have been estimated, the incoming and outgoing surface waves are separated using a VSP-type flow (Ross and Shah, 1987). In VSP processing, downgoing direct waves are removed from upgoing reflected waves by applying a static shift to align the downgoing wave, applying a horizontal median filter, and then subtracting the median filtered result from the aligned data resulting in only the upgoing waves. Similarly, now that the outgoing surface wave is flattened, we can apply the same process to uncover the incoming surface wavefield. Applying a horizontal median filter on the flattened aligned events, in this case, the outgoing surface-wave, reduces noise in the aligned event and does not have the effect of smearing the aligned event. For this reason the median filtered aligned event is often referred to as an enhanced event (Stewart, 1985). The flattened outgoing wave is enhanced (Figure 3.12a) with a 13-point median filter applied across the horizontal dimension. Then, the enhanced outgoing wave is subtracted from the flattened wave (Figure 3.11b) resulting in an incoming residual, as shown in Figure 3.12b. We will use the enhanced outgoing wave, $\hat{O}(t)_j$, later in step 3.

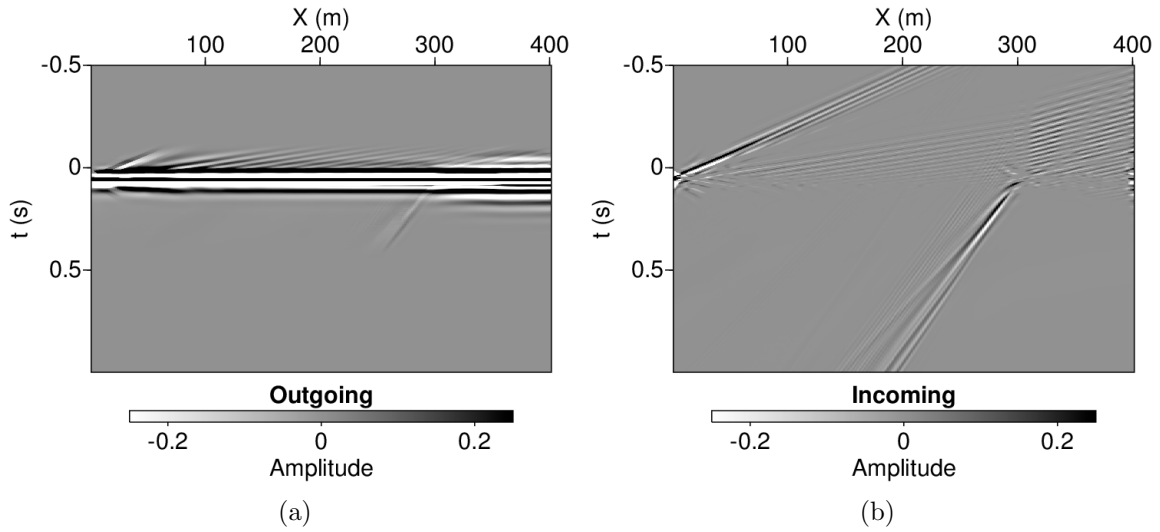


Figure 3.12: (a) Flattened outgoing wave separated and enhanced with median filter. (b) Incoming wave determined from the subtraction of the enhanced outgoing wave from the flattened wave.

The surface-wave reflection can be clearly seen originating from near time zero and traveling back towards the source as time progresses. The outgoing wave is removed and all that remains, for this example, are the direct waves that have been shifted to negative time and a small amount of residual noise.

3.3.2 Step 2: Isolating incident reflections

The incoming wavefield (Figure 3.12b) for our simple synthetic model is well separated. From a visual standpoint it is clear where the reflected wave originated. However, for a more general model, each trace may not only record the incident reflection near zero time, but may also record other events (such as reflected surface waves originating from locations further from the source and direct waves) at other times along the trace. In addition, because reflected surface-waves are weak in comparison with the outgoing surface-wave, the signal-to-noise ratio (SNR) for the reflection at the incident location may be very small.

The goal of step 2 is therefore twofold, increase the SNR and remove all events except the incident reflection near time zero.

Increasing the SNR for the incoming wavefield

The most obvious choice to increase the SNR in the incoming wavefield is to align the incoming wavefield and use a horizontal median filter in the same way as the outgoing wave. However, the result of alignment for the incoming wavefield is not the same as for the outgoing wave. Aligning the outgoing wave removes dispersion and flattens the wave thereby compressing the wave near time zero. An opposite sign for a phase-shift in the transfer function, $H(\omega)_j$, will flatten the incoming wavefield, however, the wavefield will not be flattened near time zero, nor will the wavefield be compressed. Instead, the incoming wavefield will be flattened where the wavefield crosses zero offset and the wavefield will be expanded, not compressed. The expansion of the wavefield will cause unwanted interference between incident reflections and other parts of the wavefield.

As an alternative approach, we apply an averaging filter which smooths the incoming wavefield and stacks out events that do not obey the propagation properties of the incoming surface wave, as defined by the transfer function, $H(\omega)_j$. The averaging filter is applied from later time to earlier times (that is, from near offsets to far offsets for the case of the incoming wave). We apply a transfer function, $H(\omega)_j$, to a trace at nearer offset, j , and then stack it to the adjacent trace at farther offset, $j + 1$. The stacked trace, $I(t)_j$, is then shifted with the transfer function to the next adjacent trace and stacked again. This process is repeated from near to far offset in a recursive fashion,

$$I(t)_{j+1} = \frac{I(t)_{j+1} + \mathcal{F}_\omega^{-1}\{H(\omega)_j I(\omega)_j\}}{2}. \quad (3.31)$$

If the transfer function matches the phase of an event in the trace, the event in the next trace will be additively stacked. The weight that a far offset trace is affected by a near offset at position q decreases geometrically with distance from the far offset trace as defined by,

$$I(t)_{j+1} = \sum_{q=j+1}^0 I(t)_q \left(\frac{1}{2}\right)^{i+1-q}. \quad (3.32)$$

Several passes of the averaging filter has the effect of further smoothing the incoming wavefield and increasing the SNR. Figure 3.13a shows how applying the averaging filter affects the incoming wavefield. Events which obey propagation properties of an incoming wave are slightly smoothed. In this case, there is only one incoming event. Events that do not obey the propagation properties of an incoming wave, such as the residual P-wave and outgoing wave, are “stacked out”.

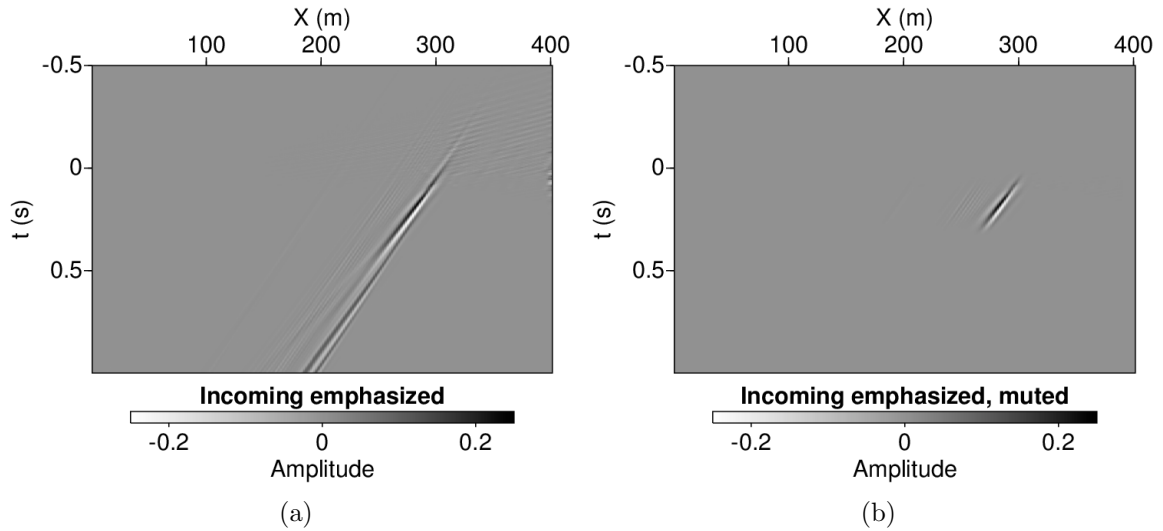


Figure 3.13: (a) Incoming surface wave emphasized by averaging filter. (b) Location of incident reflection is isolated by muting around zero time.

Muting around zero time

The process of flattening the outgoing wave in step 1 not only had the intended effect of compressing the outgoing wave, but it also compresses the incident reflections near zero time. After the outgoing wave has been removed and the SNR has been improved for the incoming wave we spatially isolate the incident location of the incoming wave by muting around time zero (or, more exactly, muting around the temporal location of the outgoing wave). Figure 3.13b shows the result of the mute. Using a mute with a smaller time gate will have the effect of increasing lateral resolution. The wavefield of isolated incident locations, $\hat{I}(t)_j$, is used in the next step.

3.3.3 Step 3: Create reflectivity map

At this point in the processing flow, the lateral location of reflectors can be inferred from the location of incident reflections. In step 3 we improve our interpretation by producing a 2D reflectivity map with sharp lateral resolution that is also a function of depth. First, we determine a spectral reflectivity map by deconvolving the incident reflections, from step 2, by the flattened outgoing wave determined in step 1. Then, maps from multiple shots are combined and the total spectral reflectivity map is converted to depth. Spectral reflectivity is also used to update velocity in step 4.

Deconvolution for reflectivity

Recall that the flattened outgoing wave for all traces, $\hat{O}(t)_j$, along the survey line has been determined by wavefield separation in step 1. The waveforms for possible incident reflections at every trace, $\hat{I}(t)_j$, has been determined by step 2. We determine the ratio between the outgoing wave and the incident reflections at every trace and interpret the

result as reflectivity. There are benefits from implementing a trace-by-trace deconvolution to determine reflectivity. Because the source waveform is present in both the outgoing wave and incident reflection the division cancels out the source term. Also, trace-to-trace variations due to the coupling of geophones to the surface of the earth are compensated for because variable coupling affect both the incoming and outgoing waves equally on each trace.

We determine reflectivity, $\tilde{R}(\omega_i, x_j)$, in the Fourier domain by damped deconvolution,

$$\tilde{R}(\omega_i, x_j) = \frac{\hat{O}(\omega_i, x_j)^* \hat{I}(\omega_i, x_j)}{\hat{O}(\omega_i, x_j)^* \hat{O}(\omega_i, x_j) + \epsilon^2}. \quad (3.33)$$

using the term, ϵ , as prescribed by Claerbout and Fomel (2006), to stabilize results. Next, we determine reflectivity as a function of horizontal distance in the form of a 1D image by summation over frequency,

$$R_0(x_i) = \sum_{\omega_i} \tilde{R}(\omega_i, x_j), \quad (3.34)$$

which also is equivalent to imaging at zero time. Figure 3.14a shows the zero-time image from deconvolving the incident reflection in Figure 3.13b. As can be seen, the reflection waveform is replaced by a band-limited spike.

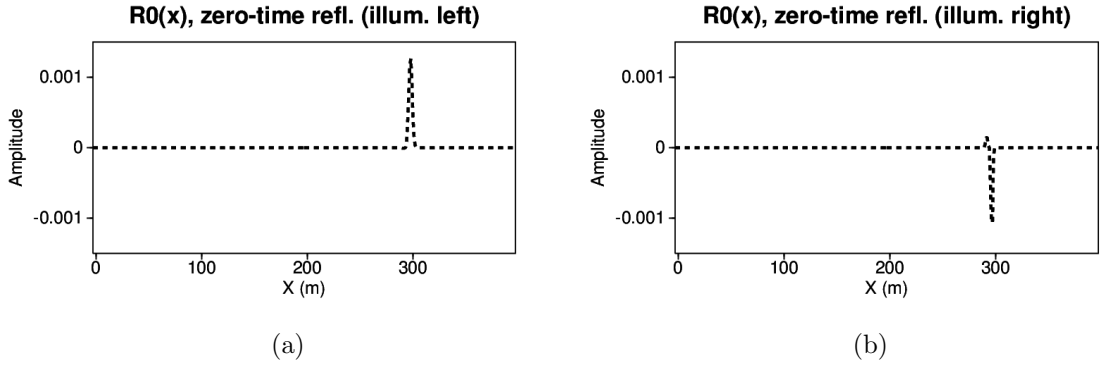


Figure 3.14: Resultant images from deconvolution of the incoming wavefield by the outgoing wave. (a) Positive, band-limited spike processed from shot at the 0 m location. (b) Negative, band-limited spike processed from shot at 400 m location.

Thus far, our examples for the processing flow have been for a source located to the left of the fault at the 0 m location. Because the shear-wave velocity is lower to the left of the fault, the reflection coefficient is positive. Figure 3.14b shows the reversed reflection coefficient for the fault from a source on the right side of the fault at the 400 m location.

To constrain the spatial extent of strong reflection coefficients in determined reflectivity, $\tilde{R}(\omega_i, x_j)$ (or $\tilde{R}(t_i, x_j)$), we apply a mask based on the zero-time image, $R_0(x_j)$. The mask is created by taking the zero norm of the zero-time image,

$$\begin{aligned}
 R(\omega_i, x_j) &= |\tilde{R}(\omega_i, x_j)| \cdot \frac{R_0(x_j)}{\|R_0(x_j)\|_0}, \\
 R(t_i, x_j) &= \tilde{R}(t_i, x_j) \cdot \left| \frac{R_0(x_j)}{\|R_0(x_j)\|_0} \right|,
 \end{aligned} \tag{3.35}$$

and is applied to either the amplitude part of the reflectivity spectrum or reflectivity in the time domain. By applying the mask to the amplitude part of the spectrum, we retain polarity information in the resultant spectral reflectivity map, $R(\omega_i, x_j)$. No polarity sign is required for determining a temporal reflectivity map, $R(t_i, x_j)$. Figures 3.15a and 3.15b respectively show the spectral reflectivity map for a source on the left side of the fault and

for a source on the right side. Similarly, Figures 3.15c and 3.15d respectively show the temporal reflectivity map for a source on the left side of the fault and for a source on the right side.

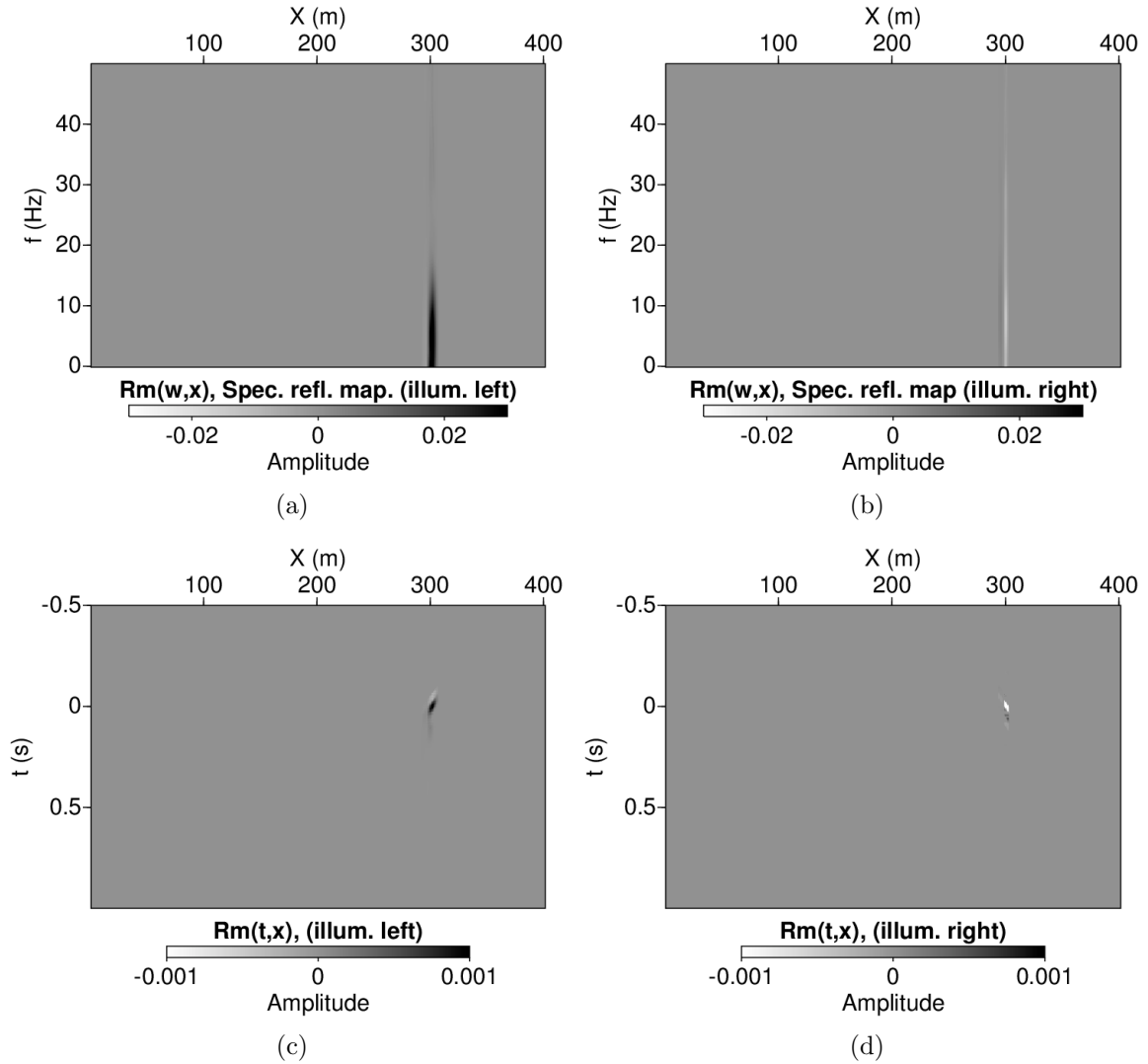


Figure 3.15: (a) Spectral reflectivity map processed from shot on left. (b) Spectral reflectivity map processed from shot on right. (c) Temporal reflectivity map processed from shot on left. (d) Temporal reflectivity map processed from shot on right.

Validation of extracting reflectivity

To confirm the accuracy of extracting reflectivity by wavefield separation and deconvolution, results are compared with semi-analytic solutions for a vertical discontinuity in the shear-

wave velocity model. Recall in chapter 2 we investigated the normalized root-mean-squared deviation (NRMSD), equation 2.42, between forward modeled reflectivity determined from elastic properties and reflectivity determined from phase-velocities. For a blind-fault model, identical to the blind fault model used in this chapter, we found a NRMSD of 51.2%. Here, we compare extracted reflectivity with both methods of forward modeling reflectivity, (Corchete, 2011) and ours (equation 2.41).

The bandwidth of the outgoing surface-wave produced by SPECFEM2D (Figure 3.16a) represents frequencies where most of the energy exists. We extract the reflection coefficient from a single trace of the deconvolved data at maximal amplitude. Figure 3.16b shows that energy contained in the reflected surface-wave (for all three estimates) is skewed toward the lower frequencies. This is consistent with the shear-wave velocity model. The higher frequency (shorter wavelength) part of the outgoing wave does not reflect from a discontinuity at depth.

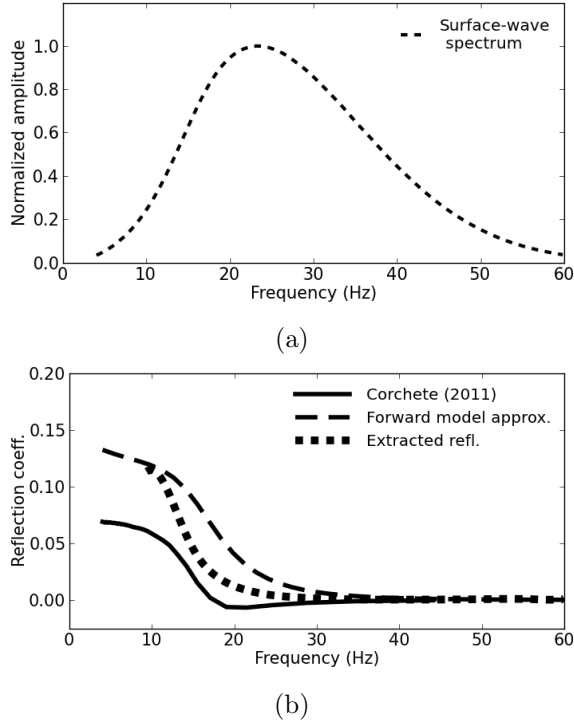


Figure 3.16: (a) Amplitude spectrum of surface-wave generated by SPEC2D. (b) Comparison of reflectivity results from analytic method based on shear-wave velocity, semi-analytic method based on phase-velocity model, and extracted reflectivity from data generated by SPEC2D.

Extracted reflectivity, as well as the forward model approximation, slightly over-predicts the analytic result derived from the shear-wave velocity model; however, both extracted reflectivity and the forward model are within a reasonable range. The NRMSD between the reflection coefficient extracted from the spectral reflectivity map and the reflection coefficient derived from elastic properties across 10 to 60 Hz is 28%. While the NRMSD between the reflection coefficient extracted from the spectral reflectivity map and the reflection coefficient derived from our forward model approximation across 10 to 60 Hz is 14%. In this case our forward model approximation is most consistent with reflectivity extracted from synthetic data produced by SPEC2D.

Multi-gather processing

Reflections occur at fixed locations on the surface regardless of shot location, x_s . Reflection polarity at those locations, however, depends on the directivity of the source. For our 2D fixed-spread geometry, we separate each temporal reflectivity map, $R(t_i, x_j, x_s)$, into two parts, negative and positive offsets. By separately stacking the left and right part of N shot gathers, $R_L(t_i, x_j, x_s)$ and $R_R(t_i, x_j, x_s)$, in the time domain we retain phase information,

$$\begin{aligned} R_L(t_i, x_j) &= \sum_{x_s}^N \frac{R_L(t_i, x_j, x_s)}{N}, \\ R_R(t_i, x_j) &= \sum_{x_s}^N \frac{R_R(t_i, x_j, x_s)}{N}, \end{aligned} \tag{3.36}$$

where the two parts are combined by reversing the sign for one part,

$$R(t_i, x_j) = \frac{-R_L(t_i, x_j) + R_R(t_i, x_j)}{2} \tag{3.37}$$

In combining shots, noise, such as back-reflections from higher modes and other conversions, is reduced. Note that because deconvolution prior to stacking balances the amplitude between the shots the amplitude of reflectivity after stacking is also preserved.

Converting to depth

Surface waves are most sensitive to the velocity structure at about one-half their wavelength (Rix and Stokoe, 1989). We thus map the spectral amplitude of reflectivity to a depth-profile using this relationship. We first create an array of points corresponding to lateral position and depth. Then, we map the nearest half-wavelength (determined by using the average velocity of the surface-wave) from wavelength to depth. The result is an image which shows reflectivity as a function of offset and depth (Figure 3.17).

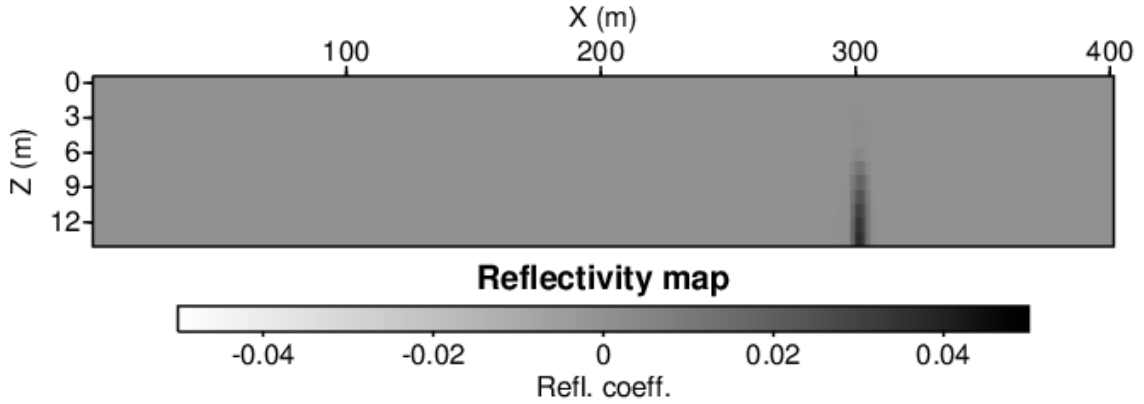


Figure 3.17: Image of reflectivity as a function of lateral position and depth.

It should be noted that this mapping is approximate. Although low-frequency waves cause strong particle displacement in deeper velocity structures, shallow structures are also affected by low frequency waves. Accordingly, a one-to-one mapping of frequency to depth is inexact. However, similar mappings of direct surface-wave spectra to depth have proved useful for near-surface interpretation (Shtivelman, 2000). Our mapping is instructive for the purpose of approximate interpretation. As can be seen in Figure 3.17, the depth of reflectivity corresponds to the depth of the fault in the shear-wave velocity model.

The shear-wave velocity profile from the location at the fault is compared with the depth-mapped reflectivity the same location to confirm the prediction of depth given by extracted reflectivity. Figure 3.18 shows the profile of shear-wave velocity and reflectivity.

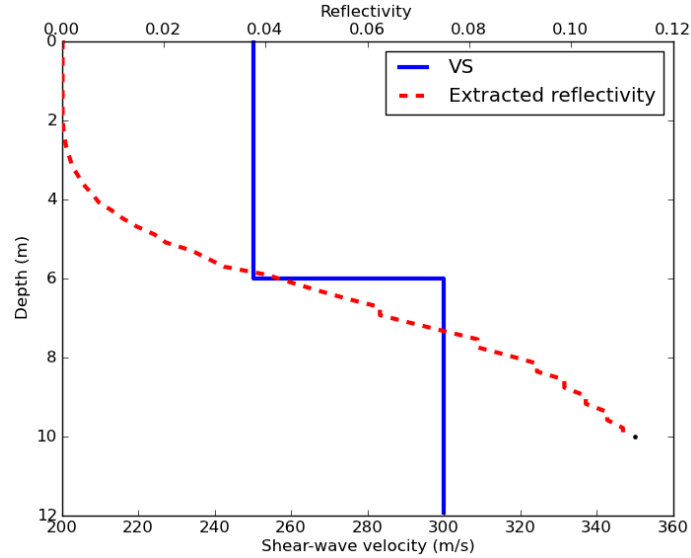


Figure 3.18: Comparison of shear-wave velocity profile (solid blue line) and depth-mapped reflectivity profile (dashed red line) at location of fault.

Note that the depth at which reflectivity becomes strong corresponds to the depth of the velocity change in the shear-wave velocity model.

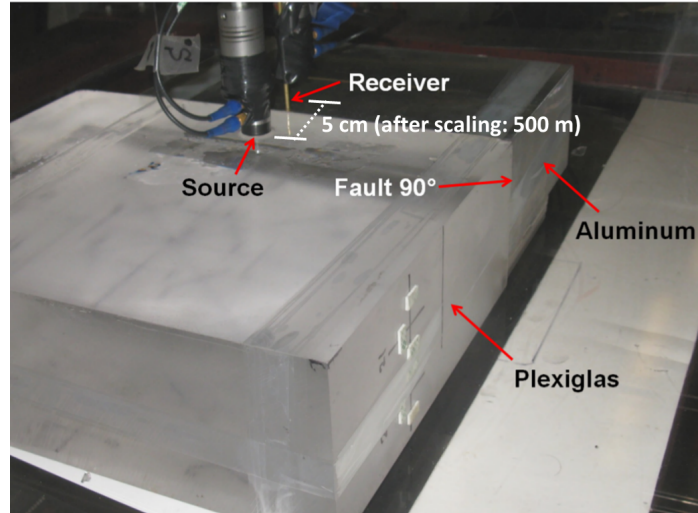
3.3.4 Example: Physical Model, 2D line perpendicular to fault

It is useful to understand simple data prior to investigating more complicated data from the field. Physical modeling fills the gap between synthetically generated data and field data. Properties of materials are known and the particle motions in materials are real in physical modeling, as opposed to synthetic data.

In the following section, data is processed from an experiment performed at the Allied Geophysical Laboratories (AGL), University of Houston, using an ultrasonic data acquisition system. Data from the system always uses a scaling factor of 110000 for time and space to convert ultrasonic measurements to values representative of seismic measurements collected by traditional field equipment. A receiver interval in the physical modeling experiment of 0.5 mm therefore translates to a 5 m receiver interval in the field.

The model was built to mimic a laterally varying structure with a vertical boundary (vertical fault). A block of plexiglas was welded to a block of aluminum using adhesives and honey as a viscous couplant, (Figure 3.19a). Compressional and shear-wave velocity in plexiglas is: $V_P = 2740$ m/s and $V_S = 1380$ m/s respectively. Compressional and shear-wave velocity in aluminum is: $V_P = 6300$ m/s and $V_S = 3100$ m/s respectively.

A roll-along source-receiver geometry was used to acquire seismic datasets with ultrasonic contact transducers Figure 3.19b shows specifications used for the physical model survey.



(a)

Source type	1 MHz vertical transducer (Central frequency: 0.95 MHz)
Receiver type	Vertical pin transducer (Central frequency: 1.5 MHz)
Source to first receiver (Near-offset)	120 m (Before scaling: 12 mm [*])
Source interval (Shot 1-9 and Shot 13-15)	20 m (Before scaling: 2 mm [*])
Source interval (Shot 10-12)	40 m (Before scaling: 4 mm [*])
Receiver interval	5 m (Before scaling: 0.5 mm [*])
Number of receivers (for each shot)	100
Sample interval	1 ms

* A scale factor of 1:10000 used in these experiments

(b)

Figure 3.19: (a) Photo of physical model and (b) table of parameters (courtesy of Soumya Roy).

Figure 3.20 shows a shot gather collected across the vertical boundary. Because the two blocks are not vertically layered the surface wave observed is non-dispersive. The vertical boundary is at an offset of 280 m. As can be seen in the shot gather, there is a strong reflection and refraction (transmission) of the surface wave, along with other converted modes, from the vertical boundary.

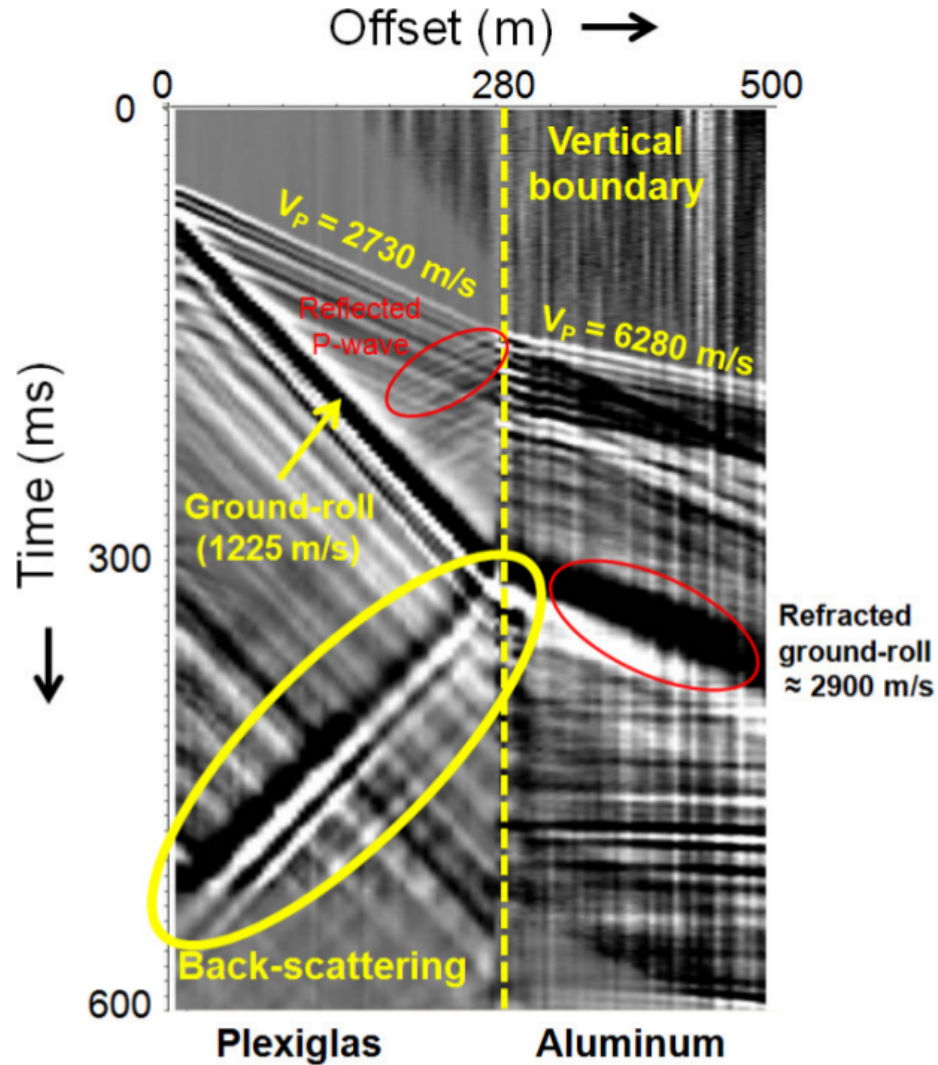


Figure 3.20: Shot gather of data with arrivals notated (courtesy of Soumya Roy).

Processing the physical model is similar to the synthetic example. However, because the surface wave is non-dispersive and the signal-to-noise ratio of the incoming surface-wave is high a simplified processing flow can be used. In this case, after separating the outgoing wave a that is identical to a VSP processing flow can be used.

Figure 3.21a shows the initial shot gather. The shot gather is first aligned on the outgoing wave as shown in Figure 3.21b. A horizontal median filter is then applied to the aligned shot gather (Figure 3.21c) and it is referred to as the outgoing wave estimate. The

outgoing wave estimate is subtracted from the aligned shot gather resulting in the incoming wave, Figure 3.21d. The steps thus far are identical to the previous processing flow.

The remaining steps are simpler than the flow used for dispersive surface-waves. The incoming wave is deconvolved (Figure 3.22a) and shifted to be aligned at the two-way travel time, Figure 3.22b. Next a corridor mute is applied (Figure 3.22c) and the data is stacked, Figure 3.22d. The result is reflectivity at the location of the fault. For a surface-wave, a corridor stack is not very useful in laterally locating an anomaly but it is shown here for those familiar with VSP processing.

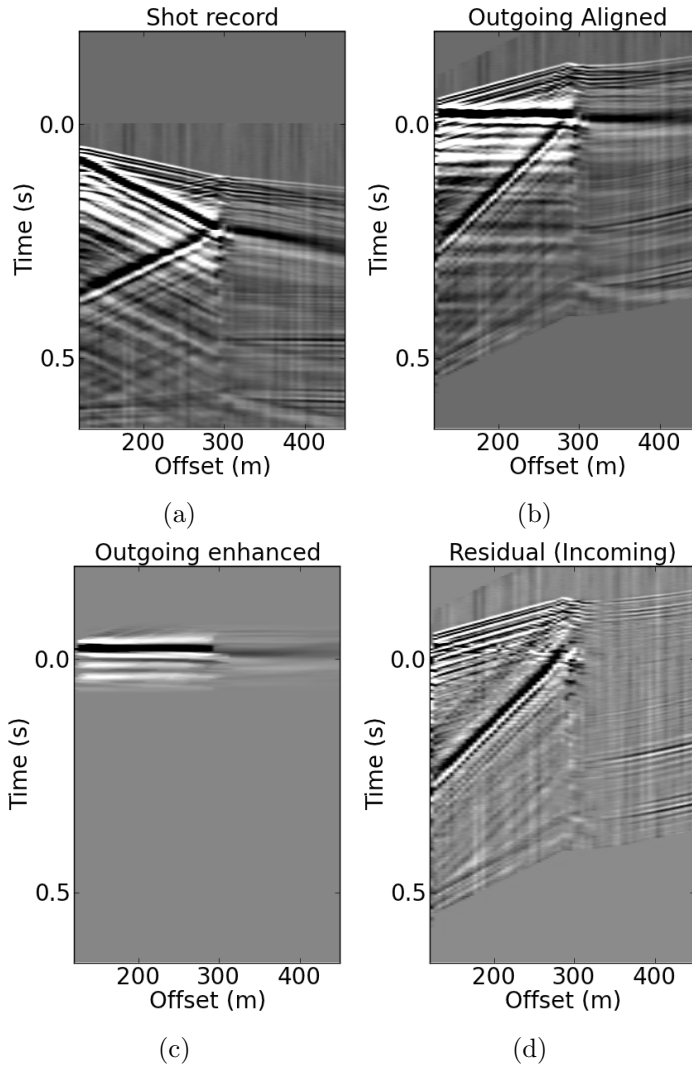


Figure 3.21: Processing flow shown for physical model. (a) Shot gather. (b) Aligned shot gather. (c) Outgoing wave. (d). Incoming wave.

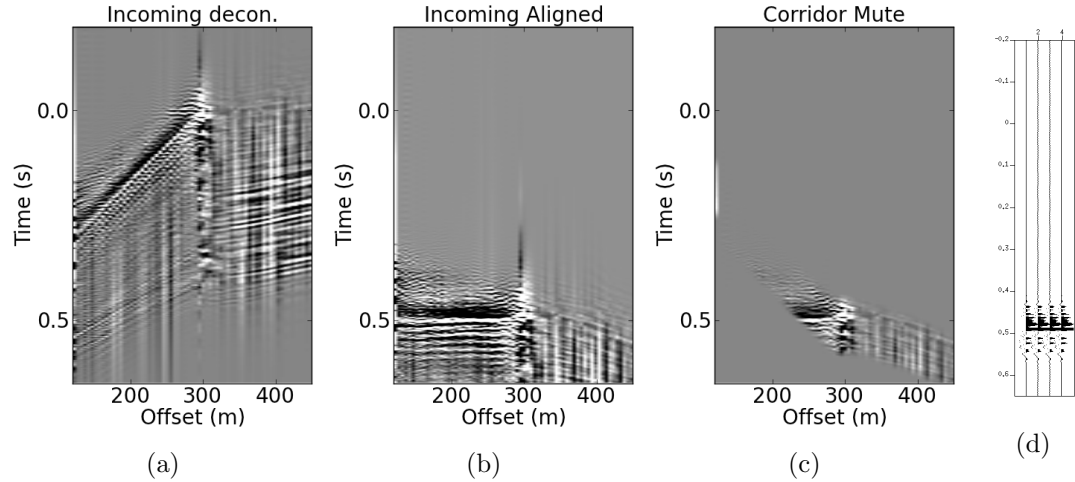


Figure 3.22: Second part of processing flow for physical model. (a) Deconvoluted incoming wave. (b) Deconvoluted incoming wave aligned. (c) Corridor mute applied. (d) Display of corridor mute stack.

Figure 3.23a shows that the spectral reflectivity map locates the vertical fault properly. Not surprisingly, reflectivity is present across all frequencies. This is consistent with the fact that the vertical fault in the physical model extends to the surface.

Additionally, the results of extracted reflectivity are compared with a known semi-analytic prediction of reflectivity from the shear-wave velocity model. Aluminum has a density of 2700 kg/m^3 and Plexiglas has a density of 1180 kg/m^3 . Density values are used with the known velocity values to determine the expected reflectivity. Figure 3.23b shows the comparison of extracted reflectivity with the semi-analytic prediction.

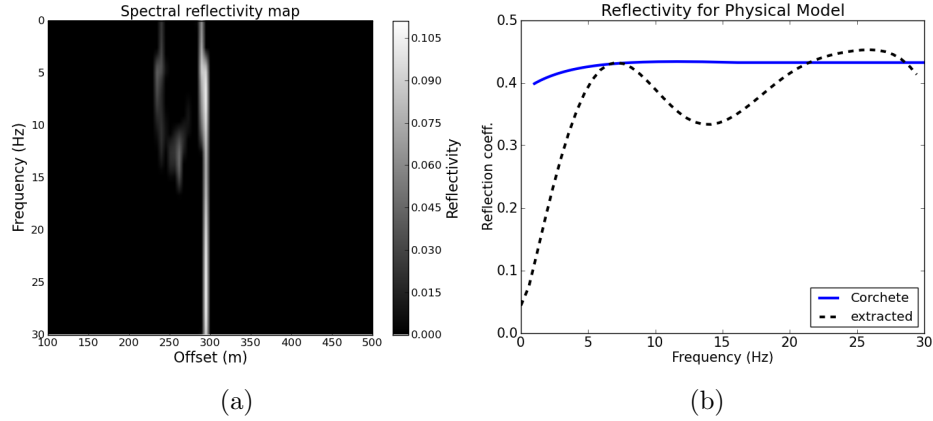


Figure 3.23: Physical model.

Results between extracted reflectivity and predicted reflectivity for the physical model are fairly close. The variation in the extracted reflectivity plot is most likely due to noise. The NRMSD between forward modeled reflectivity and extracted reflectivity across 5 to 30 Hz is 50%.

3.3.5 Example: Field, Hockley 2D line

A multi-shot processing flow for reflectivity and shear-wave velocity updates is tested using seismic data collected across the Hockley fault near Houston, TX (Khan et al., 2013). The survey was part of a larger effort to study and produce maps of surface faults in Houston. There is particular interest and concern about active faults in the area. Active faults are often due to subsidence caused by extraction of subsurface hydrocarbons and groundwater withdrawal. Depending on location, these faults can be a potential geohazard. In addition, the faults themselves can provide information about hydrocarbon accumulation.

The survey was a 2D line recorded with 216 vertical-component geophones at 5 m spacing and vertical vibrator sources at the same spacing. A 12 second linear sweep from 10 to 150 Hz was used.



Figure 3.24: Survey near Hockley fault with inlay showing map of Houston highways and location of Hockley fault.

Two types of processed data are compared:

1. Traditional seismic image processed from reflections.
2. Reflectivity image via surface-wave processing described above.

The migrated image we use was independently processed by Khan et al. (2013). We converted the image to depth using Dix's formula (Dix, 1955) and a compressional-wave velocity model based on an average shear-wave velocity determined from extracted disper-

sion curves. We assumed a V_P/V_S value of 2 to determine compressional-wave velocity from shear-wave velocity.

The interpretation of faults in the migrated image was based heavily on the noted presence of large cracks on the surface of a highway (which ran parallel to the survey line). The largest crack at 0 m was identified by Khan et al. (2013) as the location of the main fault. During the study, another fault was interpreted near the 200 m location due to both a crack on the highway and an anticlinal feature seen at depth below that location in the migrated image. Figure 3.25 shows the migrated image with both the main fault at the 0 m location and the fault near the 200 m location indicated with red arrows.

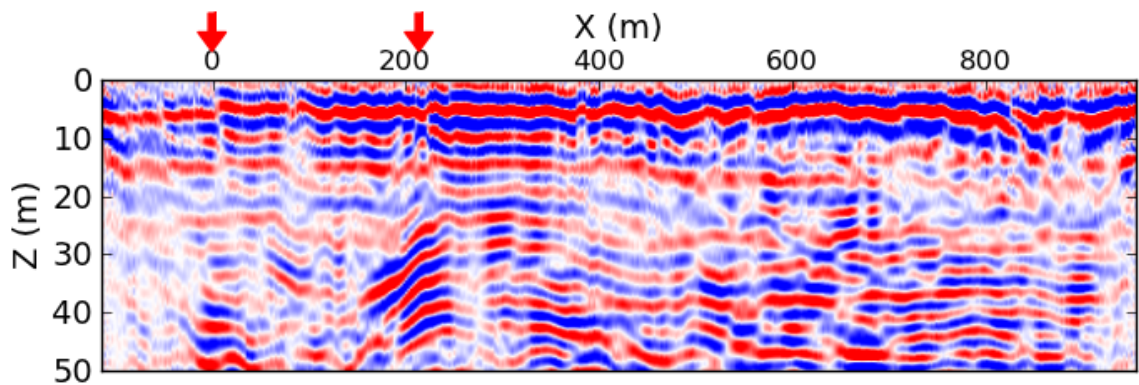


Figure 3.25: Migrated seismic image with interpreted faults marked by red arrows.

The surface wave near the fault has a central frequency of about 40 Hz (Figure 3.26a) and a dispersion image extracted near the main fault (Figure 3.26b) indicates that the velocity ranges from about 250 m/s to 400 m/s. We expect good sensitivity to discontinuities at 3 m to 5 m in depth and our expected total depth of exploration is about 20 m.

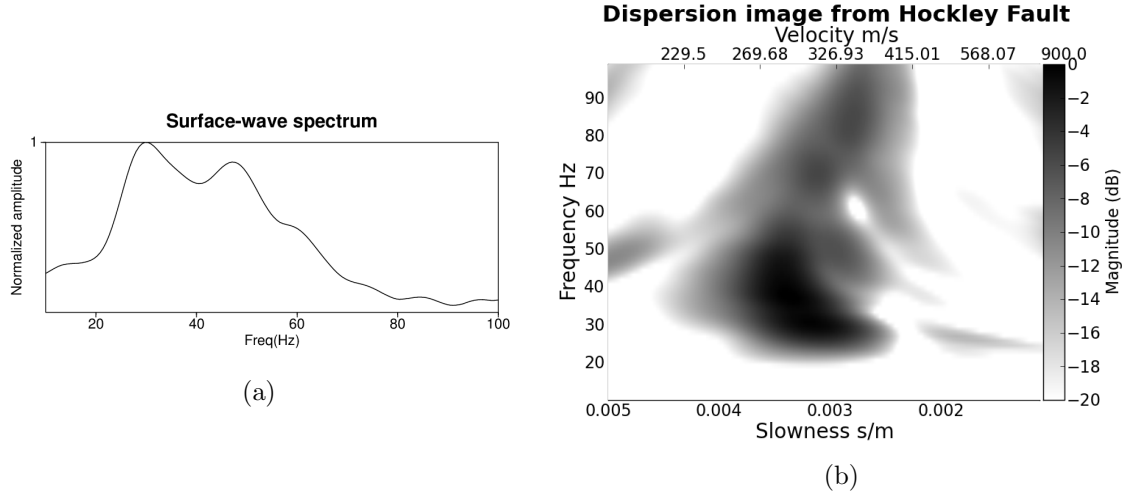


Figure 3.26: (a) Bandwidth of surface-wave from data collected at the Hockley Fault survey. (b) Dispersion image extracted near the main fault.

Prior to our processing flow we remove heavy traffic noise in a few shots on the left side of the survey line with a low-cut filter. In assessing a single raw shot 62 m to the left (D_{-62m}) of the main fault we see faint evidence of a back-reflection (Figure 3.27a) near the marked fault. We highlight the back-reflection with red lines in Figure 3.27b.

The outgoing wave is flattened and enhanced for all shots using a 5-point median filter across the horizontal dimension. The incoming wavefield is separated by subtracting the enhanced outgoing wave from the total data. Figure 3.27c shows the result of the subtraction for the shot at D_{-62m} . For visual clarity, we show the result of the subtraction after data has been unflattened. The SNR for the incoming wavefield is improved using the averaging filter. Figure 3.27d shows that the back-reflections near the fault are emphasized by the averaging filter. Again, the result for shot D_{-62m} is shown in the unflattened domain.

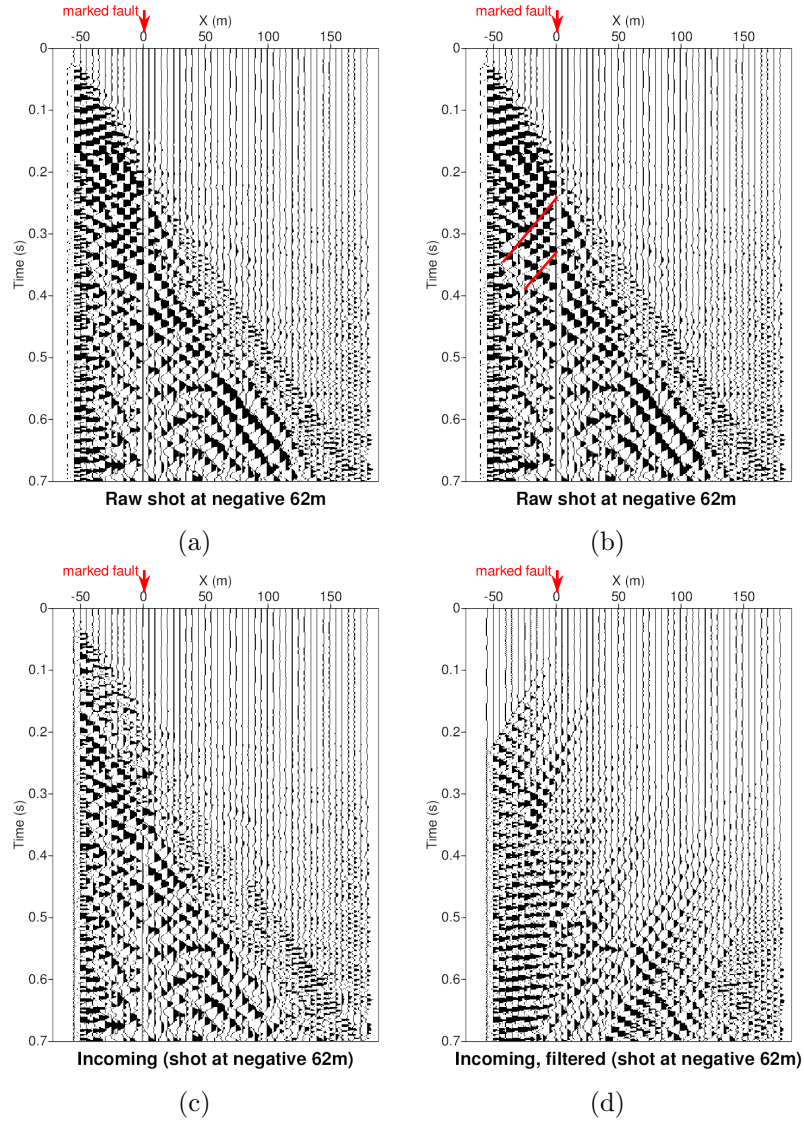


Figure 3.27: (a) Raw shot to left of the marked fault located at negative 62 m. (b) Red lines indicate the location of back-reflections. (c) Outgoing wavefield removed leaving the incoming wavefield and noise (shown unflattened). (c) Emphasized incoming wavefield (shown unflattened).

The emphasized incoming wavefield is muted near time zero, as Figure 3.28a shows for shot D_{-62m} , and the resultant incident reflections are deconvolved by the outgoing wave for all shots. Figure 3.28b shows the spectral reflectivity map for the shot at D_{-62m} . Reflection energy in the central frequency range of the surface wave is concentrated near the fault while a low frequency band is present across the record.

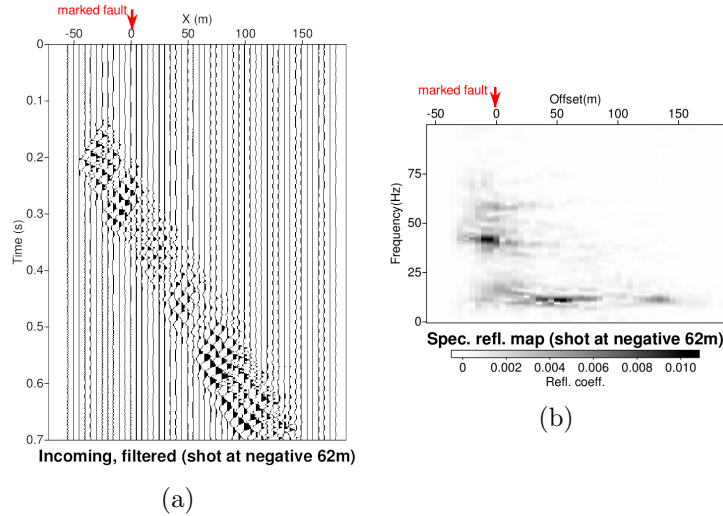


Figure 3.28: (a) Incident locations for incoming wavefield (shown unflattened). (b) Spectral reflectivity map for shot located at negative 62 m. Marked fault indicated with red arrows.

We split the two halves of the fixed-spread geometry into shots illuminating reflectors from the left and shots illuminating reflectors from the right and process each separately. A reflectivity map is created from shots illuminating from the left (Figure 3.29a) and shots illuminating from the right, Figure 3.29b. Interestingly, the map of reflectors illuminated by shots on the right shows no sign of the main fault. Upon closer inspection of individual shots on the right side of the fault evidence can be seen for the fault in a few of the shots. Unfortunately many of shots in the same area also happen to be noisy. The stacking process which is meant to accentuate concurrent reflection events across shots, in this case, stacks out reflection events with noise. Fortunately, in combining the two sides (Figure 3.29c) we regain the lost information for interpretation and phase-velocity updates.

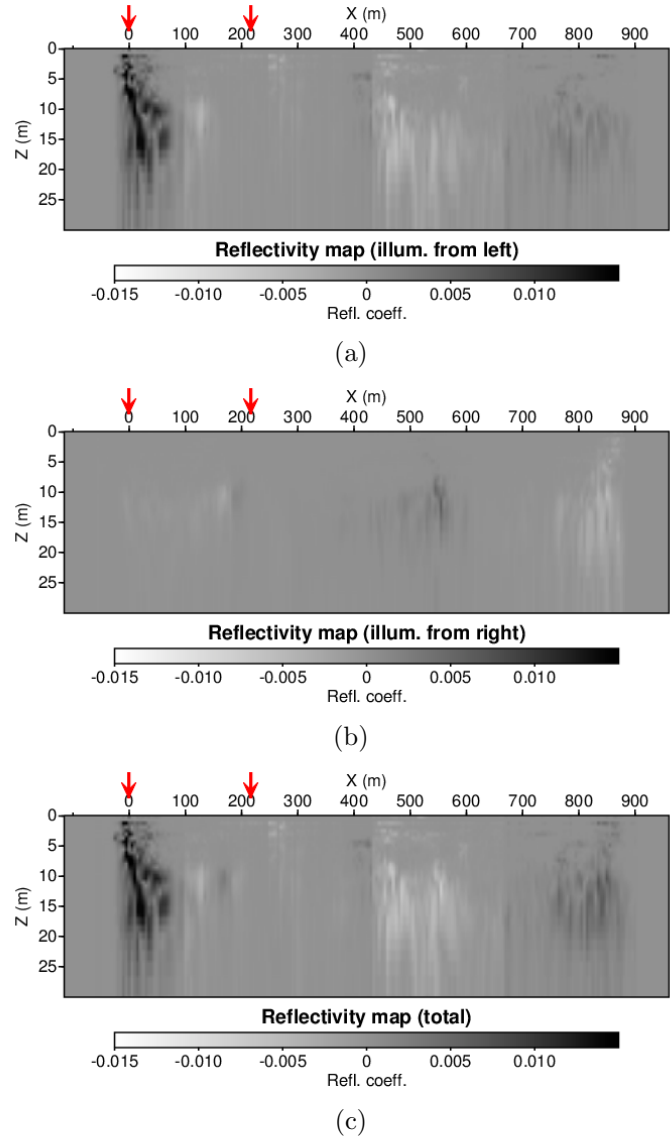


Figure 3.29: Reflectivity maps created by stacking shots which illuminated reflectors from the left side (b) and right side. (c) Left and right maps are combined to create a total reflectivity map. Surface expression of faults indicated with red arrows.

The overlay of surface-wave reflectivity on the seismic image (Figure 3.30) illuminates several structures. The main fault at the 0 m mark is highlighted by strong reflectivity. Two other areas of strong reflectivity on the right side highlight slightly deeper structures, which dip to the right, that could be interpreted as blind faults.

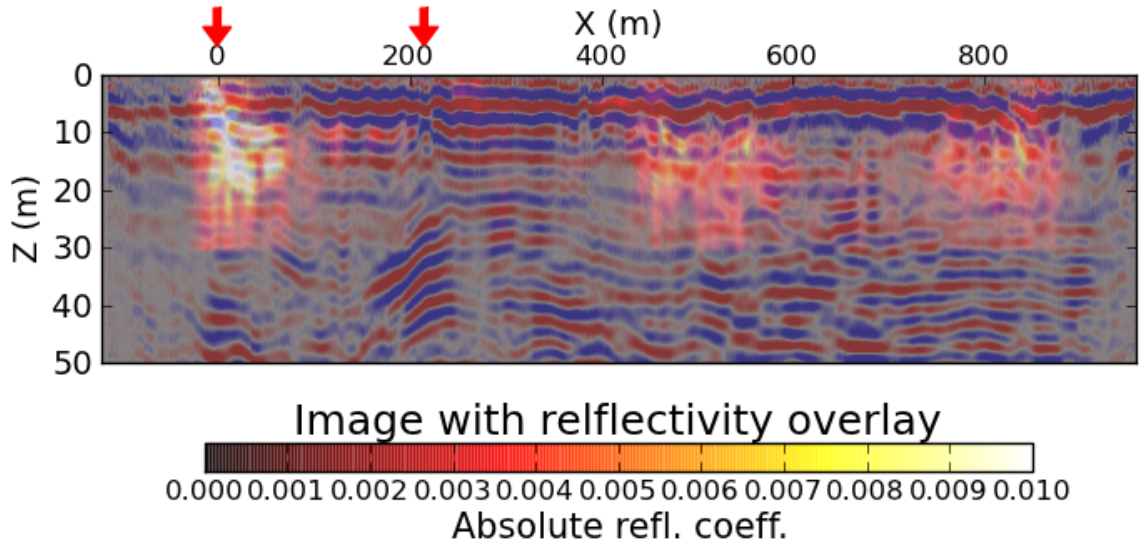


Figure 3.30: Migrated seismic image with reflectivity map overlay. Surface expression of faults indicated with red arrows.

Strong reflectivity does highlight the main fault at the 0 m location. A close inspection of the main fault in the migrated image shows a clear break in strata at a depth of 5 m. The clear break in strata supports the interpretation of a sharp change in properties in the lateral direction at the location of the main fault.

3.3.6 Example: Multi-line processing

To test the multi-shot processing flow designed to image lateral discontinuities on the scale of an engineering site, a 3D synthetic model with two vertical faults, Figure 3.31, is used. A total of twenty-three 2D survey lines running nearly perpendicular to the fault, each 200m long with a 1m receiver and 10m shot spacing, are simulated. For all shots a minimum-phase Ricker source is placed just below the surface to excite surface waves. The source wavelet is designed to have a 15 Hz central frequency. The model consists of two layers beneath the free surface. The shear-wave velocity of the upper layer is 200 m/s and the lower layer is 400 m/s, with a $V_p/V_s=2$ for the entire model.

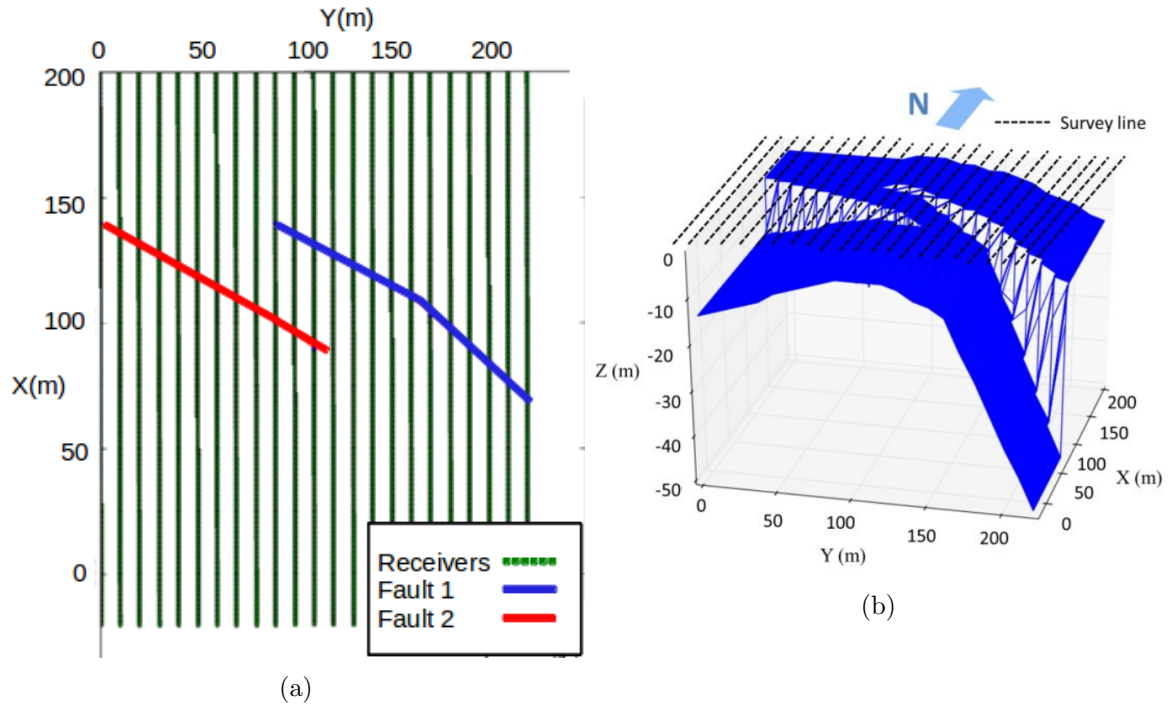


Figure 3.31: Survey geometry for multi-line processing. (a) Plan view of geometry and location of faults. (b) Three dimensional horizon with faults visible. Survey geometry indicated at the surface.

Two faults intersect the boundary between the layers. On the west fault, the up-thrown side of the horizon between the two layers remains at a constant depth of two meters; whereas the down-thrown side of the horizon is 15m on the west side and decreasing in depth towards the center of the model. Both the up-thrown and down-thrown sides of the east fault decrease in depth, eastward, from 1m and 2m respectively to 12m and 15m respectively.

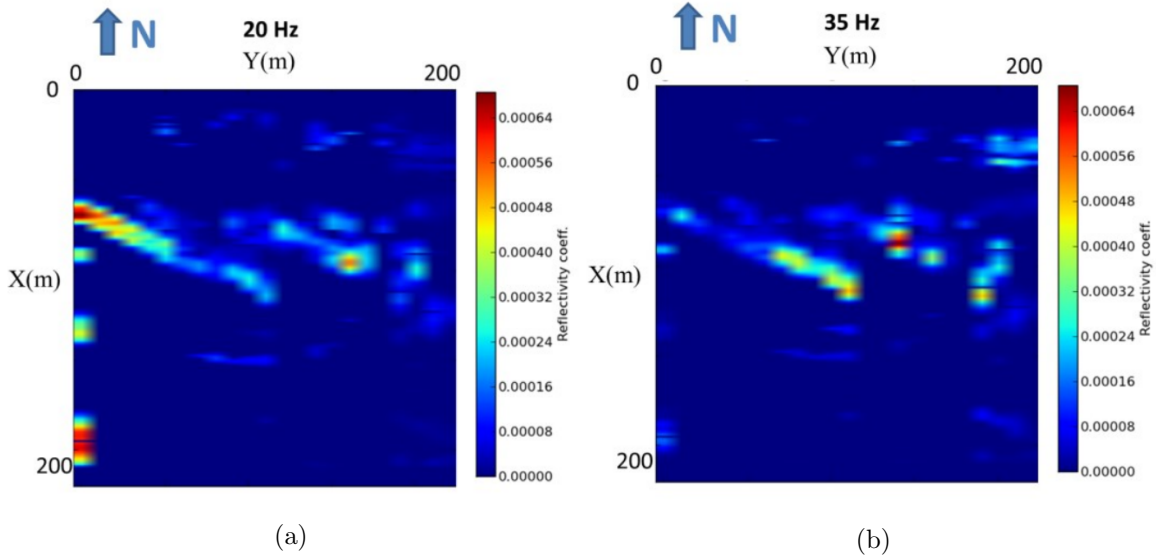


Figure 3.32: Frequency slices through reflectivity results. (a) Frequency slice at 20Hz. (b) Frequency slice at 30Hz

Data is processed for surface-wave reflectivity in each 2D line and the spectral amplitude of reflectivity from each 2D line is combined to construct a 3D reflectivity image. Frequency is the first axis and lateral space defines the other two axes. Figure 3.32 shows frequency slices through the reflectivity image at 20 Hz and 35 Hz. The frequency slices show that the amount of reflectivity at a particular frequency varies depending on how deep and how large the fault-slip is. Both images show that where the east fault is deep, on the right side of the image, no wavelength in the bandwidth of the surface wave is long enough to image the fault. At moderate depth and moderate fault-slip, both faults are imaged well at 20 Hz. At shallow depth and small fault-slip, near the center of the image, the fault is imaged well by 35 Hz.

3.3.7 Example: Sub-vertical faults

Up until this point we have assumed the fault in the model is vertical. The surface wave is expected to reflect differently from a fault that is sub-vertical. No analytic model ex-

ists for a sub vertical fault. Here, numerical techniques are used to model surface wave propagation across sub-vertical fault. First, arrivals in the numerically modeled shot gather are investigated. Further insight in regard to reflectivity from non-vertical faults can be found by using the processing flow for reflectivity described above. Three variations of fault models are investigated. Figure 3.33 shows an example for a vertical fault, a fault at a 45 degree angle with respect to the surface, and a fault at a 25 degree angle with respect to the surface.

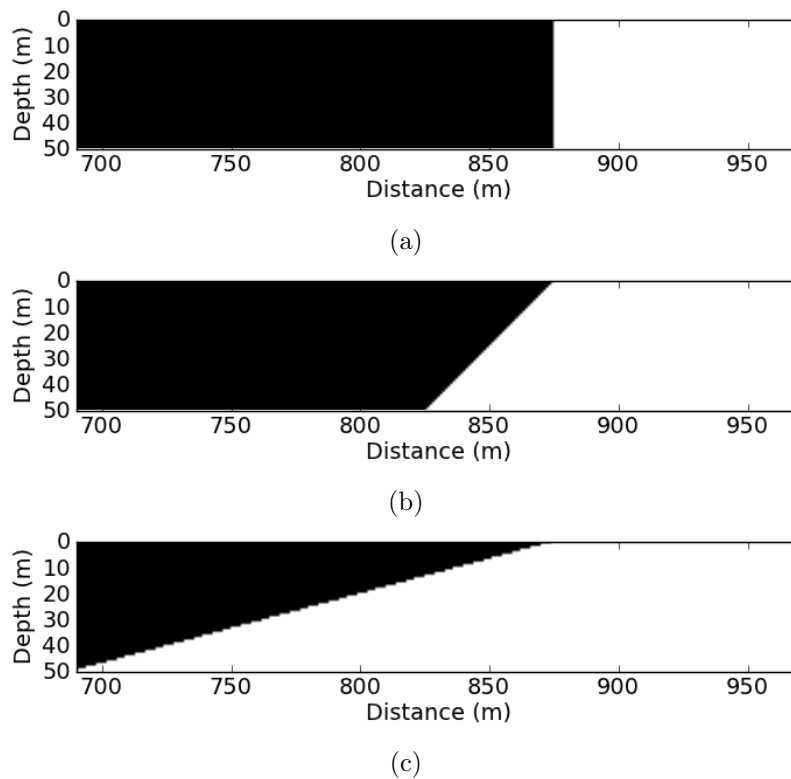


Figure 3.33: Model for sub-vertical faults. (a) Vertical fault for comparison. (b) 45 degree fault. (c) 15 degree fault.

It is expected that the low frequency part of the surface wave will reflect from a nearer-offset location than the high frequency part for faults that dip towards the source. A single 10 Hz shot is simulated on the left side for the fault models.

It is helpful to review the simple case of the vertical fault. Figure 3.34 shows simulated shots from the finite difference method for the vertical fault.

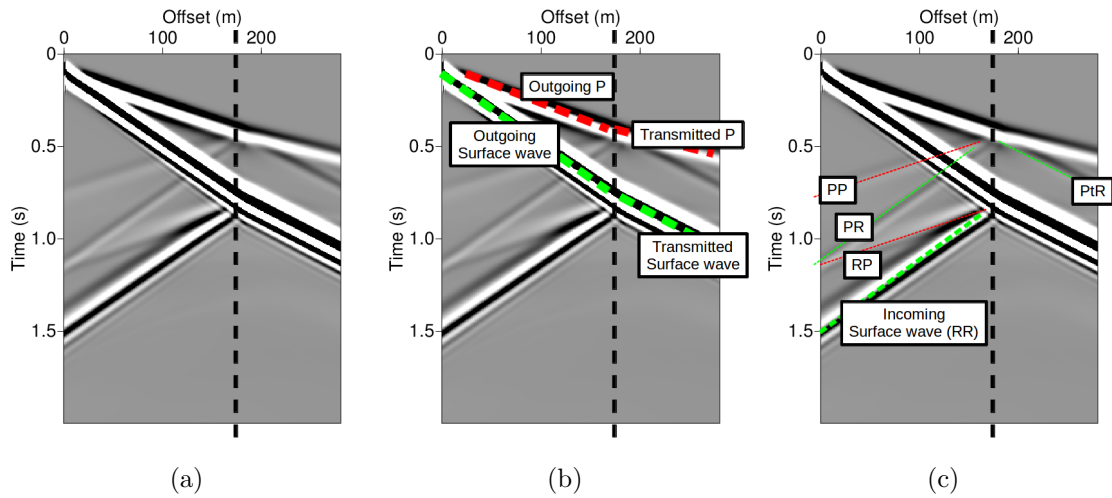


Figure 3.34: Shot gathers of finite difference generated data for vertical fault model. (a) Shot gather with location of vertical fault marked with dashed black line. (b) Shot gather with direct waves (outgoing) marked. Red is indicative of waves traveling at compressional velocity and green is indicative of waves traveling at shear velocity. (c) Shot gather with reflected waves marked.

Figure 3.34a is a clean image of the shot gather with only the vertical fault marked. Direct arrivals (outgoing wave) can be seen for the direct (outgoing) P-wave and surface wave, Figure 3.34b. Although the S-wave is difficult to distinguish from the surface wave it is nonetheless present in the record. All waves refract at the location of the fault. Each incident wave type reflects and converts into P-waves, S-waves, and surface waves, Figure 3.34c. Keep in mind that the processing flow for extracted surface-wave reflectivity is not designed to accommodate converted modes. The processing flow instead attempts to filter out converted modes.

The next case is a fault with a 45 degree slope (with respect to the surface) dipping towards the source. Figure 3.35 shows simulated shots from the finite difference method for the 45 degree fault model.

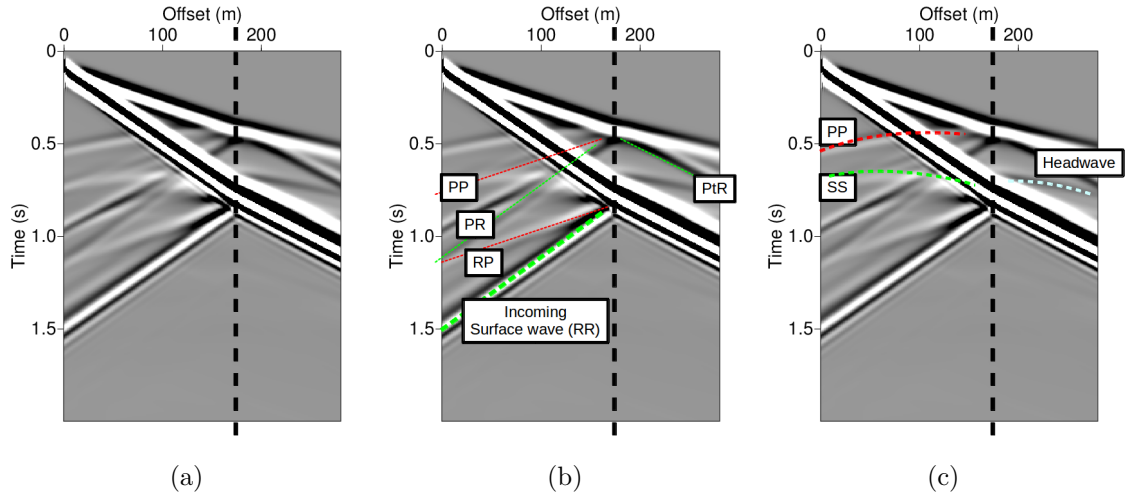


Figure 3.35: Shot gathers of finite difference generated data for 45 degree fault model. (a) Shot gather with location of fault (where it contacts the surface) is marked with dashed black line. (b) Shot gather with reflected waves marked. Red is indicative of waves traveling at compressional velocity and green is indicative of waves traveling at shear velocity. (c) Shot gather with body-waves reflected from fault at depth marked.

Figure 3.35a is an unmarked image of the shot gather with only the 45 degree fault (where it contacts the surface) marked. Direct arrivals are similar to the vertical-fault case. Also similar are the reflected waves from P-waves, S-waves, and surface-waves converting into other types of waves, Figure 3.35b. Figure 3.35c marks arrivals not present in the vertical fault model. The new arrivals in the 45 degree fault model are due to body-waves reflecting from at depth from the fault. A reflected P-wave and reflected S-wave are present in the record. In addition, there is a possible headwave which exists ahead of the surface wave.

The final case investigated is a fault with a 15 degree slope (with respect to the surface) dipping towards the source. Figure 3.36 shows simulated shots from the finite difference method for the 15 degree fault model.

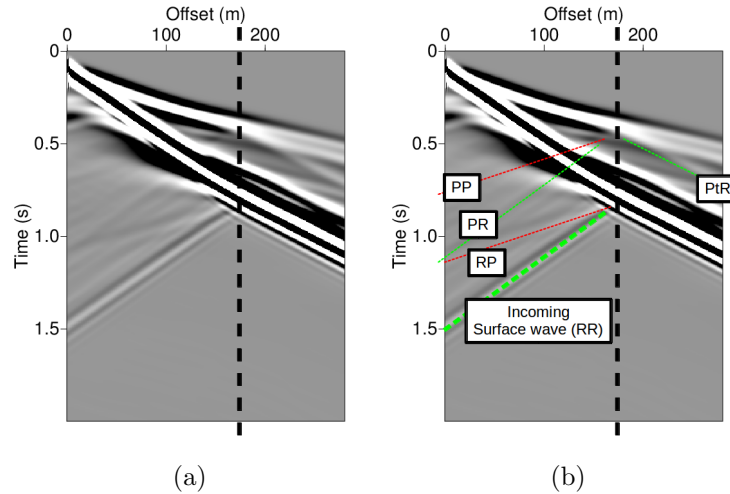


Figure 3.36: Shot gathers of finite difference generated data for 15 degree fault model. (a) Shot gather with location of fault (where it contacts the surface) is marked with dashed black line. (b) Shot gather with reflected waves marked. Red is indicative of waves traveling at compressional velocity and green is indicative of waves traveling at shear velocity.

Figure 3.36a is an unmarked image of the shot gather with only the 15 degree fault (where it contacts the surface) marked. The 15 degree fault creates a much more complicated direct wave. Prior to the location where the fault contacts the surface, the waveform can be seen to be altered. The converted waves for this case are much weaker, Figure 3.36b. The dipping fault has the effect of smoothing the lateral change. Also no longer seen are the body-waves reflecting from depth at the fault. Surface-waves, however, still reflect strongly at where the fault contacts the surface.

Extracting reflectivity from sub vertical faults

Six images, each from a different model, are created with surface wave reflectivity processing. All models are vertically homogeneous with one lateral boundary. The fault models created are: 90 degree, 75 degree, 60 degree, 45 degree, 30 degree, and 15 degree faults (measured in reference to the surface). The model properties other than the dip are the same as above.

To help ensure the converted modes are not a source of noise a higher frequency source is used. The central frequency of the source wavelet is 25Hz.

Largely the same parameters are used for processing each model. A reflectivity image mapped to depth is produced for each. Figure 3.37 shows the various model with a reflectivity overlay.

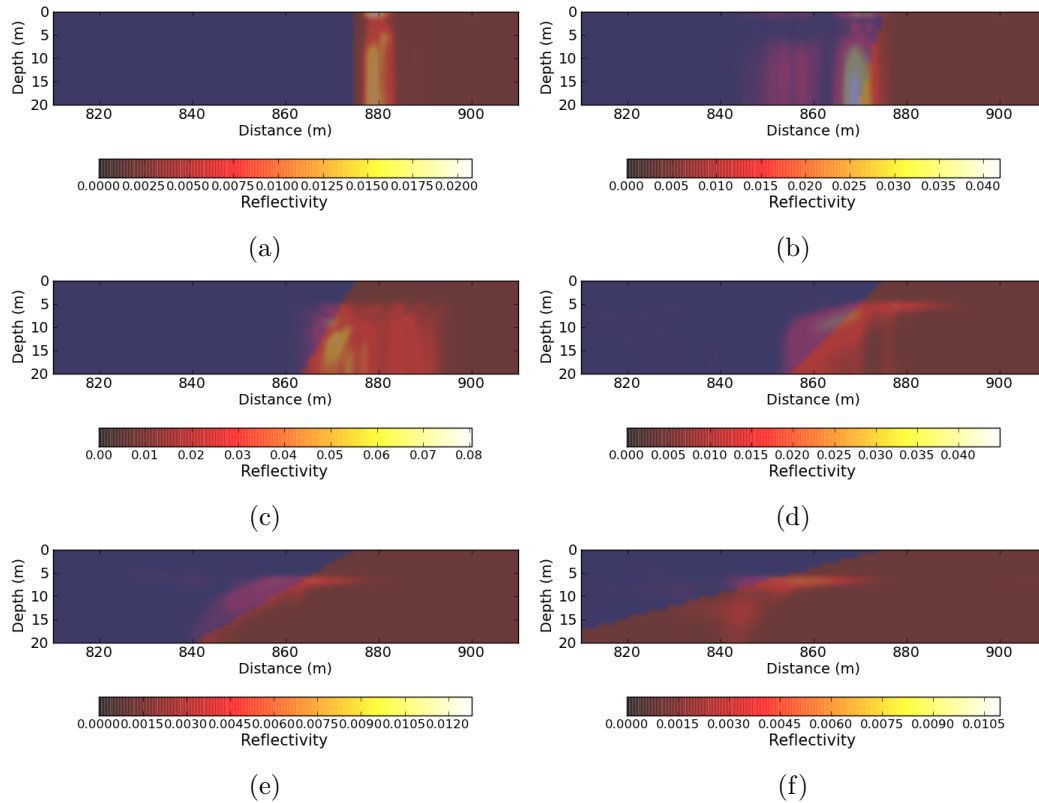


Figure 3.37: Fault models with reflectivity overlay. Various models have differently dipping faults: (a) vertical fault, (b) 75 degree fault, (c) 60 degree fault, (d) 45 degree fault, (e) 30 degree fault, and (f) 15 degree fault.

Generally, the reflectivity image corresponds with the velocity structure. The process seems most accurate for the case it was designed for: the vertical fault model. Reflectivity processing also looks to be effective in estimating the slope of the fault when the fault is between 30 and 45 degrees. A steeply dipping fault does not produce a reflectivity image much different than the vertical fault.

3.4 Summary

Many topics on processing surface waves are covered in this chapter. We first review theory about processing direct surface waves by covering multi-channel phase-velocity estimation and inversion. Our improvements to the existing method by using high resolution dispersion curve imaging and array-windowing schemes help increase lateral resolution. Nevertheless, the inverted shear-wave velocity model is shown to be a laterally smooth version of the true model.

Processing surface-wave reflections has considerable potential due to the fact that reflections are a direct result of the very property we are seeking to define, that being sharp lateral change. Synthetic reflectivity maps generated from our method locate the blind fault with high lateral resolution and accurate depth resolution. Our method of extracting reflectivity from data generated by SPECFEM2D agrees well with our semi-analytic model, exhibiting an NRMSD of only 14%. We confirm our method of extracting reflectivity using a physical model with known elastic properties. Field results show that surface-wave reflectivity maps can be helpful in identifying faults.

Although we present a 2.5D solution using 2D flow, we prefer using a 3D approach for processing reflectivity (this will be covered in chapter 5). Results from the sub-vertical faults show that our processing method is sensitive to distinguishing dips from about 30 to 45 degrees. We should note that the resolution of the lateral boundary will decrease with depth as the wavelength of the surface wave increases.

Chapter 4

Modeling surface waves: 3D

4.1 Overview

Numerical methods are often used to forward model surface waves in a 3D model. No analytic solution exists for a model which is heterogeneous in all three dimensions. We develop a semi-analytic method that is computationally efficient in comparison with numerical methods. We use a combination of semi-analytic modeling and one-way surface-wavefield extrapolation to model surface waves in a 3D heterogeneous model.

Typically, wavefield extrapolation techniques are used to model and migrate body waves through the interior of the earth. The method uses models defined by physical parameters such as P and S wave velocity, and density. We introduce the concept of using wavefield extrapolation to model and migrate surface-waves in the horizontal direction. Instead of using a model based on physical parameters, we use a model based on surface-wave phase-velocities. Frequency dependencies of the surface-wave are naturally accounted for by using phase-velocities as a model. Forward modeling is implicitly three dimensional because frequency is dependent on the structure of shear-wave velocities at depth.

4.2 One-way surface-wavefield extrapolation

4.2.1 Theory

As in the previous chapter, a survey geometry consisting of a straight line of receivers and an in-line source is again considered. Surface waves exhibit dispersive phase-velocities due to vertically varying heterogeneity in the subsurface. Assuming that phase-velocity, c , is dependent on angular frequency, ω , we write a 2D wave equation for surface-wave as,

$$\nabla^2 \psi(x, y, t, \omega) - \frac{1}{c(x, y, \omega)^2} \frac{\delta^2 \psi(x, y, t, \omega)}{\delta t^2} = 0, \quad (4.1)$$

where the wavefield at the surface, $\psi(x, y, t, \omega)$, is a function of time, t , frequency, and lateral space, x and y . We assume that receivers are well sampled in the x -direction, establishing a line in the survey. The y -direction is defined perpendicular to the receiver line.

We construct a 3D surface-wave phase-velocity model, $c(x, y, \omega)$, by calculating local 1D phase-velocity, $\hat{c}_0(\omega)$, given elastic properties as a function of depth, z , at each spatial point,

$$\hat{c}_0(\omega) = F[V_P(z), V_S(z), \rho(z)]. \quad (4.2)$$

The function, F , that defines the relationship between phase-velocity and elastic properties, P and S wave velocity, V_P and V_S , and density, ρ , is highly non-linear. For a given frequency, ω , there are solutions that exist for special values of phase-velocity, $\hat{c} = \hat{c}_m(\omega)$, $m = \{0, M\}$. These solutions represent modes, m , of surface-wave propagation. Navier's equation of motion for a 1D vertically inhomogeneous model provides solutions to equation 4.2. In

generalized compact form, the equation of motion is written as,

$$\frac{d\mathbf{f}(z)}{dz} = \mathbf{A}(z) \cdot \mathbf{f}(z) \quad (4.3)$$

where $\mathbf{f}(z)$ is a 4×1 motion-stress vector corresponding to eigenfunctions and \mathbf{A} is a 4×4 matrix of elastic properties that are independent of z (Aki and Richards, 1980). Solutions to this eigen-problem are found with the propagator matrix method (Haskell, 1953, Kennett, 1983, Thomson, 1950). The fundamental mode, $\widehat{c}_0(\omega)$, is often the most energetic mode. We, therefore, use the adiabatic mode approximation (Pierce, 1965) and consider only the contribution of the fundamental mode to surface-wave propagation.

By separation of variables the solutions to equation 4.1, for a single depth profile in the phase-velocity model, can be written in the exponential form as,

$$\psi(x, t) = Ae^{k(\omega)x - \omega t}, \quad (4.4)$$

where A is the amplitude of the wavefield and k is the wavenumber. The surface-wave dispersion relation is a function frequency,

$$k(\omega) = \frac{\omega}{\widehat{c}_0(\omega)}. \quad (4.5)$$

To illustrate the surface-wave dispersion relation we define a single vertical profile in lateral space as a half-space above a layer, shown in Figure 4.1.

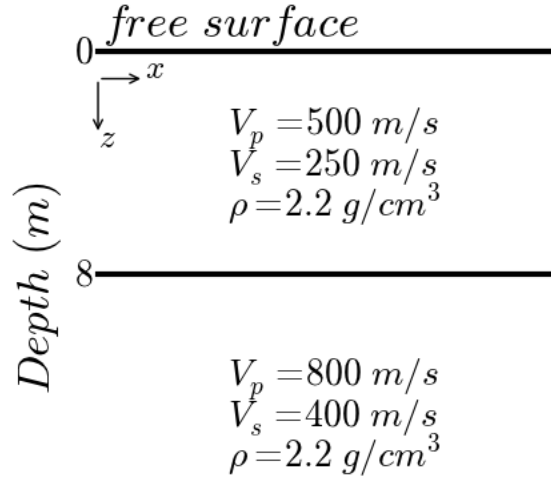


Figure 4.1: Simple model for illustrating the dispersion relations of the surface-wave.

Using the compact form of the equation of motion (equation 4.3) and solutions given by the propagator matrix method, we find the dispersion relation for the fundamental mode. Note that although this model contains only two layers, solutions for the dispersion relation may be found for any number of layers.

Figure 4.2 compares the S wave dispersion relations of the model to the surface-wave dispersion relation. Phase-velocity for S wave is equivalent to the intrinsic S wave velocity, $V_S = c_S$. The two S wave velocities, 250 m/s and 400 m/s, for each layer shown in Figure 4.2 are linear and clearly independent of k . Phase-velocity for surface-wave is a non-linear function of k . Note that phase-velocity is closely tied to S wave phase-velocity.

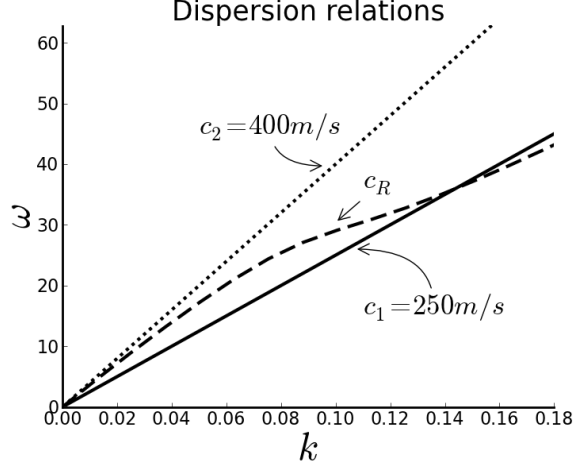


Figure 4.2: Comparison of different dispersion relations. Shear-wave velocity in the upper layer, c_1 , and lower layer, c_2 , are independent of k . Phase-velocity of the surface wave, c_R , is non-linearly dependent on k .

Following the split-step method, to account for velocity heterogeneity in the direction parallel to the line, x , velocity variance is split in space, $c(x, y, \omega)$, into a constant term $c_c(y, \omega)$ and a perturbation term, $c(x, y, \omega)$.

$$c(x, y, \omega) = c_c(y, \omega) + \Delta c(x, y, \omega). \quad (4.6)$$

After substituting the constant velocity term, c_c , into equation 4.1 and applying a two-dimensional Fourier transform over time and the x -axis we arrive at the expression:

$$\frac{\delta^2}{\delta y^2} \psi(k_x, y, \omega) + \left(\frac{\omega^2}{c_c(\omega^2)} - k_x^2 \right) \psi(k_x, y, \omega) = 0. \quad (4.7)$$

Factoring equation 4.7 provides two solutions, representing an outgoing and an incoming wavefield. Velocity, $c_c(y, \omega)$, is only approximately constant for small y intervals, Δy , therefore, the solution for the incoming wavefield is,

$$\psi(k_x, y + \Delta y, \omega) = e^{-ik_y \Delta y} \psi(k_x, y, \omega), \quad (4.8)$$

where the wavenumber, k_y , due to constant velocity is represented in the first term and the perturbation from equation 4.8 is included in the second term. The second term corrects the wavefield due to velocity variation in the x direction,

$$k_y = \sqrt{\frac{\omega^2}{c_c^2(\omega, y)} - k_x^2} + \frac{\omega}{\Delta c(x, y, \omega)}. \quad (4.9)$$

Figure 4.3 shows the dimensions considered for the surface-wavefield propagation. A single source and line of receivers exist at the northern extent of the model. The wavefield is modeled across the surface, step wise, δy , in the negative y -direction. The third dimension of frequency correctly models the non-linear dispersion characteristics of the surface-wave due to the layers below the surface.

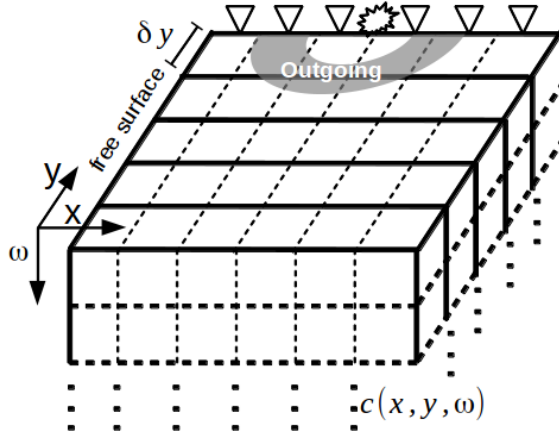


Figure 4.3: Diagram of surface-wavefield extrapolation.

Given the 2D surface of the model, and using a one-way formulation of extrapolation, there are four general directions to propagate a wavefield. The survey geometry and the choice of propagation direction dictates how the split-step method will account for heterogeneity in the model. For our example above, Figure 4.3, heterogeneity in the y -direction is accounted for by assuming small steps of y . Heterogeneity in the x -direction is accounted for in the perturbation term of equation 4.9.

In the presence of small model variations in the x -direction the split-step method will accurately extrapolate the outgoing wavefield to an opening angle of nearly 90° . However, in the presence of larger model variations in the x -direction the split-step method will be less accurate at larger opening angles. This also means that the wavefield will be poorly modeled where structures are steep in respect to the primary direction of propagation. We therefore model outgoing surface-wave in four directions, $+x, +y, -x, -y$, limit the opening angle of each to 45° , and merge the result,

$$\begin{aligned} \psi_s = & \psi_{s(315^\circ, 45^\circ)}^{+x} + \psi_{s(45^\circ, 135^\circ)}^{+y} \\ & + \psi_{s(135^\circ, 225^\circ)}^{-x} + \psi_{s(225^\circ, 315^\circ)}^{-y}. \end{aligned} \tag{4.10}$$

Figure 4.4 shows a template of angles used for combining one-way modeled data. We assume north is in the positive y -direction. The template is used for each source where the source is located at the center. The total modeled wavefield for each source is a combination of one-way wavefields merged at an opening angle of 45° from the direction of propagation.

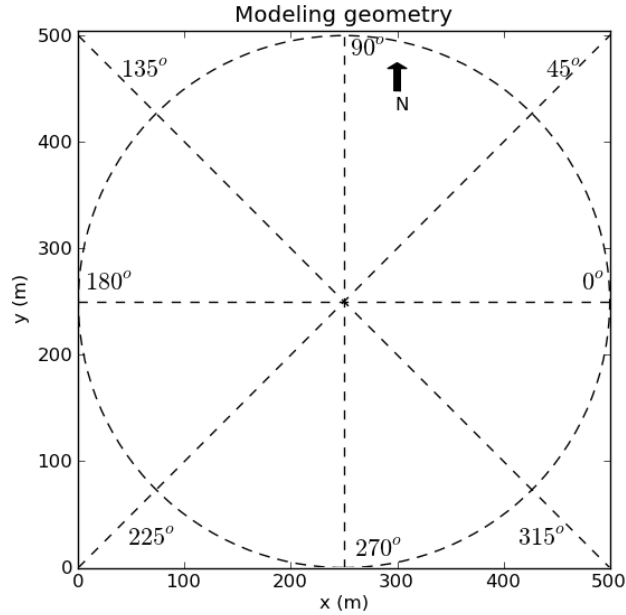


Figure 4.4: Angles used for merging one-way modeled data. Source location is assumed to be in the center of the plot.

4.2.2 Example

We create a 3D shear-wave velocity model containing four structures to show our process of modeling surface waves. Figure 4.5 shows three slices through the model. The upper left frame is a depth slice through the velocity model and the bottom left and right frames are lateral slices through the velocity model in the x and y direction respectively. The location of the lateral slices are indicated on the depth slice with a blue-line. And, the location of the depth slice is shown on the lateral slices with a blue line. Note that all subsequent figures of 3D volumes are shown in this format.

The background velocity is represented by three vertically stratified layers. Top, middle, and bottom layers have a shear-wave velocity of 150 m/s, 175 m/s, and 200 m/s respectively. All structures are bounded by a vertical fault and have a shear-wave velocity of 400 m/s. The structure to the north does not reach the surface, but terminates at a depth of 12 m.

The P wave velocity model is based on a constant V_P/V_S value of 2. Density is assumed to be a constant value of of 2200 kg/m³.

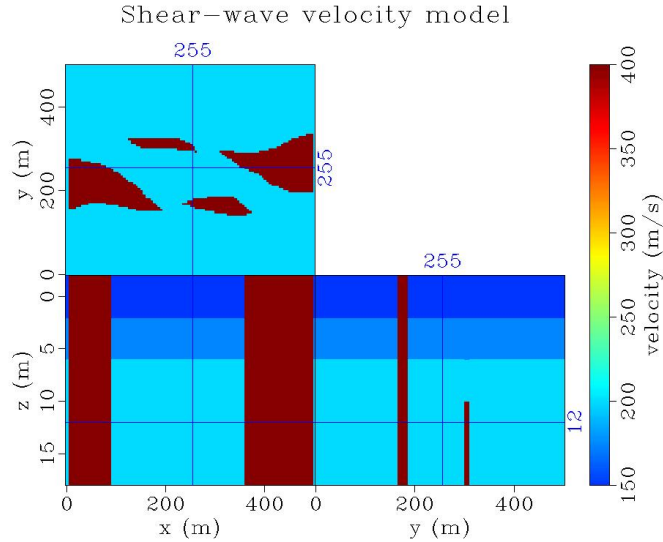


Figure 4.5: Shear-wave velocity model used for generation of synthetic data. Depth slice is shown in top left frame. Location of the lateral slice in the x -direction and y -direction indicated with blue-line on depth slice. Lateral slices are shown in bottom left and right frame.

We use a Ricker wavelet with a central frequency of 10 Hz for a source located at position: $x=250$ m, $y=250$ m, and $z=0$ m. Data is recorded at all sample points at the surface with vertical component receivers. Spatial sampling at the surface is 5×5 m. First, local surface-wave phase-velocities are determined at every lateral location. Then, the surface-wave is modeled using wavefield extrapolation in four directions (north, south, east, and west). Figure 4.6a shows our modeling result.

We compare our method of modeling surface waves with an elastic finite difference. We pad the model in all spatial directions for the finite difference simulation to reduce artifacts at the edges. The source is placed just below the surface to excite surface waves. To avoid numerical dispersion spatial sampling is increased to 2.5×2.5 m . The finite difference

result is subsampled to 5×5 m for direct comparison with our semi-analytic wavefield extrapolation. Figure 4.6b shows the result from finite difference.

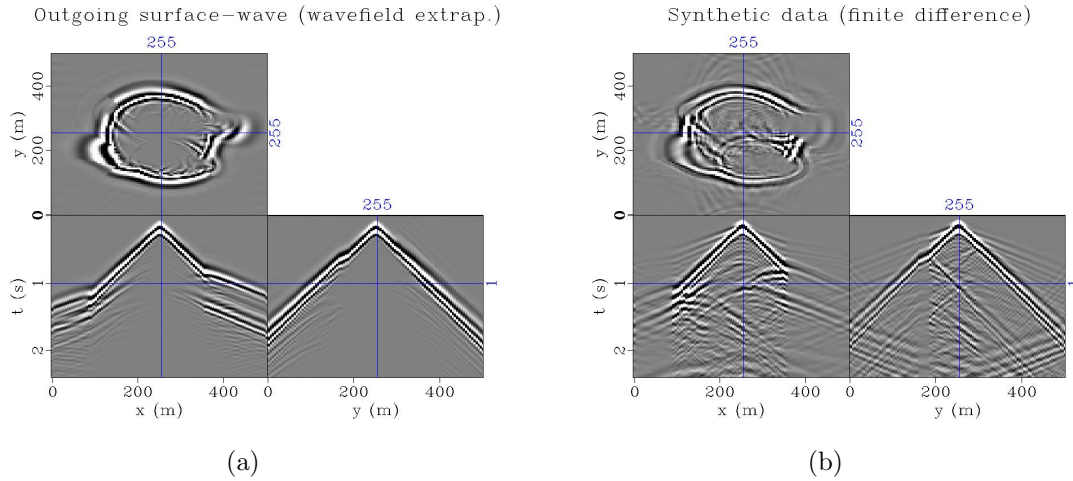


Figure 4.6: A comparison of simulated surface-waves. Time slice is shown in top left frame. The lateral slice in the x -direction and y -direction is indicated with blue-line on time slice, and lateral slices shown in bottom left and right frame. (a) Semi-analytic modeling with wavefield extrapolation, and (b) elastic finite difference.

The complicated wavefield is caused by the velocity contrast of the four structures and surface-wave dispersion. No surface-wave reflections are present in data modeled by surface-wavefield extrapolation because the method is one-way. However, the direct surface-wave modeled by the surface-wavefield extrapolation matches the direct surface-wave modeled by finite difference quite well. Note that the data generated by finite difference exhibits both surface waves and body waves.

Looking across the x -direction, the direct surface-wave suddenly changes dip (velocity) as offset increases. The high-velocity zones coincide with the east and west structures in the model. It is interesting to note that although only one-way is modeled by wavefield extrapolation, reflections appear to be modeled in the high-velocity zones. The wavefield has been bent to such a degree by the strong velocity contrasts that events similar to

reflections occur. The effect is not an artifact from the wavefield extrapolation algorithm as it is evident in the finite difference data as well.

The most obvious difference between wavefield extrapolation and finite difference is the lack of reflections in the wavefield extrapolated data. In the finite difference data, wherever the direct surface-wave exhibit a sudden change in dip, reflections also occur. Surface-wave reflections occur well within the cone of direct surface waves. To model the reflected surface waves we must combine two one-way algorithms.

4.3 Two-way surface-wavefield extrapolation

4.3.1 Theory

For the purpose of forward modeling, two, one-way modeling schemes are combined to approximate two-way modeling. The basic steps in the overall forward modeling flow are:

1. edge detect sharp contrasts in the surface-wave phase-velocity model
2. calculate reflection coefficients at edge locations,
3. extrapolate direct (outgoing) surface wave
4. convolve extracted surface wave with reflection coefficients,
5. extrapolate reflected surface wave in opposite direction, and
6. combine (sum) direct and reflected forward modeled datasets.

Before forward modeling the direct surface wave, a modeling direction is chosen with respect to the survey line. Given a laterally constant phase-velocity model, the wave equation will correctly distribute the energy of the surface wave across the wavefront out to 90 degrees

from the chosen propagation direction. The accuracy of the modeled wavefront at large opening angles will decrease in the presence of strong heterogeneity.

We first detect edges in the phase-velocity model. The reflection coefficient is calculated using the phase-velocity approximation, 2.41, at the location of detected edges. Ray-tracing provides the most accurate result; however, as a first approximation we estimate reflectivity by assuming that the wavefront is normal to the reflector. Reflectors that are at a steep angle with respect to the one-way direction and reflectors that are near the edge of the model will be less accurate.

The direct surface wave is modeled and the wavefield is convolved with reflection coefficients and stored as a separate dataset. The separate dataset represents the incident locations at a particular time and location. The dataset containing incident reflections is then modeled in the opposite direction. Finally, the direct and reflected data is combined to produce a two-way result.

4.3.2 Examples

It is helpful to define the terms “inline” and “offline” when considering the difference between 2D and 3D forward modeling. Prior to this chapter, only reflections traveling across the inline direction have been considered. It is assumed that the fault, or anomaly, of interest lies directly underneath the survey line. Reflections that have incident locations offline are not considered for 2D modeling and processing. Figure 4.7 illustrates the inline and offline assumption in respect to the orientation of the survey geometry and velocity structure.

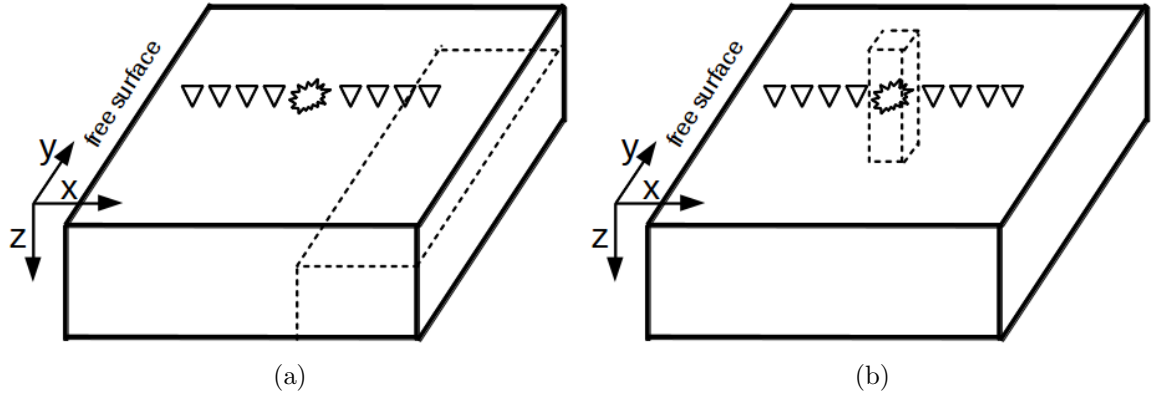


Figure 4.7: A comparison of inline and offline assumption. (a) Receiver line runs directly over, and perpendicular to, structure. (b) Structure is offline from receiver line.

The inline assumption (Figure 4.7a) is ideal when survey geometry is arranged perpendicular to subsurface structure. When structure is more complex, the inline assumption may not suffice. Figure 4.7b shows an example of a structure that is offline from the survey. Structures offline are not considered for 2D modeling and are essentially invisible to 2D processing methods covered in chapter 3.

To illustrate how data is recorded given inline and offline reflections we generate wave-field extrapolated surface waves from each model respectively, Figures 4.8a and 4.8b.

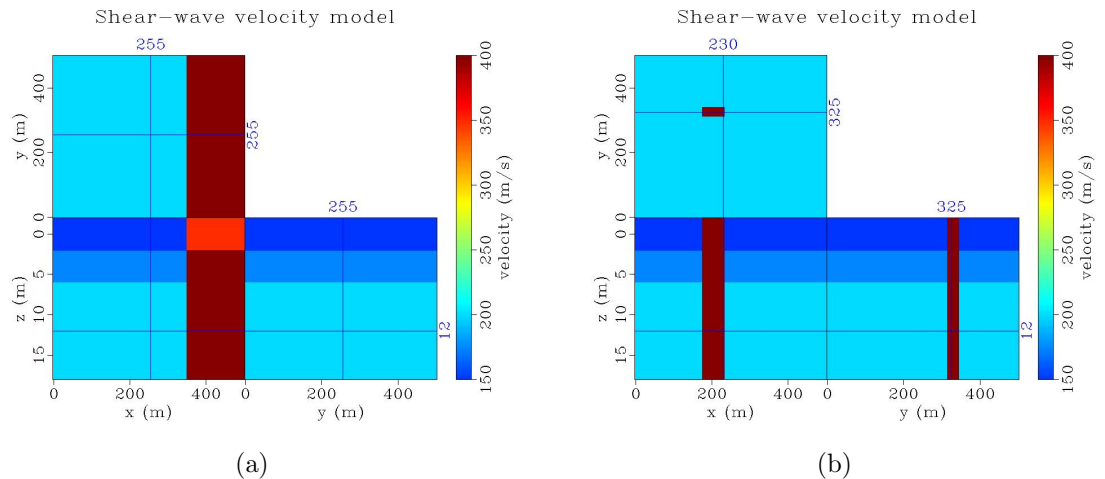


Figure 4.8: Ideal structures for (a) inline and (b) offline assumptions. Depth slice is shown in top left frame. The lateral slice in the x -direction and y -direction is indicated with blue-line on depth slice, and lateral slices shown in bottom left and right frame.

For both models, we use a background velocity comprised of three vertically stratified layers to generate dispersive surface waves. Shear-wave velocities of the background are 150 m/s, 175 m/s, and 200 m/s, from top to bottom. For the inline case, a fault across all y at $x=300$ m is placed in the model. On the right side of the fault shear-wave velocity is 375 m/s in the upper layer and 400 m/s at depth. For the offline case, a tower structure (with a shear-wave velocity of 400 m/s) is placed in the upper left-hand quadrant of the model. A constant V_P/V_S value of 2 and a constant density of 2200 kg/m^3 is specified throughout the model.

A 10Hz Ricker source is placed at: $x=250$ m, $y=250$ m, and $z=0$ m. Shear wave velocities are converted to surface-wave phase-velocities at every spatial point. Figures 4.9a and 4.9b show lateral reflectivity calculated from surface-wave phase-velocities for the inline and offline models. Note that reflectivity is frequency dependent and that only frequency at 5 Hz is shown.

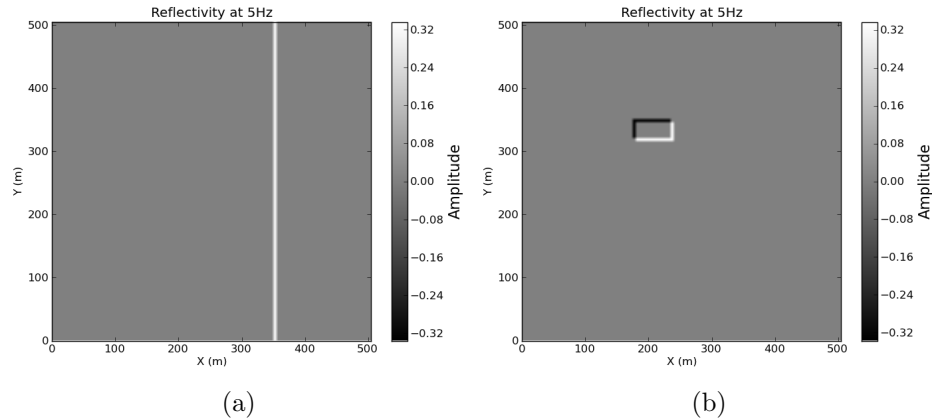


Figure 4.9: Reflectivity at 5 Hz for (a) ideal inline model and (b) offline example model.

We record data at all sample points at the surface with vertical component receivers. Spatial sampling at the surface is 5×5 m. Figure 4.10 shows our modeling results for the inline and offline case. For each of the shots we take a time slice at 1 s, and lateral slices through the middle of the volume. Only the surface wave has been modeled, other arrivals

like the P-wave are not included. Both the direct and reflected wave are shown combined in the shot gather.

The lateral slice in the x -direction across the fault (lower left frame of Figure 4.10a) illustrates the ideal wavefield recorded for the inline case. The incident reflection is recorded at the same time as the direct arrival of the surface-wave. The reflection itself propagates in the direction opposite to the direct (outgoing) wave. Processing in chapter 3 focused on separating the direct wave from the incoming wave prior to creating a reflectivity image.

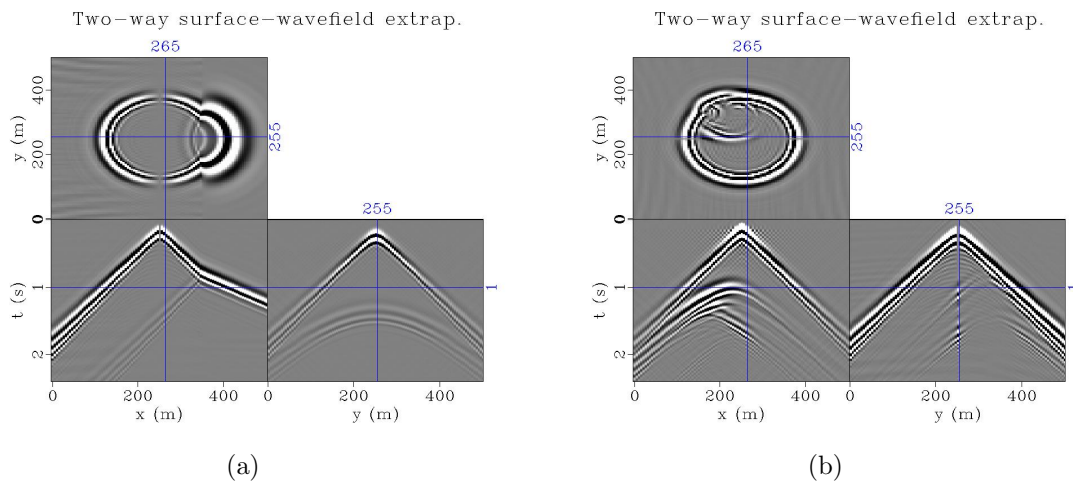


Figure 4.10: A comparison of simulated surface-waves for (a) the ideal inline case and (b) for an offline case. The top left frame shows a time slice. The lateral slice in the x -direction and y -direction is indicated with a blue-line on the time slice. Lateral slices are shown in bottom left and right frame.

Now, consider the wavefield recorded from a model where the fault does not extend fully under survey line, but instead where an anomaly exists offline (northwest) from the survey line, Figure 4.10b. The surface wave which travels in three dimensions encounters the anomaly offline, reflects, and is recorded by the receivers in the x -direction (lower left frame of Figure 4.10b). The reflection arriving from offline is hyperbolic and no longer originates from the direct surface-wave. In fact, all reflections from off-line will have an

apex which exists within the surface-wave cone (between the direct surface wave arrivals for a split spread gather).

We return to the 3D shear-wave velocity model containing four structures (Figure 4.5) to show modeling of both outgoing and reflected (incoming) surface waves for a more complicated case. Figure 4.11a shows the wavefield modeled using our two-way extrapolation method. Compared to the one-way extrapolation for the outgoing wave 4.6a, the interior of the surface wave cone is much more complex.

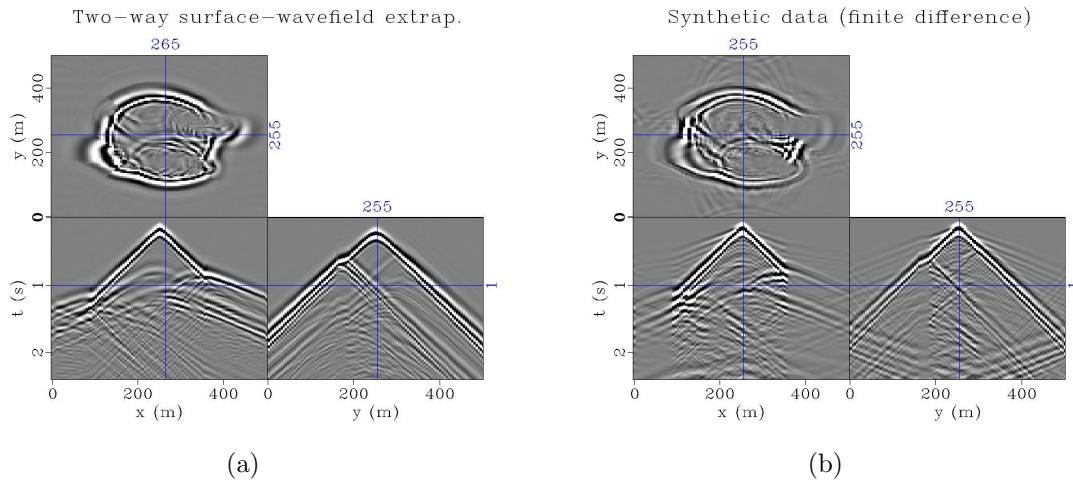


Figure 4.11: A comparison of simulated surface-waves. Time slice is shown in top left frame. The lateral slice in the x -direction and y -direction is indicated with blue-line on time slice, and lateral slices shown in bottom left and right frame. (a) Semi-analytic modeling with wavefield extrapolation, and (b) elastic finite difference.

Both directions for the direct surface-wave have been modeled in addition to the reflected surface wave. The time slice the wavefield reveals nuanced propagation through the scatterers. Visually, the surface-wave generated using wavefield extrapolation matches finite difference quite well.

4.4 Summary

We modify the split-step wavefield extrapolation method to account for dispersion in surface-wave propagation. We rely on local 1D phase-velocity solutions to convert the shear-wave velocity model to phase-velocities used in the extrapolation. The method generates direct surface waves that match surface-waves generated by finite difference. Data modeled by wavefield extrapolation is limited somewhat by the one-way formulation, however the limitation can be overcome by expressly modeling in all necessary directions. Reflectivity can also be added to the forward model to extrapolate reflected surface waves. The forward modeling is instructive in that it shows where reflections occur with respect to the direct surface wave. For reflectors offline, the reflections will be recorded within the surface-wave cone. This suggests that the noise often seen within the surface-wave cone in the field is valuable, and can be used for imaging.

Chapter 5

Imaging using surface waves: 3D

5.1 Overview

We use a modified one-way wave-equation migration to image near-surface heterogeneity in three dimensions. Instead of migrating in depth, the algorithm is modified to migrate surface-wave reflections laterally across the surface. Surface-wave dispersion is accounted for in the migration by using a phase-velocity model that is a function of frequency. Because the wavelength of the surface-wave is dependent on velocity and structures at depth, the wavelength of the migrated image will also contain information about structures at depth.

The migration is one-way, meaning that the wavefront is migrated only from the direction we choose (north, south, east, west, or any intermediate azimuth). Any number of directions may be chosen as migration directions, but the efficacy of migration in a chosen direction is dependent on the orientation of the receiver line. It is ideal to migrate in the direction perpendicular to a receiver line. Given a proper survey geometry, multiple migration directions can be combined to create a full-azimuth migration.

To migrate reflections off-line, the wavefield is extrapolated, or moved, so that the incidence of outgoing and incoming wavefields match each other in time at the reflector. This matching process is done by back-propagating the receiver (incoming) wavefield and forward modeling the source (outgoing) wavefield. It is customary to refer to the matching process as an imaging condition. We test the applicability of several types of imaging conditions for migrating surface waves. A synthetic off-line example is investigated using several imaging conditions. One imaging condition, based on deconvolution, has the potential to provide high resolution results as well as an estimate of reflectivity. Results from two field datasets show that there is a strong correlation between surface-reflectivity and surface features. Although only a single receiver line is needed to produce a migrated image, there is a directivity problem associated reflections arriving to receivers within the image space. Several solutions are provided using multiple receiver lines to solve the directivity problem of reflections.

5.2 Imaging condition

Several imaging conditions are routinely used for standard migrations. We choose three imaging conditions to test: extraction along a time curve, correlation functions, and deconvolution functions. The first, extraction along a time curve (ray-traced time curve), is the fastest to compute. Computing a simple time curve is much less intensive than modeling the outgoing wave. Second, correlation functions (cross-correlations) rely on the computation of the outgoing wave, but produce higher resolution images and are robust in comparison with deconvolution functions. Third, deconvolution functions are difficult to manage due to zeros in the denominator; however, properly applied, they produce images that remove the source term, are high resolution, and estimate reflectivity. Keep in mind that regardless of

the imaging condition used, the migrations are performed in frequency bands as dictated by frequency dependent phase-velocities.

5.2.1 Option 1: Ray-traced time curve

The simplest implementation of an imaging condition is to use a determined time-curve, t_o , at which the outgoing wavefield propagates. It is along this time curve that the migrated incoming wavefield, $\psi_r(x, y, t_o)$, can be extracted (Ng, 1994). Note that the migration direction is defined to be in the y direction. From this extraction a time migrated time image, $q(x, t)$, or a spatially migrated spatial image, $q(x, y)$, can be output depending on the axis chosen for output. For the case of spatial migration, the time curve is the combination of two travel times,

$$t_o = t_{s \rightarrow i} + t_{i \rightarrow r}, \quad (5.1)$$

which is the time at which it takes the wave to travel from the source, (x_s, y_s) , to an image point, (x_i, y_i) . The second time, $t_{i \rightarrow r}$, is the time it takes to travel from the receiver, (x_r, y_r) , to the image point, (x_i, y_i) . For this example we can use approximations,

$$t_{s \rightarrow i} = \frac{\sqrt{x^2 + y^2}}{V_{RMS}(x, y)}, \quad (5.2)$$

and

$$t_{i \rightarrow r} = \frac{y}{V_{AVG}(x, y)}. \quad (5.3)$$

5.2.2 Option 2: Cross-correlation

The first method calculates a time-curve line from which to extract the migrated incoming wavefield. The next option is to model the source wavefield instead of simply calculating a

time-curve. In this case, the modeled source wavefield (outgoing wavefield) is matched to the reflected (recorded) wavefield at the location they meet in space. One way to match the outgoing and incoming wavefields is to use a time-cross-correlation at every image location,

$$\psi(x, y, t) = \psi_s(x, y, t) \star \psi_r(x, y, t). \quad (5.4)$$

Because a time correlation should result in large amplitude at zero time, image extraction at zero time should provide an image,

$$q(x, y) = \psi(x, y, t = 0). \quad (5.5)$$

The term q is proportional to reflectivity. This is a slight modification of the up-down imaging condition presented by Claerbout (1985). Instead of up-down we have x^+ , x^- , y^+ , y^- or any other direction we may choose to migrate. In practice the imaging condition is implemented in the Fourier domain, where

$$R(x, y) = \sum_{\omega} \Psi_S(x, y, \omega) \overline{\Psi_R(x, y, \omega)}. \quad (5.6)$$

Summing over frequency, ω , is the same as imaging at zero time.

5.2.3 Option 3: Deconvolution

A correlation imaging condition simply indicates where the wavefield matches and the amplitude of the output image is a measure of how well the two wavefields match. Deconvolution brings the image one step closer to representing the actual reflectors by attempting to remove the source term. The imaging condition consists of deconvolution at every image

location of the recorded receiver wavefield, $\Psi_R(x, y, \omega)$, by the modeled source wavefield, $\Psi_S(x, y, \omega)$. The migrated image, $R(x, y, \omega)$, is represented in the Fourier domain as,

$$R(x, y, \omega) = \sum_{\omega} \frac{\overline{\Psi_S(x, y, \omega)} \Psi_R(x, y, \omega)}{\overline{\Psi_S(x, y, \omega)} \Psi_S(x, y, \omega) + \epsilon^2}, \quad (5.7)$$

where summation over frequency, ω , corresponds to imaging at zero time. The over-bar notes the complex conjugate, and epsilon, ϵ , is the damping factor to avoid zeros in the denominator. A deconvolution imaging condition provides an estimate of reflectivity in the image.

5.3 Example: Imaging conditions

5.3.1 Comparison: time curve, correlation, and deconvolution

Let us consider a surface-wave phase-velocity model where a large anomaly is located off-line. Figure 5.1 shows the mapview of a phase-velocity model at 5 Hz. The source and survey line are located to the north of the anomaly. The shot gather is forward modeled using the surface-wave extrapolation technique described in chapter 4. We use a 10 Hz Ricker source wavelet.

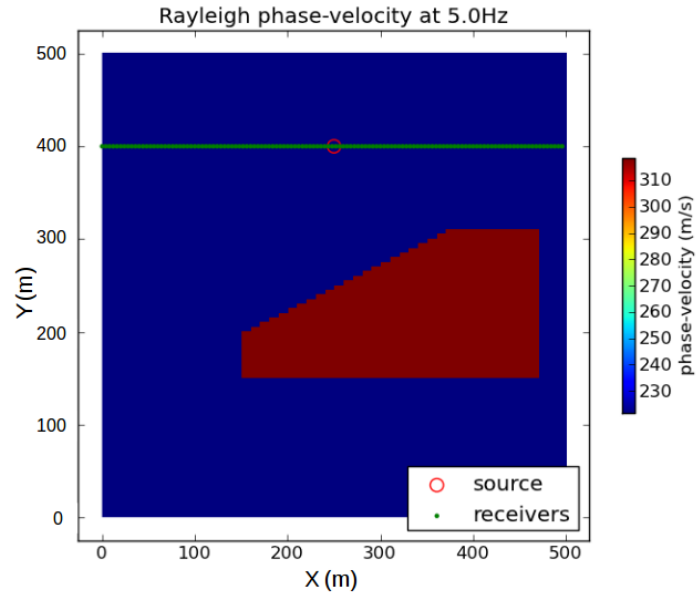


Figure 5.1: Rayleigh-wave phase-velocity model used for comparing of imaging conditions.

The resultant shot gather from the simulation is shown in Figure 5.2a. Prior to migration, the direct surface-wave is removed resulting in only the incoming wavefield, Figure 5.2b. It is not difficult to remove the direct wave for this particular record because the reflections arrive much later in time.

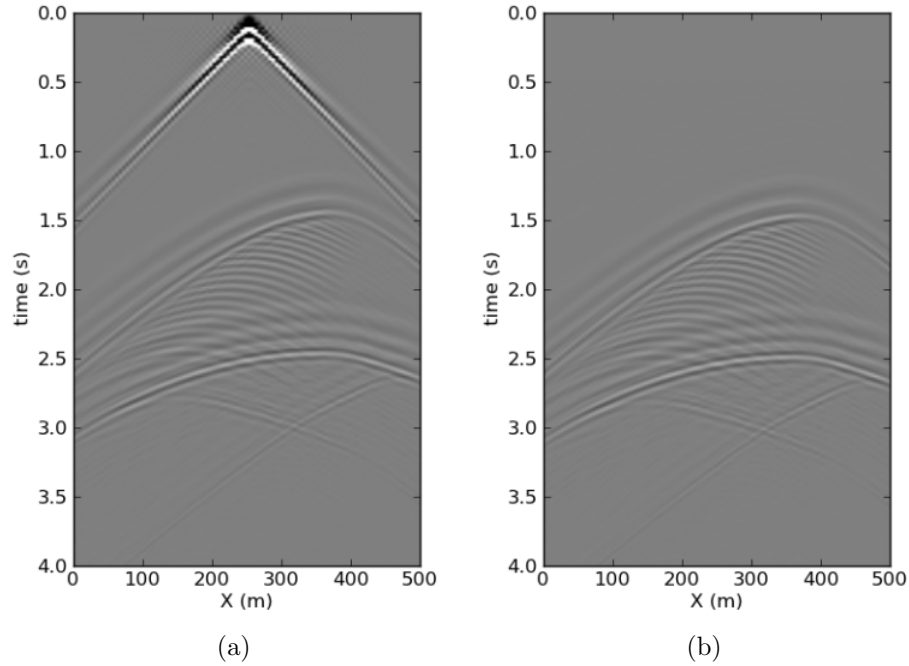


Figure 5.2: shot record of (a) full wavefield of surface wave, and (b) incoming surface wave (outgoing surface-wave removed).

The three imaging conditions are compared for this example. Figure 5.4 shows the various images. The first imaging condition with a ray-traced time-curve (Figure 5.3a) produces low resolution image. The advantage of the ray-traced time-curve is that it computationally more efficient, since the outgoing source wavefield does not need to be modeled or stored. The cross-correlation imaging condition (Figure 5.3b) produces a higher resolution image. Dispersion due to layering will be removed given that the source wavefield and velocity model have been accurately defined. However, the cross-correlation image lacks the sharpness of the deconvolution imaging condition, Figure 5.3c.

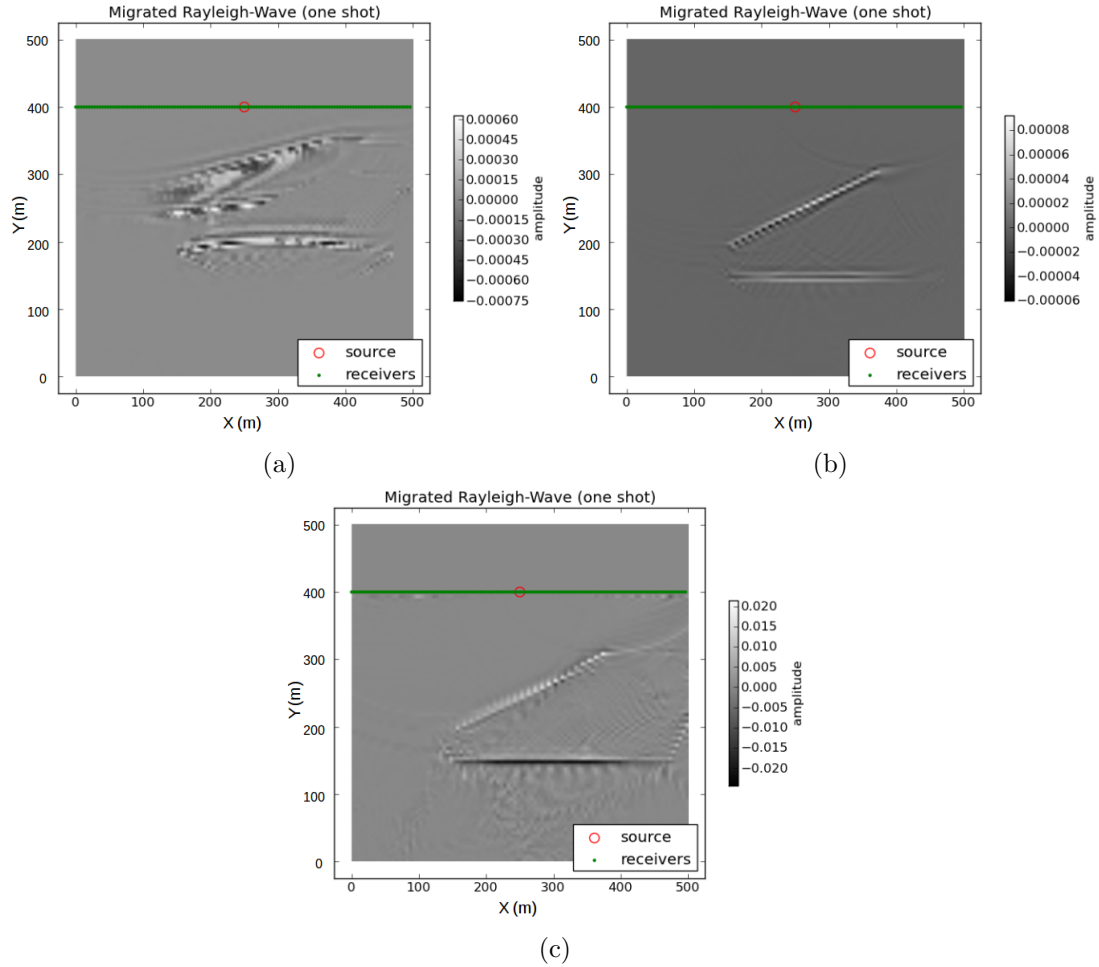


Figure 5.3: Results from three imaging conditions: (a) ray trace extraction, (b) cross-correlation, (c) and deconvolution.

The deconvolution imaging condition removes the effect of the source and provides an estimate of reflectivity. The drawback to using a deconvolution imaging condition is that it exhibits some instability due to zeros in the denominator. Although the deconvolution works well for synthetic data where the wavefields and velocity are well known we expect the cross-correlation imaging condition to be more robust for field data.

5.3.2 Extrapolating wavefields

We use the offline example model from chapter 4 to investigate wavefield extrapolation during migration. Figure 5.4a shows a schematic of the survey and model. A single source (10 Hz Ricker wavelet) is located in the center of the model. Synthetic data is recorded on a single survey line running in the x -direction. A high velocity structure exists offline.

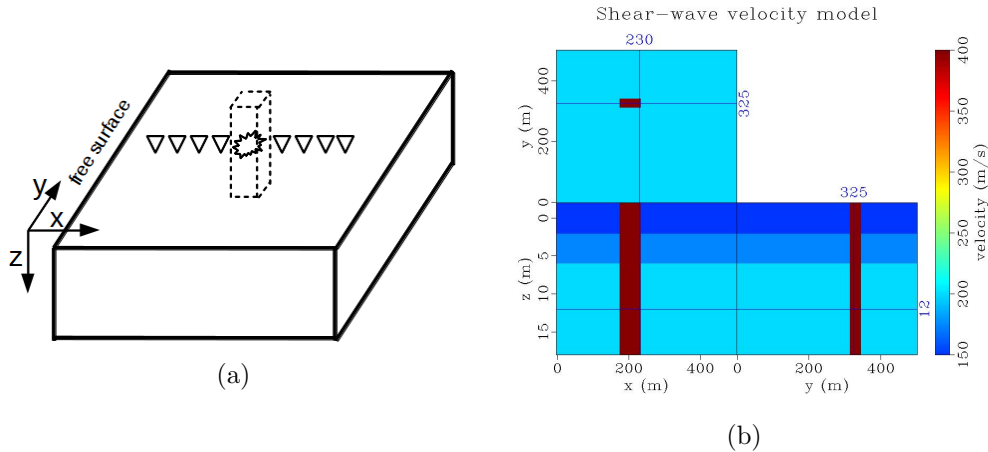


Figure 5.4: (a) Structure is offline from receiver line. (b) Shear-wave velocity model used for illustrating wavefield extrapolation during migration. Depth slice is shown in top left frame. The lateral slice in the x -direction and y -direction is indicated with blue-line on depth slice, and lateral slices shown in bottom left and right frame.

A more detailed view of the shear-wave velocity model is shown in Figure 5.4b. Each frame shows slices through the shear-wave velocity model. The background velocity comprised of vertically stratified layers, 150 m/s, 175 m/s, and 200 m/s, from top to bottom. A tower structure (with a shear-wave velocity of 400 m/s) is located in the upper left-hand quadrant of the model. A constant V_P/V_S value of 2 and a constant density of 2200 kg/m³ is used throughout the model.

The migration process prior to the imaging step is illustrated by the frames in Figure 5.5. The top frame for each subfigure shows a time snap of the wavefield overlaid on the

model. The bottom frame shows the wavefield as a function of time at the slice indicated by the dashed green line.

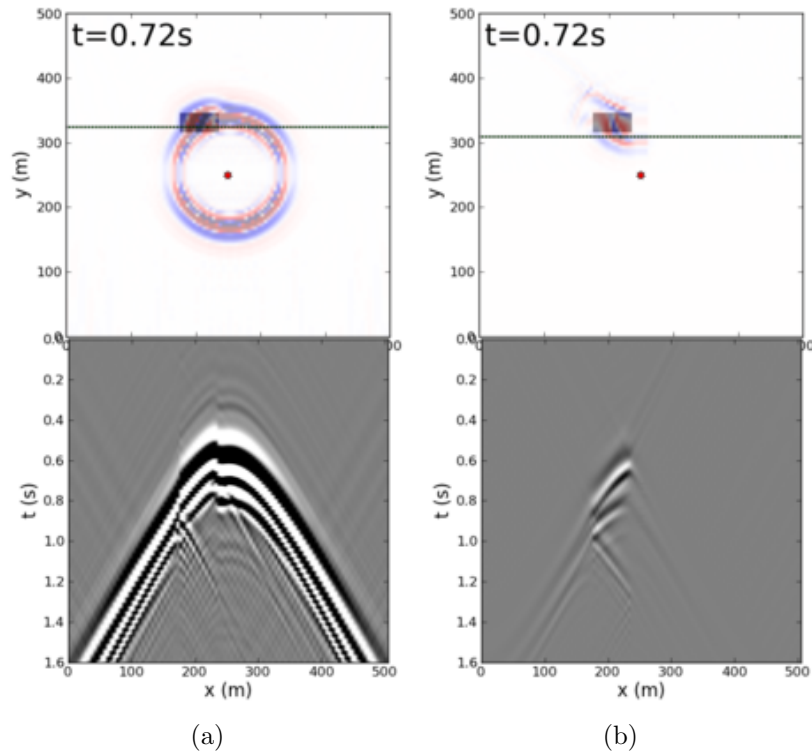


Figure 5.5: Map view of model with wavefield snapshots (top frame) and lateral slice near anomaly (bottom frame) for: (a) forward propagated source wavefield and (b) back propagated receiver wavefield.

Figure 5.5a shows the outgoing wavefield forward propagated from the source to the location of the anomaly. Figure 5.5b shows the incoming wavefield back propagated from the receiver line (located across the x -direction at $y = 250$ m). The time snapshot is taken where the two wavefields meet. Lateral slices across the x -direction near the anomaly show how the wavefields match in time. The resulting image from deconvolving the two wavefields is shown in Figure 5.6.

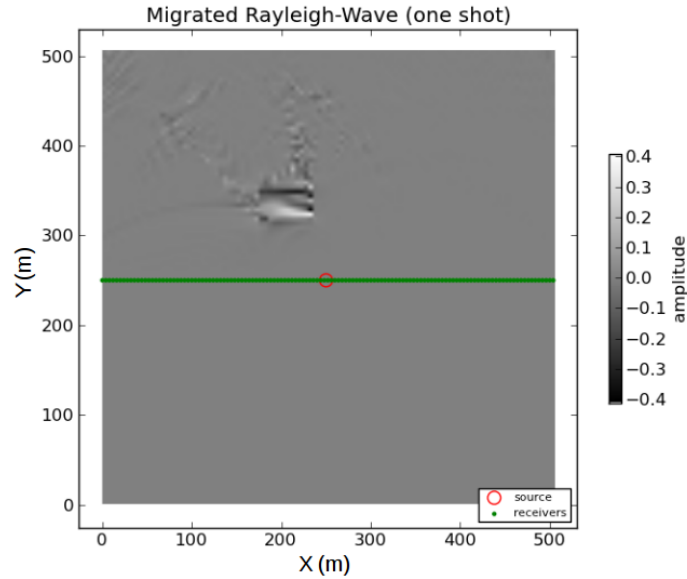


Figure 5.6: Migrated surface-wave reflection image.

Note that although there is a dispersive wavetrain associated with surface wave, the deconvolution imaging condition determines a fairly high resolution image at the location of the reflector.

5.4 Example: Physical Model, 2D line 20 degrees to fault

The picture in Figure 5.7 shows the physical model used to simulate surface waves propagating across a vertical fault. The physical model is aluminum and Plexiglas welded together. Data is collected from a single survey line which was oriented at a 20 degree angle to the fault. Note that the record has been scaled by a factor of 10000 to mimic the scale of data collected in the field.

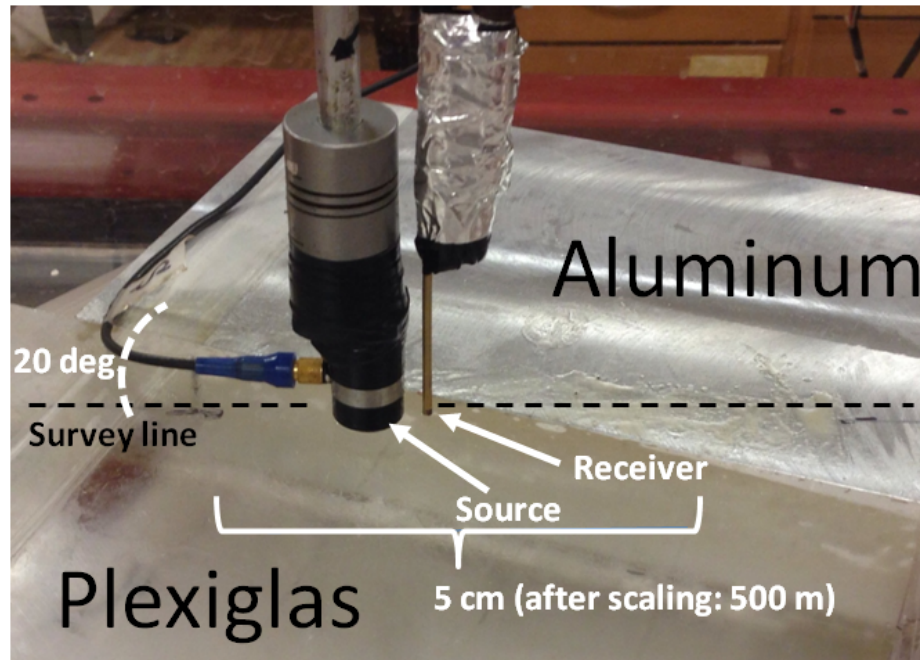


Figure 5.7: Photo of physical model with survey line indicated by a dashed black line.

Figure 5.8 illustrates the location of the survey in relation to the vertical fault. The source is offset 110 m from the first receiver. The survey line spans a total of 610 m across the vertical fault (the receiver line is 500 m long). The red line with arrows represent the possible ray-path for reflected surface waves. Using an approximated distance of 250 m for the distance of the expected ray-path we can determine time at which the surface-wave reflection will be recorded. The known shear-wave velocity for Plexiglas is 1350 m/s; therefore, surface-waves will be traveling at roughly 1227 m/s. A simple traveltime calculation, $t = \frac{250\text{m}}{1227\text{m/s}} = .2\text{s}$, provides the time we expect the surface-wave to be recorded.

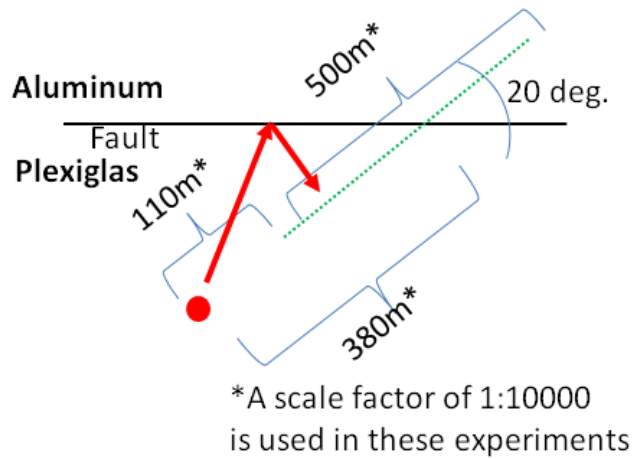


Figure 5.8: Map view diagram showing interface of Plexiglas and Aluminum. Receivers are shown in green and source in red. Red arrows the ray-path of reflected surface waves.

Figure 5.9 shows the shot record from the physical model. The shot record contains identifiable transmitted P waves from Plexiglas to the higher velocity aluminum. Much of the transmitted energy from the P wave is converted to S waves and surface waves. Surface waves can also be identified traveling at a slower velocity and refracting at the fault boundary. The surface wave reflecting at the vertical boundary and propagating back towards the source, however, is missing. Instead, there is a new event present: a reflection of the surface wave from the fault off-line. The surface-wave reflection arrives roughly at 0.2 s; the same time we expected.

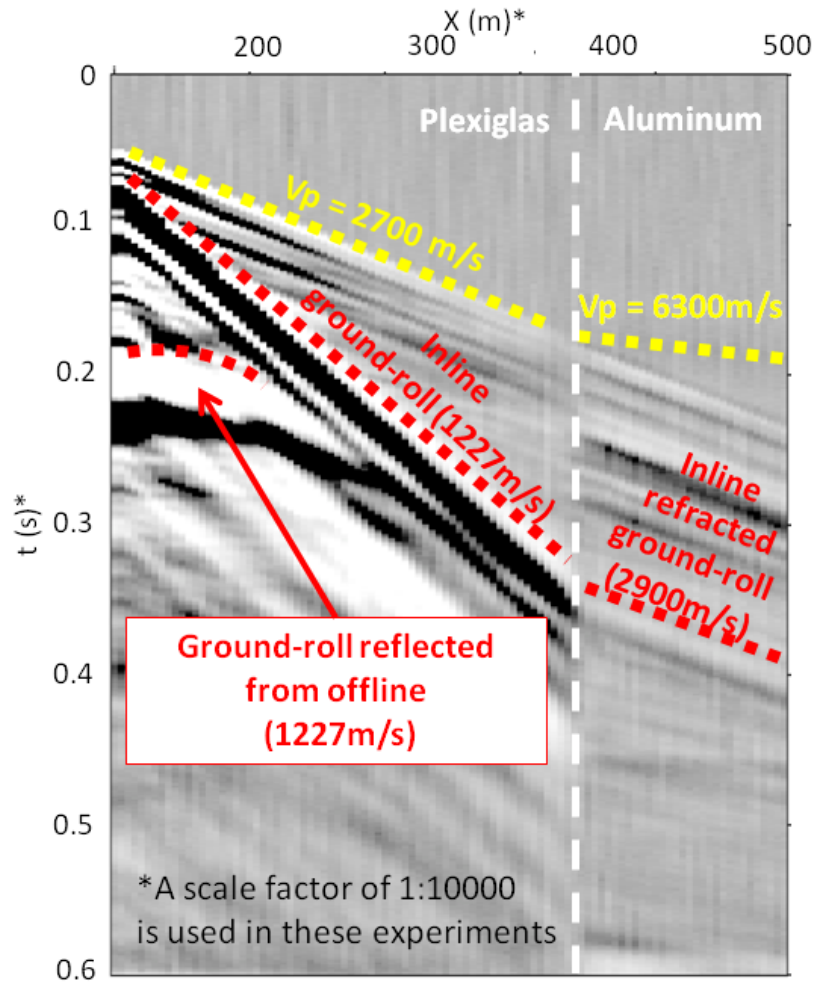


Figure 5.9: A shot gather from survey line at 20 degrees from fault. Arrivals are marked.

The only signal of interest when migrating surface waves is the reflected surface wave, which exists inside the surface wave cone. Therefore, the outgoing surface wave is removed from the record. For this example, the outgoing surface wave is removed using the flattening and filtering routine presented in the chapter 3. Direct arrivals of the P-wave are removed with a mute. Figures 5.10a and 5.10b show the originally recorded data and the filtered reflected surface wave respectively.

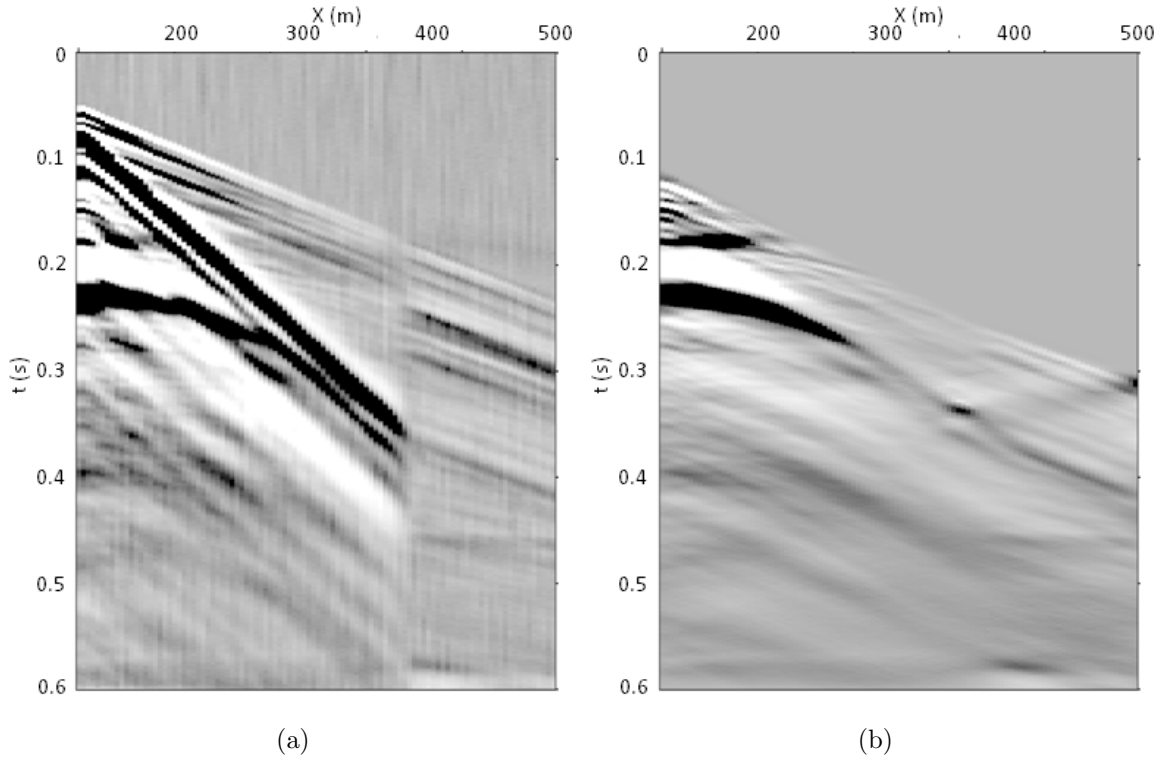


Figure 5.10: (a) Original shot record and (b) direct (outgoing) surface wave removed leaving only reflected (incoming) surface waves .

A phase-velocity model for the physical model is estimated using windowed dispersion curve imaging and lateral-interpolation presented in chapter 3. The source and receiver locations are regularized to the same sample spacing of the designed phase-velocity model. Figure 5.11 shows the model used for imaging the surface wave collected from the physical model. Note that the orientation of the survey has been rotated to horizontal; however, the orientation of the fault in respect to the survey remains the same.

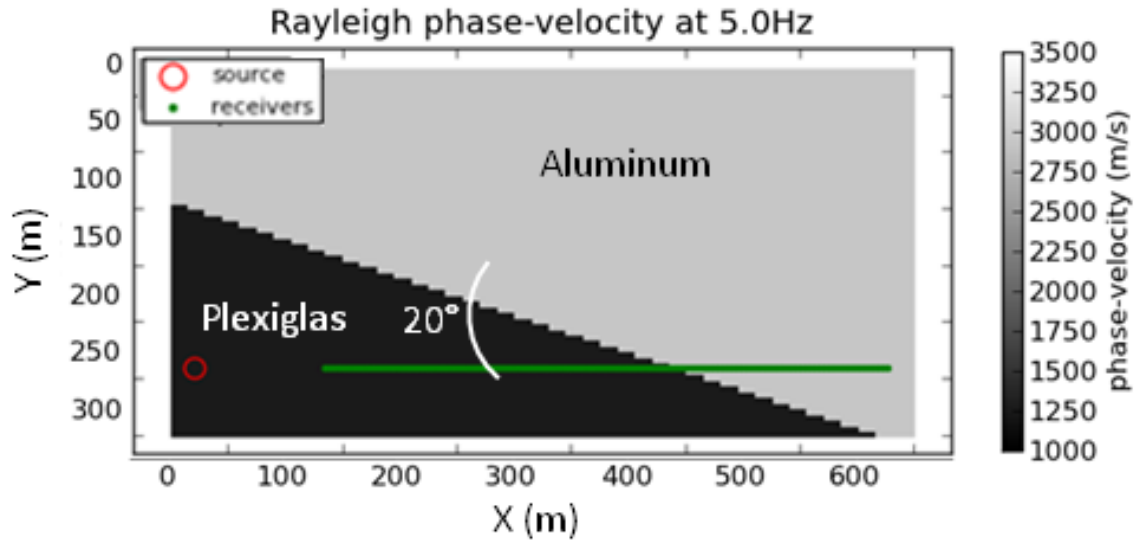


Figure 5.11: Phase-velocity model used for surface wave migration of data collected from the physical model.

Because a deconvolution based imaging condition is used, the outgoing wave is forward propagated and the incoming wave is back-propagated. Forward modeling the outgoing wave requires an initial wavelet. One option in estimating the source wavelet is to first, isolate the surface wave and attain overall the spectral amplitude, and then, design a wavelet. The source wavelet could be designed, for example, using a Ricker wavelet with the central frequency of the spectral amplitude of the surface-wave. A second option is to extract near offset traces after the surface wave has been aligned (and de-dispersed). A stack of the traces provides the estimated source wavelet.

Figures 5.12a and 5.12b compare the results from a Ricker-based source wavelet and an extracted source wavelet. The image based on the extracted source wavelet is slightly cleaner.

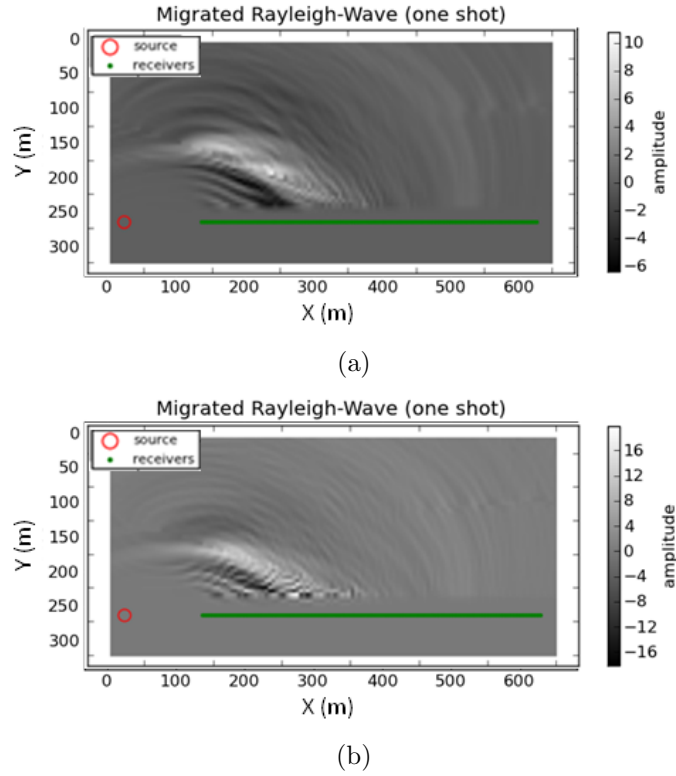


Figure 5.12: Comparison of migrated images from physical model data. Images produced by deconvolution with (a) Ricker-based wavelet, and (b) extracted wavelet.

5.5 Example: Complex Synthetic

A slightly more complex model is used to illustrate the concept of extending the image to 3D using the dispersive properties of surface waves. Figure 5.13a shows a map view of the phase-velocity model in the top frame and the cross-sectional view at $Y=300$ m in the bottom frame. Note that the velocity anomaly on the left is at depth while the velocity anomaly on the right extends to the surface. A snapshot of the wavefield at 1.12 s is overlaid on the map view of the shear-wave velocity model.

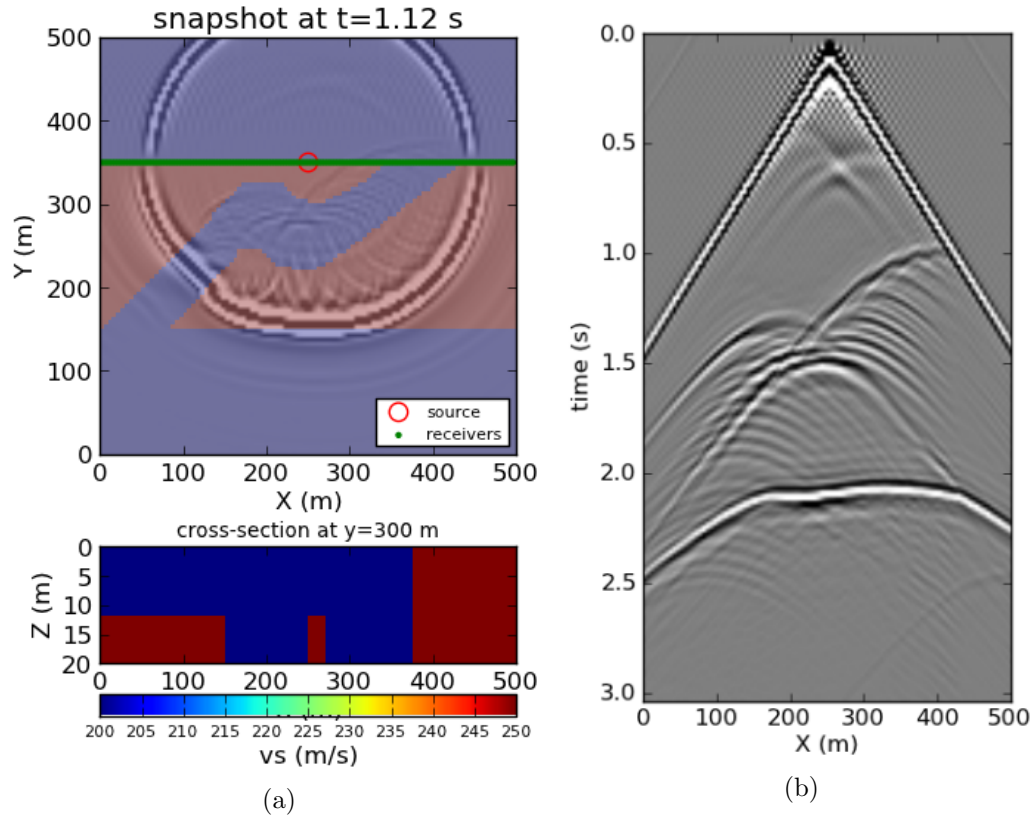


Figure 5.13: (a) Shear-wave velocity model for complex model. Map view in top frame and cross-section view in bottom frame, and snapshot of wavefield overlaid on map view. (b) Shot gather from complex model.

Figure 5.13b shows the shot gather from the synthetic forward modeling. Surface waves reflect from both the deep and shallow (surface) anomalies. As before, the outgoing surface wave is removed and only incoming surface waves are migrated. The outgoing wave is simulated for use in the deconvolution based imaging. Figure 5.14 shows the result of the migration

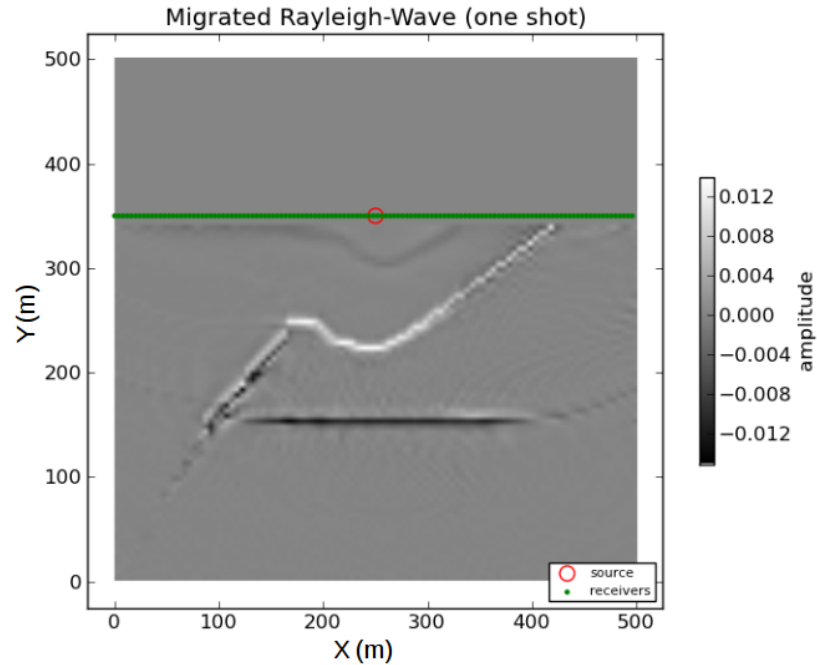


Figure 5.14: Migrated image using deconvolution based imaging condition.

The migrated image reveals the location of both the deep and shallow structure. Recall that the depth of the structure is linked to the frequency content of the surface wave. The higher frequency part of the surface wave is sensitive to the shallow structures and the lower frequency part of the surface wave is more sensitive to the deeper structures.

The resultant image is filtered based on the wavelength of the image. The first image (Figure 5.15a) is filtered to only include low wavelengths. The second image (Figure 5.15b) is filtered to only include short wavelengths. Notice that the short wavelength image (on the right) shows only a faint reflection from the deep anomaly.

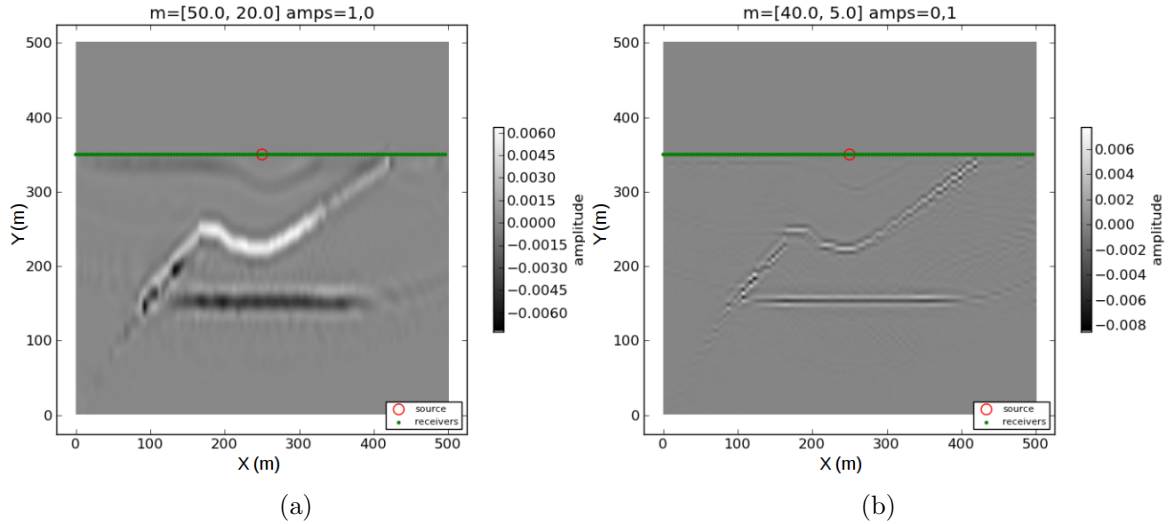


Figure 5.15: Wavelength filtered images of complex model: (a) Long wavelength image, and (b) short wavelength image.

5.6 Example: Field, Bradford

Several surveys in the AGL database were investigated to find shots that may have recorded surface-wave reflections from off-line. The Bradford survey, in the Marcellus shale region, was selected due to its potential for strong lateral heterogeneity. Varied geology in the region and surrounding mountains are likely candidates as surface-wave reflectors.

The Marcellus shale is a unit of marine sedimentary rock which extends throughout much of the Appalachian Basin. The Marcellus is a gas-rich shale. Originally the survey was conducted to assess the presence of hydrocarbons. The survey itself covers an area of about 25 km², Figure 5.16.

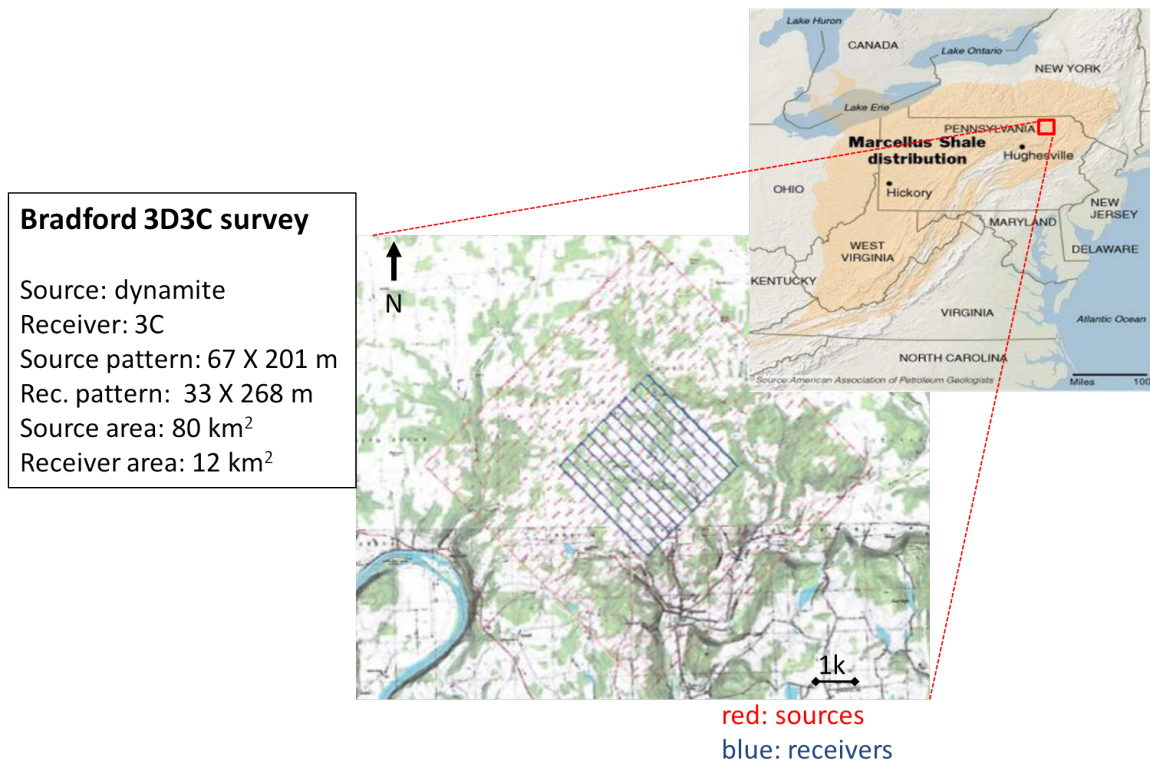


Figure 5.16: The Bradford survey area.

The inlay in the upper right of Figure 5.16 shows the location of the survey. The large map shows the layout of the survey, with the sources indicated in red and the receivers in blue. The specifications for the survey are shown in the left frame. Only a small selection of sources and receivers is selected to be processed and only the vertical component is considered.

A single shot is selected to assess the presences of surface wave reflections. Figure 5.17a shows the single shot selected (indicated by the red dot) and the group of receivers (indicated by the dark blue dots) investigated.

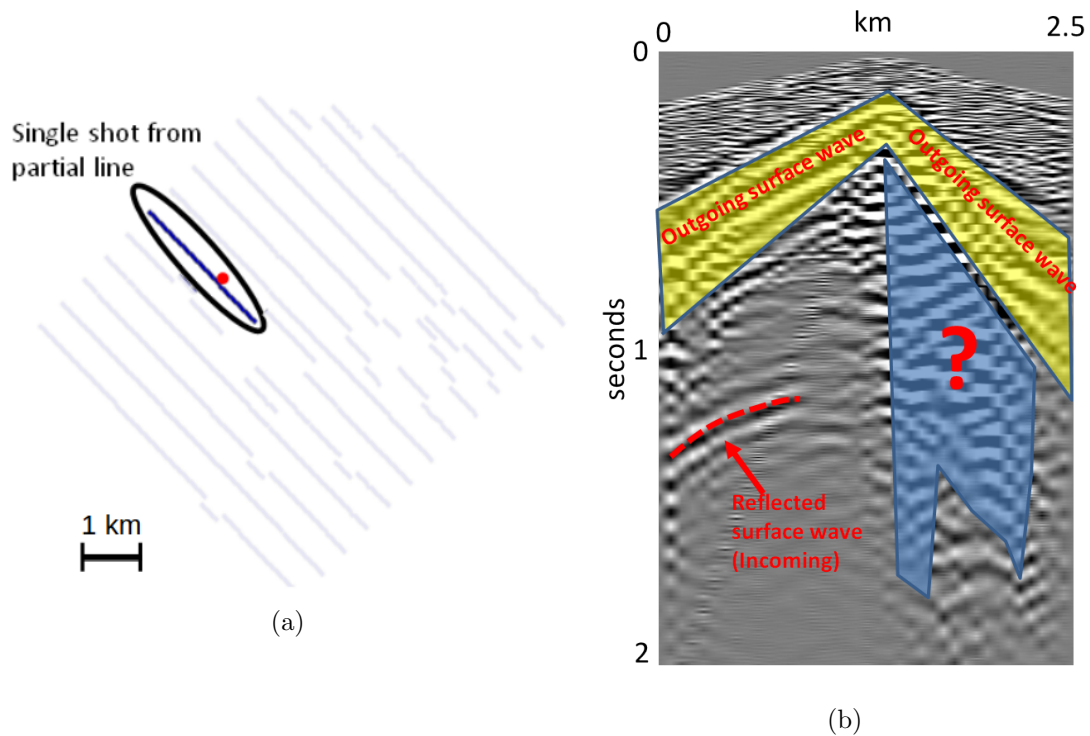


Figure 5.17: (a) Selection of shot and receivers, and (b) corresponding shot record.

Figure 5.17b shows the shot record from the selected location in the survey. The outgoing surface wave is highlighted in yellow. A reflected surface wave is identifiable on the left side of the record (marked in red). However, there still is noise in the surface wave that is unexplained (on the right).

Surface-waves in field data are often very noisy. Ideally, only the incoming (reflected) part of the wavefield should be migrated. As is the case with this shot, there are often other parts of the surface wave that are not identifiable as outgoing or incoming waves. Prior to migration, everything but the identifiable incoming wave is removed. The outgoing wave is removed from the record using the same method presented in chapter 3. Multiple shots are migrated and stacked to increase the signal-to-noise ratio in the resulting image.

Figure 5.18a shows the selection of shots chosen for migration. Surface waves were migrated to the south-west side of the line. As such, the only section of the survey modeled

is indicated by the blue square labeled Model. For simplicity, only one dispersion curve is used to represent the phase-velocity of the entire area of the model. Each shot is migrated independently and the image from each shot is stacked to produce a final result.

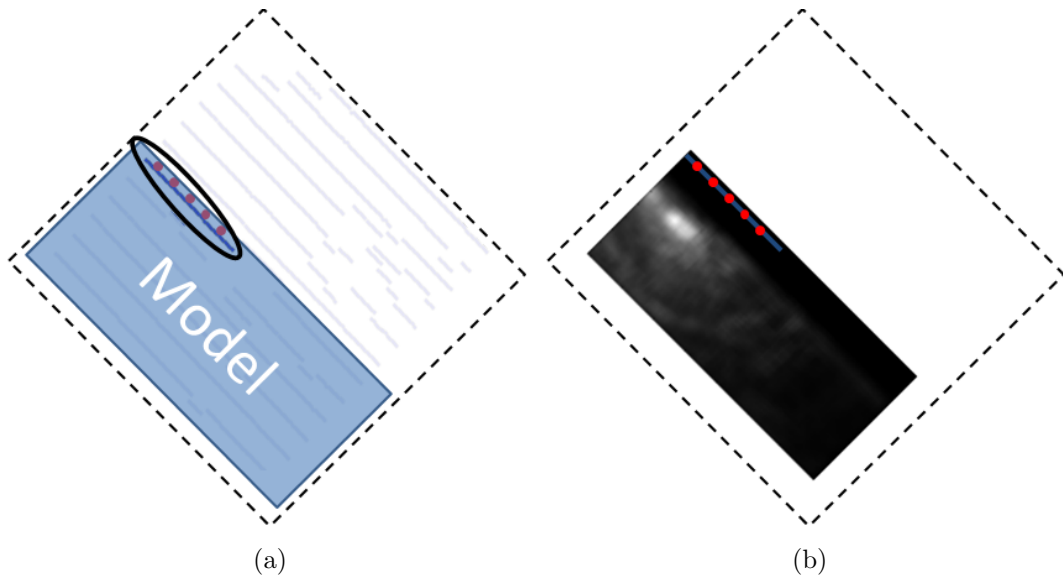


Figure 5.18: (a) Model space and selection of shots, and (b) migrated image.

The reflectivity image from the selection of shots (Figure 5.18b) shows some interesting structures. A correlation can be seen between the reflectivity image and topography by overlaying the two, Figure 5.19.

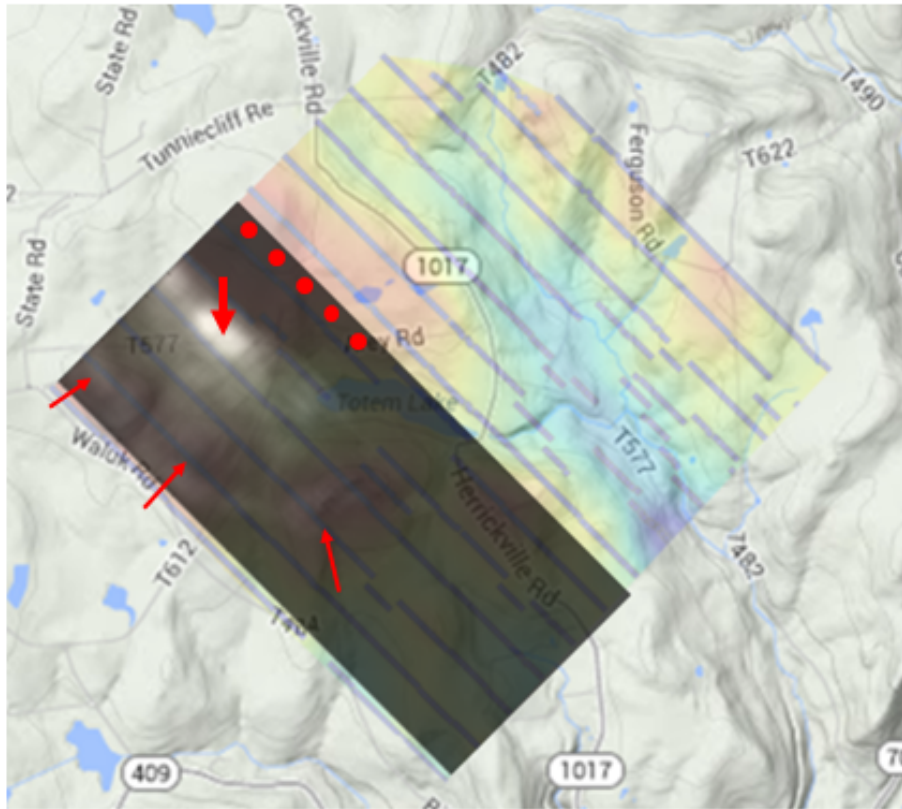


Figure 5.19: Migrated image with topographic overlay.

In this example, it seems surface reflections are dominated by topography. Strong reflectivity exists where the hill meets the valley. There is also evidence of reflections from hills further away (indicated with arrows).

These results are preliminary for a number of reasons. First, a small selection of shots and receivers were used. Second, further work is needed to determine which direction the reflections actually came from. It has been assumed that reflections came from the southwest. However, the complete opposite direction is also a valid direction to consider. Finally, the third dimension, depth, is not investigated. The reflections have not been constrained adequately to consider the reflectivity image as a function of wavelength.

5.7 Example: Field, Arctic Slope, Alaska

In 1923 President Harding designated the western half of the Arctic Slope of Alaska for the U.S. Navy as Naval Petroleum Reserve Number 4. The area was re-designated the National Petroleum Reserve, Alaska (NPRa) in 1976. Between 1974 and 1981 more than 22,500 km of 2D seismic data was acquired across the Reserve. The Uukok Carihu/Grizzly Special Management Area (USMA) in the southwestern part of the NPRa was found to have only a small amount of economically recoverable oil and gas. Figure 5.20 shows the location of NPRa in Alaska as well as the section designated as the USMA.

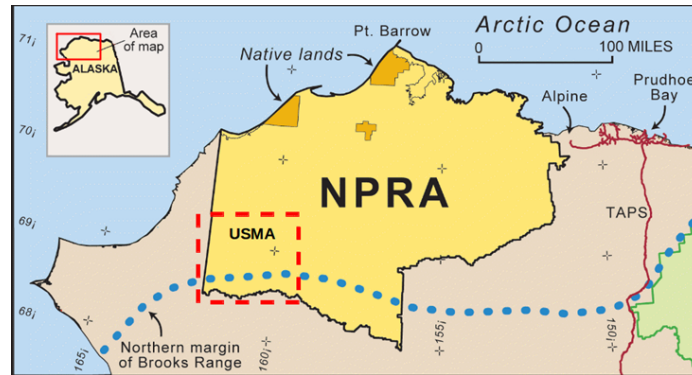


Figure 5.20

Figure 5.21: Map of the Arctic Slope, NPRa, Alaska. The section containing the seismic line of interest (USMA) is highlighted by the red-dashed line.

The area is interesting for investigation due to the numerous geologic structures in the area that could reflect surface-waves. There are many anticlines, synclines, and overturned beds in the area, some of which extend deep into the subsurface (Bascle and Foland, 1992). Figure 5.22 shows a detailed view of the USMA, which is also highlighted with a red dashed-line in Figure 5.20. The seismic line selected crosses directly over an anticline.

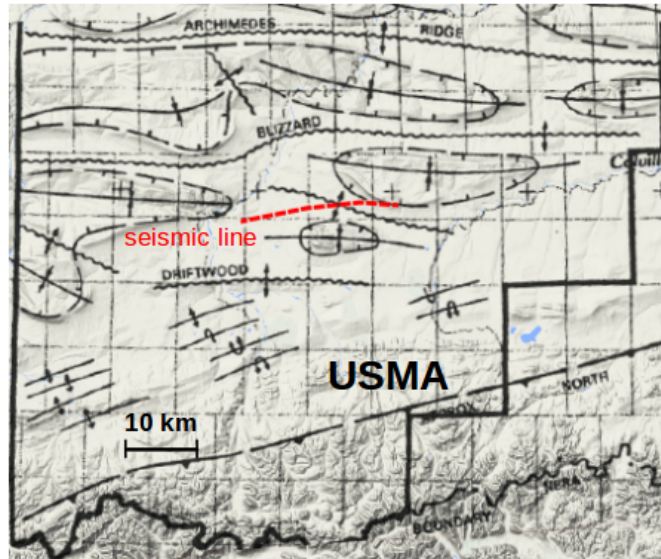


Figure 5.22

Figure 5.23: Map of the USMA in the Arctic Slope, NPRA, Alaska. Seismic line of interest is indicated with a red dashed line.

Survey geometry was designed with reflection processing in mind. The roll-along seismic survey was shot from west to east with 96 channels active for every shot. Shot spacing was 134 m and receiver spacing was 33.5 m. The shot-type was dynamite at a depth of 67 m.

A single shot is selected for processing due to the fact that surface-wave reflections were identifiable in the data. Figure 5.24a shows a close-up view of the seismic line in green and the selected shot in red. The seismic line crosses three rivers in this area. For this particular shot, no receivers cross the anticline, although the anticline is only 2000 m to the north of the survey line.

Figure 5.24b shows the shot record selected for study. The direct surface-wave is clearly visible as a high-amplitude, dispersive wave. Near the direct surface-wave several back-reflections can be seen propagating in the opposite direction. A low-frequency reflected surface-wave is also observed at a much later time in the record.

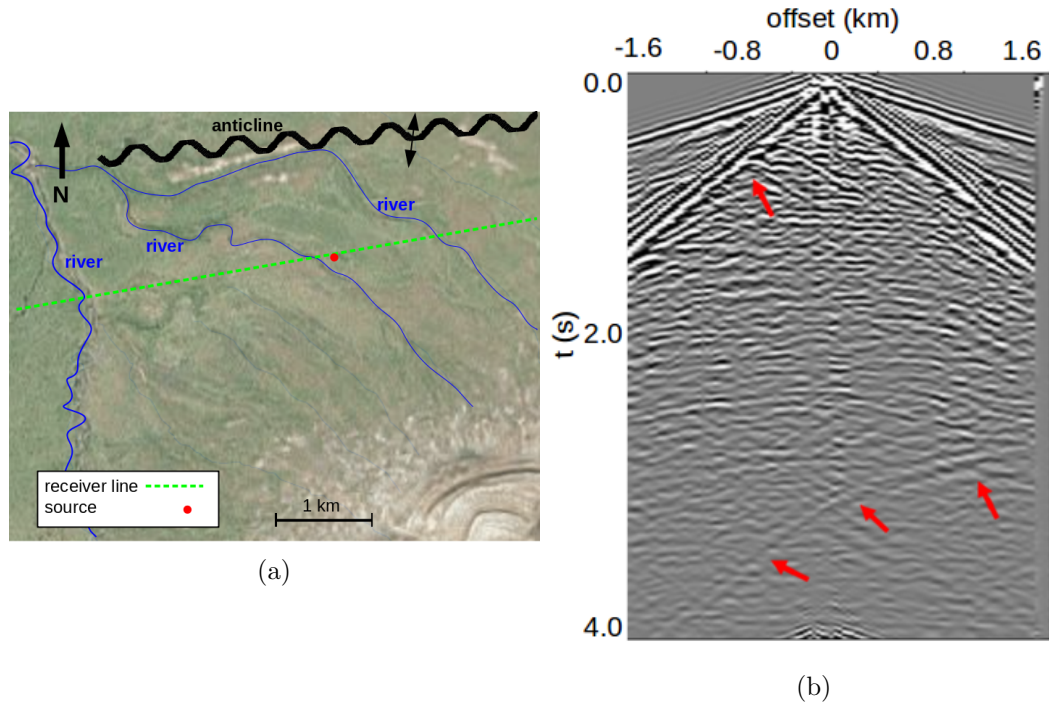


Figure 5.24: (a) Location of shot selected for migration, and (b) shot record with surface-wave reflections indicated by red arrows.

Unfortunately, it is not possible to quantitatively determine the direction from which the surface-wave reflections originated. The direction of migration was instead based on a migrated test image in both directions, and then a visual comparison with features visible on the map. For example, the migrated image of back-reflections near the direct surface wave matched the path of the river well, therefore, the south direction was determined to be the correct direction in that case. The surface-wave reflections at a later time; however, matched well with the anticline to the north when migrated. Figure 5.25 shows both reflections migrated towards their assumed originating locations.

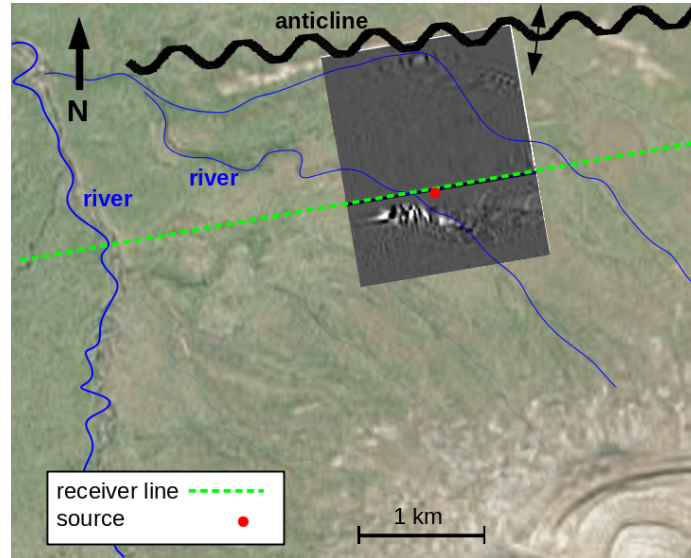


Figure 5.25: Migrated image superimposed on map.

Manually choosing the direction for migrating reflections is too tedious for more than a simple study; especially when considering multiple shots. As we shall see in the next section, at least two parallel lines are needed to determine the direction of reflections.

5.8 Dual-receiver lines and wavefield separation

There is a fundamental problem of indeterminable directionality associated with recording surface-wave reflections using a single receiver line with single component receivers. A simple example of the problem is illustrated in Figure 5.26a. Given a single receiver line, the reflection will look identical whether it propagated from the north or propagated from the south.

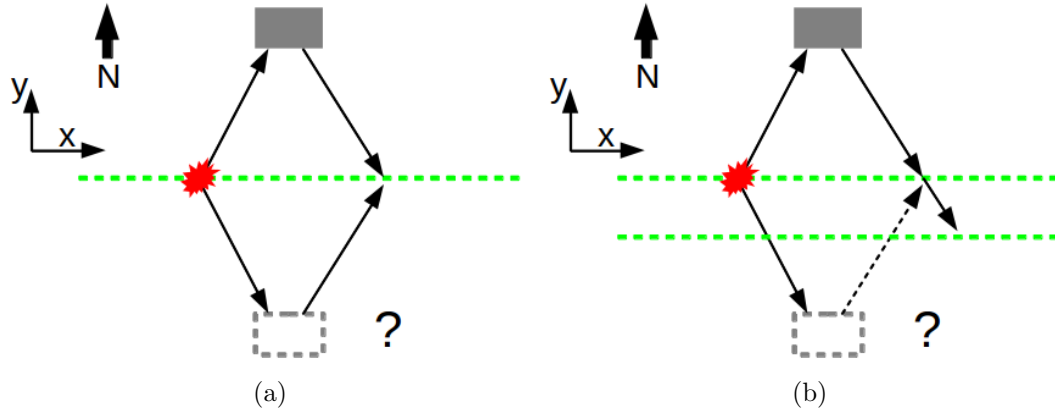


Figure 5.26: Comparison of survey geometries given a reflection from the north. (a) Data collected from a single receiver line does not indicate whether the reflection originated from the north or south. (b) Two receiver lines can be used to determine the direction of the reflection.

Migration can be performed assuming that the reflection originated from either the north or south side of the receiver line. Each image will be equally well resolved and equally valid as far as the method is concerned. Unfortunately, only one assumption, regarding which side the reflector exists on, is correct.

There are two solutions to the problem of unknown reflection directionality. One solution is to use multi-component receivers. The lateral direction in which the surface-wave is traveling could be determined from the x and y component of the receivers. The other solution is to add dimensionality to the geometry of the survey. Using two parallel receiver lines, Figure 5.26b, for each shot is the most basic way to add dimensionality to the survey. With two parallel receiver lines the wavefield can be separated into north-going and south-going components. This type of separation is the lateral analog to up/down separation introduced by Sonneland and Berg (1985).

5.8.1 Theory

We assume that the total wavefield, in the Fourier domain, for any particular y_i position, $\psi(k_x, y_i, \omega)$, is comprised of a north-going wavefield, $\psi_N(k_x, y_i, \omega)$, traveling in the $+y$ direction and a south-going wavefield, $\psi_S(k_x, y_i, \omega)$, traveling in the $-y$ direction,

$$\psi(k_x, y_i, \omega) = \psi_N(k_x, y_i, \omega) + \psi_S(k_x, y_i, \omega), \quad (5.8)$$

or written more simply,

$$\psi(y_i) = \psi_N(y_i) + \psi_S(y_i). \quad (5.9)$$

By using wavefield extrapolation the north-going component from the southern receiver line, $\psi_N(y_2)$, is moved to the northern receiver line, at y_1 , by,

$$\psi_N(y_1) = P_N(y_1, y_2)\psi_N(y_2), \quad (5.10)$$

where $P_N(y_1, y_2)$ is the extrapolation term needed to shift the wavefield from the southern receiver, y_2 , line to the northern receiver line y_1 ,

$$P_N(y_1, y_2) = e^{-i\sqrt{k^2 - k_x^2}\Delta y}, \quad (5.11)$$

where,

$$\Delta y = y_1 - y_2, \quad (5.12)$$

and wavenumbers, k and k_x , are assumed to be a function of frequency and phase-velocity, $c(\omega)$, of the surface wave,

$$k^2 = k_x^2 + k_y^2 = \left(\frac{\omega}{c(\omega)} \right)^2. \quad (5.13)$$

It is important to point out that in practice the north-going component has the south-going component superimposed on it. Applying equation 5.10 to move the wavefield recorded on the southern line to the northern line, will correctly move the north-going component to the north but will also incorrectly move the south-going component to the north.

To move the south-going component from the southern receiver line, $\psi_S(y_2)$, to the northern receiver line, at y_1 , a slightly modified extrapolation term, $P_S(y_1, y_2)$, is applied,

$$\psi_S(y_1) = P_S(y_1, y_2)\psi_S(y_2), \quad (5.14)$$

where,

$$P_S(y_1, y_2) = e^{i\sqrt{k^2 - k_x^2}\Delta y}. \quad (5.15)$$

A deconvolution can now be devised which moves the appropriate component and suppresses the incorrectly moved component. Substituting equations 5.10 and 5.14 into equation 5.9 gives the separated wavefield at the southern receiver line for the north-going and south-going component,

$$\psi_N(y_2) = \frac{P_S(y_1, y_2)\psi(y_2) - \psi(y_1)}{P_S(y_1, y_2) - P_N(y_1, y_2)}, \quad (5.16)$$

and,

$$\psi_S(y_2) = \frac{\psi(y_1) - P_N(y_1, y_2)\psi(y_2)}{P_S(y_1, y_2) - P_N(y_1, y_2)} \quad (5.17)$$

5.8.2 Example: Synthetic

The equation above is tested using a synthetic model with four, rectangular, high-velocity anomalies. The background velocity is vertically stratified, as is often the case in the near-

surface. The anomalies are essentially vertical towers placed in a stratified model, Figure 5.27a.

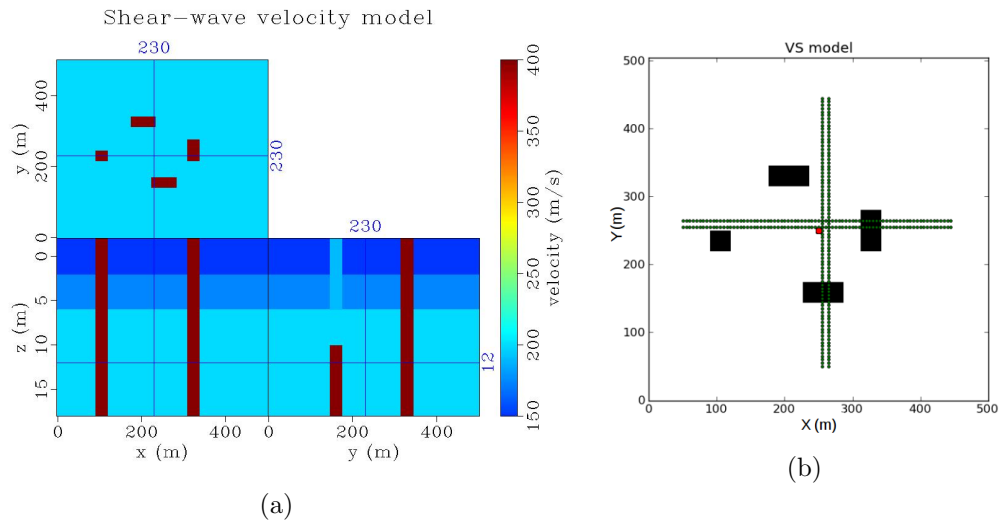


Figure 5.27: (a) Shear-wave velocity model used for testing wavefield separation. (b) Survey geometry plotted on map view of anomaly locations in shear-wave velocity model.

The survey geometry is a modified cross-spread. For each source, four receiver lines are active. Two parallel lines run west-to-east and two parallel lines run south-to-north. The source is placed at the center of the spread, Figure 5.27b. Vertical component receivers are placed at the surface with an inline spacing of 5 m. The spacing between receiver lines is 10 m.

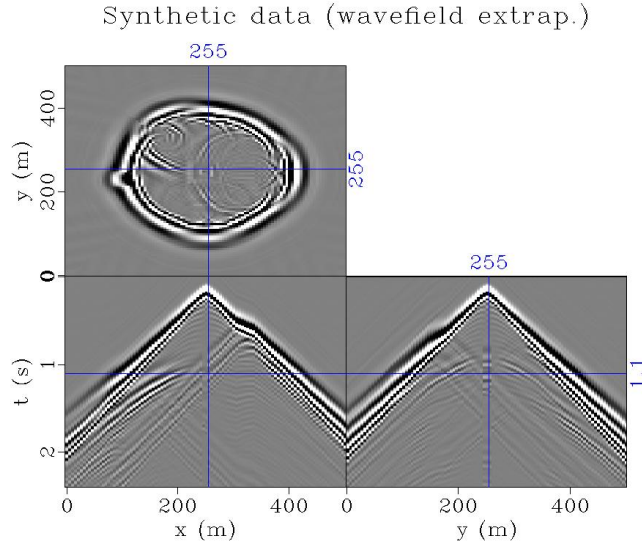


Figure 5.28: Surface-waves modeled using the split-step phase-shift method. Blue lines indicate location of lateral slices through the data-cube.

Both the outgoing and incoming surface-wave are modeled using the split-step phase-shift method. The outgoing wave uses a Ricker source wavelet with a central frequency of 10Hz. Data is modeled in four directions (east, west, south, and north) and then merged together. Figure 5.28 shows the data-cube generated by the split-step method. The top left panel shows a time-slice of the wavefield while the bottom frames show lateral-slices.

Data extracted at the receiver lines which run east-to-west is shown in Figure 5.29. The two records look nearly identical; however, there are distinguishing features between the two. The source is nearer to the southern line; and therefore, a delayed origin-time is observed on the northern line. It is difficult to discern, but surface-wave reflections inside the surface-wave cone also arrive at slightly different times.

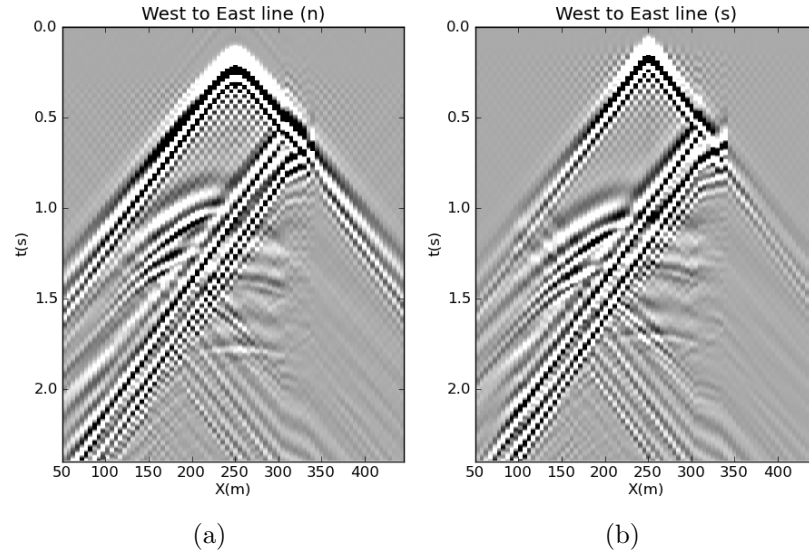


Figure 5.29: Comparison of receiver lines: (a) surface wave record at northern, east-to-west running receiver line, and (b) surface wave record at northern, east-to-west running receiver line.

There are two surface reflections that are superimposed within the surface-wave cone. The reflections originate from the anomalies directly to the north and south of the lines. The back-reflections originating from the direct-surface wave are due to the anomalies along the line to the east and to the west.

The wavefield separation method assumes that the wavefield to be separated is traveling, more or less, back towards the source, perpendicular to the lines. Therefore, prior to wavefield separation, the direct-surface wave and reflected surface-waves in the inline direction are removed. Figures 5.30a and 5.30b shows the result of filtering all but the reflected surface waves originating from the north side and south side of the east-west running lines.

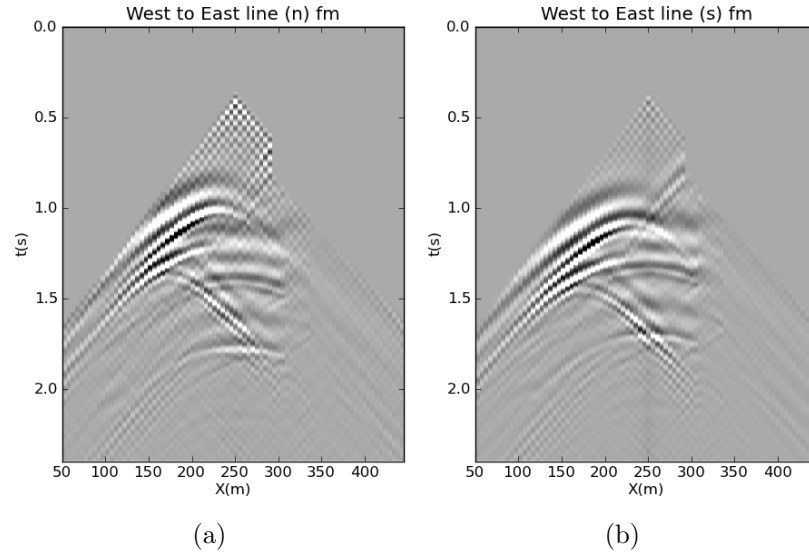


Figure 5.30: (a) Filtered, reflected surface-waves at northern, east-to-west running receiver line. (b) Filtered, reflected surface waves at southern, east-to-west running receiver line.

Even with only two surface-wave reflections present in record the wavefield is visually complicated. The complicated wavefield is due, in part, to the dispersive nature of the surface-wave. We can apply the wavefield separation modified for surface-waves, equations 5.16 and 5.17, to determine the south-going wavefield, Figure 5.31a and the north-going wavefield, Figure 5.31b.

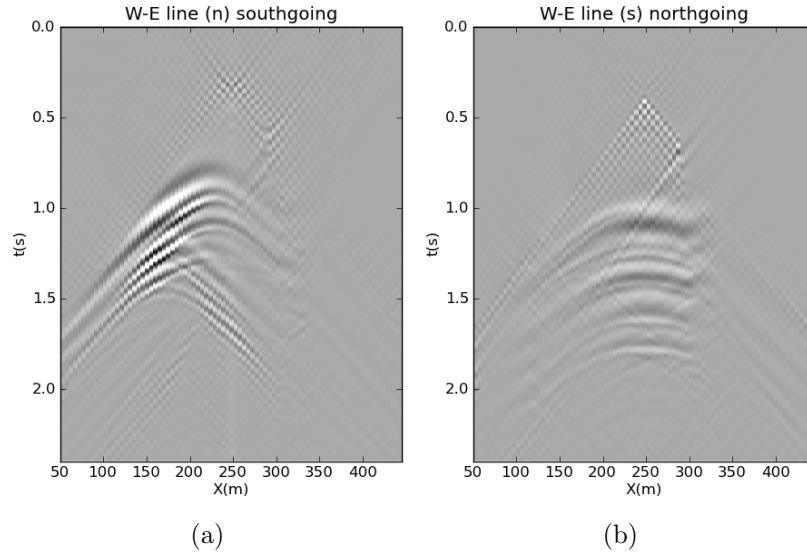


Figure 5.31: Comparison of filtered wavfields: (a) south-going wavefield, and (b) north-going wavefield.

The same process applied to separate the south-going and north-going wavefields can be considered for the east-going and west-going wavefields if lines run north-to-south as well. After all directions have been accounted for, each surface-wave reflection can be migrated to its respective origin location. Figure 5.32 shows the final migrated image.

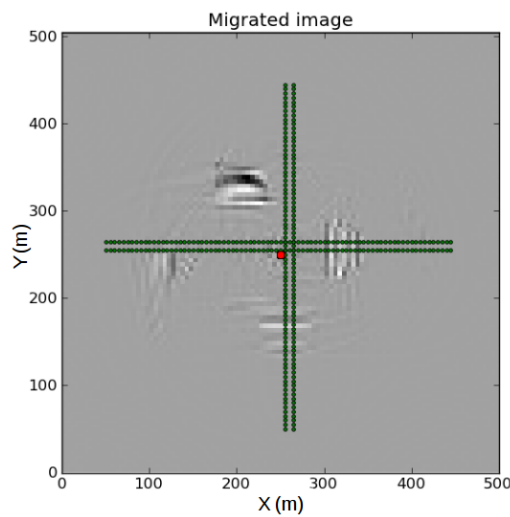


Figure 5.32: Final migrated image after wavefield separations.

5.9 Multi-receiver line migration

An alternative to relying on a deconvolution-type algorithm to separate wavefields is to add more lines and allow the incorrectly migrated wavefields to stack out. A diagram of the multi-receiver line survey geometry is shown in Figure 5.33. Given the geometry in the diagram, the incorrectly positioned reflector will be stacked out by a 4:1 factor.

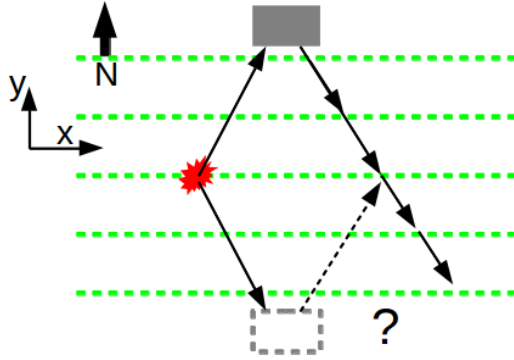


Figure 5.33: Multi-line survey geometry. Additional arrivals stack out wrongly positioned reflectors.

5.9.1 Theory

Consider again the deconvolution imaging condition from equation 5.7. The imaging condition consists of deconvolution at every image location of the recorded receiver wavefield, $\psi_r(x, y, \omega)$, by the modeled source wavefield, $\psi_s(x, y, \omega)$. For this formulation, all lines are included in the volume during migration, essentially providing a summed image. The migrated image, $R(x, y, \omega)$, is represented in the Fourier domain as,

$$R(x, y, \omega) = \sum_{shots} \left[\sum_{lines} \sum_{\omega} \frac{\overline{\psi_s(x, y, \omega)^{+y}} \psi_r(x, y, \omega)^{+y}}{\psi_s(x, y, \omega)^{+y} \psi_s(x, y, \omega)^{+y} + \epsilon^2} - \sum_{lines} \sum_{\omega} \frac{\overline{\psi_s(x, y, \omega)^{-y}} \psi_r(x, y, \omega)^{-y}}{\psi_s(x, y, \omega)^{-y} \psi_s(x, y, \omega)^{-y} + \epsilon^2} \right] \quad (5.18)$$

where the final image is a result of summation over shots, receiver lines, and frequency, ω . We note complex conjugate with the overbar, and the damping factor with epsilon, ϵ .

5.9.2 Example: Synthetic

This imaging condition is tested with a survey geometry consisting of 14 parallel lines throughout model. Figure 5.34 shows the map view of the model with the geometry of the receivers.

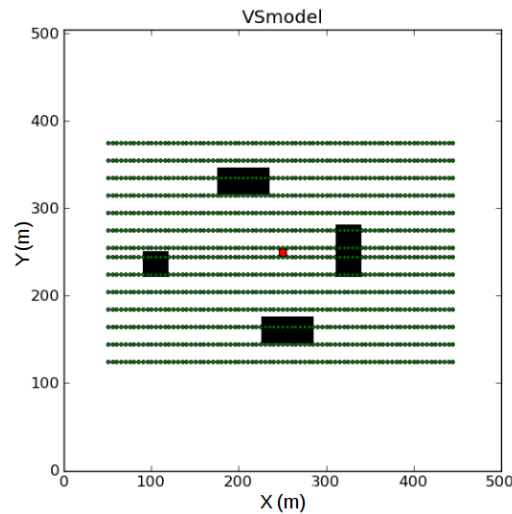


Figure 5.34: Survey geometry plotted on map view of anomaly locations in shear-wave velocity model.

Only the direct surface-wave needs to be removed prior to migration. The reflections originating near the inline direction will be handled correctly by the migration. Receiver lines are inserted into the 3D data-cube to represent the receiver wavefield. All lines are migrated simultaneously.

Figure 5.35 shows a map view of the migrated lateral-image. The complex dispersed wavefield of back-reflections from one shot are migrated to the correct spatial position. The reflections defining the structures are compressed because dispersion was accounted for in the wavefield extrapolation for both the source and receiver wavefield. In addition to

improving the resolution of the image, the deconvolution imaging condition also provided an estimate of reflectivity.

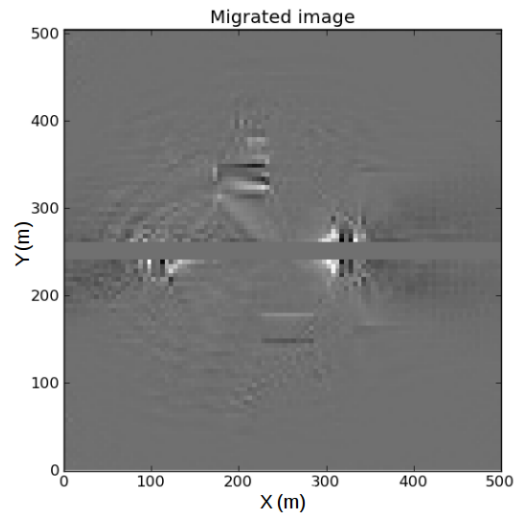


Figure 5.35: Migrated image given a multi-line geometry.

The migrated image is slightly better when compared to the cross-spread migration in Figure 5.32. The improved result is somewhat surprising because although we only migrated in the north-south direction we still resolved inline reflections. The result suggests that the previous workflow processing 2D lines, in chapter 3, can be improved by back propagating inline reflections.

5.9.3 Example: Multi-shot finite-difference

We return to the 3D shear-wave velocity model containing four structures shown in chapter 4. Figure 5.36a shows three slices through the model. The background velocity is represented by three vertically stratified layers, each 4 m thick. Top, middle, and bottom layers are have a shear-wave velocity of 150 m/s, 175 m/s, and 200 m/s respectively. Each structure is bounded by a vertical fault and has a shear-wave velocity of 400 m/s. The structure to the north does not reach the surface, but terminates at a depth of 12 m.

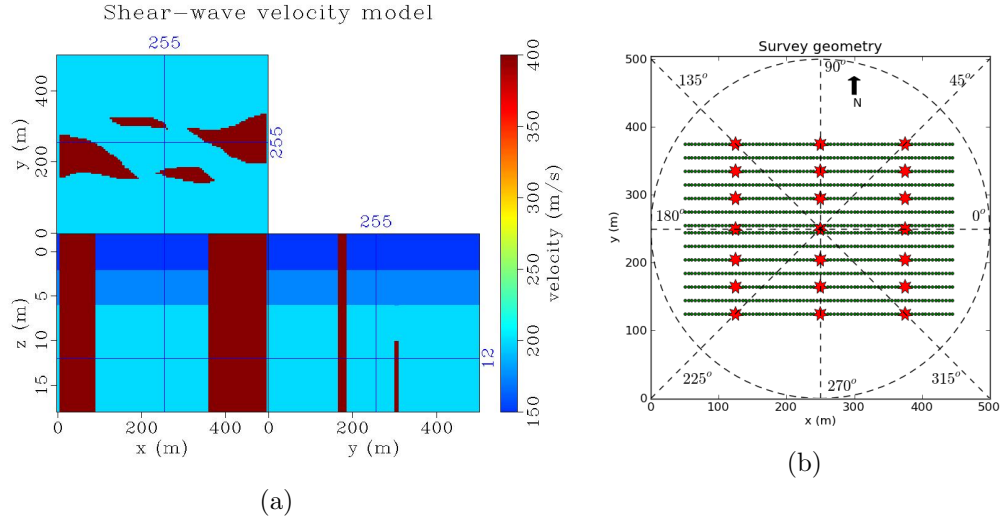


Figure 5.36: (a) Shear-wave velocity model used for generation of synthetic data and migration. Depth slice is shown in top left frame. Lateral slice in the x -direction and y -direction indicated with blue-line on depth slice, and lateral slices shown in bottom left and right frame. (b) Geometry of synthetic survey. Source locations indicated by red stars and receiver locations indicated by green markers. Polar coordinates shown as reference for migration direction and wavefield construction.

The compressional-wave velocity model is based on a constant V_P/V_S value of 2. Density is assumed to be a constant value of 2200 kg/m^3 . Note that only the shallow part of the model is shown in Figure 5.36a. For purposes of visual clarity, the entire extent of the model used for generating synthetic data using finite difference is not shown.

A fixed spread of 1120 vertical component receivers are placed at the surface at a 5 m spacing in the x -direction and a 20 m spacing the y -direction, with the exception of a 10 m spacing around $y=250$ m. The arrangement results in 14 receiver lines shown in Figure 5.36b. A total of 21 shots are simulated across the receiver lines with an interval of 125 m in the x -direction and 40 m in the y -direction. Sources are placed just below the surface to excite surface-waves.

Finite difference

Synthetic data is modeled using an elastic finite difference. We use a Ricker wavelet with a central frequency of 10 Hz for all sources. Figure 5.37 shows the resultant data-cube for a source at the location: $y=250$ m, $x=250$ m. The surface-wave is the highest amplitude event seen in the depth slice. The velocity contrast of the four structures, and dispersion create the complicated wavefield.

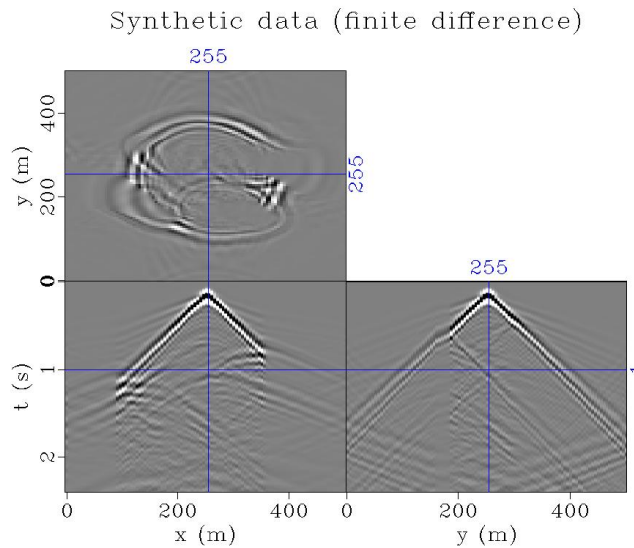


Figure 5.37: Synthetic data generated by finite difference. Time slice is shown in top left frame. The lateral slice in the x -direction and y -direction is indicated with blue-line on time slice, and lateral slices shown in bottom left and right frame.

To simulate the survey described above, data is extrapolated from the cube at the receiver positions. Figures 5.38a and 5.38b show receiver lines extracted near the source, $y=255$ m and $y=245$ m. The two receiver lines are similar in appearance.

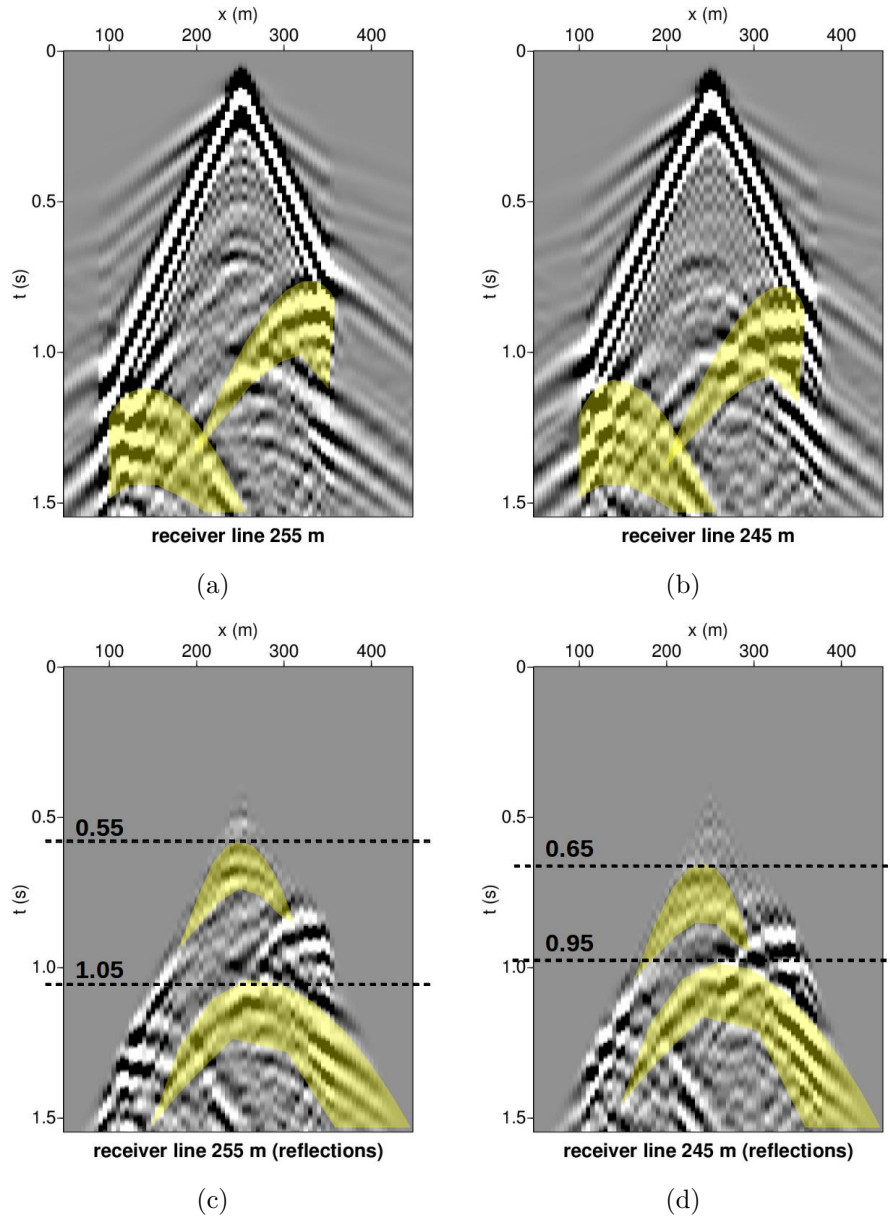


Figure 5.38: Receiver lines for source at: $x=250, y=250$ m. (a) Receiver line located at $y=255$ m and (b) receiver line located at $y=245$ m. Reflections originating from near the direct surface-wave are highlighted in yellow. (c) Receiver line located at $y=255$ m and (d) receiver line located at $y=245$ m. Reflections originating from north and south structures are highlighted in yellow.

The direct P-wave and direct surface-waves exhibit a sudden change in dip at both edges of the line. The high-velocity zones coincide with the east and west structures in the model. Surface-wave back-reflections originate from the time near to the sudden change in dip.

Two more reflections occur well within the cone of direct surface-waves. To clearly inspect the two reflections, direct surface-waves for lines $y=255$ m and $y=245$ m is removed and shown in Figure 5.38c and 5.38d. The reflections are highlighted and the arrival times are noted.

Reflection direction is confirmed by comparing line $y=245$ m with $y=255$ m. The earlier reflection arrives at a earlier time in the line to the north of the source, $y=255$ m. The later reflection arrives at a later time in the line to the north of the source, $y=255$ m. Both these observations are consistent with the interpretation that the reflection earlier in time is from the northern structure and the reflection later in time is from the southern structure.

5.9.4 Migration

The same velocity model used for finite difference is used to migrate the data and create a source wavefield. The 2D elastic models (V_P , V_S , and ρ) are used with the propagator matrix method to determine a 3D surface-wave phase-velocity model. The phase-velocity model is used to back-propagate the prepped receiver wavefield and extrapolate the outgoing wave from the source.

The receiver wavefield recorded at the lines is prepared for migration by first removing the direct arrival of surface-waves, as seen in Figures 5.38c and 5.38d. For back-propagation of the receiver wavefield, one continuation step is oriented azimuthally perpendicular to the line. We use the split-step algorithm to account for velocity heterogeneity parallel to the line (across x) and perpendicular to the line (across y).

To find a wavelet for the outgoing wave from the source, we stack the near offsets from the synthetic data generated by finite difference. A one-way extrapolation is used to

model outgoing surface-wave in the east, west, north, and south direction. The results are combined with an opening angle of 45° each, as shown in Figure 5.39a.

Figure 5.39b shows the data-cube for outgoing surface-waves. Compared to the synthetic data in Figure 5.37 the image is simpler. Only direct surface-waves are present in the data generated by wavefield extrapolation. The direct surface-wave generated by both methods is; however, very similar. Interestingly, although only the direct wave is modeled, the substantial amount of velocity variation on the eastern side of the model creates a reflection-type event.

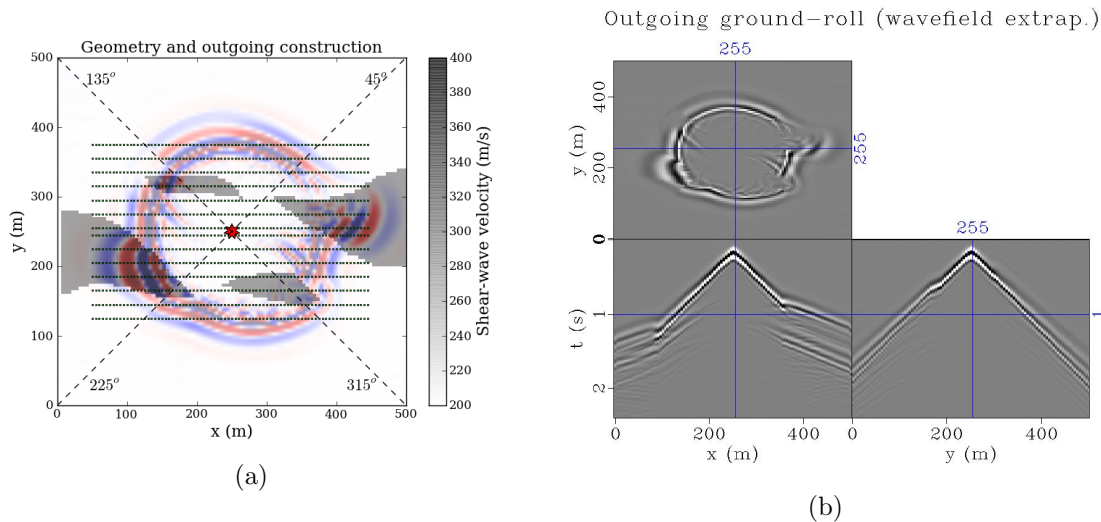


Figure 5.39: (a) Outgoing surface-waves modeled using the split-step method in four directions. Survey geometry and angles used for wavefield reconstruction shown. Shear-wave velocity model is in the background. (b) Surface-waves modeled using the split-step method shown as a 3D data-cube.

At this stage, all data needed for the imaging condition is prepared: phase velocity model, reflected data at the receivers, and the forward modeled source wavelet. Receiver lines are inserted into the 3D data-cube to represent the receiver wave field. All lines are migrated simultaneously.

Figure 5.40a shows a single shot at location $y=250$ m, $x=250$ m migrated to produce a map-view lateral-image. The complex dispersed wavefield of back-reflections from one

shot are migrated to the correct spatial position. The reflections defining the structures are compressed because dispersion was accounted for in the wavefield extrapolation for both the source and receiver wavefield. In addition to improving the resolution of the image, the deconvolution imaging condition also proved an estimate of reflectivity.

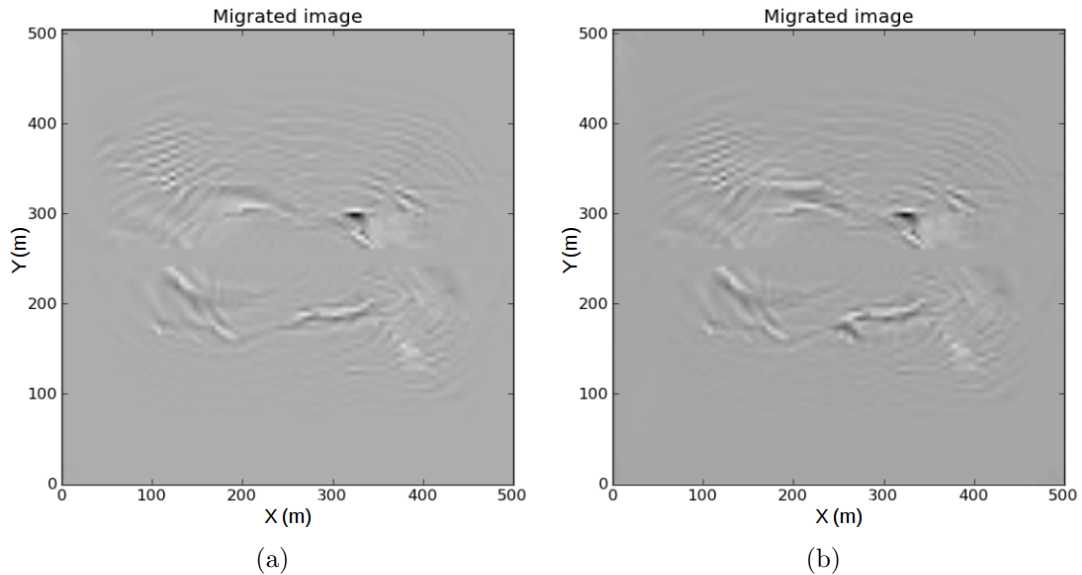


Figure 5.40: (a) Migrated image from one shot at $y=250$ m, $y=250$ m (b) Migrated image from using all shots.

Note that the structures resolved by migrating one shot are not mirrored on either the north or south side. By including multiple lines in the migration mispositioned reflections are effectively "stacked out". The structures themselves are correctly placed with a limited amount of artifacts. Figure 5.40b shows that using multiple shots improves the image further. Shots distributed throughout the image space help illuminate sections of the model which are poorly illuminated by a single shot.

Because surface-waves are dispersive and the dispersion is a function of properties at depth, the frequency content provides information about the depth of a structure.

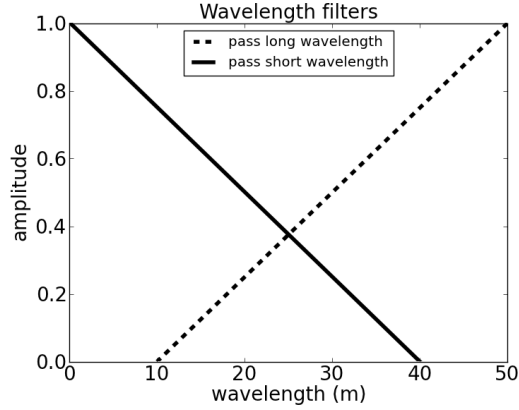


Figure 5.41: Wavelength filters for the migrated image image. Zero amplitude corresponds to complete signal rejection and an amplitude of one corresponds to a full pass.

Recall that the structure to the north does not extend to the surface but instead terminates at depth. Surface-waves are sensitive to shear-wave properties at approximately one-half its own wavelength. We test the sensitivity of our method to determine the depth of an object by filtering the spatial frequency of an image.

Figure 5.41 shows the filters applied to the migrated image. To be consistent the filters are applied in the same direction as the migration was applied, $(+y, -y)$.

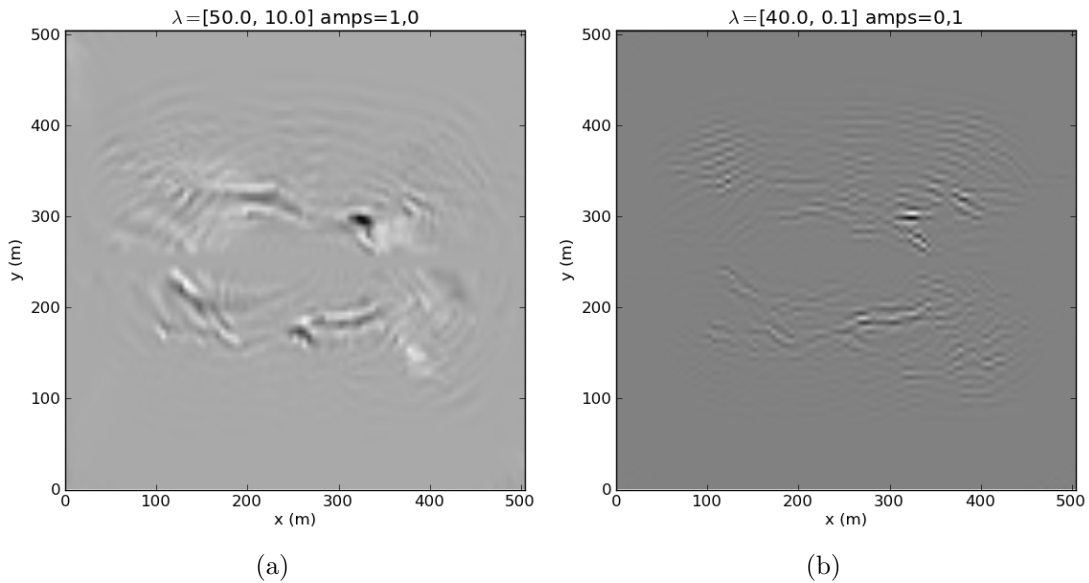


Figure 5.42: (a) High-cut applied to spatial frequency of migrated image. (b) Low-cut applied to spatial frequency of migrated image.

Figure 5.42a shows the result of applying a spatial-frequency high-cut to the image. All four structures are easily identified in a lower resolution image. Figure 5.42b shows the result of applying a spatial-frequency low-cut to the image. The structures to the south and east are still visible; however the north structure is diminished in amplitude. This is a consistent finding with the model. A reflection from a structure at depth does not include high frequencies or short wavelengths.

5.10 Summary

We directly account for sharp lateral change by processing surface-wave reflections. By leveraging the frequency content of dispersive surface-waves we add the dimension of depth to imaging at the surface. Of the three imaging conditions tested (time curve, correlation, and deconvolution), deconvolution provides the potential to remove source effects and recover reflectivity. Deconvolution is not, however, as stable as correlation. As shown for the dataset with physical model, accurately attaining the source wavelet is no easy task. We arrived at slightly better results using a source wavelet extracted from the near offsets of the record.

In the field, our imaging process identified topographical features as the cause of surface-wave reflections. All our field experiments consisted of a single line receivers. The drawback of using a single line is that the reflection may arrive from either side. At a minimum, two receiver lines are needed to determine the wavefield direction. Adding multiple lines of receivers greatly improves imaging.

Our results indicate that estimated reflectivity can be used as an attribute in highlighting the location of faulting, making it a useful tool for interpretation. Given an accurate phase-

velocity model and an accurate source, the deconvolution imaging condition resolves sharp discontinuities at high resolution and provides an estimate of reflectivity.

Chapter 6

Estimating shear-wave velocity from reflectivity

6.1 Overview

Given that the phase and polarity of the back-reflections are accurate, an inversion can be designed to update an existing surface-wave phase-velocity model in the lateral direction. Although the focus of this chapter is on updating the phase-velocity model, the overall process is as follows: extract reflectivity and find the phase-velocity model (chapter 3), update the phase-velocity with extracted reflectivity, and finally invert phase-velocity to the shear-wave velocity model. The overall flow of estimating velocity with respect to previously covered processing is shown Figure 6.1

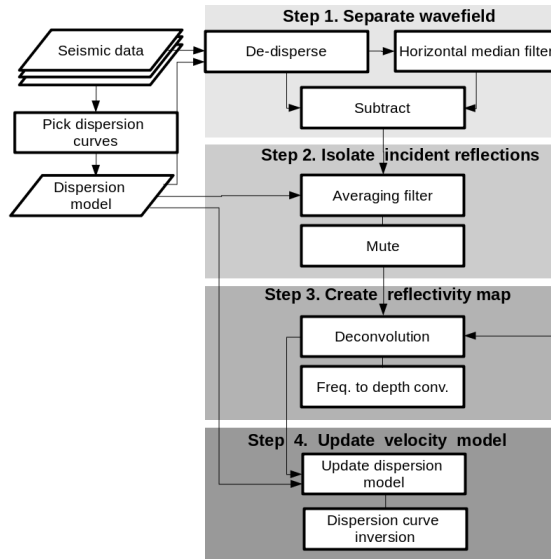


Figure 6.1: Overall method of the velocity estimation.

At minimum, a rough phase-velocity model is required to determine reflectivity. The phase-velocity model is used both to de-disperse the outgoing wave in step 1 and to enhance the incoming wavefield in step 2. After reflectivity has been estimated in step 3 a starting phase-velocity model is also needed to continue the process.

Our suggested flow, therefore, enhances the current standard flow for determining shear-wave velocity from phase-velocities. Figure 6.2 condenses our process in the context of existing methods. From seismic data, or more specifically multiple shots across a receiver line, we extract dispersion curves across many sections of the survey line. The result is a phase-velocity model, $c(\omega, x)$, which is a function of frequency, ω , and lateral space, x .

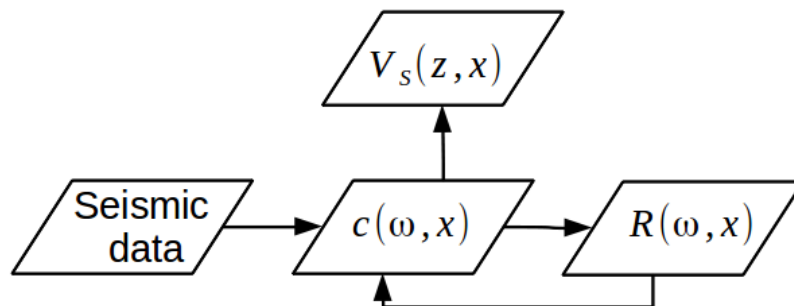


Figure 6.2: Overall method of the velocity estimation.

The standard processing route from the phase-velocity model is to invert phase-velocities at every point in the lateral direction to estimate shear-wave velocity, $V_S(z, x)$. Our processing flow estimates reflectivity, $R(\omega, x)$, (also a function of frequency and lateral space) which can be used to update the phase-velocities and attain a higher resolution shear-wave velocity model.

6.2 Theory

Several types of reflectivity maps (temporal, spectral, and depth-converted) have been generated in the previous step. We resume processing in step 4 using the spectral reflectivity map. If we assume that the polarity of the spectral reflectivity map is accurate, an inversion can be designed to update an existing surface-wave phase-velocity model. Although we will focus our description on updating the phase-velocity model, the overall process is as follows: extract reflectivity via the method described in the first three steps, determine the phase-velocity model, update the phase-velocity model with extracted reflectivity, and finally invert the phase-velocity model to the shear-wave velocity model.

We use synthetic data from a slightly more complex model (Figure 6.3a) to illustrate velocity model updates. Our shear-wave velocity model includes two examples of faults that have no surface expression (also known as blind faults). One blind fault is deep with large vertical slip, and the other blind fault is shallow with small vertical slip.

We generate synthetic data with SPECSEM2D. We simulate one shot on the left side of the model with a 25 Hz Ricker wavelet. The wavefield is recorded with vertical component receivers at a 1 m spacing across the extent of the model. Density and V_P/V_S are constant throughout the model at 2800 kg/m^3 and 2 respectively. Data is processed to create a surface-wave reflectivity image. As can be seen in the reflectivity map (Figure 6.3b), strong

reflection coefficients identify the location and depth of the faults in the shear-wave velocity model. The corresponding spectral reflectivity map (Figure 6.4a) is used for the velocity updates described below.

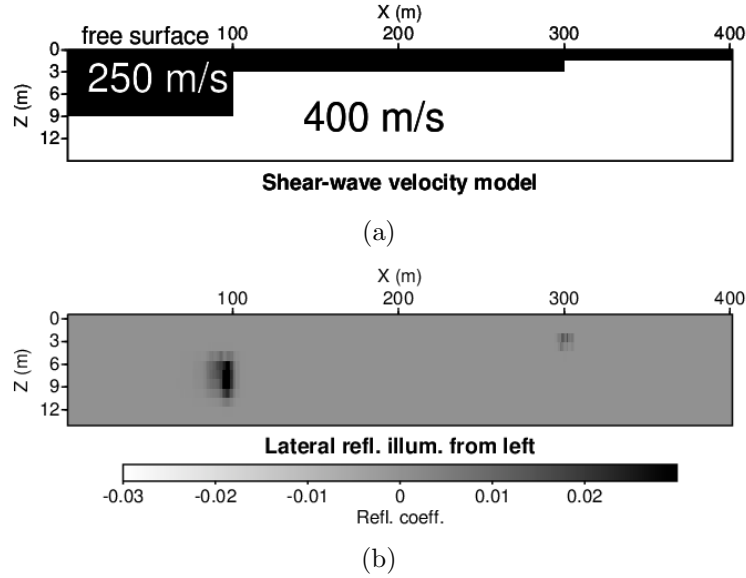


Figure 6.3: (a) Shear-wave velocity model used for illustrating velocity updates. (b) Spectral reflectivity map processed from data.

We attempt to update velocities using a technique analogous to iterative inversion, (?). We assume the deconvolution step has been successful in restoring the spectrum and our data is now a set of reflection coefficients, $R(\omega)$, at each source-receiver pair, j . We rearrange our plane-wave estimation for determining reflection coefficients within narrow frequency bands in equation 2.41 and solve for a velocity update, α , by a set of reflection coefficients,

$$\alpha = \frac{1 + R(\omega)_j}{1 - R(\omega)_j}, \quad (6.1)$$

where α is the update applied to derive the neighboring velocity, $c(\omega)$, at the source-receiver pair, $j + 1$,

$$c(\omega)_{j+1} = \alpha c(\omega)_j. \quad (6.2)$$

Each updated velocity is used with the reflection coefficient at the current source-receiver pair to derive the next velocity in an iterative manner. An initial starting velocity, representing the constant of integration, is needed to start the process. For our example, we start by windowing data near the source, extracting the dispersion curve from this window, and using this dispersion curve as a starting model.

Figure 6.4b shows the starting model used for our example. In combining negative and positive offsets of shots we have reversed polarity for the right-hand side of shots thereby choosing a left sided convention. We apply the velocity update from left to right. The iterative inversion process provides a first approximation to the phase-velocity model. After the iterative update the resultant phase-velocity model is spline-fit in the frequency domain at each location to ensure a smooth phase-velocity model along the frequency axis. Figure 6.4c shows the updated phase-velocity for our example after the trace inversion process and spline fit along frequency.

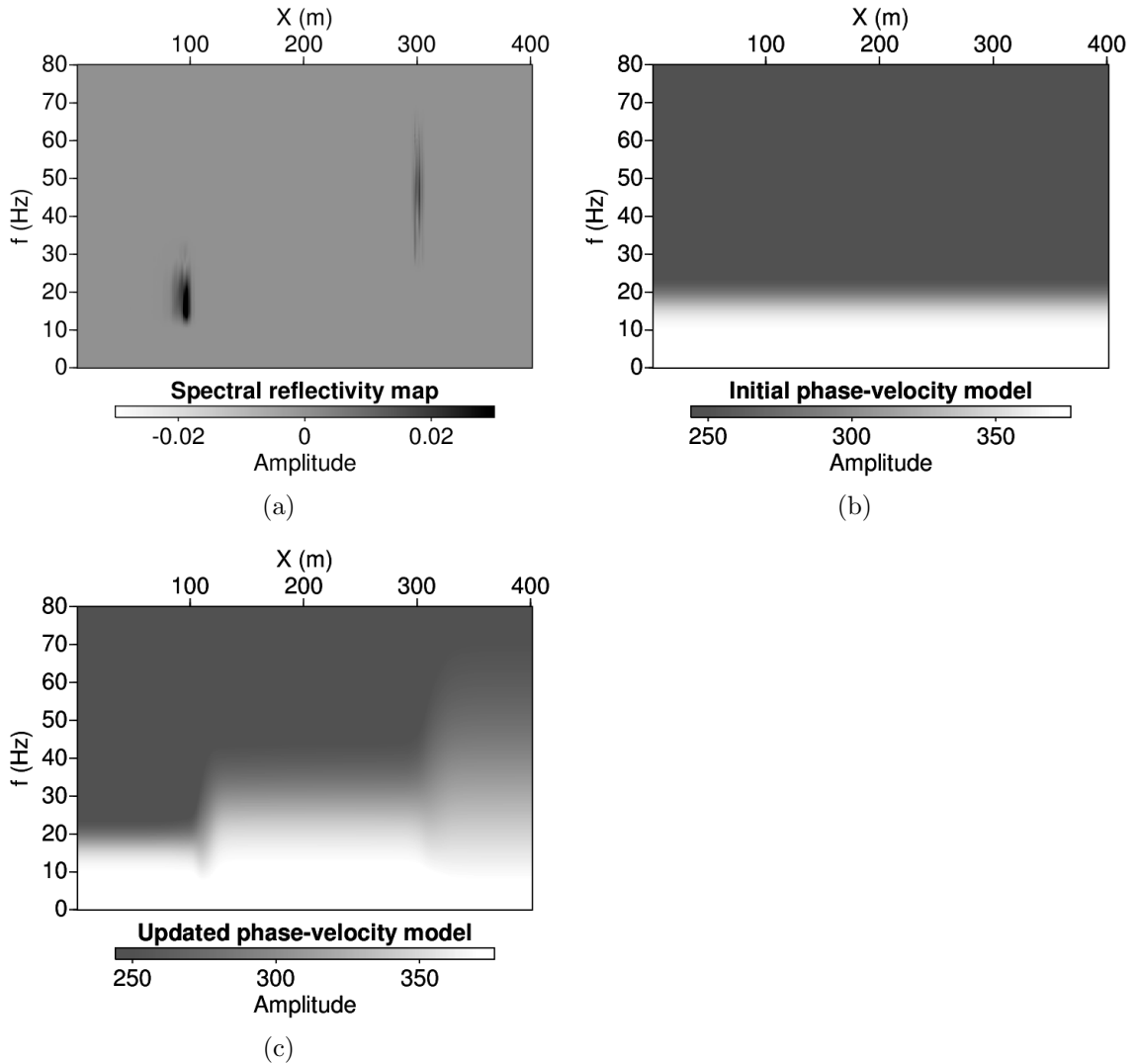


Figure 6.4: (a) Spectral reflectivity extracted from data. (b) Initial phase-velocity model and (c) updated phase-velocity model after iterative inversion and spline fit.

Once the updated phase-velocity model has been determined, we invert phase-velocity at each location for a shear-wave velocity model. Figure 6.5a shows the inverted shear wave velocity model for our synthetic double blind fault model. The fault with large vertical slip is well resolved. Although the lateral change across the fault with small vertical slip is obvious in the updated phase-velocity model, it is not as well resolved for the inverted shear-wave velocity model. The difference between the true model and updated inverted model (Figure 6.5b) shows that the overall structure of the model is a smoothed version

of the initial model. The reflectivity map (Figure 6.3b) remains helpful in determining the location of sharp lateral change.

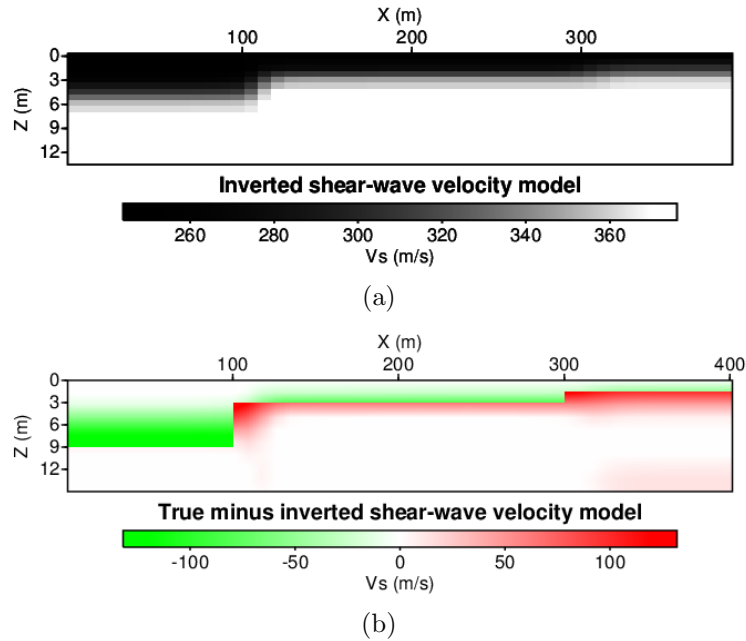


Figure 6.5: (a) Shear-wave velocity model inverted from updated phase-velocity model. (b) Difference between true and inverted shear-wave velocity model.

6.3 Reflected surface-wave processing vs. Direct surface-wave processing

Now that the process has been outlined for extracting reflectivity and updating the shear-wave velocity model with reflectivity, a comparison can be made between the shear-wave velocity model estimated through high resolution multichannel processing and the shear-wave velocity model updated using reflectivity. Multichannel methods of surface-wave analysis use the direct surface-wave. Effects observed in the direct wave are due to the averaged culmination of properties along the surface-wave path. Surface-wave reflections occur where there is sharp lateral change. Therefore, using reflections and reflectivity has the potential of resolving lateral boundaries.

Consider again the single blind fault model, Figure 6.6a, used in chapter 3. The result of high resolution multichannel processing and inversion was a somewhat smoothed model, Figure 6.6b.

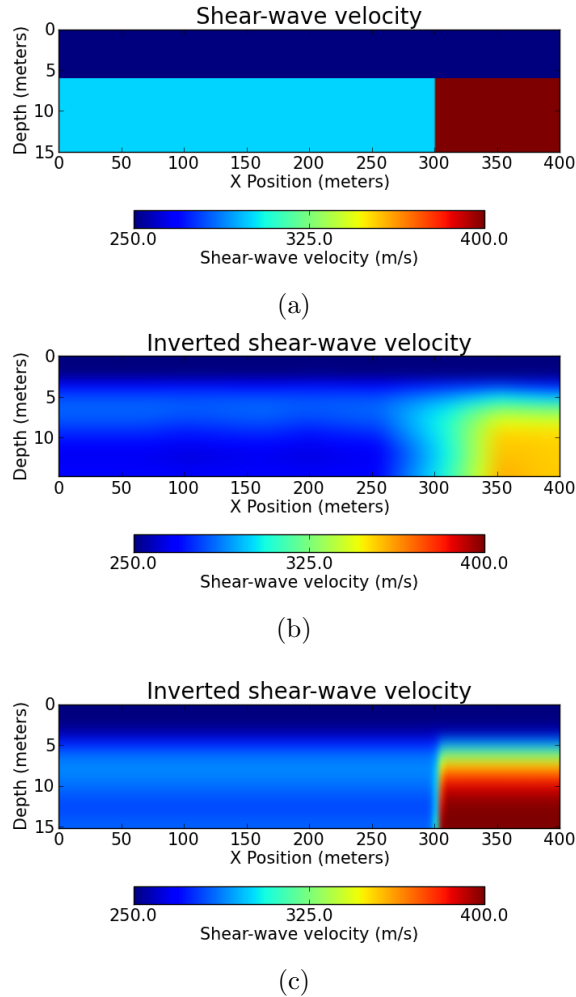


Figure 6.6: (a) True shear-wave velocity model, (b) shear-wave velocity model estimated by direct surface-wave processing, and (c) shear-wave velocity model estimated by reflected surface-wave processing.

Reflectivity is extracted from the surface wave and used to update the phase-velocity model. The phase-velocity model is then inverted for shear-wave velocity. The shear-wave velocity model estimated using reflectivity, Figure 6.6c, is substantially more resolved in the lateral direction than the model estimated using multi-channel processing.

6.4 Example: Field, Hockley 2D line

Seismic data collected across the Hockley fault near Houston, TX is used to test the velocity-update process. The survey was a 2D line recorded with 216 vertical-component geophones at 5 m spacing and vertical vibrator sources at the same spacing. A 12 second linear sweep from 10 to 150 Hz was used. Three types of processed data were compared:

1. traditional seismic image processed from reflections,
2. shear-wave velocity model (inverted from extracted dispersion curves) updated using reflectivity results.

The migrated image was independently processed in a previously published case study (Khan et al., 2013). The image has been converted to depth and marked where the main fault was previously identified, Figure 6.7. The survey was centered around a crack on the highway, indicating the surface expression of a prominent fault. The fault on the image is located at the zero mark on the horizontal axis. Red arrows indicate the location of faults noted at the surface.

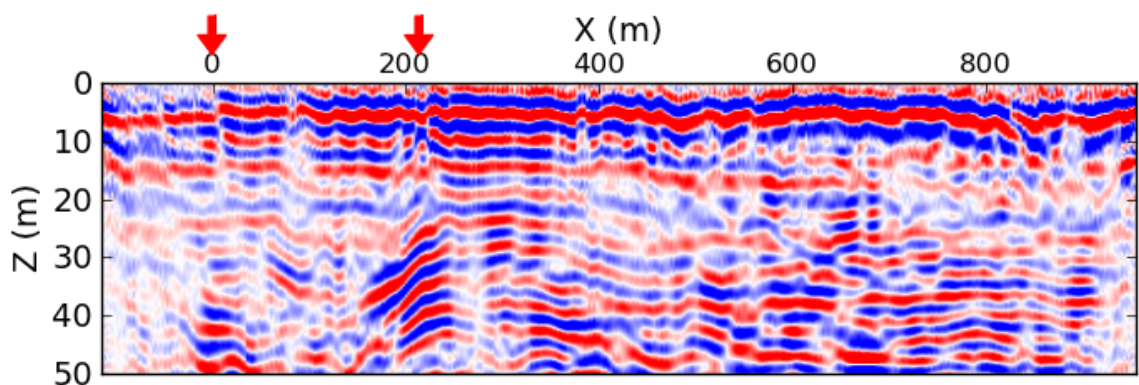
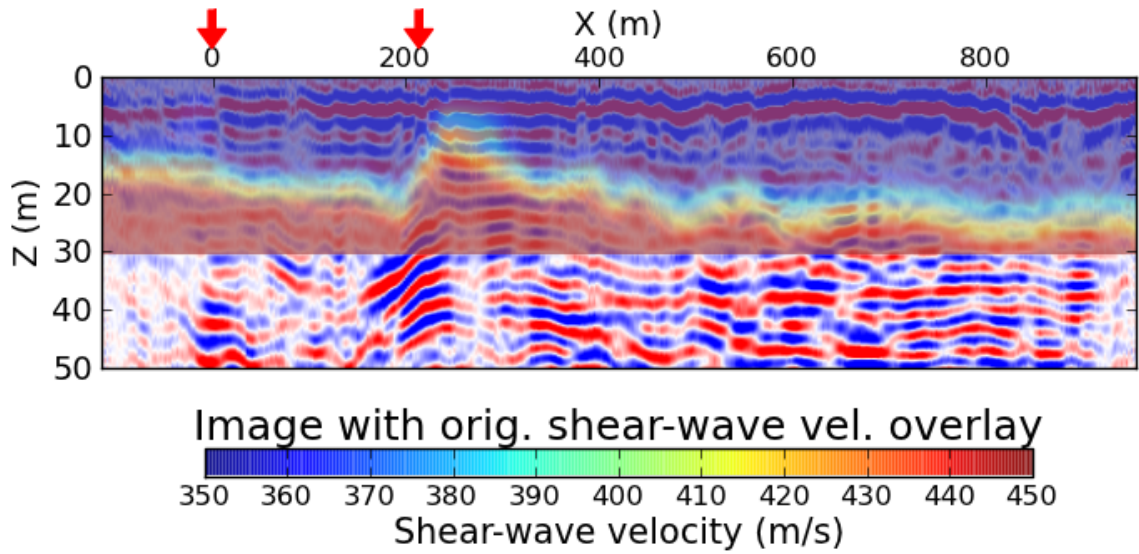


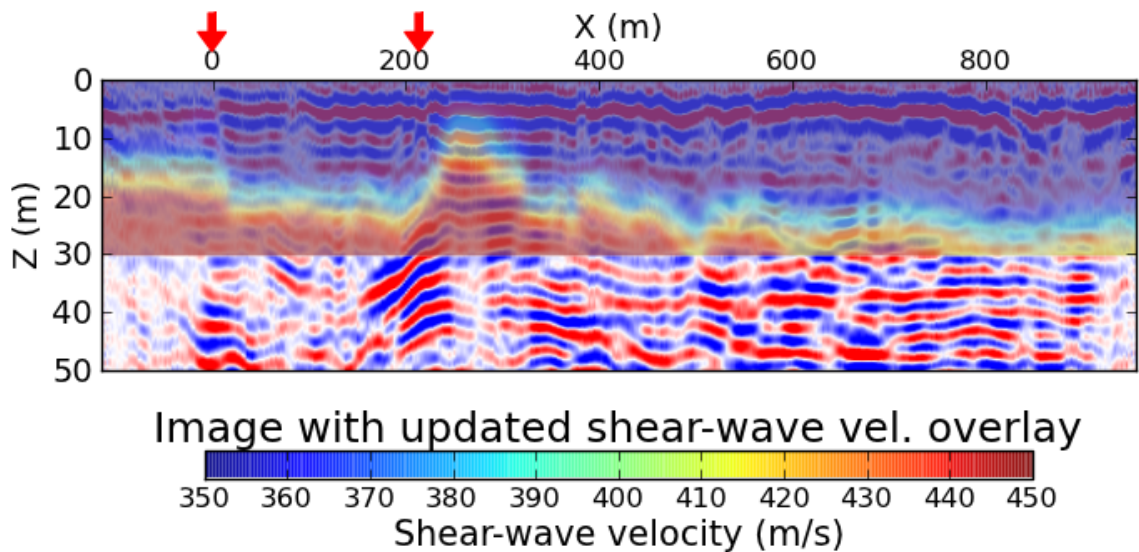
Figure 6.7: (a) Seismic image from Hockley Fault survey.

An initial phase-velocity model is determined by imaging dispersion curves within spatial windows across the extent of the survey. The initial phase-velocity model is updated using

the iterative inversion scheme described above. Shear-wave velocity is inverted from both the initial phase-velocity model and updated phase-velocity model. The original shear-wave velocity model (Figure 6.8a) and the shear-wave velocity model updated using surface wave reflectivity (Figure 6.8b) are overlain on the migrated image. Note that the frequency content of the surface wave has limited our inversion result to a 30 m depth. Below that depth shear-wave velocities are truncated.



(a)



(b)

Figure 6.8: (a) Seismic image with shear-wave velocity model overlay determined by direct surface-wave processing, and (b) seismic image with overlay determined by reflected surface-wave processing.

It is interesting that a velocity anomaly exists in both the original and updated velocity model near the surface expression of the Hockley Fault. The updated velocity model sharpens the velocity change at the fault and reveals more nuanced velocity structure elsewhere.

The large velocity structure at a location of 200 m in both the initial and updated model corresponds with the fault at the surface and an anticlinal feature slightly deeper in the migrated image. A close inspection of the main fault in the migrated image shows a clear break in strata at a depth of 5 m. The clear break in strata supports the interpretation of a sharp change in properties in the lateral direction at the location of the main fault. The largest update in the velocity model is the sharpened velocity change at the main fault ($X = 0$ m). We interpret the velocity change as a normal fault and suggest that a small graben feature exists between the two marked faults.

6.5 Summary

Multichannel analysis and inversion of the direct surface-wave provide laterally smooth shear-wave velocity models. Characteristics of the direct surface-wave at a particular location are the result of an averaged culmination of properties along the path. Surface-wave reflections occur where there is sharp lateral change. Therefore, using reflections and reflectivity has the potential of resolving lateral boundaries.

Our synthetic tests show that the potential can be used to increase the lateral resolution of the shear-wave velocity model. As illustrated by results at Hockley Fault, the updated shear-wave velocity model provides additional insight about the subsurface not apparent in the original shear-wave velocity model or reflectivity map.

Conclusions

Many assumptions about the survey and the data are made to keep the processing flow computationally efficient. For 2D modeling and processing we process along a single survey line and use a 2D model for processing. The implicit assumption is that faults or other reflectors are normal to the survey line. This assumption is sufficient for our purposes because we specifically orient the survey line to investigate reflectors of interest. For 3D modeling and processing we only discretize to the level that is needed for wavefield extrapolation and for describing boundaries and the velocity model. This allows us to save computational time.

Our 2D and 3D modeling, processing, imaging, and inversion is based on picked dispersion curves of the fundamental mode of the outgoing wave. We therefore ignore the higher modes of the surface wave. We call the result of deconvolving the filtered incoming wave and the outgoing wave “reflectivity”; however, it most likely excludes energy due to higher modes in its estimate. For synthetic and field examples presented here where the fundamental mode dominates energy in the surface wave the error will be small. Caution should be taken when strong higher modes are observed.

We chose a simple one-to-one mapping of frequency to depth to convert the frequency axis of the reflectivity model to depth. As stated earlier, this is an approximate method that

does not take into account the solution for surface-wave propagation. However, the method is sufficient for the purposes of producing an interpretation aid. Because the mapping to depth is so closely tied to velocity a better approach would be to directly invert for the underlying shear-wave velocity model given a spectral reflectivity map. The first three steps of our processing flow combined with an inverse solution could perhaps be used for a more correct mapping to depth while simultaneously determining shear-wave velocity. We also note that whatever method is used, the resolution of the lateral boundary as determined by reflected surface-waves will decrease with depth as the wavelength of the surface wave increases.

We take the approach of calculating reflectivity from the phase-velocity model in our forward model because the relationship is simple to invert and use to update phase-velocities (and the shear-wave velocity model inverted from updated phase-velocities). For the synthetic models presented here, extracted reflectivity from our processing flow matched with reflectivity predicted from our semi-analytic forward modeling.

Noise (defined as any event other than the explainable surface wave) presents a substantial challenge. Most of the 2D processing flow is designed to isolate the incoming and outgoing surface-waves and minimize other noise. Noise is less of a problem when imaging with surface waves with 3D survey geometry. Multiple shots and multiple receivers throughout the image space will have the effect of stacking out noise.

Determining the polarity of reflection coefficients is also difficult in the presence of noise or when the source wavelet is not well known. Because our algorithm for updating velocity is strongly dependent on polarity we do not suggest it's use if there is doubt about the polarity of the reflectivity map. An inversion which simultaneously determines depth and

shear-wave velocity directly from reflection coefficients may be less susceptible to errors in polarity.

Processing surface-wave reflections is a formidable task due to their complex propagation. However, complexity such as dispersion is useful for inferring properties at depth. The same relationship used between frequency and depth in processing direct surface-waves is useful in processing reflected surface-waves.

Careful processing of reflected surface waves is required to produce reflectivity maps that are sharply defined in the lateral direction. Improving the accuracy of the surface-wave dispersion model, via picked dispersion curves or a least-squared fit, results in more sharply defined reflections.

Processing reflected surface waves should also be useful for imaging other discontinuities, such as buried objects, which are difficult to detect using direct surface waves. Using reflectivity to update phase-velocities and increase lateral resolution of the shear-wave velocity model is also useful. As illustrated by field results, especially at Hockley Fault, the updated shear-wave velocity model provides additional insight about the subsurface not apparent in the original shear-wave velocity model or reflectivity map.

Surface-wavefield extrapolation provides a surface-wave reflectivity image which is 3D. Although structures on both sides of each line cause a dilemma of arbitrary reflection direction, additional receiver lines can be used to separate outgoing and incoming wavefields. Given an accurate phase-velocity model and well known source wavelet, the deconvolution imaging condition resolves sharp discontinuities at high resolution and provides an estimate of reflectivity.

Bibliography

- R. E. Abbott, L. C. Bartel, B. P. Engler, and S. Pullammanappallil. Surface-wave and refraction tomography at the FACT Site, Sandia National Laboratories, Albuquerque, New Mexico. *Technical Report SAND20065098, Sandia National Laboratories*, 2006.
- K. Aki and P. G. Richards. *Quantitative Seismology, Theory and Methods, Vol. I and II*. W. H. Freeman, San Fransisco, 1980.
- Robert J. Bascle and Richard L. Foland. Oil and gas assessment of the Utukok special management area, National Petroleum Reserve in Alaska. *Anchorage, Alaska : Bureau of Land Management, Alaska State Office*, 41, 1992.
- P. Bergamo, Daniele D. Boiero, and L.V. Socco. Retrieving 2d structures from surface-wave data by means of space-varying spatial windowing. *Geophysics*, 77(4):3–51, 2012.
- Bastian Blonk and Gerard C. Herman. Inverse scattering of surface waves: A new look at surface consistency. *Geophysics*, 59:963–972, June 1994.
- Bastian Blonk, Gerard C. Herman, and Guy G. Drijkoningen. An elastodynamic inverse scattering method for removing scattered surface waves from field data. *Geophysics*, 60(6):1897–1905, 1995.
- Xander H. Campman, Kasper van Wijk, John A. Scales, and Gerard Herman. Imaging and suppressing near-receiver scattered surface waves. *Geophysics*, 70(2):V21–V29, March–April 2005.
- J.F. Claerbout. *Imaging the Earths Interior*. Blackwell Scientific Publications, 1985.
- J.F. Claerbout and S. Fomel. Image estimation by example: Geophysical Soundings Image Construction, Multidimensional autoregression: <http://sepwww.stanford.edu/sep/prof/gee1-2012.pdf>. 2006. URL <http://sepwww.stanford.edu/sep/prof>.
- Victor Corchete. Review of the methodology for computation of transmission and reflection coefficients for the surface waves propagated through a vertical contact. *Computational Geosciences*, 15:579–586, 2011.
- C. H. Dix. Seismic velocities from surface measurements. *Geophysics*, 20:68–86, 1955.
- Huub Douma and Matthew Haney. Surfacewave inversion for nearsurface shearwave velocity estimation at Coronation field. *SEG Technical Program Expanded Abstracts 2011*, pages 1411–1415, 2011. URL <http://dx.doi.org/10.1190/1.3627466>.

- Khaled Al Dulaijan and Robert R. Stewart. Using surfacewave methods for static corrections: a nearsurface study at Spring Coulee, Alberta. *SEG Technical Program Expanded Abstracts 2010*, pages 1897–1901, 2010. URL <http://dx.doi.org/10.1190/1.3513212>.
- Inmaculada Durá-Gómez and Brian Zurek. 9c 2d Piceance survey: Near-surface velocity model building and tomostatics solution. *SEG Technical Program Expanded Abstracts 2011*, pages 1293–1297, 2011. URL <http://dx.doi.org/10.1190/1.3627440>.
- Matthew M. Haney and Huub Douma. Imaging lateral heterogeneity at Coronation Field with surface waves. *SEG Technical Program Expanded Abstracts 2010*, pages 1851–1855, 2010. doi: 10.1190/1.3513202.
- N. A. Haskell. The dispersion of surface waves on multilayered media. *Bulletin of the Seismological Society of America*, 43:17–34, 1953.
- Thomas H. Heaton. *Engineering Seismology*. California Institute of Technology, Engineering and Applied Science, CE/GE 181 ab., 2014. URL http://www.its.caltech.edu/~heatont/Eng_Seism_Notes/.
- Gerard C. Herman, Paul A. Milligan, Robert J. Huggins, and J. W. Rector. Imaging shallow objects and heterogeneities with scattered guided waves. *Geophysics*, 65(1):247–252, 2000.
- R. Herrmann and D. Russell. Ground roll: Rejection using adaptive phasematched filters. *Geophysics*, 55(6):776–781, 1990. URL <http://dx.doi.org/10.1190/1.1442890>.
- E. N. Its and T. B. Yanovskaya. Reflection and transmission of Rayleigh waves at a vertical interface, Pattern Recognition and Spectral Analysis in Seismology, Moscow. *Computational Seismology*, 10(4):214–222, 1977.
- A. L. Kafka and E. C. Reiter. Dispersion of Rg waves in Southeastern Maine: Evidence for lateral anisotropy in the shallow crust. *Bulletin of the Seismological Society of America*, 77:235–238, 1987.
- V. I. Keilis-Borok. *Seismic Surface Waves in a Laterally Inhomogenous Earth*. Kluwer Academic Publishers, 1986.
- B. L. N. Kennett. *Seismic Wave Propagation in Stratified Media*. Cambridge University Press, 1983. URL <http://press.anu.edu.au?p=63081>.
- Shuhab D. Khan, Robert R. Stewart, Maisam Otoum, and Li Chang. Case history. A geophysical investigation of the active Hockley Fault System near Houston, Texas. *Geophysics*, 78(4):B177–B185, 2013.
- Dimitri Komatitsch and Jeroen Tromp. Spectral-element simulations of global seismic wave propagation-I. Validation. *Geophysics Journal International*, 149:390–412, 2002. doi: 10.1046/j.1365-246X.2002.01653.x. URL <http://onlinelibrary.wiley.com/doi/10.1046/j.1365-246X.2002.01653.x/abstract>.
- C. E. Krohn. SWIPER multi-mode surface wave prediction and removal by waveform matching. *72nd EAGE Conference and Exhibition*, page P413, 2010. URL <http://earthdoc.eage.org/publication/publicationdetails/?publication=39873>.

- Sunwoong Lee and Warren S. Ross. 3-D mitigation of surfacewave noise in spatially inhomogeneous media. *SEG Technical Program Expanded Abstracts 2008*, pages 2561–2565, 2008. URL <http://dx.doi.org/10.1190/1.3063875>.
- D. Leparoux, A. Bitri, and G. Grandjean. Underground cavities detection: a new method based on seismic rayleigh waves. *European Journal of Environmental and Engineering Geophysics*, 5:33–53, 2000.
- Leland Timothy Long and A. H. Kocaoglu. Surface-Wave GroupVelocity Tomography for Shallow Structures. *Symposium on the Application of Geophysics to Engineering and Environmental Problems*, pages 85–94, 1999.
- Peter Malischewsky. Surface Waves in Media having Lateral Inhomogeneities. *Papegeoph, Birkhauser, Verlag, Basel*, 114:833–843, 1976.
- A. McGarr. Transmission and Reflection of Rayleigh Waves at Vertical Boundaries. *Journal of Geophysical Research*, 72(8), April 1967.
- T. Meier, P. G. Malischewsky, and H. Neunhofer. Reflection and Transmission of Surface Waves at a Vertical Discontinuity and Imaging of Lateral Heterogeneity Using Reflected Fundamental Rayleigh waves. *Bulletin of the Seismological Society of America*, 87(6): 1648–1661, December 1997.
- S. Nazarian. *In Situ Determination of Elastic Moduli of Soil Deposits and Pavement Systems by Spectral Analysis of Surface Waves Method*. PhD thesis, University of Texas at Austin, 1984.
- Mark Ng. Prestack migration of shot records using phase shift plus interpolation. *Canadian Journal of Exploration Geophysics*, 30(1):11–27, 1994.
- S. Operto, C. Ravaut, L. Improta, J. Virieux, A. Herrero, and P. Dell’Aversana. Quantitative imaging of complex structures from dense wide-aperture seismic data by multiscale travelttime and waveform inversions: a case study. *Geophysical Prospecting*, 52(6):625–651, 2004.
- Choon Byong Park, Richard D. Miller, and Jianghai Xia. Imaging dispersion curves of surface waves on multi-channel record. *68th Annual International Meeting, Society of Exploration Geophysicists, Expanded Abstracts*, pages 1377–1380, 1998. URL <http://masw.com/files/PAR-98-03.pdf>.
- Choon Byong Park, Richard D. Miller, and Jianghai Xia. Multichannel analysis of surface waves. *Geophysics*, 64(3):800–808, 1999.
- A. D. Pierce. Extension of the method of normal modes to sound propagation in an almost-stratified medium. *The Journal of the Acoustical Society of America*, 37:19–27, 1965.
- G.J. Rix and K.H. Stokoe. Stiffness Profiling of Pavement Subgrades. *Transportation Research Record No. 1235*, 1989.
- W. S. Ross and P. M. Shah. Vertical seismic profile reflectivity: Ups over downs. *Geophysics*, 52(8):1149–1154, 1987. URL <http://dx.doi.org/10.1190/1.1442379>.

- Soumya Roy, Eray Kocel, Nikolay Dyauro, and Robert R. Stewart. Lateral heterogeneity and surface-wave inversion (MASW). *SEG Technical Program Expanded Abstracts 2013*, pages 1909–1913, 2013. URL <http://dx.doi.org/10.1190/segam2013-1084.1>.
- D. R. Russell. *Multi-channel processing of dispersed surface waves*. PhD thesis, Saint Louis University, 1987.
- Bernhard Schuberth. *Seismology and Seismics Seminar*. Ludwigs-Maximilians-Universitat Munchen, 2003.
- Vladimir Shtivelman. Using surface waves for mapping lateral inhomogeneities in the shallow subsurface. *European Journal of Environmental and Engineering Geophysics*, 2000.
- S.D. Sloan, S.L. Peterie, J. Ivanov, R.D. Miller, and J.R. Mcenna. Void detection using near-surface seismic methods, in r.d. miller, j.d. bradford and k. holliger, eds. *Advances in Near-Surface Seismology and Ground-Penetrating Radar: Tulsa, Society of Exploration Geophysicists, SEG Geophysical Developments*, pages 201–218, 2010.
- L.V. Socco and C. Strobbia. Surface-wave method for near-surface characterization: a tutorial. *Near Surface Geophysics*, 2(4):165–185, 2004.
- L. Sonneland and E. Berg. A new method for separating wave fields into up-and down-going components. *47th Meeting, European Association of Exploration Geophysicists, Extended Abstract*, Abstract B-46:300–312, 1985.
- Robert R. Stewart. Median filtering: Review and a new f/k analogue design. *Journal of the Canadian Society of Exploration Geophysicists*, 21(1):54–63, 1985. URL http://209.91.124.56/publications/journal/1985_12/1985_Stewart_R_median_filtering.pdf.
- K.H. Stokoe, G.J. Rix, and S. Nazarian. In situ seismic testing with surface waves. *Proceedings of the Twelfth International Conference on Soil Mechanics and Foundation Engineering, Rio de Janeiro, Brazil*, pages 330–334, 1989.
- X. M. Tang, C. Li, and D. Patterson. A curve-fitting method for analyzing dispersion characteristics of guided elastic waves. *SEG Technical Program Expanded Abstracts 2009*, 2009.
- Albert Tarantola. Inversion of seismic reflection data in the acoustic approximation. *Geophysics*, 49(8):1259–1266, 1984. URL http://www.ipgp.fr/~tarentola/Files/Professional/Papers_PDF/InversionOfSeismic.pdf.
- A. C. Tarr. Rayleigh-wave dispersion in the North Atlantic Ocean, Caribbean Sea, and Gulf of Mexico. *Journal of Geophysical Research*, 74:1591–1607, 1969.
- W. T. Thomson. Transmission of elastic waves through a stratified solid medium. *Journal of applied Physics*, 21:89–93N, 1950.
- John E. Vidale and Robert W. Clayton. A stable free-surface boundary condition for two-dimensional elastic finite-difference wave simulation. *Geophysics*, 51(12):2247–2249, 1986.
- J. Virieux. P-SV wave propagation in heterogeneous media: Velocity-stress finite-difference method. *Geophysics*, 51(4):889–901, 1986.

Jianghai Xia, Richard D. Miller, and Choon B. Park. Estimation of near-surface shear-wave velocity by inversion of Rayleigh waves. *Geophysics*, 64(3):691–700, May-June 1999. URL <http://www.kgs.ku.edu/Geophysics2/Pubs/Pubs/XIA-99-04.pdf>.

Jia Yan and Paul Sava. Angle-domain elastic reverse-time migration. *Center for Wave Phenomena research report, CWP-597*, 2008.